

# **Photodissociation Dynamics of Halogenated Heterocyclic Molecules in Gas Phase**

*By*

**Doddipatla Srinivas**

**CHEM01201304035**

**Bhabha Atomic Research Centre, Mumbai**

*A thesis submitted to the  
Board of Studies in Chemical Sciences*

*In partial fulfillment of requirements*

*for the Degree of*

**DOCTOR OF PHILOSOPHY**

*of*

**HOMI BHABHA NATIONAL INSTITUTE**






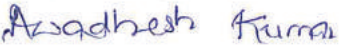
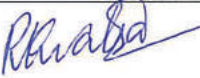
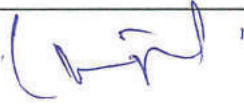
**July, 2018**



# Homi Bhabha National Institute

## Recommendations of the Viva Voce Committee

As members of the Viva Voce Committee, we certify that we have read the dissertation prepared by Mr. Doddipatla Srinivas entitled "Photodissociation Dynamics of Halogenated Heterocyclic Molecules in Gas Phase" and recommend that it may be accepted as fulfilling the thesis requirement for the award of Degree of Doctor of Philosophy.

 Chairman - Prof. P.D. Naik	Date: 12/10/2018
 Guide / Convener - Prof. Hari P. Upadhyaya	Date: 12/10/18
 Examiner - Prof. Tapas Chakraborty	Date: 12/10/2018
 Member - Prof. Awadhesh Kumar	Date: 12.10.2018
 Member - Prof. R. K. Vatsa	Date: 12/10/2018
 Member - Prof. C. Majumder	Date: 12/10/18

Final approval and acceptance of this thesis is contingent upon the candidate's submission of the final copies of the thesis to HBNI.

I hereby certify that I have read this thesis prepared under my direction and recommend that it may be accepted as fulfilling the thesis requirement.

Date: 12/10/18

Place: Mumbai

  
Guide: Prof. Hari P. Upadhyaya



## STATEMENT BY AUTHOR

This dissertation has been submitted in partial fulfillment of requirements for an advanced degree at Homi Bhabha National Institute (HBNI) and is deposited in the Library to be made available to borrowers under rules of the HBNI.

Brief quotations from this dissertation are allowable without special permission, provided that accurate acknowledgement of source is made. Requests for permission for extended quotation from or reproduction of this manuscript in whole or in part may be granted by the Competent Authority of HBNI when in his or her judgment the proposed use of the material is in the interests of scholarship. In all other instances, however, permission must be obtained from the author.

  
Doddipatla Srinivas



## DECLARATION

I, hereby declare that the investigation presented in the thesis has been carried out by me.

The work is original and has not been submitted earlier as a whole or in part for a degree / diploma at this or any other Institution / University.

  
Doddipatla Srinivas






## List of Publications arising from the thesis

### Journal

- 1 Dynamics of Chlorine Atom Formation in the Photodissociation of Halogenated Pyrimidines at 235 nm  
**D. Srinivas**, Monali N. Kawade, and Hari P. Upadhyaya  
*Chem. Phys.* Communicated
- 2 Resonance Enhanced Multiphoton Ionization Time-of-Flight (REMPI-TOF) Detection of Br ( $^2P_j$ ) Atoms in the Photodissociation of 4-bromo-2,3,5,6-tetrafluoropyridine at 234 nm: Effect of Low-lying  $\pi\sigma^*$  State.  
**D. Srinivas**, Y. Sajeev, and Hari P. Upadhyaya.  
*J. Photochem. Photobiol. A* **2017**, 345, 1–10
- 3 Dynamics of Cl( $^2P_j$ ) Formation in the Photodissociation of Halogenated Thiadiazole at 235 nm: A Resonance Enhanced Multiphoton Ionization Time-of-Flight (REMPI-TOF) Study.  
**D. Srinivas** and Hari P. Upadhyaya  
*J. Photochem. Photobiol. A* **2016**, 322, 41–52
- 4 Chlorine Atom Formation Dynamics in the Dissociation of Halogenated Pyridines after Photoexcitation at 235 nm: A Resonance Enhanced Multiphoton Ionization Time-of-Flight (REMPI-TOF) study.  
**D. Srinivas** and Hari P. Upadhyaya  
*Chem. Phys.* **2016**, 472, 208–217
- 5 Ground State Dissociation Pathways for 3,4-dichloro-1,2,5-thiadiazole: Spectroscopic Observation and Fate of NC–C(Cl<sub>2</sub>)–N=S isomer.  
**D. Srinivas** and Hari P. Upadhyaya  
*Chem. Phys. Lett.* **2016**, 660, 182–188

  
Doddipatla Srinivas



## List of publications (not included in this thesis)

### Journal

1. Rate Coefficient of Hydroxyl Radical Reaction with Dimethyl Ether Over a Temperature Range of 275-333 K  
Monali Kawade, A. Shrama, **D. Srinivas**, A. Saha, Hari P. Upadhyaya, A. Kumar, P.D. Naik  
*Chem. Phys. Lett.* **2018**, 706, 558–563
2. Gas Phase OH Radical Reaction with 2-chloroethyl vinyl ether in the 256-333 K Temperature Range: A Combined LP-LIF and Computational Study.  
Monali N. Kawade, **D. Srinivas**, Hari P. Upadhyaya  
*ChemistrySelect* **2018**, 3, 5910–5919
3. Dissociation Pathways for the Molecular Cation of 3,4-dichloro-1,2,5-thiadiazole: A Time-of-Flight Mass Spectrometry and Computational Study.  
**D. Srinivas** and Hari P. Upadhyaya  
*Rapid. Commun. Mass. Spectrom.* **2017**, 31, 121–128
4. Kinetics of gas phase OH radical reaction with thiophene in the 272–353 K temperature range: A laser induced fluorescence study  
Monali N. Kawade, **D. Srinivas**, Hari P. Upadhyaya  
*Chem. Phys. Lett.* **2017**, 682, 154–159



Doddipatla Srinivas



## Conferences

- 1 Trombay Symposium on Radiation and Photochemistry (TSRP-2018)  
Mumbai, India.
- 2 International Symposium on Molecular Beams (ISMB-2017)  
Nijmegen, the Netherlands.
- 3 Spectroscopy and Dynamics of Molecules and Clusters (SDMC-2017)  
Puducherry, India.
- 4 National Symposium on Radiation and Photochemistry (NSRP-2017)  
Manipal, India.
- 5 Trombay Symposium on Radiation and Photochemistry (TSRP-2016)  
Mumbai, India.
- 6 Spectroscopy and Dynamics of Molecules and Clusters (SDMC-2016)  
Mahabaleshwar, India.
- 7 National Symposium on Radiation and Photochemistry (NSRP-2015)  
Kanpur, India.



Doddipatla Srinivas



**DEDICATED**

**TO**

**MY PARENTS**





## ACKNOWLEDGEMENTS

*This thesis work would have not been possible without the support and inspiration of many people. Herewith, I would like to take this opportunity to express my gratitude to them for their unconditional help and support.*

*Firstly, I would like to express my gratitude to my mentor, Dr. Hari P. Upadhyaya, who has given me much guidance, support and encouragement throughout my Ph.D. work. Not only a source of knowledge whenever I needed it and it was often, but also I must thank him for his kindness and patience when the “going gets tough”. I take this opportunity to thank Dr. B. N. Jagatap (Former Director, Chemistry Group) and Dr. D. K. Palit (Former Head, Radiation and Photochemistry Division) for their constant support and encouragement during my research work. I cannot forget mentioning Dr. P. D. Naik, Associate Director, Chemistry Group, I am grateful for all time that we spent in discussion and setting up LP-LIF setup for kinetic studies. My special thanks are directed to Dr. Awadhesh Kumar, Head, E&ISS for his support. I am also thankful to Dr. Sumana SenGupta for sharing scientific knowledge with me. Drs. Ankur Saha and Monali Kawade are thanked for all the help and good times in these past few years. I appreciate all the knowledge you have imparted to me and all the help with experimental problems encountered. I also thank our “Gas-Phase Group” for providing a great time in the lab, outside of the lab and at the many conferences we attended. I also appreciate the help from Asmita Sharma, Mohini Walavalkar and Dr. Hariprasad Alwe. I wish to thank Dr. Y. Sajeev for his help in some theoretical calculation.*

*I would like to thank the members (Dr. Awadhesh Kumar, Dr. R. K. Vatsa, Dr. C. Majumder) and the chairman, Dr. P. D. Naik, of the doctoral committee for their valuable suggestions and comments during all scientific meetings. I wish to express*

*special thanks to Dr. R. K. Vatsa for meticulously going through the thesis and his constructive comments.*

*I have made many great friends since coming to BARC, Mumbai and would like to thank everyone including Avinash Singh, G. Somu Naidu, Ganga Babu, A. Satish Kumar, Tapas K Das, Bharat Bhushan, Shitiljit Sharma, Chandrakanth, Utpal Dutta, Pralay Paul, Vishal, Sivaram, Raman, shaukatali, Poojan, Kishore Babu, C. Ashok for being with me in all the time.*

*I am obligated to Department of Atomic Energy (DAE) for the award of a doctoral fellowship, Radiation and Photochemistry Division, BARC and Homi Bhabha National Institute for providing the research facilities.*

*I am also indebted to Prof. P. Shyamala, Andhra University for sending me to BARC for the project work during my M.Sc. course. During this project, BARC instigated research interest in my mind, the result of which can be seen as the successful completion of my Ph.D.*

*My deepest gratitude goes to my family for their unflagging love and support throughout my life. I am indebted to my mother and father for their encouragement. I am everything because of you and the confidence you have build on me. I should thank my siblings for providing unconditional support.*

# CONTENTS

	<b>Page No.</b>
<b>SYNOPSIS</b>	1
<b>LIST OF FIGURES</b>	9
<b>LIST OF TABLES</b>	17
<b>CHAPTER 1</b> Introduction	19
1.1 Interaction of radiation with matter	20
1.1.1 Electronic selection rules for multi-electron atoms	20
1.1.2 Electronic selection rules for diatomic molecules	21
1.1.3 Electronic selection rules for polyatomic molecules	21
1.2 Different methods of preparing electronic excited states	22
1.2.1 One photon excitation	22
1.2.2 Multiphoton excitation	22
1.2.3 Electron impact excitation	23
1.3 Fate of electronically excited molecules	23
1.3.1 Photophysical processes	24
1.3.2 Photochemical processes	25
1.4 Photodissociation processes	26

1.4.1 Types of photodissociation	27
1.5 Photodissociation dynamics	28
1.6 Techniques for probing the nascent photofragments	30
1.6.1 Resonance Enhanced Multiphoton Ionization (REMPI)	31
1.7 Experimentally obtained parameters from photodissociation process and its implication	32
1.7.1 Translational energy distribution	32
1.7.2 Branching ratio	34
1.7.3 Vector correlations	35
1.7.3.1 Recoil anisotropy E- $\mu$ - $v$ correlation	35
1.7.3.2 Rotational alignment E- $\mu$ -J correlation	36
1.7.3.3 The $v$ -J correlation and the E- $\mu$ -( $v$ -J) correlation	36
1.8 <i>Ab initio</i> methods	37
1.8.1 The Hartree–Fock (HF) self-consistent field (SCF) method	37
1.8.2 Multiconfiguration self-constitent field (MCSCF)	38
1.8.3 Density Functional Theory (DFT)	39
1.9 Programmes used to perform computational studies	39

1.9.1 Methods	40
1.9.2 Basis set	40
1.10 Motivation and outline of the thesis	41
<b>CHAPTER 2</b> Experimental methods	45
2.1 Introduction	45
2.2. Generation of molecular beam	46
2.3 Interaction of molecular beam with laser	46
2.4 Mass detection	50
2.5 Analysis of data acquired from experiment to obtain the dynamic parameters	53
2.6 Laser	56
2.6.1 Nd:YAG laser	56
2.6.2 Dye laser	57
2.7 Vacuum	59
2.7.1 Rotary pump	59
2.7.2 Turbo molecular pump	60
2.8 Microchannel plate detector	61
<b>CHAPTER 3</b> UV-Photodissociation of 3,4-dichloro-1,2,5-thiadiazole	63
3.1 Introduction	63
3.2 Experimental	66

3.2.1 REMPI-TOF-MS	66
3.2.2 Absorption and emission measurements	67
3.2.3 Computational details	68
3.3 Analysis of REMPI-TOF experimental data	69
3.4 Results	69
3.4.1 Absorption spectra and absolute cross-section	69
3.4.2 Spin-orbit branching ratio	70
3.4.3 Translational energy distribution and anisotropy parameter	71
3.4.4 Theoretical calculation on ground state dissociation of 3,4-dichloro-1,2,5-thiadiazole	73
3.4.5 UV emission	75
3.4.6 UV–Vis absorption	76
3.5 Discussion	77
3.5.1 Nature of excitation at 235 nm	77
3.5.2 Translational energy release and anisotropy parameter	82
3.5.3 UV emission spectroscopic investigations	87
3.5.4 UV–Vis absorption spectroscopic investigations	91
3.5.4.1 Isomerization reaction	91
3.5.4.1.1 Isomer 1	91

3.5.4.1.2 Isomer 2	93
3.5.4.2 Dimerization reaction	94
3.5.4.2.1 Dimer 1	94
3.5.4.2.2. Dimer 2	94
3.5.4.2.3. Dimer 3	94
3.5.4.2.4 Dimer 4	94
3.6. Conclusions	96
<b>CHAPTER 4</b> Photodissociation of Halogenated Pyridines at 235 nm	99
4.1 Introduction	99
4.2 Experimental	103
4.3 Analysis	103
4.4 Results	104
4.4.1. Absorption spectra and absolute cross-section	104
4.4.2 Spin-orbit branching ratio	105
4.4.3 Translational energy distribution and anisotropy parameter	106
4.4.4 Theoretical calculation on ground state dissociation of 3-chloropyridine	107
4.5 Discussion	110
4.5.1 Nature of excitation at 235 nm	110
4.5.2 Translational energy release and anisotropy	115

	parameter	
	4.5.3 Mechanism of the dissociation process	121
	4.6 Conclusion	123
<b>CHAPTER 5</b>	<b>C–Br Bond Dissociation Dynamics of 4-bromo-2,3,5,6-tetrafluoropyridine</b>	<b>125</b>
	5.1 Introduction	125
	5.2 Experimental	128
	5.3 Analysis	129
	5.4 Computational methods	129
	5.5 Results	130
	5.5.1 Absorption spectra and absolute cross-section	130
	5.5.2 Spin–orbit branching ratio	130
	5.5.3 Translational energy distribution and anisotropy	132
	parameter	
	5.6 Discussion	135
	5.6.1 Nature of excitation at 234 nm	135
	5.6.2 Translational energy release and anisotropy	138
	parameter	
	5.6.3 Comparison with chloropyridine and effect of	146
	fluorine substitution	
	5.7 Conclusion	147



<b>CHAPTER 6</b>	Photodissociation Dynamics of Halogenated Pyrimidines at 235 nm	149
	6.1 Introduction	149
	6.2 Experimental	152
	6.3 Analysis	152
	6.4 Computational methods	153
	6.5 Results	153
	6.5.1 Absorption spectra and absolute cross-section	153
	6.5.2 Spin-orbit branching ratio	154
	6.5.3 Translational energy distribution and anisotropy parameter	155
	6.6 Discussion	157
	6.6.1 Absorption spectra and electronic transitions at 235 nm	157
	6.6.2 Translational energy release and the dissociation mechanism	160
	6.7 Conclusion	165
<b>CHAPTER 7</b>	Summary and future direction	167
	<b>References</b>	173



**SYNOPSIS**

**Introduction**

The process of photodissociation is the breaking of one or several bonds in a molecule through the absorption of photon. The area of photodissociation dynamics concerns with the detailed mechanisms of photodissociation process investigated on molecular level. One of the principal goal of these kind of studies is to obtain a clear picture of the various dynamic processes in the excited electronic state as the molecule leaves the Franck-Condon region, traverses the ‘transition state’ (i.e., the barrier, if there is any), and finally reaches the asymptotic channel(s), where the fragments are formed. Photodissociation experiments are generally performed state selectively i.e. molecule being prepared in well defined quantum state. Therefore, results from these kinds of experiments are readily compared with the theoretical calculations, resulting in significantly enhanced understanding of the elementary chemical processes [1].

Photodissociation dynamics of various molecules of interest are studied in molecular beam (MB) generated by supersonic expansion through a pulsed valve after seeding it in Helium gas. The isolated molecules in the MB are photodissociated using ultraviolet (UV) laser. One of the resultant photofragments, in the present case mainly atomic species, is probed using Resonance Enhanced Multiphoton Ionization Time-of-Flight Mass Spectrometry (REMPI-TOF-MS). The combination of supersonic molecular beam, REMPI and TOF mass spectrometer has potential of detecting the chemical species state and mass selectively

In this thesis, the photodissociation dynamics of halogenated heterocyclic molecules has been studied. It is well known that the photodissociation of halogen containing molecules in the UV range generates halogen atoms which are detrimental for

## Synopsis

the ozone layer in the stratosphere. Also, it is fundamentally interesting to study the halogenated heterocyclic molecules because of their rich excited state dynamics due to their radiationless transitions, vibronic and spin-orbit coupling. Further, effect of fluorine atom substitution on dynamics has also been investigated. In this context, five and six member heterocyclic molecules have been chosen with one to three hetero atoms in the ring.

For a clear and systematic presentation, the work has been divided into seven chapters. The brief overview of these chapters is given in the following paragraphs.

### **Chapter 1**

This chapter gives brief account of the photodissociation dynamics and its importance. Photodissociation process involves interaction of radiation with molecules, therefore, this chapter starts with interaction of electromagnetic radiation with matter which includes electronic excited state selection rules for atoms and molecules. Various methods for preparing the molecules in electronic excited state by absorption of photons are also described. The fate of electronically excited molecule was discussed which includes photophysical and photochemical processes. One of the processes, after electronic excitation is photodissociation. Various studies in this thesis are focused on photodissociation process where photofragments are probed by REMPI technique, which is discussed in detail. The scalar dynamic parameter such as translational energy distribution and different models to explain this distribution are discussed in detail. The different types of vector correlations also occur during the photodissociation process and are also highlighted in this chapter. The theoretical calculations are employed to aid interpretation of the experimental results. Therefore, a brief note on the computational chemistry and methods employed in this thesis are presented.

### Chapter 2

The second chapter describes experimental technique and instrumentation employed to execute the work presented in this thesis. MB-REMPI-TOF-MS technique has been used to detect the nascent photofragments under collisionless conditions to obtain the dynamic information.

In the present REMPI experiments, the same laser beam was employed for photodissociation of parent molecule and ionization of photofragments such as, Cl and Br atoms, state selectively by (2+1) REMPI scheme. The required wavelength for probing the photofragments was obtained by using dye laser (Quantel) with frequency doubling and mixing modules, using Rhodamin 101 dye pumped by a Nd:YAG laser. The generated ions were detected using two-stage Wiley–McLaren[2] TOF mass spectrometer, with an extraction and an acceleration region. The polarization of the laser was rotated, using a double Fresnel rhomb to obtain the polarization dependent time-of-flight profiles.

The analysis procedure to obtain the dynamic parameters, namely translational energy distribution and anisotropy parameter from the experimental data has been discussed in detail.

### Chapter 3

In Chapter 3, the UV-photodissociation study of 3,4-dichloro-1,2,5-thiadiazole is presented. The Cl atom formation dynamics has been investigated in a supersonic molecular beam by exciting at 235 nm, which prepares the molecules in its  $\pi\pi^*$  state[3]. The primary chlorine atoms formed in nascent state are detected in their spin-orbit states, Cl( $^2P_{3/2}$ ) and Cl\*( $^2P_{1/2}$ ). The translational energy distributions could be explained with only one component for both Cl and Cl\* atom elimination channel. The TOF profiles for Cl and Cl\* are found to be independent of laser polarization, i.e., the anisotropy parameter ( $\beta$ ) has a value of  $\sim 0$ , within the experimental uncertainties. A zero value of

## Synopsis

anisotropy parameter indicates that the dissociation is slower than the rotational time period of the molecule. The energy partitioning into the translational modes is interpreted with the help of impulsive and statistical models. The vertical excitation energies for various transitions were calculated using Time-Dependent Density Functional Theory (TD-DFT). It indicates that first repulsive state involves ( $\sigma^*_{\text{N-S}}$ ,  $\sigma^*_{\text{C-Cl}}$ )  $\leftarrow \pi$  transition and it has repulsive nature for both N-S and C-Cl bonds. Therefore, the potential energy curves are generated along C-Cl and N-S bond lengths. From the experimental results and computational calculations, it is concluded that initially prepared  $\pi\pi^*$  state crosses over to a nearby  $\sigma^*$  repulsive state along the C-Cl bond, from where the dissociation takes place. The results also indicate the role of fast internal conversion to ground state from the initially prepared  $\pi\pi^*$  state from where various dissociation channels occur.

The ground state photodissociation pathways are also investigated at various wavelengths in the UV region[4]. The photolysis products are identified by the UV absorption and emission spectroscopy. The molecular chlorine ( $\text{Cl}_2$ ) elimination was observed using absorption method in the UV region. UV absorption and theoretical calculation confirms the migration of chlorine atom and subsequent ring opening to form NC-C( $\text{Cl}_2$ )-N=S isomer. The UV emission was observed at 389 nm due to CN ( $\text{B}^2\Sigma^+$ ) moiety, formed in the multiphoton excitation of the parent molecule. The new UV absorption bands observed at ~255 and ~290 nm were assigned to the its isomer NC-C( $\text{Cl}_2$ )-N=S.

## Chapter 4

In Chapter 4, the photodissociation dynamics of two halogenated pyridines, namely, 3-chloropyridine (ClPy) and 3-chloro-2,4,5,6-tetrafluoropyridine (ClFPy) are reported[5]. The excitation at 235 nm prepares both the molecules in the  $\pi\pi^*$  state. The dynamics of chlorine atom elimination channels in these two compounds are studied by

## Synopsis

determining the photofragment speed distribution, the anisotropy parameter ( $\beta$ ), and the spin-orbit branching ratio. The anisotropy parameters for both Cl and Cl\* are the same, and characterized by value of  $\sim 0$ . The translational energy distributions for the chlorine atom elimination channel in both cases are best described by only one component. However, this does not imply that there is only one channel for the Cl atom elimination. In general, if different multi-channel components have broader energy distributions, it may appear as one channel with very broad energy distribution. For ClPy, the average translational energies for Cl and Cl\* channels are determined to be  $3.7 \pm 1.0$  and  $7.0 \pm 1.5$  kcal/mol, respectively. Similarly for ClFPy, the average translational energies for Cl and Cl\* are determined to be  $8.0 \pm 1.5$  and  $9.0 \pm 1.5$  kcal/mol, respectively. The relative quantum yield,  $\Phi(\text{Cl}^*)$ , is also determined for ClPy and ClFPy during the course of studies and found to be  $0.09 \pm 0.02$  and  $0.11 \pm 0.02$ , respectively. The energy partitioning into the translational modes is interpreted with the help of various models, such as impulsive and statistical models. The higher average translational energy released into the chlorine atom elimination channel in fluorine substituted chloropyridine is explained with the help of theoretical calculation. The calculation suggests that the fluorine substitution increases the possibility of crossover to  $\pi\sigma^*$  state from initially prepared  $\pi\pi^*$  state.

## Chapter 5

This chapter deals with C–Br bond dissociation dynamics following excitation of 4-bromo-2,3,5,6-tetrafluoropyridine at around 234 nm[6]. The translational energy distributions for the bromine atom elimination was determined using polarization-dependent and state-specific TOF profiles employing a forward convolution method and taking into account the fragment anisotropy. The energy distribution is best described by two components, namely, fast and slow. The anisotropy parameter for both Br and Br\* are the same, and characterized by values of  $0.60 \pm 0.05$ . A positive and non-zero

## Synopsis

anisotropy parameter indicates that the dissociation is faster than the rotational time period of the molecule. The potential energy surfaces (PESs) were generated for various excited states for the Br atom elimination channel using two different approaches, one at single and other at multi reference level. The TD-DFT approach has been used at single reference level while multi-configurational quasidegenerate second order perturbation theory (QDMCPT2) was used for multi reference level. Both theoretical approaches suggest that the initially prepared  $\pi\pi^*$  state crosses over to a nearby  $\pi\sigma^*$  repulsive state along the C–Br bond, from where the dissociation takes place. The results also indicate the process of fast internal conversion to ground state from the initially prepared  $\pi\pi^*$  state, which eventually forms slow Br atoms after C–Br bond dissociation process on the ground state. Finally, the results are compared with chloro-pyridines and effect of fluorine substitution has been discussed.

### Chapter 6

The dynamics of chlorine atom formation in the photodissociation process of halogen substituted pyrimidines, namely, 2,4,6-trichloropyrimidine and 5-chloro-2,4,6-trifluoropyrimidine has been studied around 235 nm. In both the molecules, the TOF profiles for Cl and Cl\* are found to be independent of laser polarization suggesting a  $\beta$  value of  $\sim 0$ , within the experimental uncertainties. The nature of translational energy distribution indicates the significance of the statistical dissociation from the ground state. Computational calculations were performed to generate the potential energy curves along the dissociating C–Cl bond using Equation-of-Motion coupled cluster singles and doubles (EOM-CCSD). These computational calculations suggested that in both these molecules, initially prepared state at 235 nm excitation is  $\pi\pi^*$  state. For 2,4,6-trichloropyrimidine and 5-chloro-2,4,6-trifluoropyrimidine, the potential well depth of the  $\pi\pi^*$  state is  $\sim 16$  and  $\sim 10$  kcal/mol respectively. This clearly indicates that the lifetime of  $\pi\pi^*$  state in



2,4,6-trichloropyrimidine is more and the probability of internal conversion to the ground state is more probable. Hence, the dissociation from the ground state is more significant in case of 2,4,6-trichloropyrimidine, which is clearly visible in the average translational energy ( $E_T$ ). The excited triplet states also play a significant role in the Cl atom formation in both the molecules.

### Chapter 7

This chapter provides a summary of the work carried out in this thesis, and layout of future work in this field. This thesis presents detail on halogen atom formation dynamics of halogenated heterocyclic molecules in UV region using REMPI-TOF-MS technique. The effect of halogen atom substitution on C–Cl/C–Br bond dissociation dynamics has been investigated in five/six member heterocyclic molecules with one to three hetero atoms in the ring. Various scalar and vector dynamic parameters have been measured and computational calculations were performed to interpret the experimental results.

In this thesis, the photodissociation dynamics of one N-containing (pyridines), two N-containing (pyrimidines) and both N and S-containing (thiadiazoles) heterocyclic molecules are studied. For 3,4-dichloro-1,2,5-thiadiazole, excitation at 235 nm prepares the molecule in  $\pi\pi^*$  state. The TOF profiles for Cl and Cl\* are found to be independent of laser polarization and well explained with single velocity component. Initially prepared  $\pi\pi^*$  state crosses over to first repulsive  $\pi\sigma^*$  state. It has repulsive nature along both C–Cl and N–S bond. The energetics determined from the computational calculations suggest that N–S bond cleavage is more favorable than C–Cl bond dissociation. The ground state dissociation pathways are also investigated at various wavelengths in UV region. Molecular chlorine ( $\text{Cl}_2$ ) and CN ( $\text{B}^2\Sigma^+$ ) moiety formation were observed using UV

## Synopsis

absorption and emission spectroscopy. In the case of ClFPy translational energy released into chlorine atom elimination channel was more compared to ClPy. This is due to the fact that fluorine substitution lowers the energy of  $\pi\sigma^*$  state facilitating the cross over to  $\pi\sigma^*$  state from initially prepared  $\pi\pi^*$  state. For 4-bromo-2,3,5,6-tetrafluoropyridine initial excited state at 234 nm is  $\pi\pi^*$  state but translational energy distributions are very much different than the ClFPy. In this case, TOF profiles are well described by two velocity components which depend on the polarization of laser indicating a non-zero anisotropy parameter. A hybrid model is employed to explain the average translational energies. Finally, the results are compared with chlorinated pyridines and effect of fluorine substitution was discussed. In case of halogenated pyrimidines, namely, 2,4,6-trichloropyrimidine and 5-chloro-2,4,6-trifluoropyrimidine, TOF profiles are well described by single velocity component and independent of laser polarization. The translational energy distribution suggests that major pathway for the Cl atom formation is through ground state dissociation and a minor channel arising from the excited state, probably a triplet state.

### **Future Directions**

A REMPI technique was used to perform all the experiments carried out in this thesis and a single laser was employed, for the photodissociation of parent molecule as well as for probing the photofragments by ionization. More detailed information about excited PESs and their interactions can be deduced by accessing various excited PESs. This will be possible by populating the different PESs by using different wavelength laser for photodissociation and another laser for probing the photofragments. The resolution in translational energy distribution measurement can be improved by employing the velocity map imaging (VMI) technique.

**LIST OF FIGURES**

1.1	Schematic of energy levels of excited molecule and along with their various transitions. Vertical straight lines represent radiative transitions, wavy lines represent non-radiative transitions.	25
1.2	Photodissociation processes (a) Direct dissociation (b) Electronic predissociation in which molecules undergo radiationless transition (rt) (c) Vibrational predissociation in which the photon creates a quasi-bound state in the potential well which decays either by tunnelling (tn) or by intramolecular vibrational energy redistribution (IVR) (d) Spontaneous radiative dissociation.	27
1.3	Photodissociation processes from ground electronic state (a) the photon creates a bound level in the upper electronic state which subsequently decays as a result of a radiationless transition (rt) to the electronic ground state. In (b) overtone pumping directly creates a quantum state above the threshold of the electronic ground state	29
1.4	Schematic of one color REMPI schemes: A) (1+1) REMPI; B) (2+1) REMPI and C) (3+1) REMPI. $S_i$ , $S_f$ and IC refer the initial ground state, resonant excited state and the ionization continuum respectively.	31
1.5	Energy partitioning, using hybrid model for the dissociation process $A-BC \rightarrow A+BC$	34
2.1	A schematic diagram of MB-REMPI-TOF-MS system.	47
2.2	(2+1) REMPI scheme for Cl and Cl* detection	48
2.3	(2+1) REMPI scheme for Br and Br* detection	48

## List of Figures

2.4	Schematic of the Nd:YAG pumped dye laser system for generating ~ 234 nm.	50
2.5	Schematic of the ion source. Plates $f_1$ , $f_2$ , and $f_3$ stands for the repeller plate, extraction and acceleration grid, respectively	51
2.6	The voltage divider for supplying the requisite power to the MCP	52
2.7	Flow chart of analysis procedure of REMPI data.	56
2.8	Energy levels of Nd:YAG laser.	57
2.9	Schematic representation of energy levels of an organic dye.	58
2.10	Microchannel plate.	61
3.1	UV absorption spectrum of 3,4-dichloro-1,2,5-thiadiazole at room temperature.	69
3.2	Doppler profiles of Cl and Cl* atoms produced in the 235 nm laser photolysis of 3,4-dichloro-1,2,5-thiadiazole used for the determination of their ratio.	70
3.3	REMPI-TOF profiles of Cl ( $^2P_{3/2}$ ) and Cl* ( $^2P_{1/2}$ ) produced from the photodissociation of 3,4-dichloro-1,2,5-thiadiazole at 235 nm. The circles are the experimental data and the solid line is a forward convolution fit.	72
3.4	Centre-of-mass recoil translational energy distribution derived from figure. 3.3 for Cl ( $^2P_{3/2}$ ) and Cl* ( $^2P_{1/2}$ ), produced in the photodissociation of 3,4-dichloro-1,2,5- thiadiazole at 235 nm.	72
3.5	Relative energy diagram in kcal/mol, along with the structures, for the various products in the photodissociation of 3,4-dichloro-1,2,5-thiadiazole at 235 nm in its ground state.	73

## List of Figures

- 3.6 Temporal profiles of CN ( $B^2\Sigma^+ \rightarrow X^2\Sigma^+$ ) emission at  $\sim 388$  nm produced in the photolysis of 3,4-dichloro-1,2,5-thiadiazole at different wavelengths, namely, 266 and 235 nm. The green dotted line is laser profile (Gaussian, FWHM = 8 ns) [Inset: (a) CN ( $B^2\Sigma^+ \rightarrow X^2\Sigma^+$ ) emission spectra. (b) Magnified temporal profiles]. 75
- 3.7 Temporal profiles of CN ( $B^2\Sigma^+ \rightarrow X^2\Sigma^+$ ) emission at  $\sim 388$  nm produced in the photolysis of 3,4-dichloro-1,2,5-thiadiazole at 248 nm. The green dotted line is laser profile (Gaussian, FWHM = 15 ns) [Inset: (a) Dependence of the observed CN ( $B^2\Sigma^+ \rightarrow X^2\Sigma^+$ ) emission intensity at  $\sim 388$  nm on the laser (248 nm) intensity. The slope of the fitted linear log-log plot is  $2.0 \pm 0.1$ . (b) Magnified temporal profiles showing the rising part]. 76
- 3.8 (1a) UV absorption spectrum of the 3,4-dichloro-1,2,5-thiadiazole recorded at 2 Torr of pressure. (1b) After 10-min photolysis at 235 nm. (1c) After 20-min photolysis at 235 nm. (2a) Difference UV spectrum for 10 min photolysis. (2b) 20 min photolysis at 235 nm. 77
- 3.9 Computed HOMO, LUMO, along with other MOs involved in the transition of 1,2,5-thiadiazole and 3,4-dichloro-1,2,5-thiadiazole. 80
- 3.10 Various diabatic potential energy curves calculated for 3,4-dichloro-1,2,5-thiadiazole along the C-Cl and N-S bond length with the other geometrical parameters optimized for the ground state using TD-DFT method 86
- 3.11 Schematic potential energy diagram for various process in the photodissociation of 3,4-dichloro-1,2,5-thiadiazole at 235 nm. 87
- 3.12 Relative energy diagram in kcal/mol, along with the structures, for the 89

## List of Figures

- various channels forming  $\text{CN}(\text{B}^2\Sigma^+)$  species in the photodissociation of 3,4-dichloro-1,2,5-thiadiazole in its ground state.
- 3.13 Relative energy diagram in kcal/mol, along with the structures, for the various isomerization reaction of 3,4-dichloro-1,2,5-thiadiazole and dimerization reactions of ClCNS. 95
- 4.1 UV absorption spectrum of 3-chloropyridine and 3-chloro-2,4,5,6-tetrafluoropyridine at room temperature with their absolute absorption cross-section. 104
- 4.2 REMPI-TOF profiles of Cl ( $^2\text{P}_{3/2}$ ) and Cl\* ( $^2\text{P}_{1/2}$ ) produced from the photodissociation of A) 3-chloropyridine and B) 3-chloro-2,4,5,6-tetrafluoropyridine at 235 nm at magic angle ( $\chi = 54.7^\circ$ ). The circles are the experimental data and the solid red line is a forward convolution fit. The instrument function is depicted as the green dotted curve in lower panel of B. 106
- 4.3 Centre-of-mass recoil translational energy distribution derived from figure 4.2 for Cl ( $^2\text{P}_{3/2}$ ) and Cl\* ( $^2\text{P}_{1/2}$ ), produced in the photodissociation of A) 3-chloropyridine and B) 3-chloro-2,4,5,6-tetrafluoropyridine at 235 nm. 108
- 4.4 Relative energy diagram in kcal/mol, along with the structures, for the various products in the photodissociation of 3-chloropyridine at 235 nm in its ground state. 109
- 4.5 Computed HOMO, LUMO, along with other MOs involved in the transition of 3-chloropyridine and 3-chloro-2,4,5,6-tetrafluoropyridine. 113
- 4.6 Various diabatic potential energy curves calculated for 3-chloropyridine and 3-chloro-2,4,5,6-tetrafluoropyridine along the C-Cl 120

## List of Figures

- bond length with the other geometrical parameters optimized for the ground state using TD-DFT method
- 4.7 Schematic of mechanism for various Cl/Cl\* elimination channels for 3-chloropyridine and 3-chloro-2,4,5,6-tetrafluoropyridine. 122
- 5.1 UV absorption spectrum of 4-bromo-2,3,5,6-tetrafluoropyridine at room temperature with the absolute absorption cross-section. 131
- 5.2 REMPI-TOF profiles of Br ( $^2P_{3/2}$ ) produced from the photodissociation of 4-bromo-2,3,5,6-tetrafluoropyridine at 234 nm. The circles are the experimental data, the dashed lines are forward convolution fit for two different channels, namely, fast and slow and the solid line shows the sum. Three panels, namely, upper, middle and lower panels correspond to different experimental geometries with  $\chi=0^\circ$ ,  $\chi=54.7^\circ$ , and  $\chi=90^\circ$  respectively. 132
- 5.3 REMPI-TOF profiles of Br\* ( $^2P_{1/2}$ ) produced from the photodissociation of 4-bromo-2,3,5,6-tetrafluoropyridine at 234 nm. The circles are the experimental data, the dashed lines are forward convolution fit for two different channels, namely, fast and slow and the solid line shows the sum. Three panels, namely, upper, middle and lower panels correspond to different experimental geometries with  $\chi=0^\circ$ ,  $\chi=54.7^\circ$ , and  $\chi=90^\circ$  respectively. 133
- 5.4 Centre-of-mass recoil translational energy distribution derived from figure 5.2 and 5.3 for Br ( $^2P_{3/2}$ ) and Br\* ( $^2P_{1/2}$ ), produced in the photodissociation of 4-bromo-2,3,5,6-tetrafluoropyridine at 234 nm. 134
- 5.5 Computed HOMO, LUMO, along with other MOs involved in the transition of 4-bromo-2,3,5,6-tetrafluoropyridine. 136

## List of Figures

5.6	Various diabatic potential energy curves calculated for 4-bromo-2,3,5,6-tetrafluoropyridine along the C–Br bond length with the other geometrical parameters optimized for the ground state using TD-DFT method.	143
5.7	Various diabatic potential energy curves calculated for 4-bromo-2,3,5,6-tetrafluoropyridine along the C–Br bond length using multi configuration quasi degenerate second order perturbation theory (MCQDPT2). The ground state geometrical parameters are optimized at MP2 level.	143
6.1	UV absorption spectra of (A) 2,4,6-trichloropyrimidine (B) 5-chloro-2,4,6-trifluoropyrimidine at room temperature.	154
6.2	REMPI-TOF profiles of Cl ( $^2P_{3/2}$ ) and Cl* ( $^2P_{1/2}$ ) produced from the photodissociation of (A) 2,4,6-trichloropyrimidine and (B) 5-chloro-2,4,6-trifluoropyrimidine at 235 nm at magic angle ( $\chi = 54.7^\circ$ ). The circles are the experimental data and the solid line is a forward convolution fit. The instrument function is depicted as the blue dotted curve in lower panel of B.	155
6.3	Centre-of-mass recoil translational energy distribution derived from figure 6.2 for Cl ( $^2P_{3/2}$ ) and Cl* ( $^2P_{1/2}$ ), produced in the photodissociation of (A) 2,4,6-trichloropyrimidine and (B) 5-chloro-2,4,6-trifluoropyrimidine at 235 nm.	156
6.4	Computed HOMO, LUMO, along with other MOs involved in the transition of (A) 2,4,6-trichloropyrimidine and (B) 5-chloro-2,4,6-trifluoropyrimidine	159
6.5	Various adiabatic potential energy curves calculated for (A) 2,4,6-	163



## List of Figures

trichloropyrimidine and (B) 5-chloro-2,4,6-trifluoropyrimidine along the C–Cl bond length with the other geometrical parameters optimized for the ground state using EOM-CCSD method.



## LIST OF TABLES

1.1	Commonly used methods in Gaussian program	40
1.2	Commonly used basis functions and their description	41
3.1	Vertical excitation energies (eV) and oscillator strengths (given in parentheses) of low-lying singlet states of 1,2,5-thiadiazole and 3,4-dichloro-1,2,5-thiadiazole with respective designation. The $C_{2v}$ symmetry designation for both the compounds, nature of transition and MO's involved in the transitions are also included in the table.	79
3.2	Calculated vertical excitation energies (nm) and oscillator strengths (given in parentheses) of low-lying singlet states of 3,4-dichloro-1,2,5-thiadiazole along with its isomers, dimers of CICNS, CICNS and SNCCN. Transitions with calculated oscillator strength less than of 0.0010 are not shown in the table. Vertical excitation energies are calculated using TD-DFT method employing aug-cc-pVDZ basis set.	92
3.3	Calculated vertical excitation energies (nm) and oscillator strengths (given in parentheses) of low-lying singlet states of isomer 1, $NC-C(Cl_2)-N=S$ using various methods employing aug-cc-pVDZ basis set.	93
4.1	Vertical excitation energies (eV) and oscillator strengths (given in parentheses) of low-lying singlet states of 3-chloropyridine and 3-chloro-2,4,5,6-tetrafluoropyridine with respective designation. The $C_s$ symmetry designation for both the compounds, nature of transition and MOs involved in the transitions are also included in the table.	112
4.2	The average translational energy, $\langle E_T \rangle$ , available energy ( $E_{avail}$ ), $f_T$ value, and the relative quantum yield ( $\Phi$ ) for photodissociation of 3-	118

## List of Tables

chloropyridine and 3-chloro-2,4,5,6-tetrafluoropyridine at  $h\nu=235$  nm. The excitation energy is 122 kcal/mol. The  $D_0^0$  (C-Cl) is taken as 95.0 kcal/mol. All energies are in kcal/mol.

- 5.1 Vertical excitation energies ( eV, nm) and oscillator strengths (given in 136 parentheses) of low-lying singlet states of 4-bromo-2,3,5,6-tetrafluoropyridine with respective designation calculated using TD-DFT method. The  $C_{2v}$  symmetry designation, nature of transition and MO's involved in the transitions are also included in the table.
- 6.1 Vertical excitation energies and oscillator strengths (given in parentheses) 158 of low-lying singlet states of 2,4,6-trichloropyrimidine and 5-chloro-2,4,6-trifluoropyrimidine with respective state designation calculated using EOM-CCSD. The  $C_{2v}$  symmetry designation, nature of transition and MO's involved in the transitions are also included in the table.

# Chapter 1

## Introduction

---

The process of photodissociation is the breaking of one or several bonds in a molecule through the absorption of photon. This process is sometimes referred as second half of the full collision of a bimolecular reaction. Whereas, in a bimolecular reaction, two reactants form an intermediate complex during the collision which decays to form products, in the case of photodissociation process, an intermediate state is formed by exciting the reactant with absorption of a photon[7]. It is not only an elementary process in the interaction of light with matter but also of considerable importance in different areas of chemistry and physics[8]. Photodissociation is one of the first steps in the whole field of photochemistry, generating radicals that initiate the subsequent reactions. It is also one of the crucial processes in stratosphere[9,10]. Therefore, understanding of such processes in atomic level is important. The discipline which deals with photodissociation reaction in the microscopic level is called photodissociation dynamics. One of the principal goal of these kind of studies is to obtain a clear picture of the various dynamic processes happening in the excited electronic state as the molecule leaves the Franck-Condon region, traverses the 'transition state' (i.e., the barrier, if there is any), and finally reaches the asymptotic channel(s), where the fragments are formed. Photodissociation experiments are generally performed state selectively wherein the molecule of interest is prepared in well defined quantum state. Therefore, results from these kinds of

experiments are readily compared with the theoretical calculations, resulting in significantly enhanced understanding of the elementary chemical processes[1]. The application of lasers in these studies made it possible to prepare a molecule in a particular excited state prior to its dissociation. Therefore, this leads to the true study of the state specified dynamics.

### **1.1 Interaction of radiation with matter**

Electromagnetic radiation is referred as the wave with synchronized oscillation of electric and magnetic fields propagate with the speed of light in vacuum. The oscillations of the two fields are perpendicular to each other and perpendicular to the direction of wave propagation. Different regions of electromagnetic radiation have different effect upon matter. In this thesis, we are mainly concerned with UV radiation so we will restrict our discussion to UV region. When UV radiation interacts with an atom or a molecule, the oscillating electric field component of the radiation disturbs the charge cloud around the atom or the molecule and induces an oscillating dipole moment in the atom or the molecule. This oscillating dipole moment interacts with the electromagnetic radiation. When the frequency of incident radiation matches with the natural frequency required by the energy states, a resonance condition is established and under such condition, a photon is absorbed by the molecule. Absorption of radiation is governed by various selection rules which are discussed below.

#### **1.1.1 Electronic selection rules for multi-electron atoms**

The electronic states in multi-electron atoms are described by quantum numbers. These quantum numbers are given as, principal quantum number ( $n$ ), total orbital angular momentum quantum number ( $L$ ), total spin quantum number ( $S$ ) and total angular momentum quantum number ( $J$ ). Following four general selection rules govern the electronic transition between the atomic states[11].

Rule 1:  $\Delta L = 0, \pm 1$  except  $L=0 \leftrightarrow L=0$

Rule 2: even  $\leftrightarrow$  even, odd  $\leftrightarrow$  odd and even  $\leftrightarrow$  odd

Here even and odd refer to  $\sum_i l_i$  over all electrons

Rule 3:  $\Delta J = 0, \pm 1$  except  $J=0 \leftrightarrow J=0$

Rule 4:  $\Delta S = 0$

### 1.1.2 Electronic selection rules for diatomic molecules

Like in atoms, electronic states in diatomic molecule can be also described by quantum numbers which are i) total orbital angular momentum along the internuclear axis ( $\Lambda$ ) ii) total spin angular momentum along the internuclear axis ( $\Sigma$ ) iii) total angular momentum along the internuclear axis ( $\Omega$ )

Rule 1:  $\Delta \Lambda = 0, \pm 1$

Rule 2:  $\Delta S = 0$

Rule 3:  $\Delta \Sigma = 0$  and  $\Delta \Omega = 0, \pm 1$

along with these, symmetry properties are also involved in the transitions.

Rule 4:  $+\leftrightarrow-; + \leftrightarrow +; - \leftrightarrow -$

Rule 5:  $g \leftrightarrow u; g \leftrightarrow g; u \leftrightarrow u$

### 1.1.3 Electronic selection rules for polyatomic molecules

The total spin quantum number remains similar in polyatomic molecules and selection rule is  $\Delta S = 0$ , however, in the presence of an atom with high nuclear charge, this selection rule relaxes. For orbital part, selection rule depends entirely on symmetry properties. The intensity of electronic transition between two electronic states is proportional to  $|R_e|^2$ , where  $R_e$  is the electronic transition moment, given by

$$R_e = \int \psi_e'^* \mu \psi_e'' d\tau_e \quad (1.1)$$

For an allowed electronic transition  $|R_e| \neq 0$  and symmetry requirement for this is

$$\Gamma(\psi_e') \times \Gamma(\mu) \times \Gamma(\psi_e'') = A \text{ or } \Gamma(\psi_e') \times \Gamma(\mu) \times \Gamma(\psi_e'') \subset A \quad (1.2)$$

The symbol A refers to a totally symmetric representation of concerned point group.

## 1.2 Different methods of preparing electronic excited states

There are different methods to prepare a molecule in the electronic excited state by absorption of photons and electrons, which are mentioned below.

### 1.2.1 One photon excitation

A single UV photon is required to prepare a molecule or an atom in electronic excited state. Electronic excitation is linearly dependent on the intensity of excitation light. Typical single photon absorption cross section is of the order of  $10^{-17}$  cm<sup>2</sup>. The selection rules which govern the single photon excitation are similar to that of electronic selection rules discussed in previous sections.

### 1.2.2 Multiphoton excitation

In many cases, the single UV photon absorption cannot prepare the molecule in some of the excited states due to selection rule restrictions. However, in the presence of high intensity of excitation light, molecule or atom may absorb more than one photon simultaneously. The selection rules for the transition between the two real states are similar to single photon absorption as mentioned above. If all the intermediate states during the multiphoton absorption are real then odd number of photons will lead to gerade  $\leftrightarrow$  ungerade transition, which is similar to single photon absorption. However, in the case of even number of photon absorption, gerade  $\leftrightarrow$  gerade or ungerade  $\leftrightarrow$  ungerade transitions are also possible which are otherwise not possible with single photon absorption [12].

Transition probability for multiphoton absorption is given as

$$W^{(N)} = \sigma_N I^N \quad (1.3)$$

Where  $W^{(N)}$  is the  $N$ -photon transition probability (sec<sup>-1</sup>),  $\sigma_N$  is the  $N$ -photon absorption cross-section with units cm<sup>2N</sup> sec<sup>N-1</sup> and  $I$  is the light intensity expressed as photons cm<sup>-2</sup>



$\text{sec}^{-1}$ . Typical two and three photon absorption cross-section are of the order of  $\sigma_2 \sim 10^{-51} \text{cm}^4 \text{sec}$  and  $\sigma_3 \sim 10^{-82} \text{cm}^6 \text{sec}^2$ , respectively. The single photon absorption cross-section is much higher than that of multiphoton, so higher intensity of light is required for the multiphoton absorption to take place.

### 1.2.3 Electron impact excitation

To prepare a molecule in relatively higher excited state, extreme UV or X-ray radiation is required, which is not easily available, except in expensive synchrotron radiation. In such case, the electrons can be used as a source to prepare the molecule in a higher excited state. The collision of electron with molecule leads to variety of processes like scattering, excitation, ionization and electron capture etc. For slow electrons, optical selection rules are not obeyed. The transition to symmetry and/or spin forbidden states can also be achieved at large scattering angle and hence we are able to observe the excited states, which are otherwise not seen during the excitation by photons. At high impact energy and small scattering angle, the excitation process by electrons is similar to that of photons, which makes electrons as pseudo photons for excitation[13].

### 1.3 Fate of electronically excited molecules

In the process of UV photon absorption by a molecule, electronic excited states are prepared. Different vibrational levels of the electronic excited states are also populated depending on the energy of the photon and Franck-Condon principle. The properties of the electronic excited states are quite different from that of the ground electronic state. The excited states are generally unstable and very short lived. The “short” in this context means lifetime of the excited state ranges from sub-nano second to nano second for an allowed process and the lifetime is extended up to milliseconds for a forbidden process. After photo excitation of a molecule, there are several channels/routes available for an excited molecule to dissipate the energy of excitation; some are radiative,

and some are non-radiative. Some of the channels are grouped under photophysical processes in which intrinsic properties of the molecule are unimolecular in nature. Some other processes depend on external factors and may involve a bimolecular collision.

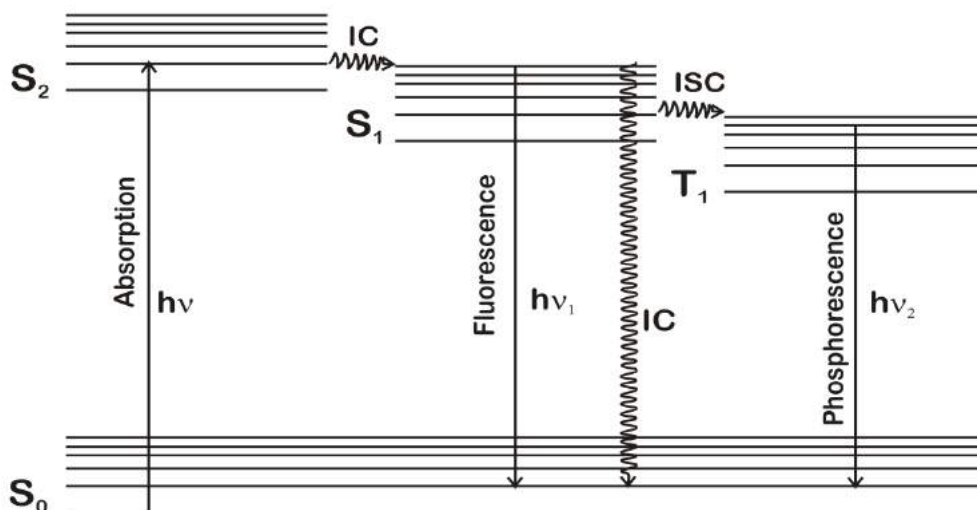
### 1.3.1 Photophysical processes

The electronic excited states of polyatomic molecules are denoted by their spin multiplicity defined as  $2S+1$ , where  $S$  is the spin quantum number. Thus, an electronic state, with all the electrons paired, has  $S=0$  with spin multiplicity of 1, and is referred as a singlet state and denoted as  $S$ . If the electronic state has two electrons with the same spin, then  $S=1$  and spin multiplicity 3, then this is referred as triplet state and denoted as  $T$ .  $S_0$  represents the ground state.  $S_1$  and  $S_2$  represent the first and second singlet excited states respectively. The triplet manifolds are generally represented by  $T_1$  and  $T_2$  and so on. Once the molecule is excited to electronic excited state it can decay to ground electronic state by unimolecular and/or bimolecular processes. In gas phase at low pressure, unimolecular processes are generally more favorable, whereas, in gas phase with higher pressure and condensed phase both unimolecular and bimolecular processes can occur. The various unimolecular processes are given below.



$A^*$  is the molecule with excess vibrational energy in excited singlet states  $S_1$ ,  $S_2$ , etc.  $A^*$ ,  $^3A$  and  $A$  are molecules in the first excited singlet state, triplet state and ground state respectively.

The absorption of photon excites the molecule to higher vibrational levels of  $S_1$ ,  $S_2$ ,  $S_3$ , etc. From these states, molecule relaxes to the lowest vibrational level of  $S_1$  state by internal conversion (IC) process, which is non-radiative. From  $v=0$  level of first excited state, molecule relaxes to the ground electronic state by dissipating its energy in the form of light called as fluorescence emission. However, the molecule can also relax to the ground state without emitting any fluorescence by IC process. It can also undergo non-radiative transition from singlet to triplet state which is referred as inter system crossing (ISC). First triplet state which is populated by ISC decays to ground electronic state by radiative phosphorescence emission. Various photophysical processes in gas-phase are shown in figure 1.1



**Figure 1.1:** Schematic of energy levels of excited molecule and along with their various transitions. Vertical straight lines represent radiative transitions, wavy lines represent non-radiative transitions.

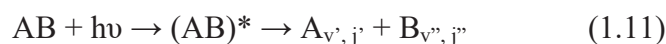
### 1.3.2 Photochemical processes

A molecule in the excited state differs from its ground electronic state with respect to energy and also its geometry, and as a result its chemistry also differs from the ground

state. When a molecule in the ground electronic state absorbs a photon, different vibrational and rotational levels of higher electronic states can be populated in accordance with Franck-Condon principle. This brings about the reactions like photodissociation, photo-rearrangement, and electron transfer etc. which are not feasible in the ground state. The work presented in this thesis is mainly based on photodissociation process which will be described in detail in subsequent sections.

### 1.4 Photodissociation process

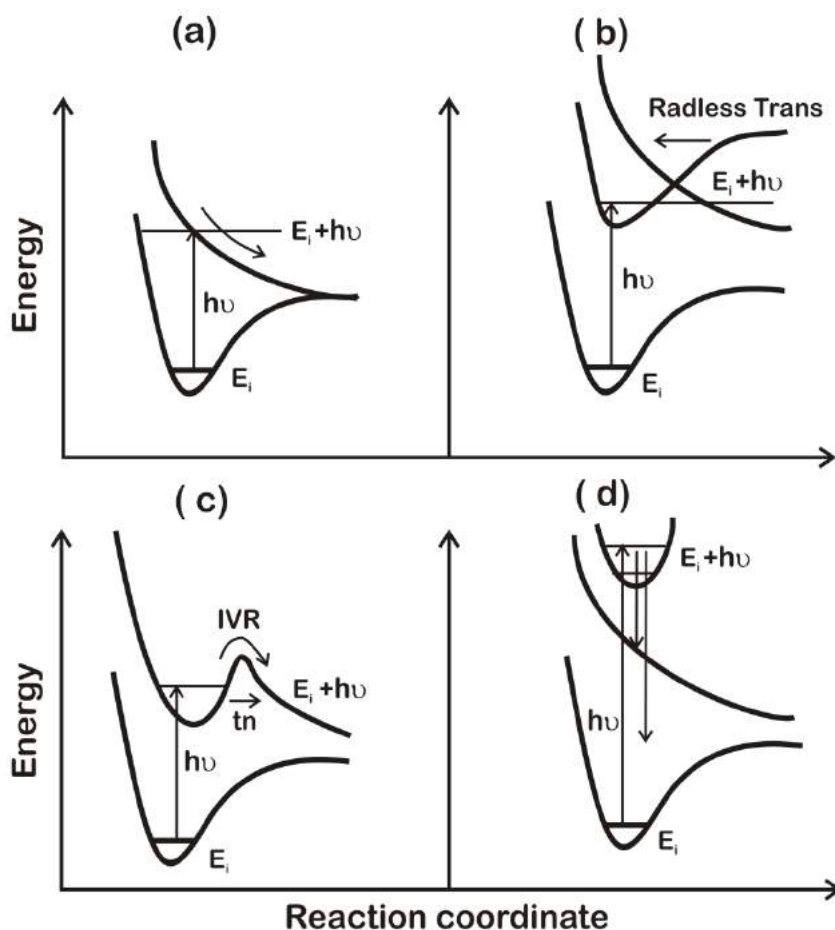
When a photon is absorbed by the molecule, the photon energy converted into internal energy of the molecule, and if this energy exceeds the bond dissociation energy of any chemical bond, the molecule will irreversibly break apart. Fragmentation of a molecule upon absorption of one or more photon(s) is called photodissociation. Let us consider dissociation of a parent molecule AB into products A and B, where A and B represent the atom or radical with internal energy obtained during the dissociation process. In a simple form, the photodissociation process can be represented as



Where  $h\nu$  is the energy of a photon with frequency  $\nu$ ,  $(AB)^*$  is the excited complex and products A and B are formed in its various internal quantum states. The photon energy required for dissociation of the bond varies from few kcal/mol to hundreds of kcal/mol depending on the nature of bond. The light source of various wavelengths are required to dissociate the bonds, due to the wide range of bond dissociation energies. For example, van der Waals bonds can be fragmented with single IR photon where as to dissociate chemical bond single UV photon is required. However, in case of high intense IR laser a polyatomic molecule can absorb tens of IR photons through its vibrational ladder upto sufficiently high energy level which leads to dissociation of chemical bond in the ground electronic state which is referred as Infrared Multiphoton Dissociation (IRMPD)

### 1.4.1 Types of photodissociation

The photodissociation process can be classified into two categories, direct and indirect photodissociation. In direct photodissociation, as shown in figure 1.2 (a) the photon excites the molecule from ground electronic state to excited electronic state, which is repulsive in nature along the reaction coordinate and so, the excited complex ultimately dissociates. Since, the process of spontaneous emission is slow compared to the dissociation process, virtually all absorption leads to dissociation. In indirect dissociation type 1 (shown in figure 1.2 (b)), molecule is initially excited to a bound state from which it can't dissociate into fragments.

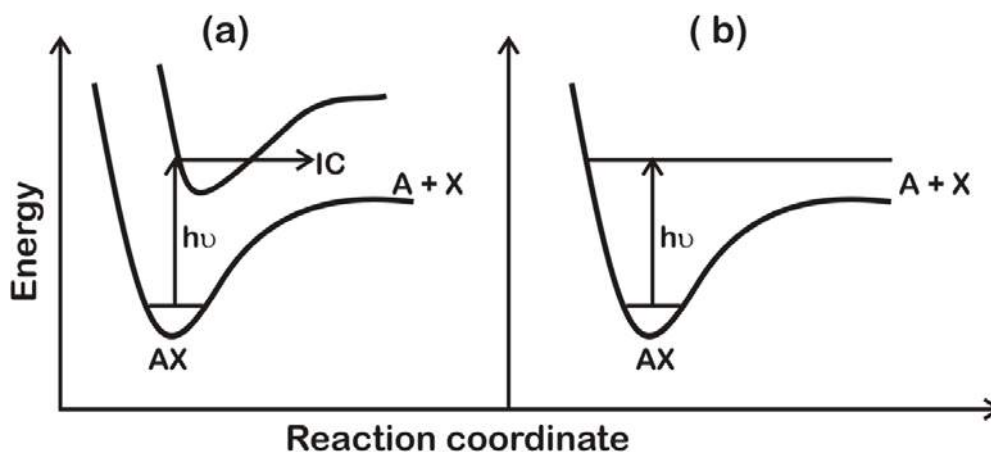


**Figure 1.2:** Photodissociation processes (a) Direct dissociation (b) Electronic predissociation in which molecules undergo radiationless transition (Radless Trans) (c) Vibrational predissociation in which the photon creates a quasi-bound state in the potential well which decays either by tunnelling (tn) or by intramolecular vibrational energy redistribution (IVR) (d) Spontaneous radiative dissociation

However, it can cross over to the repulsive electronic state, from where the excited molecule will decay with the rate which depends on the coupling between these two states. This process is called electronic predissociation or Herzberg's type I predissociation. In case of indirect dissociation type 2 (shown in figure 1.2 (c)), excited state potential energy surface (PES) has a well at close distance and barrier which prevents the direct dissociation. The barrier might be due to an avoided crossing from the higher electronic PESs. When the molecule is excited to quasi-stable (resonant) states inside the potential well it can decay either by tunneling through the barrier or by internal vibrational energy redistribution among the various nuclear degrees of freedom. This process is termed as vibrational predissociation or Herzberg's type II predissociation. Apart from the above mentioned predissociation process, a molecule from the excited bound state can decay to lower repulsive state by emitting a photon is shown in figure 1.2 (d). These direct and indirect dissociation processes are taking place from the excited state. However, there are two additional type of dissociation in which dissociation takes place from the ground state. The excited bound electronic state can relaxes to ground electronic state. This will populate the vibrational-rotational levels of the ground electronic state which are higher than the threshold dissociation energy, so the molecule breaks apart. Alternatively, highly excited quantum states in the ground electronic state are populated by pumping a large amount of energy into the molecule. Both these processes are known as unimolecular reactions and are shown in figure 1.3.

### **1.5 Photodissociation dynamics**

Photodissociation dynamics deals with the mechanism of photodissociation processes in atomistic details, tracing the time evolution of every microscopic step, as far as possible. The energy and angular momentum are conserved in a photodissociation reaction.



**Figure 1.3:** Photodissociation processes from ground electronic state (a) the photon creates a bound level in the upper electronic state which subsequently decays as a result of a radiationless transition (*rt*) to the electronic ground state. In (b) overtone pumping directly creates a quantum state above the threshold of the electronic ground state

The available energy after photodissociation  $E_{\text{avail}}$  defined as  $E_{\text{avail}} = h\nu - D$ , where  $h\nu$  and  $D$  are photon energy and dissociation energy respectively. The  $E_{\text{avail}}$  is distributed between the translational ( $E_{\text{T}}$ ) and the internal energy ( $E_{\text{INT}}$ ) of the photofragments. The internal energy includes electronic, vibrational and rotational energy of the photofragment. The way in which the available energy is distributed among the translational and internal degrees of freedom is called energy distribution. Apart from these scalar properties, there are vector properties by which we can make more detailed dynamic characterization of a photodissociation process. Such vector properties are the electric field vector of light ( $\mathbf{E}$ ), transition moment of the parent molecule ( $\boldsymbol{\mu}$ ), velocity vector ( $\mathbf{v}$ ), and angular momentum vector ( $\mathbf{J}$ ) of recoiling fragments.

With advent of lasers and fast response detectors, a large impetus to the research in photodissociation dynamics field has been given[14]. Some advantages of using laser in photodissociation experiments are given below.

1) The narrow band width of the laser makes it possible to prepare the molecule in particular vibronic and even rotational-vibronic level. In gas phase, under collision less condition, the fate of these excited molecules can be followed in a cleanest way.

- 2) Photofragments can be probed state selectively by employing various laser based detection techniques such as, Laser-Induced Fluorescence (LIF) and Resonance Enhanced Multiphoton Ionization (REMPI) techniques, which give wealth dynamic information.
- 3) Time evolution of process can also be studied using pico- and femto- second lasers
- 4) Vector properties of photodissociation reaction can be obtained by using polarized laser light.

### **1.6 Techniques for probing the nascent photofragments**

A variety of experimental techniques have been developed over the years to characterize the photofragments. The state selective experiments give detailed dynamical information in which most of the quantum numbers of reactant and products are specified. Ideally, such probing techniques are highly sensitive and selective. An ideal detection system should combine three-dimensional spatial resolution with temporal resolution. No single technique is ideal for all photodissociation experiments. Each technique represents a compromise between the generality, sensitivity and resolution. Few of the probing techniques are given below.

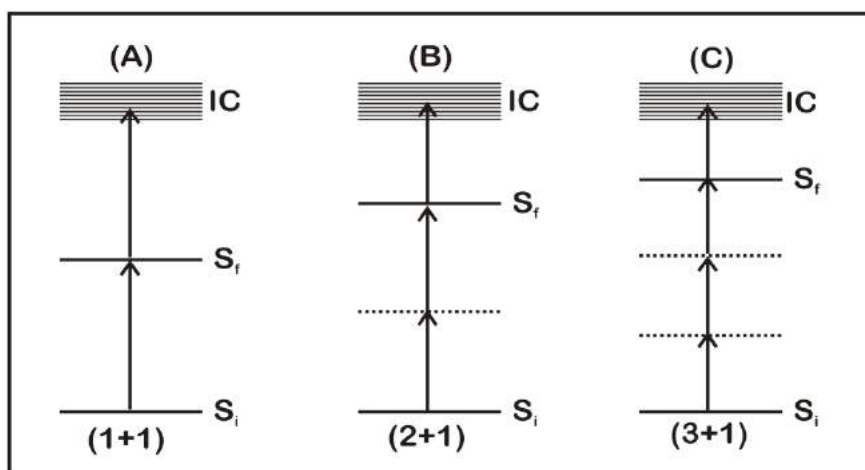
- 1) Photofragment translational spectroscopy[15]
- 2) Laser Induced Fluorescence (LIF) [16]
- 3) Resonance Enhanced Multiphoton Ionization (REMPI) [17]
- 4) Photofragment imaging [18]
- 5) Coherent Anti-Stokes Raman Spectroscopy (CARS) [19]
- 6) Cavity Ring-Down Spectroscopy (CRDS) [20]

REMPI technique has been used to probe the photofragments in the work carried out in this thesis. This technique is discussed below.



### 1.6.1 Resonance Enhanced Multiphoton Ionization (REMPI)

Generally, with the low intensity light one photon absorption process is possible. However, under the high intense light condition, multiphoton absorption can take place. The ionization caused by simultaneous absorption of several photons is called multiphoton ionization (MPI). In Resonance Enhanced Multiphoton Ionization (REMPI) as the name suggests, it proceeds via an intermediate state that is resonant with photon. This resonant state is long lived than the other non-resonant states, which enhances the rate of absorption. REMPI is designated on the basis of the number of photons required to prepare the species in electronic excited state and number of photons required to pump into continuum. REMPI process in which one photon is used for resonant excitation to an upper state and one more photon is used to pump to ionization continuum, is designated as (1+1) REMPI. Other commonly employed REMPI schemes are (2+1) and (3+1) where two and three photons are used for excitation to a resonant intermediate excited state and one photon for pumping to ionization continuum, respectively. The schematic of these REMPI schemes are shown in figure 1.4.



**Figure 1.4:** Schematic of one color REMPI schemes: A) (1+1) REMPI; B) (2+1) REMPI and C) (3+1) REMPI.  $S_i$ ,  $S_f$  and IC refer the initial ground state, resonant excited state and the ionization continuum respectively.

In the above processes, the second-step of transition i.e. ionization is saturated at the typical intensity of about  $10^{26}$  photons  $\text{cm}^2/\text{s}$  obtained from nanosecond pulsed laser

system. REMPI is a convenient method because laser light from the tunable dye laser can be used to ionize the molecule or atom fragments. The ionized species formed are detected by mass spectrometer.

### **1.7 Experimentally obtained parameters from photodissociation process and its implication**

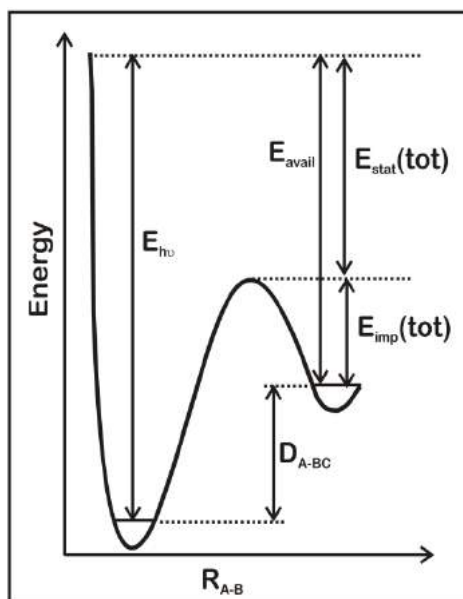
The main aim of photodissociation studies is to obtain the clearest picture of various dynamical processes, once the molecule is excited. When the molecule is electronically excited it leaves the Franck-Condon region, traverses the 'transition state' and finally reaches the asymptotic channel(s), where the fragments are formed. The whole process can be understood by determining both scalar (translational energy distribution, internal energy distribution and branching ratio, etc.) and vector properties (recoil anisotropy parameter) of photofragments formed.

#### **1.7.1 Translational energy distribution**

The measured translational energy of the photofragment provides crucial dynamical information. The recoil velocity of two photofragments after dissociation process must be related by the momentum conservation. Therefore, by measuring the translational energy of one photofragment in center-of-mass frame in turn determines the velocity distribution of the other photofragment. The partitioning of available energy into various degrees of freedom of photofragments is mainly governed by the nature of dissociative PES involved. Different models are often employed to explain the experimentally obtained energy partitioning data. These models range from the statistical model at one end and the impulsive model at another end. The statistical model is often starting model to understand any dissociation event. If the photoexcited molecule is long-lived, then the available energy is distributed statistically among the available degrees of freedom. This dissociation process can be explained predominantly by the statistical

model. This is possible when the rapid internal conversion occurs to ground electronic state, from where subsequent dissociation takes place. Under these conditions relatively small amount of excess energy is partitioned into the translational energy of the photofragments. An analytical expression demonstrated by Klots [21], relates the mean translational energy  $E_T$  and  $E_{avail}$  for statistical barrier less dissociation. On the other hand in the impulsive model, distribution of energy among the photoproducts is governed by the repulsive force acting during the breaking of parent molecule into products. Tuck [22] has proposed a model for calculating the impulsive energy of photofragments. In this model, it is assumed that the available energy is channeled into translational energy of dissociating atoms and these atoms are assumed to be independent of rest of atoms in fragment in the event of dissociation. The conservation of linear momentum may be applied to recoiling atoms to obtain the translational energy of dissociating atoms. Further, fragment translational energy can be calculated by applying conservation of momentum to each of the fragment as recoiling atom in each is slow down by the remainder of the fragment. But in this model, no assumption is made about the stiffness of the bonds, which means no restrictions are placed on the amount of energy which may appear as the fragment vibrational energy. However, it has been observed that neither impulsive model nor statistical model explains the partitioning of the available energy if there is an energy barrier on the dissociative potential energy surface. In such case, combination of the statistical and impulsive model is applicable, which is known as “barrier impulsive model”. In this model, total available energy is divided into impulsive and statistical reservoir. The division of available energy into statistical and the impulsive reservoirs are shown in figure 1.5

$$E_{avail}(tot) = E_{stat}(tot) + E_{imp}(tot) \quad (1.12)$$



**Figure 1.5:** Energy partitioning, using hybrid model for the dissociation process  $A-BC \rightarrow A+BC$

The energy content in the impulsive reservoir is considered as the height of the exit barrier. The localized release of potential energy from the exit barrier after the molecule crosses the transition state is described by the impulsive model. The remaining energy  $E_{stat}(tot)$  is partitioned among the all the rotational, vibrational, and translational degrees of freedom of fragment according to the statistical model. The translational energy from the impulsive model is fixed with the barrier height and the total translational energy increases with increase in available energy [23].

### 1.7.2 Branching ratio

Upon excitation to electronic excited states, several product channels are energetically accessible in photodissociation reaction resulting into various photofragments. These photofragments are mostly radicals which have unpaired electrons often possessing spin and orbital angular momentum. In such cases, photofragments are formed in different energy levels which arise from the coupling between spin and orbital angular momentum. For example, in the present studies, branching ratio of Cl and Br in there spin-orbit states ( $^2P_{3/2}$  and  $^2P_{1/2}$ ) are determined. The relative population of atoms in

their spin-orbit states provides valuable information for understanding the nonadiabatic processes taking place on excited PESs. Two factors governing the branching ratio, are the structure of excited state wave function in Franck-Condon region and coupling between the PESs [24].

### 1.7.3 Vector correlations

In this section the correlation between different vector properties involved in photodissociation process has been discussed for providing a better understanding of dynamics of dissociating event. The most interesting vector properties are

- i) The recoil velocity vector ( $\mathbf{v}$ ) of departing photofragment
- ii) Angular momentum vector(s) ( $\mathbf{J}$ ) of photofragment(s)
- iii) Transition dipole moment ( $\boldsymbol{\mu}$ ) of parent molecule
- iv) Electric field vector of dissociating light ( $\mathbf{E}$ )

Electric field vector of the dissociating light is easy to fix in space. It helps to align the transition dipole moment vector of parent molecule in lab frame. The absorption probability is proportional to  $|\mathbf{E} \cdot \boldsymbol{\mu}|^2$ , which is responsible for alignment of parent molecule in lab frame. After absorption of photon, the parent molecules immediately align such that the probability of finding the molecule along the angle  $\theta$ , angle between the electric field vector and transition dipole moment, is proportional to  $\cos^2\theta$ .

#### 1.7.3.1 Recoil anisotropy $\mathbf{E}$ - $\boldsymbol{\mu}$ - $\mathbf{v}$ correlation

Zare and Herschbach first observed the fact that vector correlation between  $\boldsymbol{\mu}$  and  $\mathbf{v}$  leads to an anisotropic distribution of photofragments. In every molecule, there is a fixed angular correlation between the direction of transition dipole moment and direction of recoil photofragment. In most of the cases, direction of recoil of the fragment is along the bond breaking during the photodissociation process. The alignment of  $\boldsymbol{\mu}$  in laboratory frame by polarized photodissociation light leads to alignment of  $\mathbf{v}$  if bond breaking occurs

on the time scale shorter than the rotational period of the parent molecule. The measurement of anisotropy of recoil velocity distribution gives information about the time scale of dissociation event and symmetry of transition in parent molecule.

### 1.7.3.2 Rotational alignment E- $\mu$ -J correlation

Like  $\mu$ - $v$  vector correlation, there is an angular correlation between transition dipole moment and the plane of fragment rotation. This leads to alignment of rotational angular momentum in the lab frame. Since,  $\mu$  is aligned in the lab by  $E$ , therefore,  $J$  will be also aligned. This alignment is strong when the dissociation is on shorter time scale than parent molecule rotational time period.

### 1.7.3.3 The $v$ -J correlation and the E- $\mu$ -( $v$ -J) correlation

The  $J$  and  $v$  are correlated with  $\mu$ , therefore, it is not surprising to have the correlation between  $v$  and  $J$ . The above mentioned two correlations E- $\mu$ - $v$  and E- $\mu$ - $J$  depend on the relative rate of dissociation and parent molecule rotational time period, whereas, the  $v$ - $J$  correlations are independent of these factors. This is because, the anisotropy and alignment depends on the  $\mu$  which is aligned in laboratory frame. These correlations will be lost if molecule rotates prior to dissociation. Whereas, the  $v$ - $J$  correlation is not achieved with the instant of dissociation and hence it is always independent of laboratory frame. If dissociation is rapid both  $v$  and  $J$  will show correlation in the lab frame [25,26].

The experimentally obtained parameters provide us the knowledge of partitioning of available energy among the photoproducts, coupling between the electronic states and time taken for the bond dissociation. These results, when compared with the various models help in formulating the mechanism for reaction. The results obtained from various models can be elucidated by computational calculations. The computational methods used to support the experimental work carried out in this thesis are explained below.

### 1.8 *Ab initio* methods

In a simple term, theoretical chemistry may be defined as the mathematical description for understanding the chemistry. The term computational chemistry is usually used when a mathematical method is sufficiently well developed and that can be automated for implementation on a computer. There are two broad areas within computational chemistry devoted to the structure of molecules and their reactivity: Molecular mechanics and electronic structure theory. Molecular mechanics uses the laws of classical physics to predict the structure and properties of the molecule. The electronic structure methods use laws of quantum mechanics for computational purpose. The quantum mechanics states that the energy and other properties of a molecule may be obtained by solving the Schrödinger equation,  $H\Psi=E\Psi$ . The exact solution of Schrödinger equation is not possible except in the case of smallest and totally symmetric system. Electronic structure methods are characterized by various mathematical approximations to its solutions and these can be categorized as *ab initio* and semi-empirical. The semi-empirical method uses a simpler Hamiltonian than the correct molecular Hamiltonian and adjustable parameters obtained from the experimental data. In *ab initio* method computations are based solely on the laws of quantum mechanics and on values of physical constants like the speed of light, mass, and charge of electron and nuclei and Planck's constant etc. The main advantages of *ab initio* method are i) it is applicable for the broad range of systems, ii) does not depend on experimental data and iii) capable of calculating transition states and excited states.

#### 1.8.1 The Hartree-Fock (HF) self-consistent field (SCF) method

The Hartree-Fock method is the starting point for many *ab initio* methods. The Schrödinger equation has the exact solution for  $H_2^+$  molecule and one electron systems. In general case, for finding solution of Schrödinger equation, we have to rely on

approximations of relativistic effects. The electron-electron repulsion is one of the important effects which must be incorporated in electronic structure calculation for accurate results. In Hartree-Fock method electron-electron repulsion is treated in an average way, where each electron is considered in the electrostatic field of nuclei, and remaining electrons. A spinorbital is a product of an orbital wavefunction and a spin wavefunction. The spinorbitals that give best wavefunction are obtained by the variational theorem. The application of this minimization procedure leads to Hartree-Fock equations for individual spinorbitals states. Each spinorbital state is obtained by solving in an iterative manner and stopped when solution is self-consistent, hence, the name self-consistent field (SCF) is given to this approach [27].

### **1.8.2 Multiconfiguration self-consistent field (MCSCF)**

In this thesis, the studies are mostly focused on bond breaking by exciting molecules to higher electronic states. The reactant (before bond breaking) and products (after bond breaking) are reasonably well described by using simple wave function however, it is not true for the intermediate states, such as transition states, reactive intermediates, and excited electronic states. Such states are often described by more complex wave functions in which several different arrangements of electrons (electron configuration) are taken into account. MCSCF is appropriate to compute the energy of this kind of states. In MCSCF the wave function is written in configuration interaction (CI) form as a linear combination of Salter determinants and CI coefficients are determined variationally. MCSCF method is particularly important for excited state calculations. The orbitals involved are divided into three categories

1. Inactive orbitals: Composed of lowest energy orbitals which are doubly occupied
2. Virtual orbitals: Very high energy orbitals which are unoccupied
3. Active orbitals: Orbitals energetically between inactive and virtual orbitals.



Active electrons are those electrons which are not present in doubly occupied inactive orbitals [27].

### **1.8.3 Density Functional Theory (DFT)**

The electronic wave function of an  $n$ -electron molecule depends on  $4n$  variables, three spatial and one spin coordinate for each electron. The electron density is the square of the wave function. The advantage of considering electron density over wave function is that density depends on the same number of variables and independent of the size of the system whereas, wave function complexity increases with increase in the number of electrons. The problem with electron density is that it is not known how electron density depends on energy but it is proven that different electron density yields different energy. The goal of DFT method is to design functionals connecting electron density with energy.

A function is a prescription for producing a number from a set of variables. A functional is a prescription for producing a number from a function, which in turn depends on variables. DFT methods have become popular because it gives better results even for large polyatomic molecules[28].

### **1.9 Programmes used to perform computational studies**

The computational studies are carried out in this thesis by using Gaussian 03[29] and GAMESS-US quantum chemistry packages[30]. Optimization, single point energy, and TD-DFT excitation energies are calculated using Gaussian 03 program. The Gauss View program is used to visualize the molecules and orbitals. The excitation energy calculations with MCSCF are performed by GAMESS program with molecules and orbitals are visualized using WxMacMolPlt software.

### 1.9.1 Methods

The Gaussian 03, program offers different methods corresponding to different approximations. Some of the keywords for the methods used in this work are listed in table 1.1.

**Table 1.1:** Commonly used methods in Gaussian program

Keyword	Methods
HF	Hartree-Fock Self-Consistent Field
MP2	2 <sup>nd</sup> Order Møller-Plesset Perturbation Theory
QCISD	Quadratic Configuration Interaction Singles and Doubles
CIS	Configuration Interaction Singles
MP3	3 <sup>rd</sup> Order Møller-Plesset Perturbation Theory
MP4	4 <sup>th</sup> Order Møller-Plesset Perturbation Theory
QCISD(T)	Quadratic CI Singles, Doubles and Triples

### 1.9.2 Basis set:

One of the essential steps in all *ab initio* methods is introducing basis set. Expanding the unknown molecular orbital function in known function is not an approximation if the basis set is complete. Complete basis set includes infinite functions it is not possible in actual scenario. When a finite basis set is used, only the components of the molecular orbital along those coordinate axes corresponding to the selected basis functions can be represented. Smaller basis set leads to a poorer representation of molecular orbital and influence the accuracy of the calculation. In real scenario, molecular orbitals (MOs) are represented by finite basis set, which leads to imperfect representation causing basis-set truncation error. In table 1.2 some commonly used basis set are given.

**Table 1.2:** Commonly used basis functions and their description

Basis set	Description	No. of basis function	
		heavy atom*	hydrogen
STO-3G	Minimal basis set: Used for more qualitative results for big systems	5	1
3-21G	2 sets of functions in the valence region: Used when 6-31G is too expensive	9	2
6-31G(d)	Adds polarization functions to heavy atoms: Used for most jobs up to medium size systems	15	2
6-31G(d,p)	Adds polarization functions to hydrogen as well: Used when hydrogens are the site of interest	15	5
6-31+G(d)	Adds diffuse functions: Most important for systems with lone pairs, anions, excited states	19	2
6-31+G (d,p)	Adds p functions to hydrogen as well: Used when diffuse functions are needed over 6-31G(d,p)	19	5
6-311+G (d,p)	Adds extra valence functions (3 sizes of s and p functions) to 6-31+G(d,p)	22	6
6-311+G (2d,2p)	Puts 2d and 1f functions (and diffuse functions) on heavy atoms and 2p functions on hydrogens.	27	9
6-311++G (2df,2pd)	Puts 2d and 1f functions (and diffuse functions) on heavy atoms and 2p and 1d functions on hydrogens	34	14
6-311++G (3df,3pd)	Puts 3d and 1f functions (and diffuse functions) on heavy atoms and 3p and 1d functions on hydrogens	39	18

\* Lithium through Neon

### 1.10 Motivation and outline of the thesis

In this thesis, halogenated five/six member heterocyclic compounds with nitrogen and sulfur as hetero atoms, were studied to understand the halogen atom formation dynamics. In these molecules, extra  $n\pi^*$  excited states exist, unlike in homocyclic molecules, which introduce interesting excited state dynamics, e.g. radiationless transitions, vibronic and spin-orbit coupling, etc., It is interesting to investigate how

hetero atom affects the excited state dynamics in five/six member heterocyclic compounds. Apart from the hetero atom, effect of fluorine substitution on ring was also investigated. Also, it is well known that the halogen atoms have detrimental effect on ozone layer [31,32] and Cl and Br atoms have great potential to deplete it. Iodine containing gases generally have very short lifetimes and, as a result, most are removed in the troposphere before they reach the stratosphere and fluorine atom has relatively very less efficiency for ozone depletion compare to chlorine and bromine [33]. Therefore, effect of these two halogen atoms (F and I) are insignificant in this context. Hence, it is important to understand the C–Cl/Br bond dissociation process in atomic level. Therefore, the present work on C–Cl/Br bond dissociation dynamics was undertaken by probing nascent Cl/Br photofragments, under collision-less conditions using molecular beam resonance enhanced multiphoton ionization time-of-flight mass spectrometry. The translational energy distribution, anisotropy parameter and the relative quantum yield of the halogen photofragment was determined. Simple models such as impulsive, statistical and hybrid models were used to understand the partitioning of the available energy into translational degrees of freedom of the photofragment. Finally theoretical calculations were performed to aid interpretation of the experimental results and to obtain a correlation between the dynamics of dissociation and features of PESs.

The outline of the thesis is as follows **Chapter 1** is an introductory chapter providing a general overview of photodissociation dynamics and its importance. **Chapter 2** gives a description of the experimental method and analysis of experimental data to obtain dynamic parameters. In **chapter 3**, Cl atom formation dynamics of 3,4-dichloro-1,2,5-thiadiazole after photoexcitation with 235 nm was reported. It was observed that ring opening mechanism is more favorable in both ground and excited states than direct chlorine atom formation by C–Cl bond cleavage. Further, Photodissociation pathways

were investigated in its ground state at various wavelengths in UV region. The photolysis products were identified by the UV absorption and emission spectroscopy. NC–C(Cl<sub>2</sub>)–N=S isomer was observed as a intermediate in the Cl<sub>2</sub> and CN formation channels. **Chapter 4** deals with photodissociation dynamics of halogen substituted pyridines, namely, 3-chloropyridine and 3-chloro-2,4,5,6-tetrafluoropyridine. The translational energy distribution, the recoil anisotropy parameter,  $\beta$ , and the spin-orbit branching ratio, for chlorine atom elimination channels were determined. It has been observed that fluorine atom substitution in pyridine changed the translational energy distribution of the Cl atom formation channel. The theoretical calculation suggests that the fluorine substitution increases the possibility of cross over to the  $\pi\sigma^*$  state from the initially prepared  $\pi\pi^*$  state. **Chapter 5** covers the Br atom formation dynamics from 4-bromo-2,3,5,6-tetrafluoropyridine after photoexcitation at 234 nm. Translational energy distribution of Br and Br\* elimination channels indicates minimum two channels are possible for Br and Br\* formation. A strong polarization dependence of time-of-flight profiles suggests anisotropic distributions of the Br and Br\* fragments. For both Br and Br\* elimination channels, similar value of the anisotropy parameters was determined ( $0.60 \pm 0.05$ ). To get more insight, potential energy curves along the C–Br coordinate were generated using Multi Configuration Quasi Degenerate second order Perturbation Theory (MCQDPT2). **Chapter 6** deals with the dynamics of chlorine atom formation in the photodissociation process of halogen substituted pyrimidines, namely, 2,4,6-trichloropyrimidine and 5-chloro-2,4,6-trifluoropyrimidine has been studied around 235 nm. The nature of translational energy distribution indicates significance of the statistical dissociation from the ground state. Computational calculations are performed to generate the potential energy curves along the dissociating C–Cl bond using Equation-of-Motion coupled cluster singles and doubles (EOM-CCSD). These calculations suggested that the

## Introduction

dissociation from the ground state is more significant in case of 2,4,6-trichloropyrimidine, which is clearly visible in the nature of translational energy distribution. The excited triplet states also play a significant role in the Cl atom formation in both the molecules. Finally **Chapter 7** presents the summary of the thesis as well as future directions which can provide more insight into the mechanism of photodissociation process.

# Chapter 2

## Experimental Methods

---

### 2.1 Introduction

For a detailed understanding of the dynamics of photodissociation reactions in gas phase, at least one of the photofragments should be detected before undergoing any collision. To achieve this goal, all the experiments during the course of work were performed under collisionless conditions. For this, we have adopted Molecular Beam-Resonance Enhanced Multiphoton Ionization Time-of-Flight Mass Spectrometry (MB-REMPI-TOF-MS) technique. In this chapter, experimental technique along with its various components and also the analysis of the experimental data is discussed in detail.

At room temperature, only a small fraction of the total available molecules are accessible to the excitation process due to a broad population distribution in the ro-vibrational states (Boltzmann distribution). The sensitivity can be improved and the transitions can be made sharp by enhancing the population in the ground ro-vibrational state and minimizing the collisions between reagent molecules or with the background gas molecules. Both these objectives can be achieved by employing supersonic molecular beams. The molecular beam (MB) systems are ideal for studying the reaction under collisionless conditions, which enable us to extract the microscopic parameters of the process. It can also provide an intense source of molecules travelling with a fixed velocity in a particular direction in the vacuum, having an extremely narrow velocity distribution,

## Experimental Methods

isolated from each other, and cooled to such an extent that the higher rotational and vibrational levels are almost depopulated. Thus, it enables to prepare molecular reactants in well-defined quantum states, with known translational energy. Thus, supersonic molecular beams are employed for carrying out quantum state selective chemistry.

### 2.2 Generation of molecular beam

Chemical species of the interest is seeded in Helium gas to generate the supersonic molecular beam. For this purpose, Helium gas at stagnation pressure of 1500 Torr was bubbled through the sample maintained at room temperature, and the mixture was expanded through the solenoid pulsed valve (Parker). Typical operating pressures for the source and the ionization regions were in the order of  $10^{-5}$  and  $10^{-7}$  Torr, respectively. To achieve this high vacuum, the system was differentially pumped by using two similar 9" turbomolecular pumps (TMP), backed by rotary pumps. A pulsed supersonic molecular beam was generated using a solenoid valve with a 0.8 mm nozzle and 500  $\mu$ s opening time. A 1.9 mm diameter conical skimmer was used to skim off the molecular beam to the interaction region. The pulsed valve was located  $\sim$ 2 cm from the skimmer and  $\sim$ 7.5 cm from the interaction region. The schematic experimental setup is shown in figure 2.1.

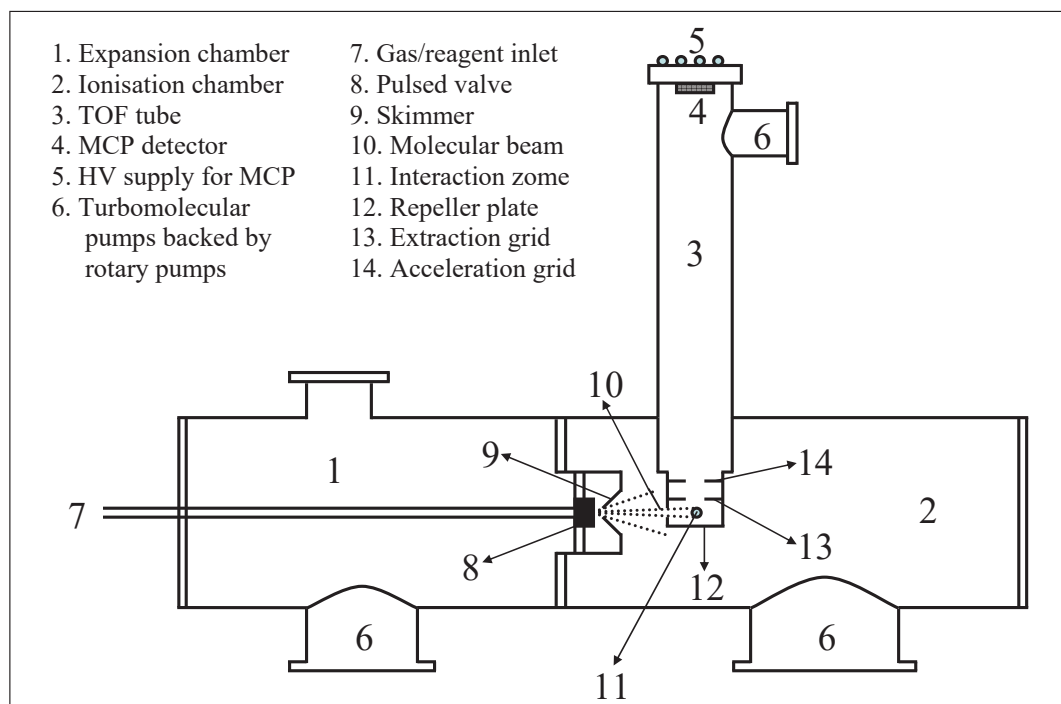
### 2.3 Interaction of molecular beam with laser

In the interaction region, the laser beam interacts with the sample molecular beam where the sample molecule is dissociated by a single photon and the resultant photofragments are ionized using REMPI scheme. Various precautions were taken in this step which are as follows

- 1) It was ensured that any interference to the measurements due to cluster photofragmentation was negligible by operating at a low stagnation pressure, and using only the rising part of the molecular beam pulse.



## Experimental Methods



**Figure 2.1:** A schematic diagram of MB-REMPI-TOF-MS system.

2) The velocity spread of the parent molecular beam parallel to the detector axis is minimized by maintaining the MB direction perpendicular to the detector axis. This step is necessary to minimize the spread in the velocity distribution of the photofragments.

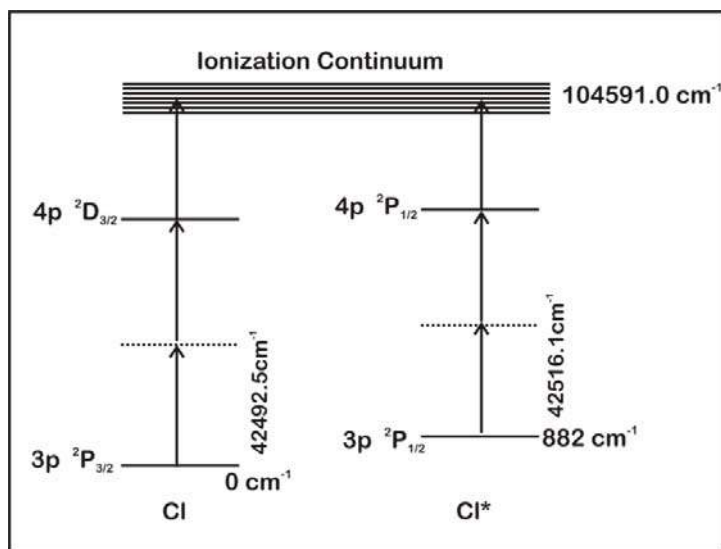
3) The internal energy of the parent molecule is minimized by employing the supersonic expansion.

These factors can effect the angular distribution as well aside from the translational energy of the photofragments. Hence, all the above factors are considered before performing experiments.

Studies in the present thesis are mainly focused on the halogenated molecules. Halogen atom (Cl/Br) formed after photodissociation of parent molecule are detected by there respective ionization using (2+1) REMPI scheme. Both chlorine and bromine atoms are having one unpaired electron in p orbital in their ground state leading to the term symbol,  $2P$ , and due to the spin-orbit interaction it splits into  $^2P_{3/2}$  and  $^2P_{1/2}$ . A typical (2+1) REMPI scheme for the chlorine and bromine atoms is given in figure 2.2 and figure

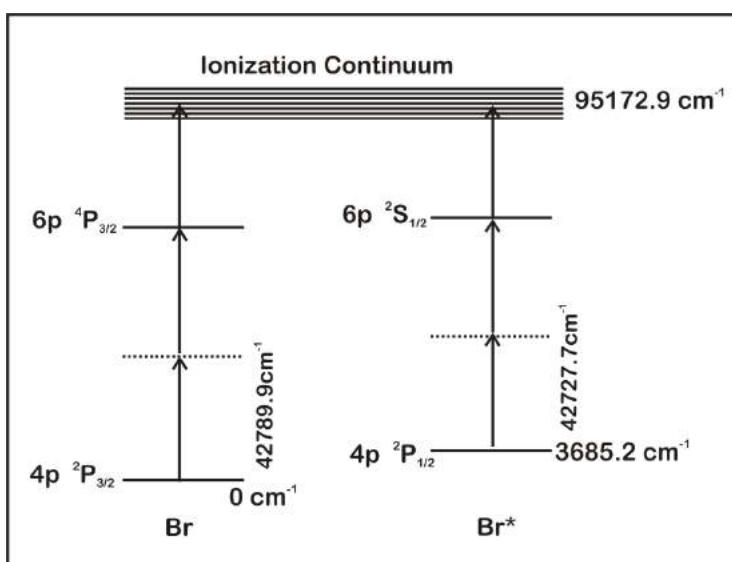
## Experimental Methods

2.3. In case of chlorine atom, the two spin-orbit states are separated by  $882\text{ cm}^{-1}$ . The ionization limit for chlorine atom is  $104591.0\text{ cm}^{-1}$ .



**Figure 2.2:**  $(2+1)$  REMPI scheme for Cl and Cl\* detection

The chlorine atoms in two spin-orbit states Cl ( $^2P_{3/2}$ ) and Cl ( $^2P_{1/2}$ ) requires two photons of frequency of  $42492.5\text{ cm}^{-1}$  and  $42516.1\text{ cm}^{-1}$  for excitation to an intermediate state, respectively. It is then followed by one photon absorption to ionize the excited chlorine atoms.



**Figure 2.3:**  $(2+1)$  REMPI scheme for Br and Br\* detection

Similarly, in bromine atom the two spin-orbit states are separated by  $3685.2\text{ cm}^{-1}$ . The ionization limit for bromine atom is  $95172.9\text{ cm}^{-1}$ . The bromine atom in two spin-orbit

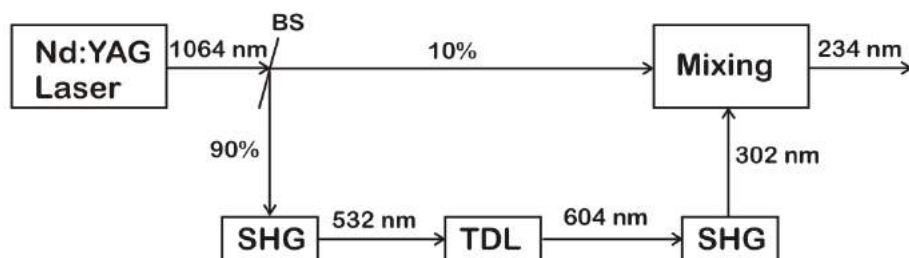
## Experimental Methods

excited state Br ( $^2P_{3/2}$ ) and Br\* ( $^2P_{1/2}$ ) requires two photons of frequency  $42789.9\text{ cm}^{-1}$  and  $42727.7\text{ cm}^{-1}$  for excitation to an intermediate state. It is then followed by one photon absorption to ionize the excited bromine atoms [34]. The use of excessive laser flux is avoided as it can result in multiphoton processes and saturation of signal. To ensure the monophotonic nature of the dissociation, power dependence measurements were also performed by measuring the integrated chlorine/bromine atom REMPI signal, i.e., measuring boxcar gated signal on the  $m/z$  35 and 37 or  $m/z$  79 and 81 peaks in the TOF spectrum. The log-log plot of REMPI signal intensity vs. laser intensity shows a slope of  $\sim 3$ , which ensures the monophotonic dissociation of the parent molecule followed by the (2+1) REMPI detection of Cl/Br photo fragment. The ionization step is saturated in the present case and does not contribute to the power dependence studies. The REMPI transitions are state-selective, hence, fragments in a specific quantum state are detected by simply tuning the wavelength of the ionizing laser. The state selectivity of (2+1) REMPI detection of the halogen atom also ensures the characterization of the quantum state of the detected photofragment.

In all the experiments, same laser beam was employed as a pump as well as a probe, i.e., for both photodissociation of the parent molecule and ionization of the photoproduct like Cl ( $^2P_{3/2}$ ), Cl\* ( $^2P_{1/2}$ ), Br ( $^2P_{3/2}$ ) and Br\* ( $^2P_{1/2}$ ). The laser pulse was generated by a dye laser (TDL 90, Quantel), using Rhodamine 101 dye. The dye laser was pumped by 532 nm light from the second harmonic of a Nd:YAG laser (YG-981-C, Quantel), operating at repetition rate of 20Hz. The fundamental dye laser output was frequency doubled in KDP crystal, and mixed with the fundamental output of the Nd:YAG laser, to obtain an output in the range of 230-236 nm. The above laser output was separated from the rest of laser beams, using a set of four Pellin-Broca prisms. The laser beam was focused by a lens, and the distance of the lens from the center of the

## Experimental Methods

molecular beam axis was varied, to obtain the best ratio of on- and off resonant signals. The polarization of the resultant light is rotated using a double Fresnel rhomb, and a polarizer which ensured  $\sim 99\%$  polarization of the light entering the chamber. The laser power is monitored, using a power meter, and is typically maintained at  $50\text{-}100 \mu\text{J}/\text{pulse}$ . A schematic of the procedure used to generate required wavelength is shown in figure 2.4



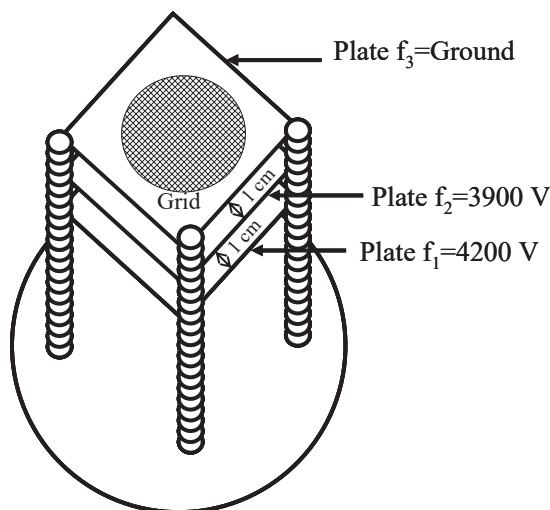
**Figure 2.4:** Schematic of the Nd:YAG pumped dye laser system for generating  $\sim 234 \text{ nm}$

### 2.4 Mass detection

Once the desired photofragments are ionized state selectively, the next step is to detect the photofragment mass selectively. The detector system consists of a two-stage Wiley-McLaren time-of-flight mass spectrometer (TOF-MS), with an extraction and an acceleration region [2]. The TOF-MS system is mounted vertically, perpendicular to the direction of MB. The extraction region consists of a repeller electrode of dimension  $5 \text{ cm} \times 5 \text{ cm}$ , which is a solid stainless steel plate, and an extraction grid mounted  $10 \text{ mm}$  above the repeller electrode. Interaction region lies in between the repeller electrode and extraction grid. The acceleration region is defined by the extractor electrode and a grid held at the ground potential, separated from each other by  $10 \text{ mm}$ . Both these grids ( $5 \text{ cm} \times 5 \text{ cm}$ ) are constructed from stainless steel mesh, with  $\sim 90\%$  transmission. To collect the total ion signal, the extraction region was held at field of  $\sim 300 \text{ V/cm}$ , and the acceleration region was held at  $\sim 3900 \text{ V/cm}$ . Schematic of the ion source is shown in figure 2.5. After passing through the acceleration region, the ion packet passed through a  $1035 \text{ mm}$  long field-free flight tube to the detector. Two sets of deflector plates placed

## Experimental Methods

perpendicular to the detector axis ( $z$ - axis) allowed the ion packet to be translated in the ( $x$ ,  $y$ ) plane to guide the ion packet on the detector. The typical field strength for the deflector plates is 2-6 V/cm.

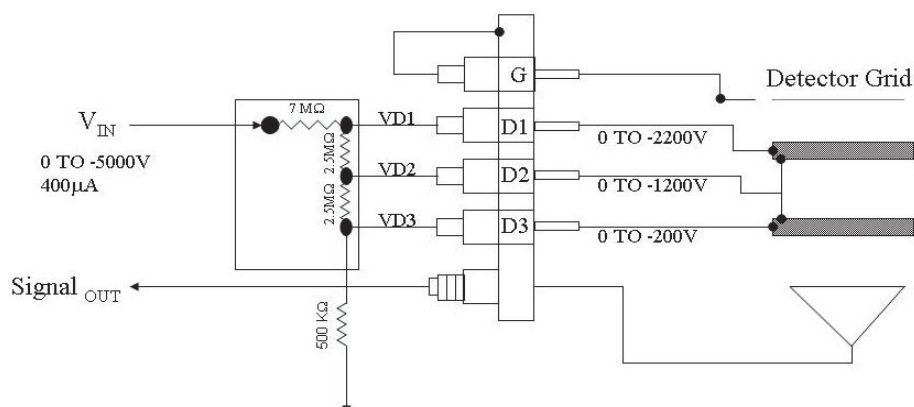


**Figure 2.5:** Schematic of the ion source. Plates  $f_1$ ,  $f_2$ , and  $f_3$  stands for the repeller plate, extraction and acceleration grid, respectively

The ions, after passing through the acceleration region, are accelerated to very high energy, and thus initial energy spread effect is reduced. The kinetic energy of all the ions in a given ion pulse coming out of the ion source is almost same, and, therefore, the velocity of each ion depends on its mass to charge ratio. The mass analyzer is a field-free drift tube, also called flight tube, wherein the ions travel under field-free conditions, with the velocity obtained in the acceleration region. Here, the ions are spatially dispersed according to their  $m/z$  ratio. Lastly, ions are detected by a set of 18 mm dual microchannel plates (MCP) at the end of the flight tube. A single compact high voltage source, having multiple output voltage ports, is employed to power the TOF ion optics, the deflection plates, and the MCP detector. Before applying any voltage to the MCP, it is pumped at a dynamic vacuum of  $< 10^{-7}$  Torr for 2-3 days. The grid of the MCP is grounded, while the MCP plates are powered, using a divider box. The applied voltage to the voltage divider box is divided, to provide the requisite voltages to the dual channel MCP detector. The voltage divider for supplying the requisite power to the MCP is shown

## Experimental Methods

in figure 2.6. TOF analyzer allows all the ions to pass through, thus the complete mass spectrum of the sample can be obtained from a single pulse.



**Figure 2.6:** The voltage divider for supplying the requisite power to the MCP.

In TOF-MS, identification of the ions is made on the basis of their flight time from the region of their generation to the detector. If the length of the field-free tube is very much longer than the acceleration region, then  $m/z$  of the ion is related to its flight time 't' by an expression,  $t^2 = a(m/z) + b$ .

To obtain the TOF spectrum, the output signal from MCP is sent to a 1 GHz digital oscilloscope (LeCroy Wavesurfer 44MXS-B) for storage. Subtracting the off-resonant signals from the on-resonant signals effectively removed the minor pump-oil related background contribution to the TOF spectrum, and the contribution from a multiphotonic process. A delay generator (DG 535, SRS) with pulse resolution of 20 ps was employed as the master to trigger all the instruments for time synchronization. The time delay between the trigger pulse applied to the pulsed valve and the valve opening was obtained by measuring the delay between the trigger pulse and the fast ionization gauge (FIG) signal, employing a digital oscilloscope. The flow velocity of the molecular beam can be also estimated by measuring time delays for different FIG positions with respect to the skimmer. The time required for the molecular beam to reach the interaction region can be then easily obtained. This delay is the sum of the time required to open the

## Experimental Methods

pulsed valve from its trigger input and for the molecular pulse to reach FIG from its position of generation, i.e., the nozzle exit. Fast photodiodes (Becker-Hickl Model PDM-400) are used to measure the time delays between the external-trigger inputs and the laser outputs at  $\sim 235$  nm from Nd:YAG pumped dye laser. Based on the above measured delays, the trigger pulses of different instruments are adjusted. All the experiments were carried out with single colour laser, i.e., the same laser beam is used for both photolysis and probing. The laser pulse and the rising part of molecular beam pulse are temporarily and spatially overlap in the ionization/extraction region of TOF system. The ion signal was gate integrated by a boxcar, averaged for 20000 laser pulses, and fed into an interface (SRS 245), for A/D conversion. A PC is used to control the scan of the dye laser via an RS232 interface and collect data from SRS 245, through a GPIB interface, using a control and data acquisition program.

### 2.5 Analysis of data acquired from experiment to obtain the dynamic parameters

In the present studies, we are mainly interested in three dynamic parameters of the photodissociation process, which are, namely, translational energy distribution, anisotropy parameter, and spin-orbit branching ratio. These parameters will help us to understand the overall mechanism of the photodissociation process. The present section will explain how to get these dynamic parameters from the experimental data.

Translational energy distribution  $g(v)$  and the recoil anisotropy parameter ( $\beta$ ) are obtained by analyzing the observed TOF profiles of photofragments (Cl, Cl\*, Br and Br\*) using a forward convolution method [35,36]

To begin with, the experimentally obtained TOF profiles,  $I(t, \chi)$ , at a particular geometry  $\chi$  (the angle between the laser polarization and the detection axis), are transformed into the velocity domain,  $I(v_z, \chi)$ . Under space focusing conditions, a simple linear relation, was used, as follows,

## Experimental Methods

$$v_z = \frac{(t-t_0)qV_{ex}}{m} \quad (2.1)$$

where  $q$  and  $m$  are the charge and mass of the photofragment,  $V_{ex}$  is the electric field in the extraction region, and  $t_0$  is the mean time-of-flight. The distribution of  $v_z$ ,  $f(v_z, \chi)$ , generates the observed velocity domain TOF signal,  $I(v_z, \chi)$ , on convolution with an instrument response function (IRF). The function  $f(v_z, \chi)$  is described by an equation as follows

$$f(v_z, \chi) = \int_{|v_z|}^{\infty} \frac{g(v)}{2v} \left[ 1 + \beta P_2(\cos \chi) P_2\left(\frac{v_z}{v}\right) \right] dv \quad (2.2)$$

Where  $v_z$  is the velocity component along the  $z$ -axis,  $v$  is the recoil speed of the fragment,  $\beta$  is the anisotropy parameter,  $P_2(\cos \chi)$  is the second-order Legendre polynomial, and  $\cos \chi = \varepsilon \cdot z$ , implying the projection of the pump laser electric field  $\varepsilon$  on the detection axis  $z$ .

We have determined the instrument response function by measuring the (1+1) REMPI signal of an aniline beam at 293.77 nm. The aniline molecular ion signal was measured as a function of laser intensity and found to be quadratic dependent. This shows that at 293.77 nm, the REMPI is (1+1) type due to one photon,  $^1A_1 \rightarrow ^1B_2$ , resonant transition, followed by pumping to the ionization continuum with absorption of the second photon. Since the  $v_z$  for aniline molecule in the beam is almost zero, measurement on the single ro-vibrational state of aniline molecule can be used to determine the IRF. The function was found to be Gaussian in the time domain, with FWHF of 27 ns at aniline mass ( $m/z=93$ ). The IRF includes a number of experimental factors, such as the duration of the laser pulse, the finite time response of the detector, diffraction from the ion optics grids, and inhomogeneities in the electric fields. Other factors, such as space-charge distortions and the finite dimensions of the ionization region, coupled with deviations from space focusing, may also, give rise to a minor contribution. Thus, under space focusing conditions it generates a convolution function in the velocity domain, which depends linearly on the electric field in the extraction region. In present work, we



## Experimental Methods

have employed a procedure of non-core sampling data, with an assumption that the nature and shape of TOF profiles for photofragment are independent of the probe polarization. But, this assumption can only be approximate because of the presence of atomic  $v \cdot j$  correlations. However, these correlations are generally weak [37,38] and can be neglected.

We assumed an initial center-of-mass photofragment speed distribution  $g_i(v)$  for each active decay channel  $i$ , to extract the photofragment speed distribution,  $g_i(v)$  and anisotropy,  $\beta_i$ , of each decay channel  $i$  contributing to the experimental TOF profiles,  $I(v_z, \chi)$ . The dependence of  $\beta$  on  $f(v_z, \chi)$  can be eliminated by either measuring data at the magic angle ( $\chi=54.7^\circ$ ), where  $P_2(\cos\chi)$  is zero or by co-adding normalized profiles with  $\chi=90^\circ$  and  $\chi=0^\circ$ , in 2:1 ratio. Both the approaches yield isotropic  $f(v_z, \chi)$ . Thus, the TOF profile at the magic angle,  $I(v_z, 54.7^\circ)$ , gives an estimate of the total center-of-mass speed distribution  $g(v)$ , and provides an indication of the form of the individual speed distributions  $g_i(v)$ . These are usually modeled with the functional form as follows

$$g_i(v) = (f_T)_i^{a_i} [1 - (f_T)_i]^{b_i} \quad (2.3)$$

Where  $(f_T)_i$  is the fraction of the available energy channeled into translation,  $a_i$  and  $b_i$  are adjustable parameters. The function  $f(v_z, \chi)$  is calculated simultaneously for all three geometries  $\chi=0^\circ$ ,  $54.7^\circ$  and  $90^\circ$ , using an adjustable anisotropy parameter  $\beta_i$  and weight for each decay channel. Then, this function is convoluted with the instrument response function (IRF) to simulate TOF profiles, which are compared with the experimental results,  $I(v_z, \chi)$ . The adjustable parameters are then varied to achieve a satisfactory agreement with the experimental data. The determined photofragment speed distribution are transformed into centre-of-mass translational energy distribution  $P(E_T)$ , using the following equation.

$$P(E_T) = g(v) \frac{dv}{dE_T} \quad (2.4)$$

The analysis procedure can be summarized in the following flow chart figure 2.7

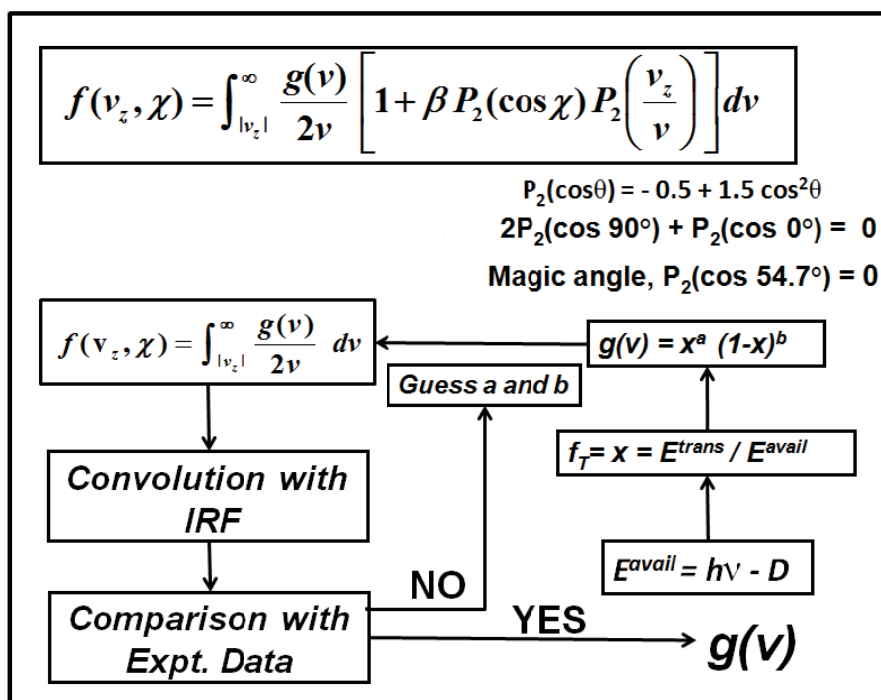


Figure 2.7: Flow chart of analysis procedure of REMPI data.

Various components employed in the above technique are discussed in detail in following sections.

## 2.6 Laser

Laser (acronym: Light Amplification by Stimulated Emission of Radiation) can be considered as a source of a narrow beam of monochromatic, coherent light in the visible, IR, or UV parts of the spectrum. Laser light is distinguished from the conventional light source based on the following properties. i) Monochromaticity, ii) Directionality, iii) Coherence, iv) Intensity, v) Tunability, vi) Short pulse capability.

### 2.6.1 Nd:YAG laser

In Nd:YAG laser,  $\text{Nd}^{3+}$  ions are incorporated into YAG crystal where YAG acronym for Yttrium Aluminium Garnet of formula  $\text{Y}_3\text{Al}_5\text{O}_{12}$ . About 1% of  $\text{Y}^{3+}$  is substituted by  $\text{Nd}^{3+}$ . The Nd:YAG laser is a four-level laser the levels are shown in the figure 2.8. The laser transition, having a wavelength of 1064 nm, originates from the  ${}^4\text{F}_{3/2}$  level and terminates at the  ${}^4\text{I}_{11/2}$  level. The upper laser level,  ${}^4\text{F}_{3/2}$ , has a fluorescence

## Experimental Methods

efficiency greater than 99.5% and a fluorescence lifetime of  $230\mu\text{s}$ . It should be noted that the F $\rightarrow$ I transitions are forbidden in the dipole approximation, since the orbital quantum number change by three. Hence, F levels are metastable levels.  $^4\text{I}_{11/2}$  level is about  $2000\text{ cm}^{-1}$  above the ground state and, hence, at room temperature this level is virtually empty in the thermal equilibrium. Any population in the level  $^4\text{F}_{3/2}$  gives rise to an inversion [39,40]

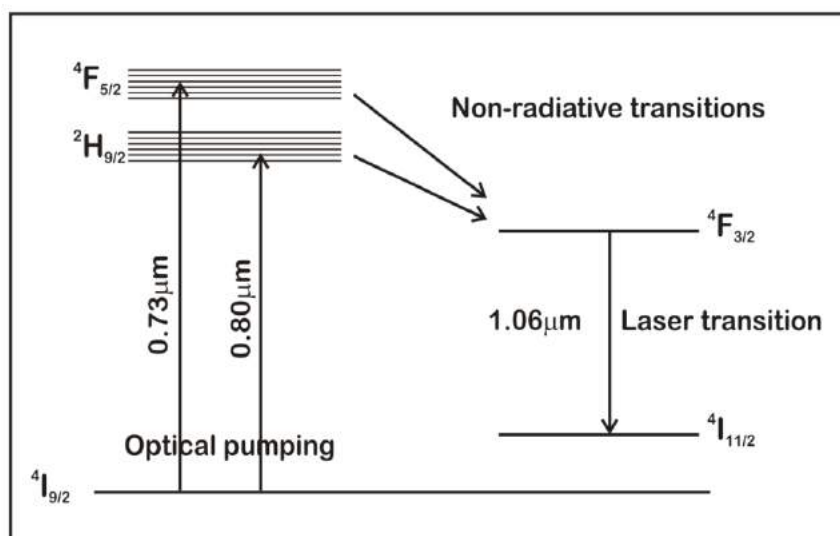


Figure 2.8: Energy levels of Nd:YAG laser

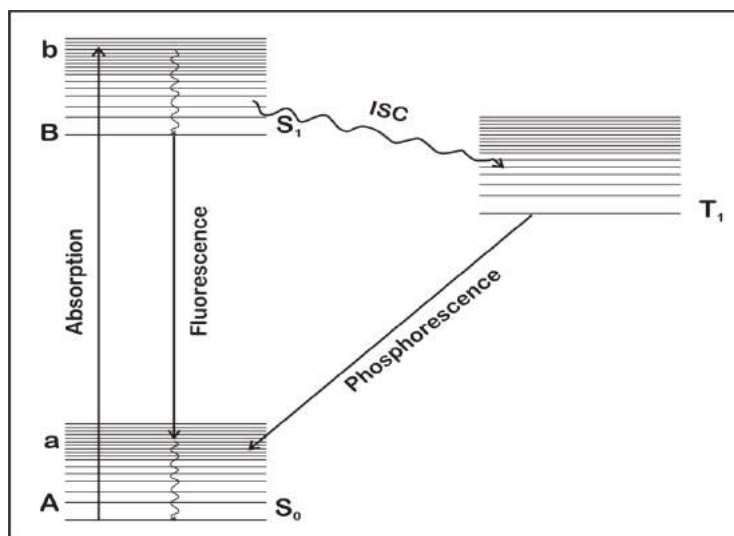
### 2.6.2 Dye laser

Dye laser is used to excite the molecules and atoms into electronic excited states in REMPI experiment. The active medium of dye lasers is organic dye dissolved in solvents, and these dyes show strong broadband fluorescence spectra under excitation by UV or visible light.

In a dye laser, the pump laser light is absorbed by dye molecule in the lowest vibrational sublevel A of  $S_0$  ground state and produces transitions to one of the upper vibrational levels of  $S_1$ , as denoted by b in figure 2.9. The dye molecule then undergoes a radiationless decay to the bottom of  $S_1$ . Lasing may occur between vibrational sublevel B in  $S_1$  and an excited sublevel of  $S_0$ .

## Experimental Methods

The molecule in the upper lasing level B in  $S_1$  may decay to the triplet state ( $T_1$ ) by the radiationless transition. This is a forbidden transition in the sense that it is far less



**Figure 2.9:** Schematic representation of energy levels of an organic dye

probable than Singlet-Singlet transition. Nevertheless, the molecule can undergo intersystem crossing (ISC) in time scale of  $\sim 50$  ns.  $T_1$  is a metastable state with the lifetime of  $10^{-7}$  to  $10^{-3}$  sec for decay. Hence the molecule can pile up in  $T_1$ , stealing the power that could go into lasing via  $B \rightarrow T$  transition. A second problem is that the Triplet to Triplet ( $T_1 \rightarrow T_2$ ) absorption can occur overlapping the lasing wavelength. Triplet to Triplet absorption can be so strong that excitation mechanism may not have sufficient power to overcome the absorption loss. Hence, the triplet population needs to be controlled. In the present studies, we have used a rapid flow of dye solution to overcome the above problem. The dye flows very rapidly through the active region where pump beam is focused. In flowing through this region each dye molecule sees a pulse of pump light. If the dye is circulated fast enough, the individual dye molecule will be irradiated by the light pulse of duration short compared to triplet decay but long compared to the life time of lasing transition.

### 2.7 Vacuum

The term *vacuum* is generally used to denote a volume or region of space in which the pressure is significantly less than 760 Torr. Under normal environmental conditions, creation of vacuum requires a removal of gases, contained in atmospheric air, from a given vessel or a chamber. There are a few basic ways to remove air (or another gas) from the space of a vacuum chamber.

1. Gas can be removed by an action of positive displacement devices, such as rotary vanes
2. Another way is by partial displacement or momentum transfer, such as fast-moving blades (fan or turbine)
3. Vacuum can also be created by refrigeration to temperatures at which the gas either becomes solid or can be adsorbed on the surface of a suitable porous material.
4. Gas can be removed from space by chemical reaction, which produces a solid residue.
5. Finally, the gas can be ionized and expelled from space either by the action of suitable electromagnetic fields or implanted into a solid surface inside the pump due to the high velocity achieved by acceleration in a high voltage field.

Generally, pumps which create vacuum based on first two methods, namely, 1 and 2, are called *throughput* pumps and remaining methods, namely, 3, 4 and 5, are called *capture* pumps.

In MB-REMPI-TOF-MS setup rotary and turbomolecular pump have used to obtain high vacuum. The following sections will discuss about the rotary and turbomolecular pump.

#### 2.7.1 Rotary pump

The rotary pump is a mechanical vacuum pump, which works on positive gas displacement principle. The pump periodically creates increasing and decreasing volume

to remove gases from the system. The vacuum can be achieved using rotary pump is of the order  $\sim 10^{-3}$  Torr. The rotary vane pump consists of vanes mounted to a rotor that rotates inside the cavity. The vanes are metallic in oil-sealed pumps. The oil in an oil-sealed pump acts as a lubricant along with providing a vacuum seal at the pump exhaust and cooling for the pump.

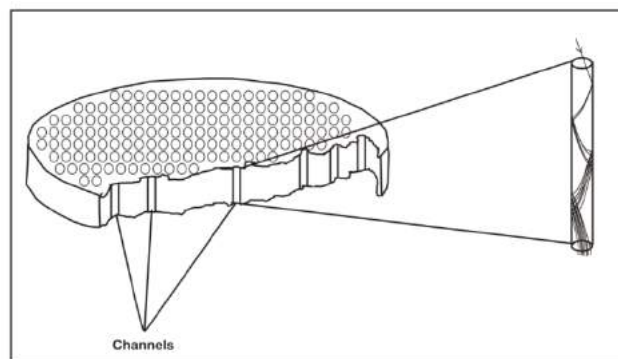
### **2.7.2 Turbomolecular pump**

Turbomolecular pumps work on the principle that the gases can be removed within a vacuum vessel if the gas molecules are given a directional momentum transfer such that they flow in a particular direction. This is made possible by a rapidly moving surface of a rotor imparting a directional force to gas molecules.

Pumping part consists of a rotor and a stator. Turbine blades at very specific angles are located around the circumferences of the stator and rotor. Each rotor-stator pair of circular blade rows forms one stage so that the assembly is composed of a multitude of stages mounted in series. The gas molecules are given a directional momentum due to these rather large radial blades and are compressed and pushed down to lower compression stages, whose blades have shorter radial spans, where the gas is again compressed to backing pressure or rough vacuum pressure. At a pressure below  $10^{-3}$  mbar, the mean free path of the gas molecules is larger than the spacing between rotor and stator blades. Consequently, the molecules collide primarily with the rotor blades with the result that the pumping process is highly efficient. At pressure higher than  $10^{-1}$  mbar the action of the rotor is diminished by the frequent collisions between the molecules. Therefore, a turbomolecular pump is not capable of pumping gases against atmospheric pressure and has to be backed by an adequate fore vacuum pump like rotary pumps [41].

## 2.8 Microchannel plate detector

A microchannel plate (MCP) is a planar component used for detection of single particles such as electrons, ions etc. It is closely related to a secondary electron multiplier (SEM), as both intensify single particles by the multiplication of electrons via secondary emission. However, because a microchannel plate detector has many separate channels, it can additionally provide spatial resolution. In other words, one can imagine MCP as an assembly of millions miniature SEMs. MCP consists of a two-dimensional periodic array of very-small diameter glass capillaries (channels) fused together and sliced into thin plate. A single incident particle (ion, electron, photon etc.) enters a channel and emits an electron from the channel wall. Secondary electrons are accelerated by an electric field developed by a voltage applied across both ends of the MCP. They travel along their parabolic trajectories until they, in turn, strike the channel surface, thus produces more secondary electrons. This process is repeated many times along the channel and as a result the cascade process yields a cloud of several thousand electrons which emerge from the rear of the plate. The length of the channel of a MCP is virtually its thickness. The gain of the MCP is not a function of channel length ( $L$ ) or channel diameter ( $d$ ) alone but the function of ratio  $L/d$ , as well as the inherent secondary emission factor of the channel wall material. The standard MCPs are fabricated with an  $L/d$  ratio about 40 to 80. The cross section of MCP and the electron multiplication mechanism is shown in figure 2.10.



**Figure 2.10:** *Microchannel plate*





## Chapter 3

### **UV-Photodissociation of 3,4-dichloro-1,2,5-thiadiazole**

---

#### **3.1 Introduction**

One of the major goals in the area of photodissociation dynamics is to understand the nature of the translational and internal energy partitioning among the photofragments. In general, these studies also provide information on the dissociation channels, their branching ratios, and fragment state distributions [26,42,43]. These experimental parameters along with the appropriate theoretical calculation may help to explain the processes that are occurring on various potential energy surfaces. Recently, many experiments in ultraviolet (UV) region, supported by theoretical studies, have been performed, to investigate the photodissociation dynamics of halogen-containing hydrocarbons, which may produce halogen atoms in the photodissociation process [44-50]. It is well established that these halogen atoms are responsible for ozone destruction in the stratosphere [31,32]. However, such studies for more complex molecules, especially, cyclic compounds, have been less studied because of their complex photodissociation mechanism resulting into multiple channels [44]. In this context a detailed study was undertaken, to understand the dynamics of chlorine atom formation in the photodissociation of halogen containing thiadiazole.

Thiadiazoles ( $c\text{-C}_2\text{H}_2\text{N}_2\text{S}$ ) are five-membered heterocyclic compound, containing two carbon atoms, two nitrogen atoms and one sulfur atom in the ring. In the conjugated  $\pi$  system, the delocalization of electron lone pairs on sulfur makes thiadiazoles behave like an aromatic compound. These thiadiazoles, in general, are planar and aromatic molecules. The planar structure of these thiadiazoles has been confirmed by various experimental techniques like microwave spectroscopy and gas-phase electron diffraction [51-54]. Various theoretical studies pertaining to their structure and stabilities are also available in the literature [55]. Some theoretical studies have been performed for their respective cations also [56]. Thiadiazole occur in nature in four isomeric forms such as 1,2,3-thiadiazole; 1,2,4-thiadiazole; 1,2,5-thiadiazole and 1,3,4-thiadiazole. In this study, we have undertaken chlorine substituted 1,2,5-thiadiazole. Hence, we will be restricting our discussion to 1,2,5-thiadiazole isomer only.

The photochemistry and spectroscopy of 1,2,5-thiadiazoles (TDZ), especially in UV region, has been a subject of investigations, both experimentally and theoretically. Few spectroscopic lines in the first band of the UV spectrum were interpreted with a double well potential arising from an excited state which is non planar in nature [57]. The recent work includes the experimental studies related to its UV-VUV absorption spectrum in the gas phase, and the assignments of various band system using theoretical methods [55]. Ionization energies have been evaluated for the parent as well the chloro derivatives of 1,2,5-thiadiazole. These experiments were done using He I and He II UV-photoelectron spectroscopy [55,58,59]. In another similar experiment using same technique (He I and He II UV-photoelectron spectroscopy), various parameters were determined for a series of substituted 1,2,5-thiadiazoles and the substituent effects were studied [56]. Moreover, they have determined electronic structure, information about their ionic states and ionization energies. These experimental results were well supported with

the various theoretical methods. Apart from these experiments, few experiments pertaining to absorption spectra in the UV region have been reported for parent and various substituted 1,2,5-thiadiazole as well. These spectra show a series of vibronic structure in the first band which originate from a  $\pi^* \leftarrow \pi$  transition [55,60,61]. For parent unsubstituted 1,2,5-thiadiazole, the wavelength position at which the absorbance is the greatest, defined as  $\lambda_{\max}$ , occurs at  $\sim 248$  nm (5.0 eV). However, for chlorine substituted 1,2,5-thiadiazole (3,4-dichloro), the position of  $\lambda_{\max}$  occurs at  $\sim 267$  nm (4.64 eV, see spectrum, figure 3.1). For unsubstituted parent molecule, the vibronic spectra are characterized with two vibrational frequencies in the excited state, namely,  $\nu_4$  and  $\nu_5$  with their respective values of 990 and 640  $\text{cm}^{-1}$  [57]. In the same study, they also concluded the non-planar structure of excited state of the 1,2,5-thiadiazole. The photochemistry of parent and substituted 1,2,5-thiadiazole in gas phase has been studied mostly for the production and characterization of various nitrile N-sulfides (R-CNS). Pasinszki *et al.* have generated various R-CNS such as ClCNS,  $\text{CH}_3\text{CNS}$ , ClNCNS and NCCNS in the low temperature He matrix by UV irradiation of parent and various substituted 1,2,5-thiadiazole [60,61]. Similarly, electron impact ionization studies of 1,2,5-thiadiazole have been studied for the generation of nitrile N-sulfides such as, NCCNS,  $\text{H}_2\text{NCNS}$ ,  $\text{H}_3\text{CSCNS}$ , and ClCNS as ions. They have identified these nitrile sulfides using collisional activation and neutralization-reionization method using gas phase mass spectrometer. These results were also supported using chemical ionization and vacuum pyrolysis experiments [62,63].

In addition to the spectroscopic and photochemistry studies of these class of compounds, attention have received recently due to their use as the starting materials for the various reactive nitrile sulfides intermediates in the photochemical synthesis or the preparative chemistry [64]. Several studies have been initiated using these thiadiazoles

due to their potential use as insecticides, herbicides and various drugs [65,66]. Also, thiadiazoles and its derivatives exhibits a wide variety of biological activities because of their liposolubility. For example, 3,4-dichloro-1,2,5-thiadiazole, is a starting material in the synthesis of the drug Timolol, a  $\beta$ -adrenergic blocking agent. Various properties of these 1,2,5-thiadiazoles have been utilized in the drugs industry for many years. The ring opening behaviour of 3,4-dichloro-1,2,5-thiadiazole has been utilized for the synthesis of various 3,4-disubstituted-1,2,5-thiadiazole which are the precursor of different drugs [67].

To best of our knowledge, no dynamics studies in the photodissociation process of these 1,2,5-thiadiazoles are available in the literature. In this context, the present study is undertaken to understand the photodissociation dynamics of halogen substituted 1,2,5-thiadiazole, namely, 3,4-dichloro-1,2,5-thiadiazole. We have investigated dynamics of chlorine atom ( $\text{Cl}/\text{Cl}^*$ ) formation, around 235 nm, in a supersonic molecular beam, using REMPI-TOF technique. We have also measured the translational energy distributions and the relative quantum yields for chlorine atom formed during the photodissociation process. Besides, we have also measured the anisotropy parameters ( $\beta$ ) for  $\text{Cl}/\text{Cl}^*$  atom formation process. Theoretical calculations have been carried out to understand the dissociation dynamics. Further, photodissociation in the UV region at various wavelengths has been studied using absorption and emission spectroscopy. Various dissociation mechanisms operating in the ground state of the molecule are supported by suitable theoretical calculations.

## **3.2 Experimental**

### **3.2.1 REMPI-TOF-MS**

The experiment was performed using a molecular beam time-of-flight mass spectrometer system (MB-TOF-MS), as described in chapter 2. The  $\text{Cl}$  and  $\text{Cl}^*$  atoms formed during the photodissociation of 3,4-dichloro-1,2,5-thiadiazole were probed using

(2+1) REMPI transitions in the region of 234-236 nm. The transitions,  $4p\ ^2D_{3/2} \leftarrow 3p\ ^2P_{3/2}$  and  $4p\ ^2P_{1/2} \leftarrow 3p\ ^2P_{1/2}$  are selected for probing Cl and Cl\*, respectively. The 3,4-dichloro-1,2,5-thiadiazole (Aldrich, 98% purity) was used after repeated freeze-pump-thaw cycles. Helium was bubbled through the sample, maintained at room temperature, and the mixture was expanded through the nozzle at a stagnation pressure of 1500 Torr. It was ensured that any interference to the measurements due to cluster photofragmentation was absent, or negligible, by operating at a low stagnation pressure, and using only the rising part of the molecular beam pulse. The power dependence measurements revealed a three photon dependency, which is consistent with one-photon dissociation of 3,4-dichloro-1,2,5-thiadiazole, followed by (2+1) REMPI of the chlorine atoms, assuming that the ionization step is saturated. Apart from the power dependence studies, we also systematically monitored the shape and the width of TOF profiles of Cl atoms at various laser intensities. All the experiments were performed in the intensities, which are much lower than the intensity at which the shape and width of the TOF profiles were invariant. This experimental condition ensures that the translational energy distributions and the anisotropy parameters are invariant over the laser fluences used.

### 3.2.2 Absorption and emission measurements

The photolysis study was performed by using the laser photolysis combined with UV-Vis absorption and UV emission spectroscopy. Briefly, the photolysis was initiated by different lasers operating at 248 nm (KrF excimer laser), 266 nm (fourth harmonic of Nd:YAG laser) and 235 nm (Nd:YAG pumped dye laser). The UV emission spectroscopy was performed in a flow condition at a pressure range of 100-200 mTorr. For all the experiments, the photolysis laser was unfocussed. The reaction chamber was made of glass with crossed arms at right angles, one pair provided for the entrance of the photolysis laser and the other for the collection of fluorescence emission. The

fluorescence detection system consisted of a suitable lens to collect the fluorescence, a monochromator and a photomultiplier tube (Hamamatsu, model R 928P) to detect it, and a suitable band pass filter to cut off the scattering from the photolysis laser light. The fluorescence temporal profile at various wavelengths were averaged over 1000 laser shots and saved for further processing. Fluorescence intensities were normalized with respect to the photolysis laser to correct for the laser intensity fluctuation, if any. The UV-Vis absorption spectroscopy was performed in a static condition at a pressure range of 1-3 Torr in a 1 cm × 1 cm quartz cell. Absorption spectra were recorded with a UV-Vis spectrophotometer (Jasco V530, Tokyo, Japan). Spectral data were collected in the 200-600 nm region.

### 3.2.3 Computational details

Molecular orbital (MO) calculations were carried out to generate the relative potential energy diagram for the dissociation channels of 3,4-dichloro-1,2,5-thiadiazole molecule on its ground state. Calculations were done at G3 level of theory, using Gaussian suite of program [29]. All the stationary points were calculated in the ground state, for the various dissociation channels. The G3/G3B3 level of theory is very accurate and has the fewest convergence problems which calculates  $\Delta H_{298}^0$ , within an error of ~ 1 kcal/mol, especially for halogenated heterocyclic compounds [68]. Vertical excitation energies/UV-Vis absorption spectra of parent compound and various dimer species were calculated using Time-dependent Density Functional Theory (TD-DFT) at MPW1PW91/aug-cc-pVDZ level of theory. We have also calculated these excited state parameters using other methods also. Equation-of-motion coupled with CCSD (EOM-CCSD) and Symmetry Adapted Cluster/Configuration Interaction (SAC-CI) methods were also tried for the parent compound and its isomer.

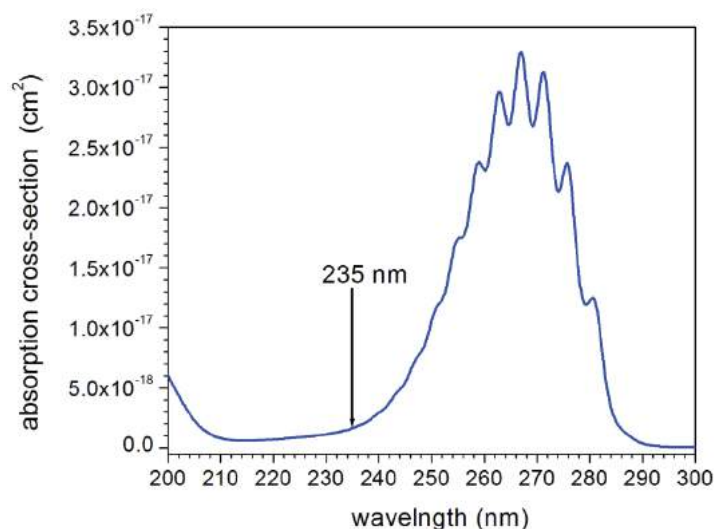
### 3.3 Analysis of REMPI-TOF experimental data

The TOF profiles of Cl and Cl\* are measured at different laser polarizations. The translational energy distributions and the anisotropy parameters for both Cl and Cl\* are determined from these TOF profiles, using a commonly used forward convolution (FC) technique, as described in Chapter 2. Using this method, the parameters are adjusted until a satisfactory agreement with the experimental data is achieved. Once the photofragment speed distributions are determined, these are used to obtain the corresponding anisotropy parameters.

## 3.4 Results

### 3.4.1 Absorption spectra and absolute cross-section

The absorption spectra were measured using a commercial UV spectrophotometer at different pressures of 3,4-dichloro-1,2,5-thiadiazole. Figure 3.1 shows the spectrum of 3,4-dichloro-1,2,5-thiadiazole with absolute absorption cross-section.



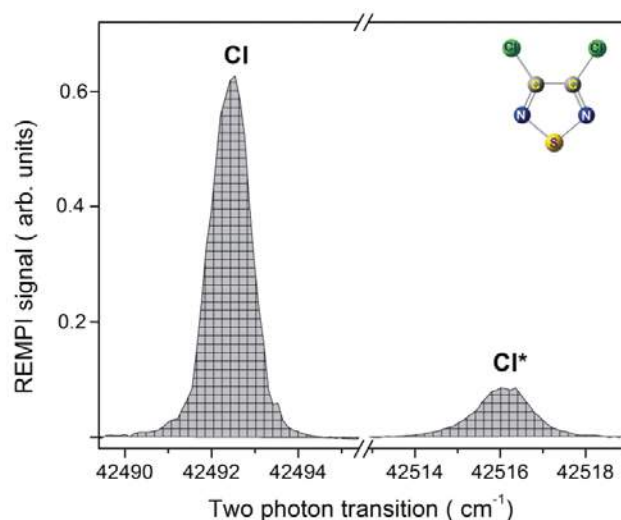
**Figure 3.1:** UV absorption spectrum of 3,4-dichloro-1,2,5- thiadiazole at room temperature.

These measurements were further verified by measuring the absorption cross-sections at 235 nm using a 50-cm long absorption cross-section cell. For this purpose, the ratios of intensities,  $I/I_0$ , were measured at different pressure of compound, where  $I$  and  $I_0$  is the laser intensity with or without the sample in the cell, respectively. The sample pressure in

the cell was measured with a capacitance manometer. The laser light was attenuated heavily by suitable attenuator, and was collimated to get a very low-intensity laser beam. The intensity of the laser beam was measured by photodiodes (Becker and Heckl, PDM-400). The absorption cross-section of 3,4-dichloro-1,2,5-thiadiazole at 235 nm thus measured was found to be  $(1.5 \pm 0.3) \times 10^{-18} \text{ cm}^2 \text{ molecule}^{-1}$ .

### 3.4.2 Spin-orbit branching ratio

The molecules/atoms moving with different velocity absorbs different frequency of radiation for the same transition. This leads to broadening of the spectral line; it is referred as Doppler broadening. Figure 3.2 shows such Doppler profiles for the resonance enhanced multiphoton absorption of photons (transitions involved in the present interested region are described in Chapter 2) by the Cl ( $^2P_{3/2}$ ) and Cl\* ( $^2P_{1/2}$ ) atoms, produced in the dissociation of 3,4-dichloro-1,2,5-thiadiazole scanned in the wavelength region of  $42492.5 \text{ cm}^{-1}$  and  $42516.1 \text{ cm}^{-1}$ , respectively.



**Figure 3.2:** Doppler profiles of Cl and Cl\* atoms produced in the 235 nm laser photolysis of 3,4-dichloro-1,2,5-thiadiazole used for the determination of their ratio

The relative quantum yield of the Cl atom formed in different spin-orbit states (X, X\*), were calculated by normalizing the integrated intensity, i.e., the peak areas  $S(X)$ , or  $S(X^*)$ , of the respective (2+1) REMPI transitions with respect to the laser intensity, and the ratio of the two-photon absorption coefficients. The ratio of the measured areas  $S(X)$



and  $S(X^*)$  of (2+1) REMPI lines is proportional to the product ratio,  $N(X)/N(X^*)$ , as given in Eq. (3.1), where  $k$  is the relative ionization probability.

$$\frac{N(X^*)}{N(X)} = k \frac{S(X^*)}{S(X)} \quad (3.1)$$

The intensities  $S(X)$  and  $S(X^*)$  were obtained by integrating the measured ion signal intensities over the proper range, covering the Doppler width and the probe laser bandwidth. The measurements were repeated at different laser light intensities. From the experimentally measured integrated intensity ratios,  $S(\text{Cl}^*)/S(\text{Cl})$ , one can easily obtain the product ratios, using Eq. (3.1), in which the relative ionization probability,  $k$  was taken to be  $0.85 \pm 0.10$  for chlorine atom [24].

The relative quantum yields,  $\Phi(X)$  and  $\Phi(X^*)$ , can be determined from the product ratio, and  $\Phi(X^*)$  can be expressed as

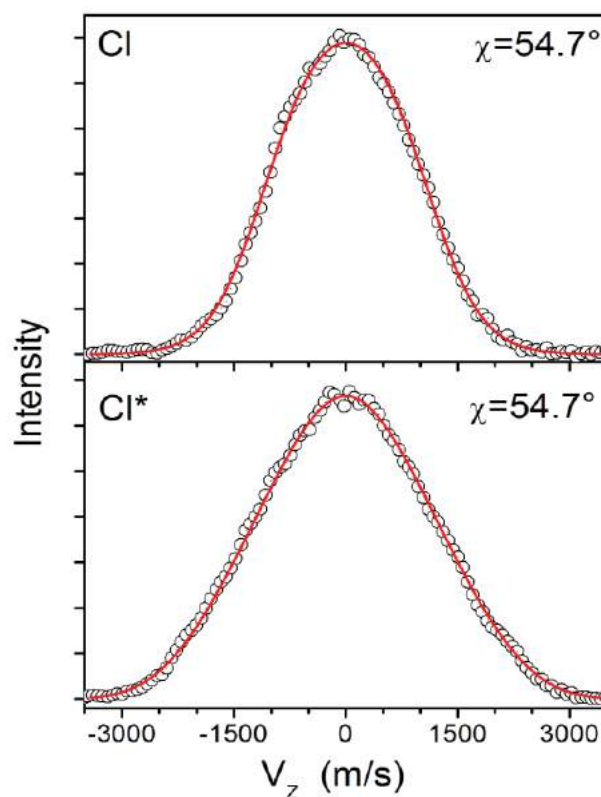
$$\Phi(X^*) = \frac{N(X^*)}{N(X^*)+N(X)} \quad (3.2)$$

The  $\Phi(\text{Cl}^*)$  obtained in the photodissociation of 3,4-dichloro-1,2,5-thiadiazole is found to be  $0.24 \pm 0.06$ .

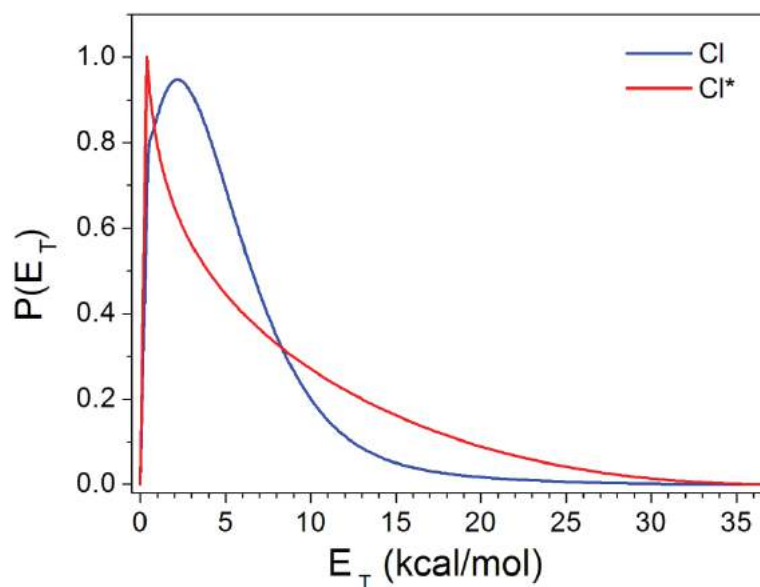
### 3.4.3 Translational energy distribution and anisotropy parameter

The TOF profiles of the Cl and Cl\* atoms were converted into the velocity domain as discussed in Chapter 2. The TOF profiles of the Cl and Cl\* have been found to be independent of laser polarization. TOF profiles recorded for the Cl/Cl\*, fragments, for the laser polarization at the magic angle  $\sim 54.7^\circ$  to the detection axis are shown in figure 3.3. TOF data were analyzed as described in Chapter 2. The predicted TOF spectra were calculated and convoluted with the instrumental response function as described in Chapter 2, [35,36,45]. The final calculated TOF profiles are displayed by the red solid line (figure 3.3). It should be noted that the TOF profile for both Cl and Cl\* are well fitted with one component only. The photofragment translational energy distributions,  $P(E_T)$ , determined from the data in figure 3.3, for the Cl and Cl\*, are depicted in figure 3.4. The

average translational energies of the Cl and Cl\* channels are  $5.2 \pm 1.5$  and  $7.9 \pm 1.5$  kcal/mol, respectively.



**Figure 3.3:** REMPI-TOF profiles of Cl ( $^2P_{3/2}$ ) and Cl\* ( $^2P_{1/2}$ ) produced from the photodissociation of 3,4-dichloro-1,2,5-thiadiazole at 235 nm. The circles are the experimental data and the solid line is a forward convolution fit.

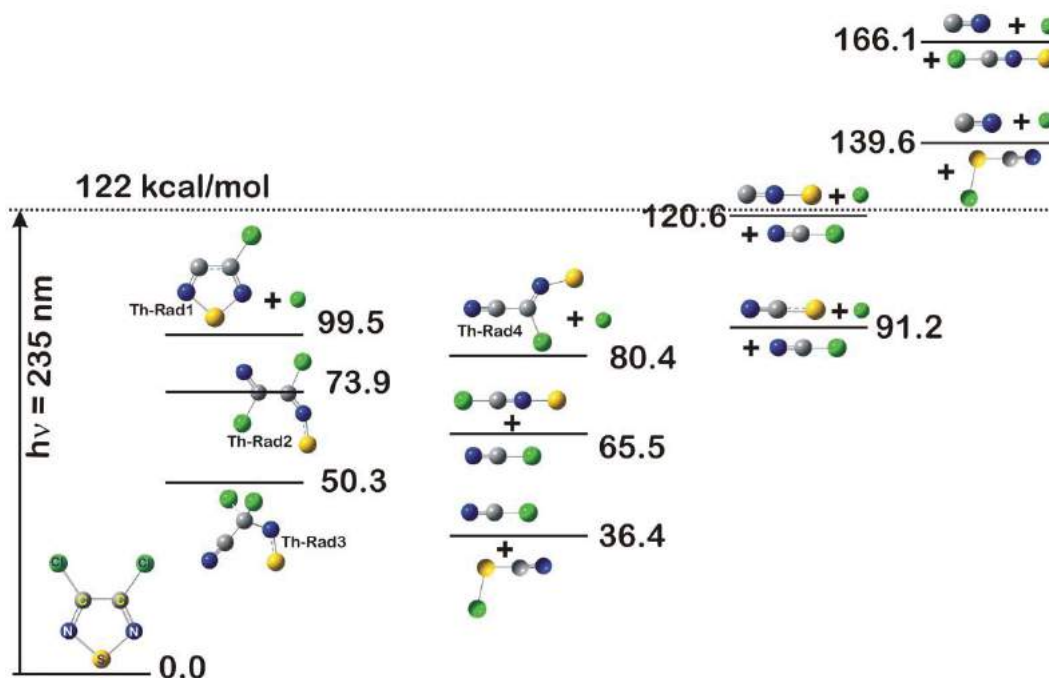


**Figure 3.4:** Centre-of-mass recoil translational energy distribution derived from figure 3.3 for Cl ( $^2P_{3/2}$ ) and Cl\* ( $^2P_{1/2}$ ), produced in the photodissociation of 3,4-dichloro-1,2,5-thiadiazole at 235 nm.

Since the TOF profiles for Cl and Cl\* are independent of laser polarizations, the  $\beta$  parameter is well characterized by a value of  $\sim 0$ , within the experimental uncertainties

### 3.4.4 Theoretical calculations on ground state dissociation of 3,4-dichloro-1,2,5-thiadiazole

Molecular orbital (MO) calculations were carried out to generate the relative potential energy diagram for the dissociation channels, of 3,4-dichloro-1,2,5-thiadiazole on its ground state, accessible on laser excitation at 235 nm. Calculations were done at G3 level of theory, using Gaussian suite of program. All the stationary points were calculated in the ground state, for the various dissociation channels. We did not try to locate the various transition states involved in the different potential energy surfaces (PESs). Hence, we report here only the relative energy diagram for various channels occurring on the ground PES of 3,4-dichloro-1,2,5-thiadiazole. The energy levels are schematically represented in figure 3.5, with the energy of each channels marked in kcal/mol.



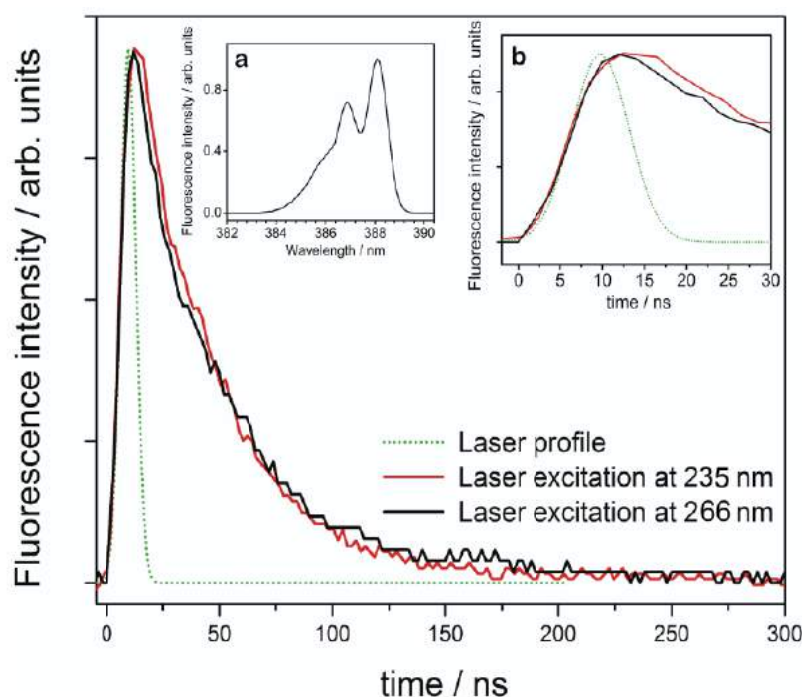
**Figure 3.5:** Relative energy diagram in kcal/mol, along with the structures, for the various products in the photodissociation of 3,4-dichloro-1,2,5-thiadiazole at 235 nm in its ground state.

The initial step is shown as either the cleavage of the C–Cl bond, forming thiadiazole radical (Th-Rad1) and Cl atom, or the cleavage of the N–S bond. Since the two N–S bonds are equivalent, their cleavage opens up the ring structure, forming same intermediate (Th-Rad2, shown in figure 3.5). There are various structures possible after the initial N–S bond cleavage. However, in the figure the most stable structure is shown as (Th-Rad2). Apart from the initial C–Cl or the N–S bond cleavage, a third channel is also identified in the theoretical calculation. It involves the Cl atom migration to neighbouring C atom and subsequent cleavage of N–S bond forming nitrile containing intermediate which is also shown in figure as (Th-Rad3). The thiadiazole radical (Th-Rad1) formed after the initial Cl atom elimination can also undergo ring-opening process by the N–S bond cleavage, forming structure (Th-Rad4) (depicted in figure 3.5). The same structure, Th-Rad4, can also be formed from the primary structures, Th-Rad2 and Th-Rad3, by Cl atom elimination. All these channels are well within the available photon energy (~122 kcal/mol, figure 3.5). The structures Th-Rad2 and Th-Rad3 can also form various fragments, after a C–C bond cleavage. The Th-Rad2 structure can produce ClCN and its co-fragment ClCNS, whereas the Th-Rad3 structure can form CN and Cl<sub>2</sub>CNS, as shown in figure 3.5. However, no attempts were made to characterize the various transition states involved in the above reactions. Similar dissociation channels were also reported by Pasinszki *et al.* in 254 nm irradiation of parent and various substituted 1,2,5-thiadiazole by detecting various radicals such as ClCNS, CH<sub>3</sub>CNS, ClCNS and NCCNS using infra-red coupled with matrix isolation technique [60,61]. In the same study, they have also suggested the elimination of Cl<sub>2</sub> which validates our assumption and calculation showing the migration of Cl atom. In another study, using electron impact ionization of 1,2,5-thiadiazole, similar channels generating nitrile N-sulfides such as, NCCNS, H<sub>2</sub>NCNS, H<sub>3</sub>CSCNS, and ClCNS has been reported [62]. However, in the present study,

we are mainly concerned about the Cl/Cl\* production channel. From our calculations, it is clear that there are at least four different channels which can produce Cl atom in the ground state dissociation of 3,4-dichloro-1,2,5-thiadiazole at 235 nm.

### 3.4.5 UV emission

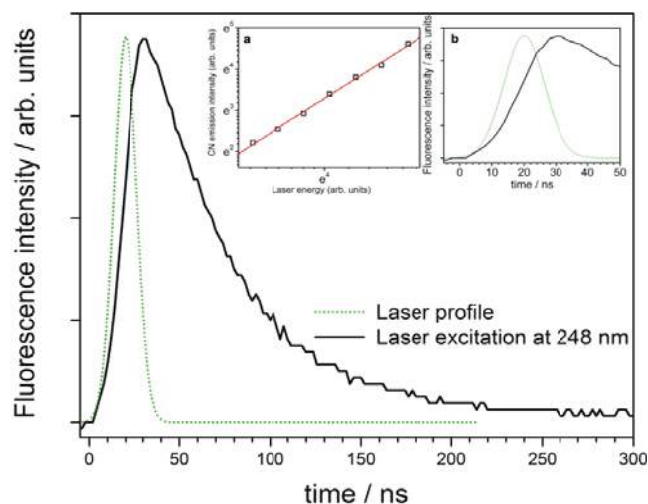
In the photodissociation of 3,4-dichloro-1,2,5-thiadiazole at 235, 248 and 266 nm, a strong and sharp emission in the range of 384-390 nm has been observed (see figure 3.6, inset a). The emission is detected at the pressure of 100-200 mTorr of parent compound and assigned for different band heads characteristic of the CN ( $B^2\Sigma^+ \rightarrow X^2\Sigma^+$ ) emission, corresponding to  $\Delta v = 0$  for (0, 0) (1,1) and (2,2) transitions, respectively [69]. The power dependence measurements have been performed by measuring the emission intensity at  $\lambda_{\text{max}} \sim 388$  nm, at various laser powers.



**Figure 3.6:** Temporal profiles of CN ( $B^2\Sigma^+ \rightarrow X^2\Sigma^+$ ) emission at  $\sim 388$  nm produced in the photolysis of 3,4-dichloro-1,2,5-thiadiazole at different wavelengths, namely, 266 and 235 nm. The green dotted line is laser profile (Gaussian, FWHM = 8 ns) [Inset: (a) CN ( $B^2\Sigma^+ \rightarrow X^2\Sigma^+$ ) emission spectra. (b) Magnified temporal profiles].

The signal shows a linear behaviour in a log-log plot over the range of powers used in the present study and the line exhibits a slope of  $2.0 \pm 0.1$  (see figure 3.7, inset a).

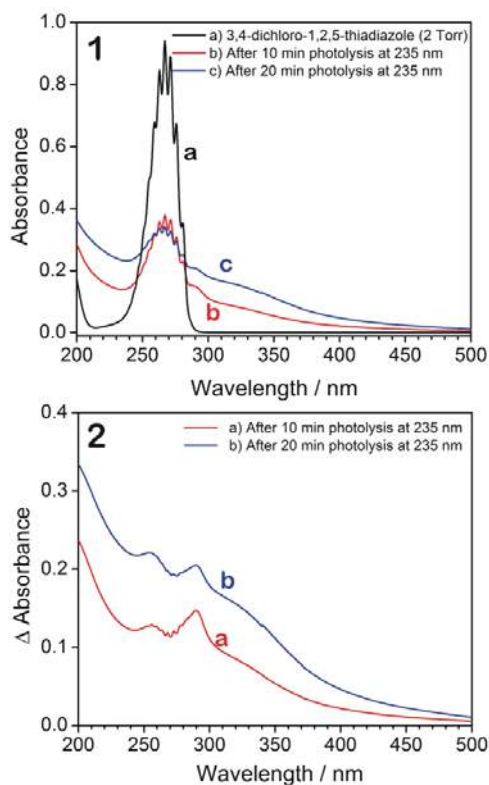
The power dependence studies clearly indicate the role of multiphotonic process in the formation of electronically excited CN radical. To elucidate the formation mechanism of the excited state CN radical, temporal profiles were also taken at  $\lambda_{\text{max}} \sim 388$  nm for various excitation laser wavelengths



**Figure 3.7:** Temporal profiles of CN ( $B^2\Sigma^+ \rightarrow X^2\Sigma^+$ ) emission at  $\sim 388$  nm produced in the photolysis of 3,4-dichloro-1,2,5-thiadiazole at 248 nm. The green dotted line is laser profile (Gaussian, FWHM = 15 ns) [Inset: (a) Dependence of the observed CN ( $B^2\Sigma^+ \rightarrow X^2\Sigma^+$ ) emission intensity at  $\sim 388$  nm on the laser (248 nm) intensity. The slope of the fitted linear log-log plot is  $2.0 \pm 0.1$ . (b) Magnified temporal profiles showing the rising part].

### 3.4.6 UV-Vis absorption

The UV-Vis absorption spectroscopy was performed in a static condition at a pressure range of 1-3 Torr in a 1 cm  $\times$  1 cm quartz cell. Upon irradiation, few new absorption bands emerged at 255, 290 and  $\sim 325$  nm. The bands at 290 and 325 nm were very conspicuous, while the band at 255 nm was only visible after calculating the difference absorption spectra. The absorption bands for the parent precursor were decreased due to its photolysis and can be seen in figure 3.8. Similar new band at 296 nm was also observed by Krebsz *et al.* in the photolysis of 3,4-dichloro-1,2,5-thiadiazole in the matrix isolation study at low temperature [60]. However, the band at 255 and 325 nm were not present in their study. Our main aim here is to identify the species responsible for the new UV-Vis absorption bands in the photolysis of the parent compound 3,4-dichloro-1,2,5-thiadiazole at room temperature.



**Figure 3.8:** (1a) UV absorption spectrum of the 3,4-dichloro-1,2,5-thiadiazole recorded at 2 Torr of pressure. (1b) After 10-min photolysis at 235 nm. (1c) After 20-min photolysis at 235 nm. (2a) Difference UV spectrum for 10 min photolysis. (2b) 20 min photolysis at 235 nm.

### 3.5 Discussion

#### 3.5.1 Nature of excitation at 235 nm

In the following paragraphs we will discuss the UV absorption spectra of the parent compound, i.e. unsubstituted 1,2,5-thiadiazole, and our compound of interest 3,4-dichloro-1,2,5-thiadiazole along with their various excited states and transitions. The onset of optical absorption in 1,2,5-thiadiazole is at about 4.6 eV (270 nm). The gas phase UV absorption spectrum of 1,2,5-thiadiazole with  $\lambda_{\max} = 250$  nm, has a long vibrational progression, with the band origin at 264 nm, for the lowest absorption [55]. The nature of this band has been attributed to the vibrational origin of the  $1^1A_1 \rightarrow 2^1A_1$  or  $\pi^* \leftarrow \pi$  transition. On the other hand, UV absorption of 3,4-dichloro-1,2,5-thiadiazole with  $\lambda_{\max} = 266$  nm, extends up to 290 nm (figure 3.1). It also shows vibronic structure similar to that of 1,2,5-thiadiazole. To understand the nature of the transitions involved in these

halogenated thiadiazole at 235 nm, *ab initio* molecular orbital (MO) calculations were performed in detail, on chlorine substituted thiadiazole, along with the unsubstituted one. Ground state geometries were optimized for 1,2,5-thiadiazole ( $C_{2v}$ ) and 3,4-dichloro-1,2,5-thiadiazole ( $C_{2v}$ ), employing density function theory (DFT) calculation, using aug-cc-pVDZ set of basis sets, maintaining their point group, as mentioned in the parenthesis. The vertical excitation energies for various transitions were then obtained using Time-Dependent Density Functional Theory (TD-DFT) employing the augmented basis set, with diffuse and triple zeta functions, namely, aug-cc-pVTZ. Although the calculated vertical transition energies slightly differ as compared to the experimental results, the nature of transitions and that of the orbitals involved are accurately predicted, using this method. The orbitals participating in the different electronic transitions were visualized using suitable visualization program, for better understanding of the MOs involved in the various transitions. The vertical excitation energies and the respective oscillator strengths of several low-lying singlet states of 1,2,5-thiadiazole and 3,4-dichloro-1,2,5-thiadiazole are shown in table 3.1 . The present computational results for 1,2,5-thiadiazole agree well with the previous results [55]. So, the present computational method can be well applied, to understand the excited states of chloro substituted thiadiazole as well, and may provide very accurate data. Several singlet excited states are considered, out of which, almost all states are valence states. The various computed MOs, including HOMO and LUMO involved in the transition of above two compounds are depicted in figure 3.9 and will be now discussed in brief.

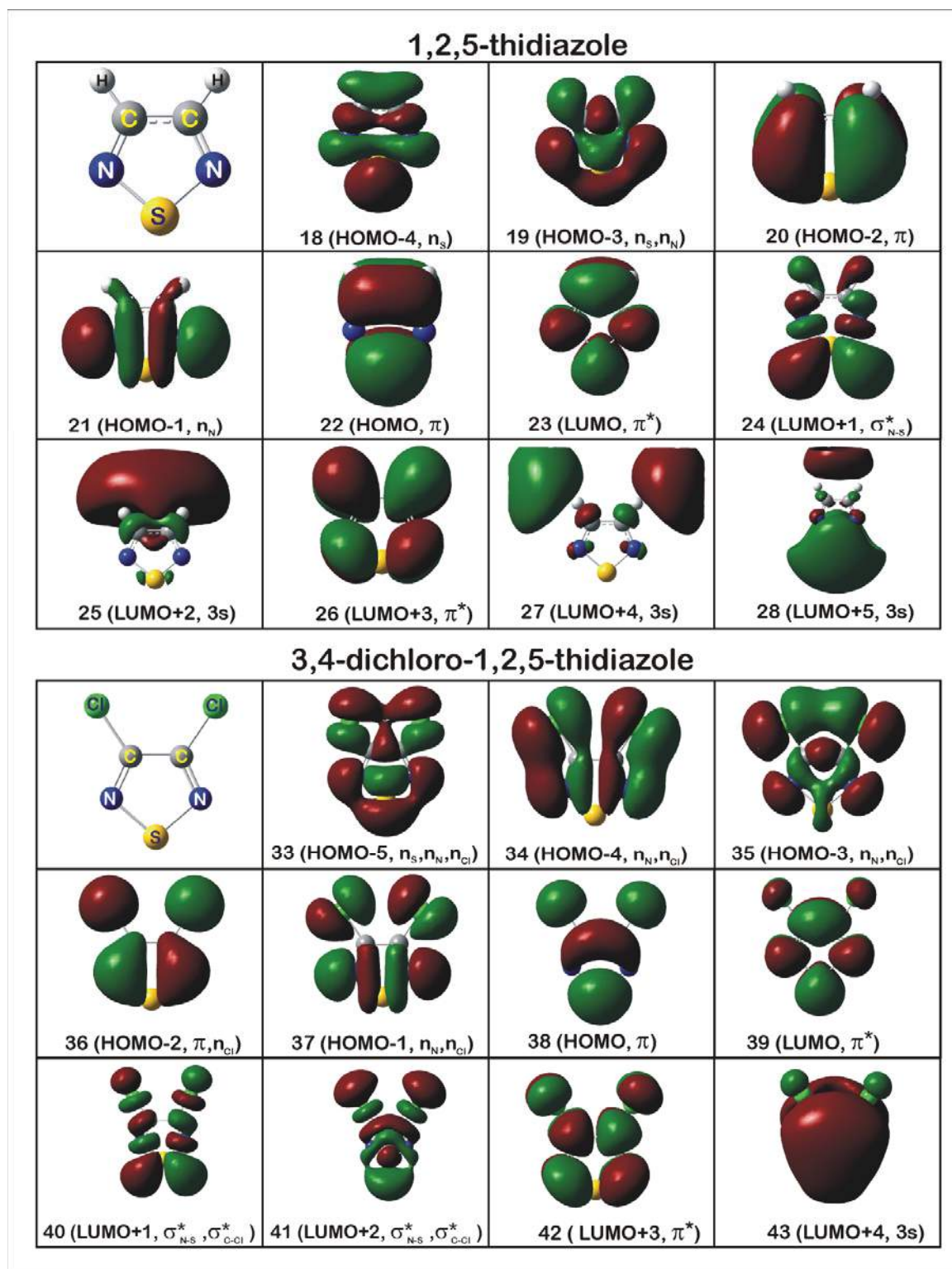
The valence states are primarily due to excitations from the  $\pi$  orbitals, mostly, HOMO and HOMO-1, to  $\pi^*$  orbitals, mostly, LUMO. The other valence states are from the non-bonding electrons of N and S ( $n_N$ ,  $n_S$ ) orbitals to  $\pi^*$  orbitals, for 1,2,5-thiadiazole,



## UV-Photodissociation of 3,4-dichloro-1,2,5-thiadiazole

**Table 3.1:** Vertical excitation energies (eV) and oscillator strengths (given in parentheses) of low-lying singlet states of 1,2,5-thiadiazole and 3,4-dichloro-1,2,5-thiadiazole with respective designation. The  $C_{2v}$  symmetry designation for both the compounds, nature of transition and MO's involved in the transitions are also included in the table.

1,2,5-thiadiazole ( $C_{2v}$ )			3,4-dichloro-1,2,5-thiadiazole ( $C_{2v}$ )		
Excited State	State designation and Type of transition	Vertical excitation energy (eV) and Osillator strength (in parenthesis)	Excited State	State designation and Type of transition	Vertical excitation energy(eV) and Osillator strength (in parenthesis)
S <sub>1</sub>	1 <sup>1</sup> A <sub>2</sub> n <sub>N</sub> → π* 21 → 23	5.14 (0.000)	S <sub>1</sub>	2 <sup>1</sup> A <sub>1</sub> π → π* 38 → 39	4.87 (0.1622) (λ <sub>max</sub> = 4.64 eV) (see spectrum)
S <sub>2</sub>	2 <sup>1</sup> A <sub>1</sub> π → π* 22 → 23 20 → 26	5.41 (0.1380) (λ <sub>max</sub> = 5.00 eV, Ref. 17)	S <sub>2</sub>	1 <sup>1</sup> A <sub>2</sub> n <sub>N</sub> , n <sub>Cl</sub> → π* 34,37 → 39	5.16 (0.0000)
S <sub>3</sub>	1 <sup>1</sup> B <sub>1</sub> n <sub>N</sub> , n <sub>S</sub> → π* 19 → 23	5.97 (0.0019)	S <sub>3</sub>	2 <sup>1</sup> A <sub>2</sub> π → σ* <sub>C-Cl, N-S</sub> 38 → 40	5.49 (0.0000)
S <sub>4</sub>	2 <sup>1</sup> A <sub>2</sub> π → σ* <sub>N-S</sub> 22 → 24	6.20 (0.0000)	S <sub>4</sub>	1 <sup>1</sup> B <sub>1</sub> n <sub>N</sub> , n <sub>Cl</sub> → π* 33,35 → 39	6.05 (0.0034)
S <sub>5</sub>	1 <sup>1</sup> B <sub>2</sub> π → π* 20 → 23	6.58 (0.0194)	S <sub>5</sub>	1 <sup>1</sup> B <sub>2</sub> n <sub>N</sub> , n <sub>Cl</sub> → π* 36 → 39	6.06 (0.0000)
S <sub>6</sub>	2 <sup>1</sup> B <sub>1</sub> π → 3s 22 → 25	6.94 (0.0009)	S <sub>6</sub>	2 <sup>1</sup> B <sub>1</sub> π → σ* <sub>C-Cl, N-S</sub> 38 → 41	6.24 (0.0008)
S <sub>7</sub>	3 <sup>1</sup> A <sub>1</sub> n <sub>N</sub> → σ* <sub>N-S</sub> 21 → 24	7.16 (0.0041)	S <sub>7</sub>	3 <sup>1</sup> A <sub>2</sub> n <sub>N</sub> , n <sub>Cl</sub> → π* 34 → 39	6.38 (0.0000)
S <sub>8</sub>	3 <sup>1</sup> B <sub>1</sub> n <sub>S</sub> → π* 18 → 23	7.43 (0.0018)	S <sub>8</sub>	3 <sup>1</sup> B <sub>1</sub> n <sub>N</sub> , n <sub>S</sub> , n <sub>Cl</sub> → π* 33 → 39	6.76 (0.0003)
S <sub>9</sub>	2 <sup>1</sup> B <sub>2</sub> π → π* 22 → 26	7.57 (0.0479)	S <sub>9</sub>	3 <sup>1</sup> A <sub>1</sub> n <sub>N</sub> , n <sub>Cl</sub> → σ* <sub>C-Cl, N-S</sub> 34,37 → 40	6.86 (0.0115)



**Figure 3.9:** Computed HOMO, LUMO, along with other MOs involved in the transition of 1,2,5-thiadiazole and 3,4-dichloro-1,2,5-thiadiazole.

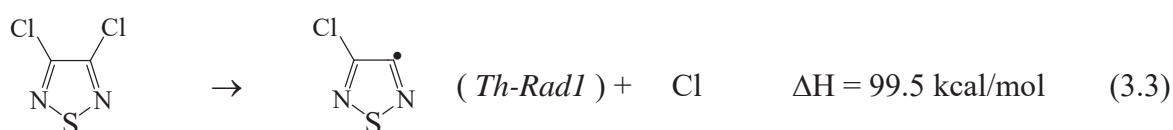
and  $n_N$ ,  $n_S$ , and  $n_{Cl}$  orbitals to  $\pi^*$  orbitals for 3,4-dichloro-1,2,5-thiadiazole. Few other valence states also arises from  $\pi$  orbitals to  $\sigma_{N-S}^*$  or  $\sigma_{C-Cl}^*$  for these thiadiazoles. Besides these valence states, Rydberg states involving excitations to a diffuse  $3s$  orbital are also

included, for comparison. For 3,4-dichloro-1,2,5-thiadiazole, the  $S_1$  ( $2^1A_1$ ) state is a  $\pi^* \leftarrow \pi$  transition, with an oscillator strength of  $\sim 0.16$  at 4.87 eV (255 nm). This calculated value agrees well with the experimental value with  $\lambda_{\max} = 4.64$  eV (267 nm, see spectrum, figure 3.1). Also, the ratio of absorption cross-section for both the compounds, namely, 1,2,5-thiadiazole and 3,4-dichloro-1,2,5-thiadiazole agrees well with the ratio of oscillator strengths calculated theoretically. The second ( $1^1A_2$ ) and third ( $2^1A_2$ ) excited states are basically  $\pi^* \leftarrow n_{N,n_{Cl}}$  and  $\sigma^*_{N-S}, \sigma^*_{C-Cl} \leftarrow \pi$  transition with non-existent oscillator strength. The fourth excited state ( $1^1B_1$ ) arises from a  $\pi^* \leftarrow n_{N,n_{Cl}}$  transition with an oscillator strength of  $\sim 0.0034$  at 6.05 eV (205 nm). The fifth ( $1^1B_2$ ) and seventh ( $3^1A_2$ ) states are  $n_{N,n_{Cl}}\pi^*$  states with missing oscillator strength. The sixth excited state ( $2^1B_1$ ) arises from  $\sigma^*_{N-S}, \sigma^*_{C-Cl} \leftarrow \pi$  transition with an oscillator strength of 0.0008 at 6.24 eV (199 nm). The  $\sigma^*_{C-S,C-Cl} \leftarrow n_{N,n_{Cl}}$  transition gives rise to ninth excited state ( $3^1A_1$ ) with an oscillator strength of 0.0115 at 6.86 eV (181 nm). The first Rydberg state ( $4^1B_1$ ) occurs at 6.89 eV (180 nm) with an oscillator strengths of 0.0307. The second  $\pi^* \leftarrow \pi$  transition which is eleventh excited states ( $2^1B_2$ ) occurs at 6.92 eV (180 nm) with an oscillator strength value of 0.1158. Considering the corresponding wavelengths for vertical excitation energies and the respective oscillator strengths of the various transitions, it is evident that at 235 nm, 3,4-dichloro-1,2,5-thiadiazole have a  $\pi^* \leftarrow \pi$  transition. Since the excited state, with  $\pi^* \leftarrow \pi$  transition, adiabatically correlates with highly excited photoproducts, which is not feasible in a single-photon excitation in the present case. Hence, it is assumed that the initially prepared  $\pi\pi^*$  state crossover to the nearby states, mostly some  $\sigma^*_{N-S,C-Cl}$  state, from where the C–Cl bond can cleavages, forming Cl atoms, and also, the ring opening may occurs, by scission of the N–S bond. Moreover, the initially prepared  $\pi\pi^*$  state can undergo rapid internal conversion to the ground state,

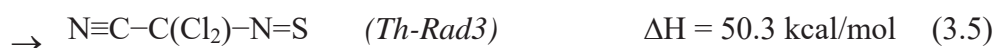
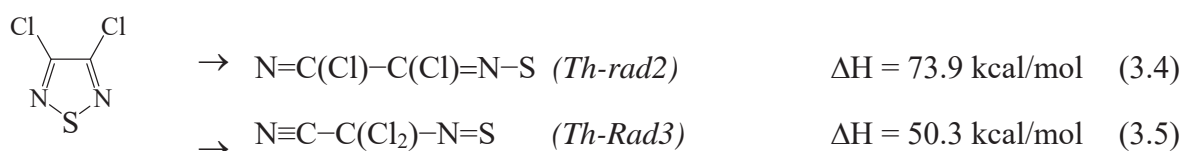
from where various other dissociation channels can occur, in addition to the above mentioned pathways.

### 3.5.2 Translational energy release and anisotropy parameter

The photoexcitation of 3,4-dichloro-1,2,5-thiadiazole at 235 nm (122 kcal/mol) generates Cl atom with absorption of one photon in the simple C–Cl bond cleavage process, and is given as follow:

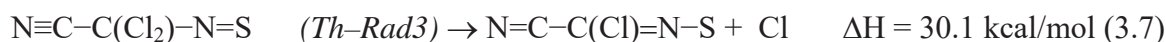
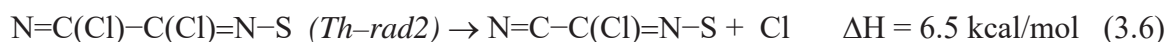


As discussed earlier,  $\Delta H$  values are calculated at G3 level of theory. Reaction (3.3) involves the cleavage of the C–Cl bond, forming Th-Rad1 and Cl atom. For the above reaction, the available energy,  $E_{\text{avail}}$ , which is defined as  $E_{\text{photon}} - \Delta H$ , comes out to be 22.5 kcal/mol. The maximum velocity in the centre-of-mass (CM) coordinate for above reaction is determined to be 2640 m/s and 2490 m/s for Cl and Cl\* elimination channel, respectively. However, the maximum experimental CM velocity obtained for these channels is  $\sim 3000$  m/s (see TOF figure 3.3). This is only possible if there are other low energy Cl atom elimination channels operating at this photoexcitation wavelength. To explore these possibilities, various other reaction channels were also investigated for Cl atom elimination process as described in earlier section. Few reaction channels are as follows:



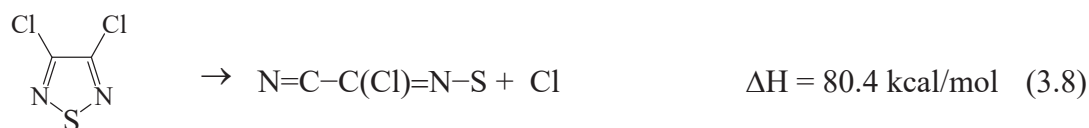
Reactions (3.4) involves ring opening of thiadiazole structure, by N–S bond cleavage, forming Th-Rad2 and similarly reaction (3.5) involves the migration of Cl atom to adjacent C atom and subsequent cleavage of N–S bond forming Th–Rad3. The Cl atom

then can be produced from the subsequent dissociation of the radicals, Th-Rad2 and Th-Rad3, as shown below.



Also, the Th-Rad1 can also generate same reaction by simple N–S bond cleavage.

The overall reaction can be written as



In this scenario, for Cl atom elimination channel, the maximum available energy,  $E_{\text{avail}}$ , will be 41.6 kcal/mol. Apart from these channels, other channels are also possible within the photon energy of 122 kcal/mol and can be seen in figure 3.5.

In the case of 3,4-dichloro-1,2,5-thiadiazole,  $P(E_T)$  for Cl ( $^2\text{P}_{3/2}$ ) formation channel was well described by one component only. The  $P(E_T)$  for Cl ( $^2\text{P}_{3/2}$ ) channel peaks near  $\sim 3$  kcal/mol, and extends up to  $\sim 20$  kcal/mol (figure 3.4). Similarly, the  $P(E_T)$  for Cl\* ( $^2\text{P}_{1/2}$ ) channel peaks near origin, and extends up to  $\sim 35$  kcal/mol (figure 3.4). Although, in the case of substituted halo thiadiazole, the transition at 235 nm is pure  $\pi^* \leftarrow \pi$  in nature, the molecule can predissociate after crossover to the nearby C–Cl repulsive state and also it can relaxes to the ground state via internal conversion from where various other reaction channels can operate.

The partitioning of the available energy into various degrees of freedom of the fragments is mainly governed by the nature of the dissociative potential energy surface, and can be predicted, using simple models, such as impulsive and statistical. It is well known that the energy partitioning in a dissociative event on a repulsive surface is well described by an impulsive model [22]. In this model, the distribution of energy among the product states is governed by the dissociative event, i.e., by the repulsive force acting

during the breaking of the parent molecule into the fragments. In this model, the fraction of the available energy ( $E_{\text{avail}}$ ) released as translational energy is given by

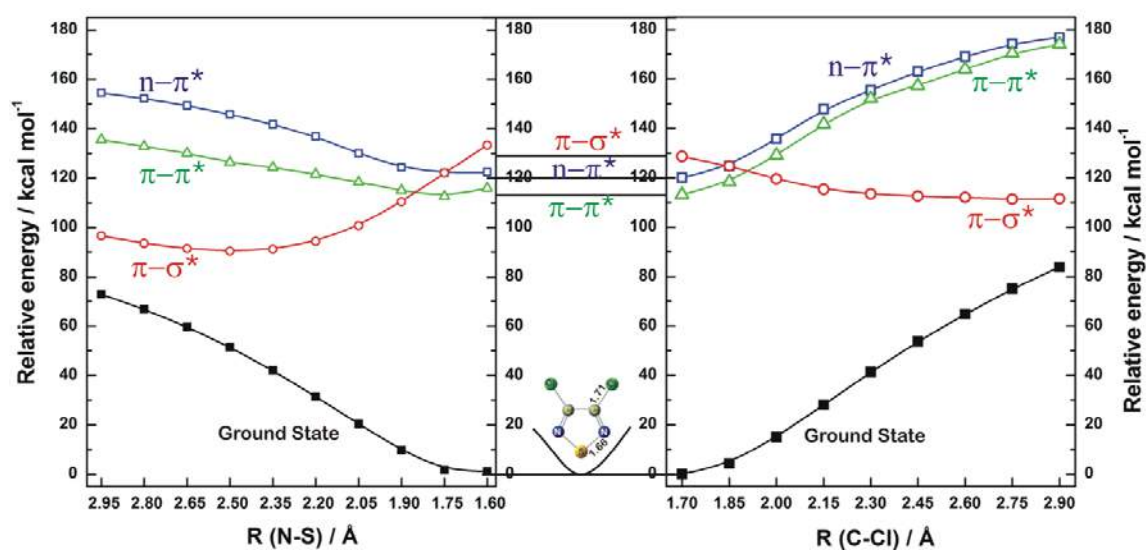
$$E_{\text{T}} = \left( \frac{\mu_{\text{C-Cl}}}{\mu_{\text{C}_2\text{ClN}_2\text{S-Cl}}} \right) E_{\text{avail}}, \text{ and } f_{\text{T}} = E_{\text{T}}/E_{\text{avail}} \quad (3.9)$$

where  $\mu_{\text{C-Cl}}$  is the reduced mass of the C and Cl atoms,  $\mu_{\text{C}_2\text{ClN}_2\text{S-Cl}}$  is the reduced mass of the thiadiazole radical and Cl,  $E_{\text{avail}}$  is the available energy and  $f_{\text{T}}$  is the fraction of the available energy going into the translational modes of the fragments. In the case of 3,4-dichloro-1,2,5-thiadiazole, the ratio of the reduced masses is 0.33. The experimental average translational energies ( $E_{\text{T}}$ ) for the Cl and Cl\* are found to be  $5.2 \pm 1.5$  and  $7.9 \pm 1.5$  kcal/mol, respectively giving the  $f_{\text{T}}$  values of 0.13 and 0.20. The experimentally determined  $f_{\text{T}}$  is considerably lower than the value of 0.33 predicted, using the impulsive model.

A statistical dissociation process occurs predominantly, if the photo-excited parent molecule is so long-lived that the excess energy is partitioned statistically amongst the available degrees of freedom of the products. This may be applicable in a process where a rapid internal conversion to the ground electronic state, followed by the subsequent slow dissociation. Under these circumstances, in a large molecule, with many low frequency modes, a relatively small amount of the excess energy is partitioned into translational motion of the products. For this kind of dissociation process, a priori calculations [70] were adopted, along with a simple analytical expression established by Klots [21], relating the mean translational energy release,  $E_{\text{T}}$ , and the  $E_{\text{avail}}$ , for a statistical barrierless dissociation process, which give a  $f_{\text{T}}$  value of  $\sim 0.07$ . The calculated statistical value of  $f_{\text{T}}$  matches well with the experimental value of 0.12 for Cl atom elimination channel. Similarly, the measured  $f_{\text{T}}$  value of 0.20, for the Cl\* channel, lies in between the values predicted by the impulsive and statistical models. A careful examination reveals that the

$f_T$  value for Cl\* (0.20) is higher than that for Cl (0.12), despite its low  $E_{\text{avail}}$ . If the dissociation occurs on the ground state potential energy surface, then the  $f_T$  value is expected to be the same for both Cl and Cl\*. Hence, the initially prepared 3,4-dichloro-1,2,5-thiadiazole (3,4 DC-1,2,5 TDZ) in the  $\pi\pi^*$  state may cross over to the nearby  $\pi\sigma^*$  state, and subsequently the C–Cl cleavage occurs. Moreover, these  $f_T$  values are determined by taking a  $\Delta H$  value of 80.4 kcal/mol for Cl atom elimination channel from the ground state. If the dissociation process occurs on the excited repulsive state which directly produce Cl and thiadiazole radical (Th-Rad1), then the  $E_{\text{avail}}$  will be  $\sim 22$  kcal/mol by taking  $\Delta H$  value of 99.5 kcal/mol (reaction 3.3). In this scenario, the  $f_T$  values come out to be 0.23 and 0.39 for Cl and Cl\* respectively, which are well within the purview of impulsive model. To further investigate this issue, we have mapped the potential energy (PE) curves for various excited states for the Cl atom elimination channel for 3,4-dichloro-1,2,5-thiadiazole using TD-DFT methods. The third excited state ( $2^1A_2$ ) which has the  $\pi\sigma^*$  character is mainly responsible for the C–Cl bond cleavage in the excited state. However, this excited state has a mixed character comprising of  $\sigma^*_{\text{C-Cl}}$  and  $\sigma^*_{\text{N-S}}$ . Hence, we also decided to map various PE curves for the N–S bond cleavage resulting to the ring opening of the thiadiazole. The PE curves of various excited states along the C–Cl and N–S bond length were calculated. For this purpose, single point TD-DFT calculations on different fixed C–Cl and N–S bond lengths were performed at uMPW1PW91/aug-cc-pVDZ level with all other internal coordinates of ground-state optimized at uMPW1PW91/aug-cc-pVDZ level. For this purpose, the C–Cl and N–S bond lengths were varied from 1.7 Å and 1.6 Å to  $\sim 3.0$  Å, respectively, which is asymptote to its dissociation limit. The sanity of the present theoretical method employed here is confirmed by comparing our results on vinyl chloride with that of Nakatsuji *et al.*,

for its electronic spectra and photodissociation, using symmetry-adapted cluster configuration interaction theory (SAC-CI) [50,71]. Figure 3.10 shows the result of above



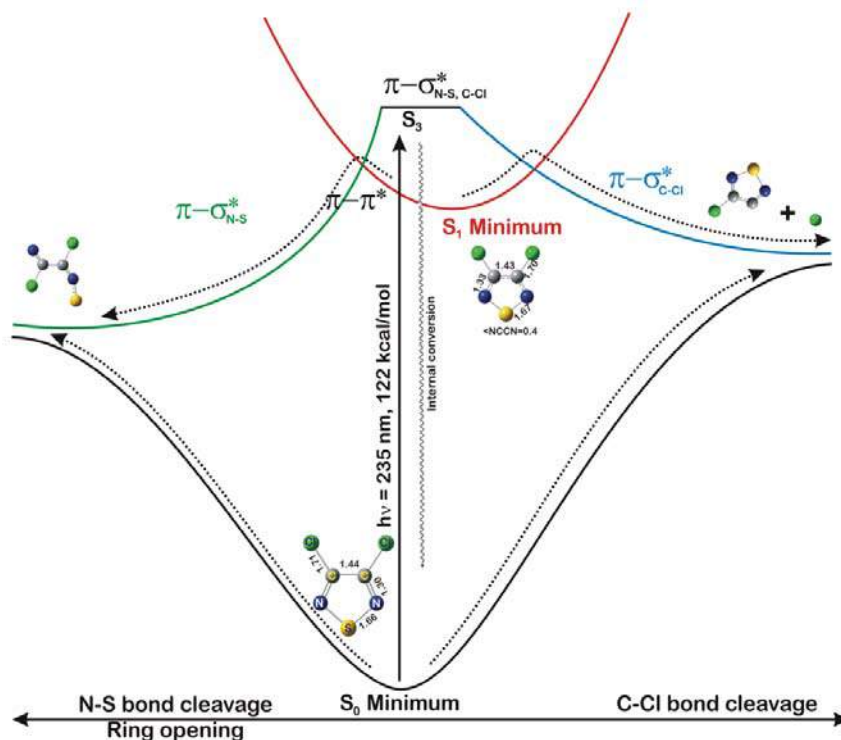
**Figure 3.10:** Various diabatic potential energy curves calculated for 3,4-dichloro-1,2,5-thiadiazole along the C–Cl and N–S bond length with the other geometrical parameters optimized for the ground state using TD-DFT method.

such calculation. From the figure it can be easily seen that the  $\pi\pi^*$  and  $n\pi^*$  states are bound in nature. As mentioned earlier, these states adiabatically correlate with highly excited photoproducts, which is not feasible in a single-photon excitation in the present case. Whereas, the  $\pi\sigma^*$  state is repulsive in nature and intersect both  $\pi\pi^*$  and  $n\pi^*$  states at different internuclear distances. For dissociation along the C–Cl and N–S bond, the cross over from initially prepared  $\pi\pi^*$  to and  $\pi\sigma^*$  states is evident. However, the slope and the energetics of  $\pi\sigma^*$  state along the N–S bond indicates that the N–S bond cleavage seems to be more favourable compare to C–Cl bond cleavage both in excited and ground state. An overall schematic of dissociation process in ground and excited state is presented in figure 3.11.

In the limit of an instantaneous dissociation process, the parameter  $\beta$  is given by  $\beta = 2\langle P_2(\cos \theta_m) \rangle$ , where  $\theta_m$  is the molecular frame angle between the molecular transition dipole moment and the photofragment recoil direction, and  $P_2(\cos \theta_m)$  is the second order



Legendre polynomial. Hence, for a parallel or a perpendicular transition, one would expect anisotropy of +2 or -1, respectively. The recoil anisotropy,  $\beta$ , for the all the halogen atom fragments, measured in the present work is  $\sim 0$ , which indicates an isotropic dissociation process.



**Figure 3.11:** Schematic potential energy diagram for various process in the photodissociation of 3,4-dichloro-1,2,5-thiadiazole at 235 nm.

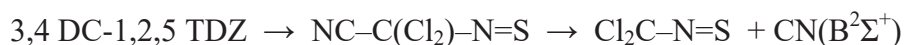
This value of  $\beta$  does not give any indication of the nature of the transition dipole moment in dissociation of halogenated thiadiazoles. The absence of recoil anisotropy in the present studies is expected mainly due to the multiple channels operating for the Cl/Cl\* elimination process. Also, the relatively longer dissociation lifetime associated with the dissociation process from the ground state leads to the absence of recoil anisotropy.

### 3.5.3 UV emission spectroscopic investigations

The nature of the temporal profile especially in the rising part of the CN emission differs for different wavelengths, (figure 3.6 inset b and figure 3.7 inset b) indicating

different mechanism for the formation of the CN radical or its precursor. The temporal profiles at the excitation wavelengths of 235 and 266 nm, show similar behaviour and the formation is well within the laser pulse. However, at 248 nm it shows a slow rise as compared to 235 and 266 nm photolysis. This clearly indicates that the formation of excited state of CN radical is not a one-step process, at least in 248 nm. At 248 nm photolysis, initial formation of intermediate which is a precursor of excited state of CN radical is suggested. Meanwhile, the precursor/intermediate can subsequently absorb another 248 nm photon forming the excited state of CN radical. This observation suggests that the transition state for the formation of precursor/intermediate may be within the vicinity of 248 nm energy. However, at 235 nm, since the energy is well above the transition state, the formation may be very fast and within the laser pulse. However at 266 nm, the mechanism may be quite different. At 266 nm, the energy may be lower than the transition state and the parent molecule may absorb two photons giving rise to excited CN radical in a single process. To shed more light on the above conjecture, detailed *ab initio* calculations have been performed for various channels responsible for the formation of excited state CN radical and we have arrived at three most plausible pathways.

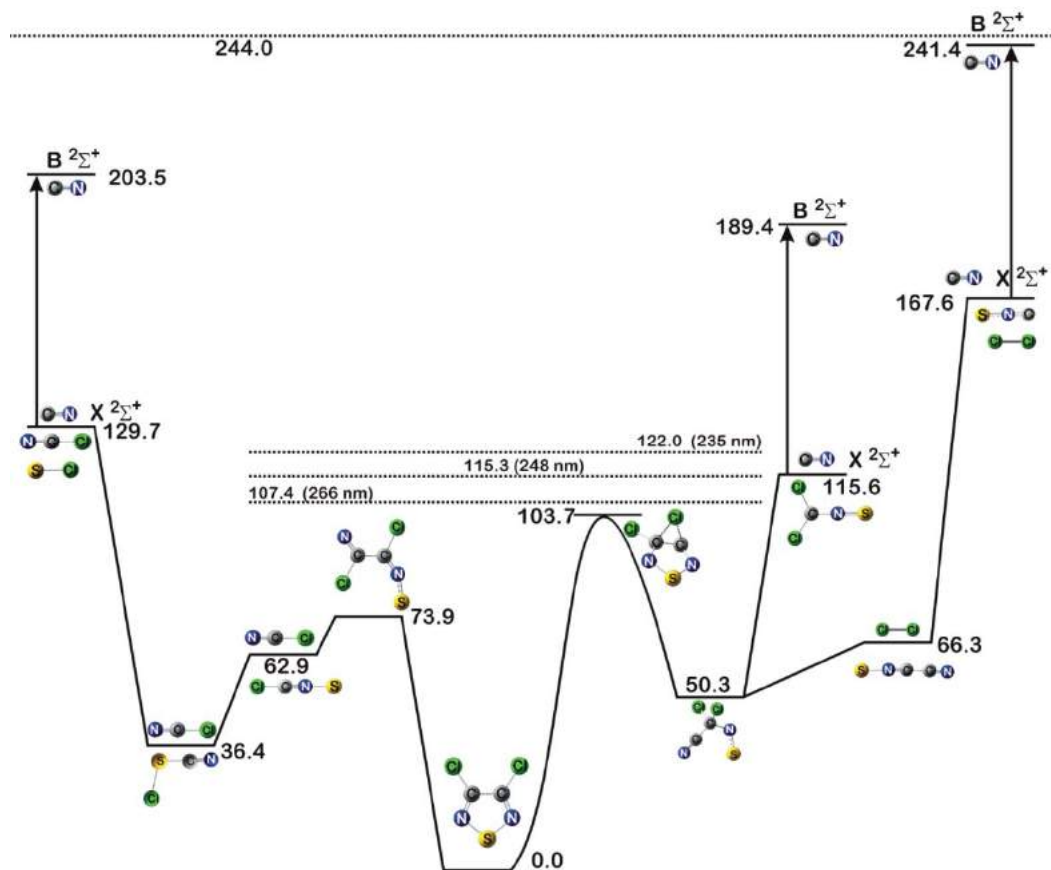
The first pathway involves the Cl atom migration and subsequent ring opening by N-S bond cleavage forming isomer of the parent molecule, namely, NC-C(Cl<sub>2</sub>)-N=S as depicted in figure 3.12. The Cl atom migration process involves a transition state. The transition state for this migration was optimized and the energy was calculated at G3 level of theory. This isomer subsequently absorbs one more photon and dissociates to give CN (B<sup>2</sup>Σ<sup>+</sup>) which is responsible for the emission at 388 nm. The overall ΔH value for this reaction is calculated as 189.4 kcal/mol at G3 level of theory.



$$\Delta H = 189.4 \text{ kcal/mol} \quad (3.10)$$

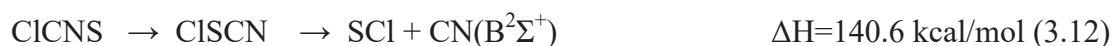
The above mechanism is energetically favourable at all three wavelengths used in the present experiments, namely, 266, 248 and 235 nm.

The second pathway involves the direct ring opening by N–S bond cleavage forming the biradical N(Cl)C–C(NS)Cl and subsequent cleavage of C–C single bond forming ClCN and ClCNS molecule [3].



**Figure 3.12:** Relative energy diagram in kcal/mol, along with the structures, for the various channels forming  $CN(B^2\Sigma^+)$  species in the photodissociation of 3,4-dichloro-1,2,5-thiadiazole in its ground state.

The ClCNS may isomerizes to ClSCN which can subsequently dissociates to give excited state CN radical. The reaction mechanism can be written as

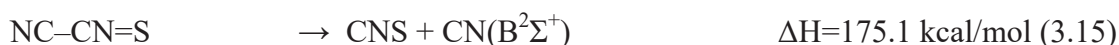
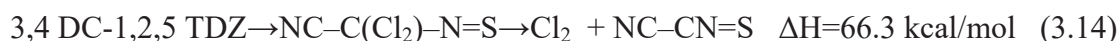


The overall reaction



can be easily achievable with the absorption of two photons of all the laser wavelength used in the experiments. However, some portion of the energy may be imparted in the relative translational mode of the products which may reduce the total available energy and this mechanism may not be feasible at 266 nm, where the total two photon energy is  $\sim 214.8$  kcal/mol.

The third and the last pathway involves the  $\text{Cl}_2$  elimination from the isomer 1 forming  $\text{Cl}_2$  and  $\text{NC-CN=S}$ . The  $\text{NC-CN=S}$  molecule can dissociate to give CN radical in the excited state as follows



The overall reaction can be written as



The overall energetics of this pathway does not agree with the experimental results. Hence, this pathway is certainly not operating in our present experimental condition.

The rising part in the temporal profile at 248 nm and the theoretical calculation confirms the existence of transition state in the vicinity of the energy of 248 nm. These observations conclude that the first pathway, as discussed above, is responsible for the formation of excited state of CN radical. Although theoretically, the transition state lies below the available energy of 266 nm (see figure 3.12), but in real scenario, it may be above the energy of 266 nm. This may explain that at 266 nm it does not show any rising part. At 266 nm, the parent molecule can directly absorb two photons forming  $\text{CN}(\text{B}^2\Sigma^+)$  state. The whole process can be seen in figure 3.12.

### 3.5.4 UV-Vis absorption spectroscopic investigations

As the experiments were performed in a static condition, possibilities of various dimerization reactions were also considered before arriving any conclusions. The most probable dimer is the dimer of ClCNS molecule and we have considered four such dimers in the present study which have been discussed in the following paragraphs.

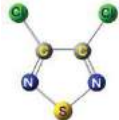


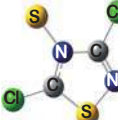

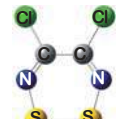
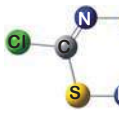


These dimerization reactions were studied theoretically and the UV-Vis absorption spectra of various dimer species were calculated using Time-dependent Density Functional Theory (TD-DFT) at MPW1PW91/aug-cc-pVDZ level of theory by calculating their singlet excitation energies. We have also calculated these singlet excited states at higher basis set such as aug-cc-pVTZ. However, both the calculations end up with similar results. Hence, all other calculations were done at MPW1PW91/aug-cc-pVDZ level of theory only. Although the calculated vertical transition energies slightly differ as compared to the experimental results (see table 3.2 for parent compound), the nature of transitions and that of the orbitals involved are accurately predicted, using this method [5,72,73]. In the following paragraph, we will discuss various reactions, namely, isomerization and dimerization after the photolysis of the parent compound. The singlet excitation energies of these isomers and dimers with their respective oscillator strengths are shown in table 3.2.

#### 3.5.4.1 Isomerization reaction

**3.5.4.1.1 Isomer 1** As described in the earlier section, the formation of first isomer pathway involves the Cl atom migration and subsequent ring opening by N-S bond cleavage. Various vertical excitation wavelengths can be easily seen in the table 3.2 with their respective oscillator strengths. The calculated first and second excited states appear at 318 and 308 nm with their respective oscillator strengths of 0.0025 and 0.0015. The other most prominent calculated excited states, namely, 3rd, 4th, 6th and 8th appear at

293 (0.0314), 264 (0.0066), 239 (0.0707) and 200 (0.1021) nm respectively. The first and second calculated peak can be compared to experimentally observed peak at 290 nm. Similarly the calculated peak at 293 nm can be compared with 255 nm. It is well known in the literature that TD-DFT methods are not reliable for the calculation of vertical excitation energies. Hence, we have decided to calculate the vertical excitation energies using other more accurate methods. Here, we have chosen two methods for such calculations. The first method is based on the Equation-of-motion coupled with CCSD

**Table 3.2:** Calculated vertical excitation energies (nm) and oscillator strengths (given in parentheses) of low-lying singlet states of 3,4-dichloro-1,2,5-thiadiazole along with its isomers, dimers of CICNS, CICNS and SNCCN. Transitions with calculated oscillator strength less than of 0.0010 are not shown in the table. Vertical excitation energies are calculated using DFT method employing aug-cc-pVDZ basis set.

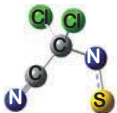
3,4 DC-1,2,5-TDZ 	Isomer 1 	Isomer 2 	Dimer 1 (CICNS dimer) 	Dimer 2 (CICNS dimer) 
252 (0.1616) 267 (expt.) 252 (0.1775)* 246 (0.2702)** 203 (0.0034) 177 (0.0118) 177 (0.0287) 177 (0.1161)	318 (0.0025) 308 (0.0015) 293 (0.0314) 264 (0.0066) 252 (0.0013) 239 (0.0707) 222 (0.0014) 200 (0.1021)	235 (0.0849) 202 (0.0016) 197 (0.0954) 186 (0.0074) 176 (0.1963) 174 (0.0515) 174 (0.0108) 167 (0.0019)	406 (0.0723) 303 (0.0043) 279 (0.1181) 251 (0.0037) 241 (0.0028) 237 (0.0225) 234 (0.1027) 225 (0.0285) 215 (0.0136)	382 (0.1321) 315 (0.0318) 273 (0.0874) 228 (0.0010) 227 (0.09420) 221 (0.0759) 212 (0.0212) 206 (0.0012)
Dimer 3 (CICNS dimer) 	Dimer 4 (CICNS dimer) 	NC-CN=S 	Cl-CNS 	
338 (0.0021) 262 (0.0952) 233 (0.1033) 228 (0.0287) 215 (0.0034)	264 (0.0019) 228 (0.0018) 225 (0.1016) 215 (0.0225) 214 (0.0820)	211 (1.3444) 202 (0.0009) 202 (0.0009)	215 (0.0218) 215 (0.0218) 202 (0.0036) 200 (0.7622) 188 (0.0164) 188 (0.0164)	

\*Calculated at EOM-CCSD/aug-cc-pVDZ level of theory

\*\*Calculated at SAC-CI/ aug-cc-pVDZ level of theory

(EOM-CCSD) and second is Symmetry Adapted Cluster/Configuration Interaction (SAC-CI) method. These methods were used for calculating the excitation energies and the results can be seen in tables 3.2 and 3.3 for parent molecule and isomer, respectively. A detailed comparison of TD-DFT method with EOM-CCSD and SAC-CI can be seen in the recent articles by Caricato *et al.* [73] and Bousquet *et al.* [74].

**Table 3.3:** Calculated vertical excitation energies (nm) and oscillator strengths (given in parentheses) of low-lying singlet states of isomer 1,  $NC(Cl_2)-N=S$  using various methods employing aug-cc-pVDZ basis set.

Isomer 1 		
TD-DFT	EOM-CCSD	SAC-CI
318 (0.0025) A'	272 (0.0010) A''	294 (0.0010) A''
308 (0.0015) A''		
293 (0.0314) A'	223 (0.0232) A'	215 (0.0504) A'
	211 (0.0014) A''	212 (0.0184) A''
264 (0.0066) A''		
252 (0.0013) A''	210 (0.0662) A'	209 (0.0811) A'
239 (0.0707) A'	198 (0.0017) A''	206 (0.0063) A''
222 (0.0014) A'		
200 (0.1021) A'	184 (0.1000) A'	199 (0.0510) A'

**3.5.4.1.2 Isomer 2** It is known in the literature that the lowest energy and barrierless dissociation pathways for the parent molecule is to form ClCN and ClCNS molecules after initial N-S bond cleavage followed by the C-C bond cleavage. There are various possibilities of dimerization of ClCNS molecule because of presence of sulfur atom. However, the ClCN and ClCNS molecules themselves can recombine to form isomer 2, which is 3,5-dichloro-1,2,4-thiadiazole as shown in figure 3.13. For this isomer, the most intense peak is at 235 nm with oscillator strength of 0.0849. All other peaks with considerable oscillator strength are at much higher energies.

### 3.5.4.2 Dimerization reaction

**3.5.4.2.1 Dimer 1** The first ClCNS dimer as shown in figure 3.13 shows three intense peaks at 406, 279 and  $\sim 235$  nm. This isomer also contains a 1,2,4-thiadiazole ring structure. Although the calculated peak at 279 nm can be compared with experimental peak at 290, we fail to observe any peak in the vicinity of 400 nm experimentally. Also, it will be erroneous to compare the calculated peak at 235 nm with the experimental peak at 255 nm. Hence this dimer is also tentatively ruled out.

**3.5.4.2.2. Dimer 2** Similarly, the second dimer is also depicted in figure 3.13 and in table 3.2. This isomer possesses a 1,2,5-thiadiazole ring structure. For this dimer, the most intense calculated peak lies at 382 nm. Here also, it is really hard to compare these calculated peaks with the experimental peaks. Hence, the formation of this dimer is also ruled out in the present experimental condition.

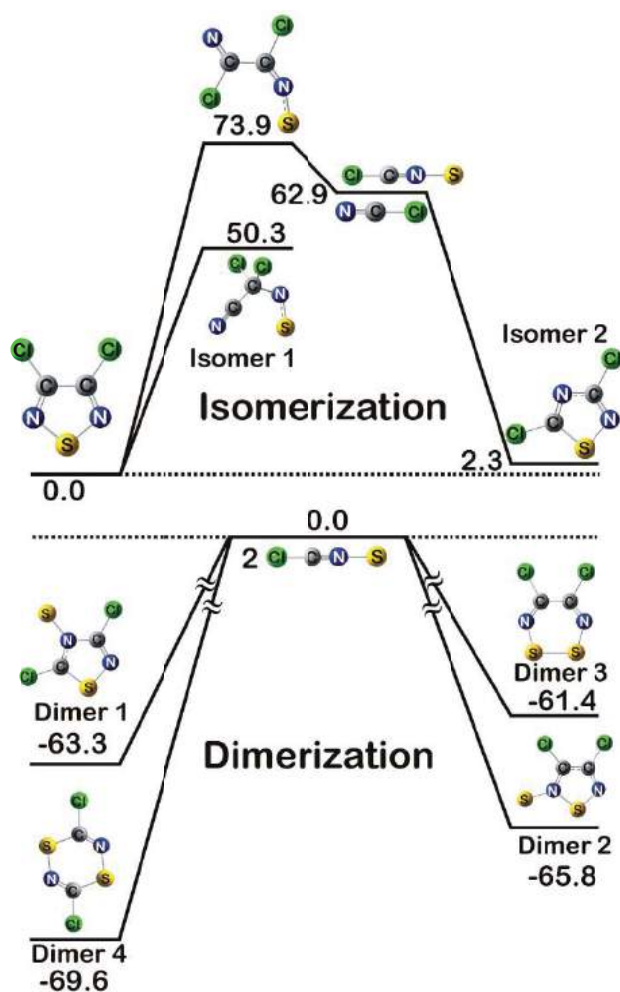
**3.5.4.2.3. Dimer 3** The dimer 3 has a disulfide link in a six membered ring structure as shown in figure 3.13. For this dimer the most intense peaks are calculated at 262 and 233 nm. In this case also, there is vast difference in the calculated and the experimental peaks. Detail comparison with the energetics of various dimers formation will be discussed in later section.

**3.5.4.2.4 Dimer 4** As shown in figure 3.13, it has hexagonal structure with two carbon, nitrogen and sulfur in the ring. This particular isomer has intense calculated peak at 225 nm which can't be compared with experimental peak at 290 nm.

Apart from the calculated singlet excitation energies for various isomer and dimers, their formation enthalpies also play a major role in their formation. The formation route for the isomer 1 has a barrier of  $\sim 104$  kcal/mol and can be easily achieved at 235 nm. Apart from this route, all other routes are basically involved in the recombination reaction and can be called as bimolecular reaction. These bimolecular reactions also have



barrier for the formation. However, in the present case we have not calculated the barrier for the recombination reaction. Assuming that the system has enough energy to cross the barrier for dimerization, the relative stability of various dimers plays a major role in their formation. Hence, a relative energy diagram was calculated at G3 level theory for various isomer and dimers and can be seen in figure 3.13. The most stable dimer is thus dimer 4 and its excitation energies do not match with experimental peaks. Moreover, in the present experimental condition, the ClCNS molecule can also subsequently absorb one more photon and may dissociate to form ClCN and S atom. In fact, sulfur particles have been observed on the glass cell surface during photolysis of the parent compound 3,4-dichloro-1,2,5-thiadiazole. Hence, in the present experimental condition, the dissociation



**Figure 3.13:** Relative energy diagram in kcal/mol, along with the structures, for the various isomerization reaction of 3,4-dichloro-1,2,5-thiadiazole and dimerization reactions of ClCNS.

of ClCNS molecule to form ClCN and S atom seems to be more favourable compared to its dimerization reaction. In this scenario, the most probable isomer which explains the experimental results is isomer 1. Also, the broad peak at 325 is assigned to Cl<sub>2</sub> molecule [75], which can be formed either directly from the parent compound itself or from the isomer 1 forming SNCCN and Cl<sub>2</sub> molecule. In the previous study performed at low temperature in matrix, the formation of SNCCN molecule was confirmed using IR absorption spectroscopy [60]. The observation of Cl<sub>2</sub> spectra tentatively confirms the presence of isomer 1 as a photolysis product.

### 3.6. Conclusions

The photodissociation of 3,4-dichloro-1,2,5-thiadiazole has been carried out at around 235 nm, and the dynamics of C–Cl bond dissociation is investigated, using resonance-enhanced multiphoton ionization, coupled with a time-of-flight mass spectrometer. The excitation at 235 nm prepares the molecule in the  $\pi\pi^*$  state. We have determined the photofragment speed distribution, the anisotropy parameter  $\beta$  and the spin-orbit branching ratio, for chlorine atom elimination channels, to gain insights into the dynamics of halogen atom formation. Polarization dependent and state-specific TOF profiles are utilized, to get translational energy distributions, using a forward convolution method and taking into account the fragment anisotropies. The anisotropy parameters for both Cl and Cl\* are the same and characterized by values of  $\sim 0$ . In the translational energy distribution for Cl and Cl\* are well characterized by one component. The average translational energies for Cl and Cl\* channel are  $5.2 \pm 1.5$  and  $7.9 \pm 1.5$  kcal/mol, respectively. The partitioning of energy into the translational modes is interpreted with the help of various models, such as impulsive and statistical models. Finally, it is concluded that the dissociation is mostly from the excited state which is  $\pi\sigma^*$  in nature and

also from the ground electronic state after internal conversion process from initially prepared  $\pi\pi^*$  state.

The ground state photodissociation mechanism of 3,4-dichloro-1,2,5-thiadiazole was studied using UV-Vis emission and absorption technique in flow and static conditions at various wavelengths, namely, 266, 248 and 235 nm. Results were augmented with the help of theoretical methods. Multiphotonic excitation leading to the UV emission in the range of 389 nm was observed due to the formation of CN ( $B^2\Sigma^+$ ) moiety. The mechanism of CN( $B^2\Sigma^+$ ) formation was attributed to the formation of isomer 1, namely NC-C(Cl<sub>2</sub>)-N=S. Absorption band at 325 nm was attributed to the formation of molecular chlorine (Cl<sub>2</sub>) elimination. Two new UV absorption bands at ~255 and ~290nm were tentatively assigned to the new isomer NC-C(Cl<sub>2</sub>)-N=S using theoretical methods. Dimerization reactions of ClCNS molecule was also studied using theoretical methods. The extent of dimerization reaction seems to be very small in the present experimental conditions. UV absorption and quantum calculation confirms the migration of chlorine atom and subsequent ring opening to form NC-C(Cl<sub>2</sub>)-N=S isomer.



## Chapter 4

### Photodissociation of Halogenated Pyridines at 235 nm

---

#### 4.1 Introduction

Photodissociation dynamics of relatively large polyatomic molecules are often complex owing to their multiple dissociation channels. However, studies related to simple polyatomic molecules are well understood. These studies often provide detailed information about various excited states for a given molecular system [1,42]. In recent years, pyridine and its derivatives, especially, halogen substituted, have received great attention because of their occurrence in the environment [76,77]. It is well known that the photodissociation of chlorine containing molecules in the ultraviolet (UV) range generates chlorine atoms which are detrimental for the ozone layer in the stratosphere [31,32]. Pyridines, in general, have moderately acute toxicity and show teratogenic character. Various pyridines containing halogen atoms were reported to show mutagenic activity [78]. Pyridine and its derivatives, in the long run, may enter the environment as a result of their extensive use as insecticides, herbicides and in various industries. Widespread use of these compounds can result in the contamination of surface and ground water in areas around their application or discharges zones. Therefore, the knowledge of the fate of these heterocyclic pollutants in various ecosystems is an important environmental consideration [77]. Owing to its volatility, these pyridines based compounds may enter the upper atmosphere where the photodissociation process can

occur. In this context, the current study presents the photodissociation dynamics of halogenated pyridines. The present study not only gives the detail dynamics of the chlorine atom formation channel, but also the dissociation dynamics of pyridines, in general.

Photodissociation of pyridine was earlier investigated at 193 nm by Lee and his group [79,80] using photofragmentation translational spectroscopy and the multimass ion imaging technique and reported at least six different dissociation channels occurring at the energy of 148 kcal/mol. In another study using time resolved photoelectron imaging experiment using ultrafast lasers, a dramatic decrease in the fluorescence quantum yield of photoexcited pyridine was observed when the excitation wavelength was shorter than 275 nm. This was interpreted as a result of a non radiative pathway, termed as “channel three” region. Upon excitation to the “channel three” region, an ultrafast decay of the  $S_1$  ( $n\pi^*$ ) state was observed with the lifetime of  $\sim 4$  ps. This experiments also suggested that the excited pyridine relaxes to an optically dark state within this short time scale [81]. Vapor-phase fluorescence from the  $S_1$  ( $n\pi^*$ ) state decreases sharply as excitation energy is raised to the value corresponding to  $S_2$  ( $\pi\pi^*$ ) state. The fast non-radiative decay responsible for the sharp decrease of the fluorescence quantum yield was attributed to the  $S_0 \leftarrow S_1$  internal conversion [82]. Fluorescence lifetime of pyridine vapor was measured to be 35–50 ps, which was dependent on the various vibrational levels excited in the lower energy region of  $S_1 \leftarrow S_0$  transition [83]. Excitation energies of pyridine has been calculated using complete active space self consistent field (CASSCF) method and compared with experimental results [84].

Substituted pyridines occur more commonly than pyridine. Photolytic destruction of 2-halogenated pyridine was studied at 254 nm [85]. 2-hydroxypyridine was reported as a primary intermediate formed by destruction of 2-chloropyridine, 2-bromopyridine and 2-

iodopyridine. 2-hydroxypyridine was further restructured to form Dewar pyridine [85]. The comparative study of photocatalytic degradation of 3-chloropyridine was studied in both homogeneous and heterogeneous phase in UV and solar light [86]. In the same study, standard molar enthalpy of formation of 3-chloropyridine at 298.15 K was reported as  $25.7 \pm 0.4$  kcal/mol. Similarly, the photodissociation of 3-iodopyridine was studied with state selective photofragment translational spectroscopy at 266 nm and 304 nm [87]. For the iodine (I) atom formation channel, a fast and a slow recoil speed distribution was observed at both the wavelengths studied. The fast translational energy distribution was proposed to result from the dissociation process from  $n\sigma^*$  state directly whereas the slow translational energy component was suggested to arise from the predissociation process from initially excited  $\pi\pi^*$  state after mixing with the nearby repulsive  $n\sigma^*$  state.

Since benzene and pyridine have similar photophysical and photochemical properties and similar resonance structures, the photodissociation dynamics of chlorinated benzene is worth mentioning in the present context. Photodissociation dynamics of chlorobenzene (ClBz) has been studied at 266 nm by femtosecond pump-probe spectroscopy [88] and crossed laser-molecular-beam technique [89]. TOF distribution of Cl fragment in photodissociation of ClBz at 193 nm, 248 nm and pentafluorochlorobenzene at 193 nm has been studied [90-92]. Three major channels in the photodissociation of ClBz at 193 nm have been suggested with similar probabilities. The first channel was assigned to a direct dissociation or very fast predissociation, the second channel is via vibrationally excited triplet levels, and the third dissociation channel is via highly excited vibrational levels of the ground electronic state. The photodissociation of ClBz at 248 nm and pentafluorochlorobenzene at 193 nm was proposed to occur dominantly via the second and third channel as mentioned above. However, at 266 nm, it was proposed that the vibrationally hot ground state molecule is

responsible for the dissociation process [89]. On the other hand, Kadi *et al.* [88] assigned the dissociation process to the crossover of an initially excited  $\pi\pi^*$  state to a nearby repulsive triplet  $n\sigma^*$  state due to spin-orbit coupling.

In our previous studies, we have reported the dynamics of Cl and Br atom formation in the photodissociation of halogenated heterocyclic molecules such as 2-furoyl chloride [93], 2-chlorothiophene and 2-bromo-5-chlorothiophene[47] at 235 nm using REMPI-TOF technique. Similar to benzene and pyridines, photoexcitation at 235 nm prepares these heterocyclic molecules in the  $\pi\pi^*$  state. These studies reveal that in 2-chlorothiophene photodissociation, Cl photofragment shows bimodal translational energy distribution similar to that of ClBz. While fast energy component was suggested to result from the crossing of initially prepared  $\pi\pi^*$  to nearby  $n\sigma^*_{C-Cl}$  state, the slow energy component was attributed to the ground electronic state dissociation. Similar results were also reported in the case of 2-bromo-5-chlorothiophene dissociation for Cl and Br atom photofragments. The only difference between benzene/pyridine with respect to substituted thiophene was in ground state dissociation process where the most favorable process was the ring opening process resulting from weakest C–S bond cleavage.

In this context, we have undertaken the photodissociation dynamic studies of 3-chloropyridine and 3-chloro-2,4,5,6-tetrafluoropyridine where the Cl atom is directly attached to heterocyclic ring using resonance enhanced multiphoton ionization (REMPI) with time-of-flight (TOF) Mass spectrometry. The presence of the N atom in the ring can also change the nature of the dynamics of the dissociation process. It is also interesting to see whether there is any ground state contribution for the Cl atom formation process as observed in case of 2-chlorothiophene or the dissociation is solely from the excited state. We have also studied the fluorine substitution effect on the photodissociation dynamics, quantum yield determination of Cl and Cl\*, power dependent measurements, translation



energy distribution and fragmentation pattern of the parent molecule. This study will also provide an answer about the effect of fluorination on the nature of various excited states in an aromatic molecule.

## 4.2 Experimental

The experiment was performed using a molecular beam time-of-flight mass spectrometer system (MB-TOF-MS), as described in the chapter 2. The 3-chloropyridine of 99% purity and 3-chloro-2,4,5,6-tetrafluoropyridine of 98% purity supplied by Aldrich were used after repeated freeze-pump-thaw cycles. Helium was bubbled through the sample, maintained at room temperature, and the mixture was expanded through the nozzle at a stagnation pressure of 1500 Torr. It was ensured that any interference to the measurements due to cluster photofragmentation was absent, or negligible, by operating at a low stagnation pressure, and using only the rising part of the molecular beam pulse. The power dependence measurements revealed a three photon dependency, which is consistent with one-photon dissociation of test molecules, followed by (2+1) REMPI of the chlorine atoms, assuming that the ionization step is saturated. Apart from the power dependence studies, we also systematically monitored the shape and the width of TOF profiles of Cl atoms at various laser intensities. All the experiments were performed in the intensities, which are much lower than the intensity at which the shape and width of the TOF profiles were invariant. This experimental condition ensures that the translational energy distributions and the anisotropy parameters are invariant over the laser fluences used.

## 4.3 Analysis

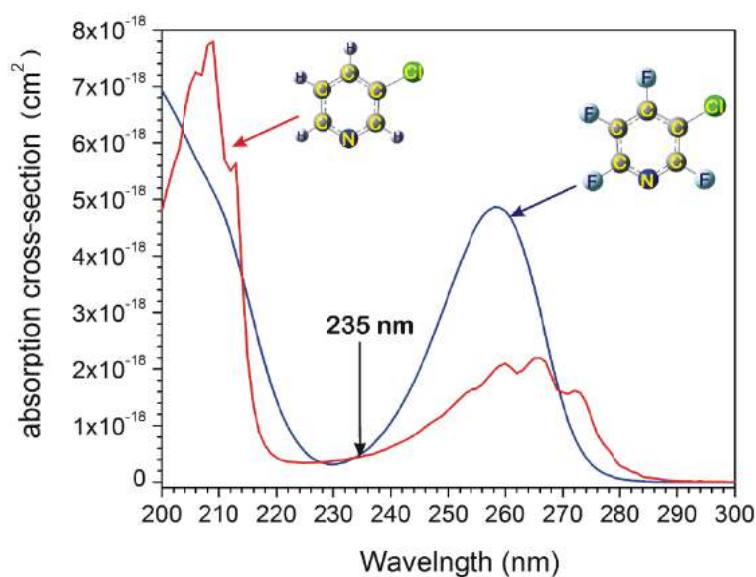
The TOF profiles of Cl and Cl\* are measured at different laser polarizations. The translational energy distribution and the anisotropy parameter for both Cl and Cl\* are determined from these TOF profiles, using a commonly used forward convolution (FC)

technique, as described in the chapter 2. Using this method, the parameters are adjusted until a satisfactory agreement with the experimental data is achieved. Once the photofragment speed distributions have been determined, these were used to obtain the corresponding translational energy distributions.

## 4.4 Results

### 4.4.1 Absorption spectra and absolute cross-section

The absorption spectra for both the compounds were recorded using a commercial UV spectrophotometer at various pressures. The absolute absorption cross-sections were then calculated using Beer-Lambert law. Figure 4.1 shows such absorption spectrum with its absolute absorption cross-section for 3-chloropyridine and 3-chloro-2,4,5,6-tetrafluoropyridine, respectively. These absolute absorption cross-section values were



**Figure 4.1:** UV absorption spectrum of 3-chloropyridine and 3-chloro-2,4,5,6-tetrafluoropyridine at room temperature with their absolute absorption cross-section.

further verified by measuring the same at 235 nm using a 50-cm long absorption cross-section cell as described in chapter 3. The absorption cross-section for both the compounds, namely, 3-chloropyridine and 3-chloro-2,4,5,6-tetrafluoropyridine, at 235 nm are nearly same and found to be  $(5.0 \pm 1.5) \times 10^{-19} \text{ cm}^2 \text{ molecule}^{-1}$  (figure 4.1).

#### 4.4.2 Spin-orbit branching ratio

Doppler profiles of Cl ( $^2P_{3/2}$ ) and Cl\* ( $^2P_{1/2}$ ) atoms produced in the dissociation of 3-chloropyridine and 3-chloro-2,4,5,6-tetrafluoropyridine are scanned in the wavelength region of  $42492.5\text{ cm}^{-1}$  and  $42516.1\text{ cm}^{-1}$ . The relative quantum yield of the Cl atom formed in different spin-orbit states (X, X\*), were calculated by normalizing the integrated intensity, i.e., the peak areas S(X), or S(X\*), of the respective (2+1) REMPI transitions with respect to the laser intensity, and the ratio of the two-photon absorption coefficients as discussed in our previous work [45]. The intensities S(X) and S(X\*) were obtained by integrating the measured ion signal intensities covering the Doppler width and the probe laser bandwidth. The measurements were repeated at different laser light intensities, giving similar relative signal intensities. From the experimentally measured integrated intensity ratios, S(Cl\*)/S(Cl), one can easily obtain the product ratios N(Cl\*)/N(Cl). The relative quantum yields,  $\Phi(X^*)$ , as described in our earlier work [45] can be calculated as follows

$$\Phi(X^*) = \frac{N(X^*)}{N(X^*)+N(X)} \quad (4.1)$$

The  $\Phi(\text{Cl}^*)$  obtained in the photodissociation of 3-chloropyridine and 3-chloro-2,4,5,6-tetrafluoropyridine is found to be  $0.09 \pm 0.02$  and  $0.11 \pm 0.02$ , respectively.

The relative quantum yield is usually governed by nature of excited potential energy surfaces (PESs) in Franck-Condon region as well as subsequent coupling between the PESs as products depart.

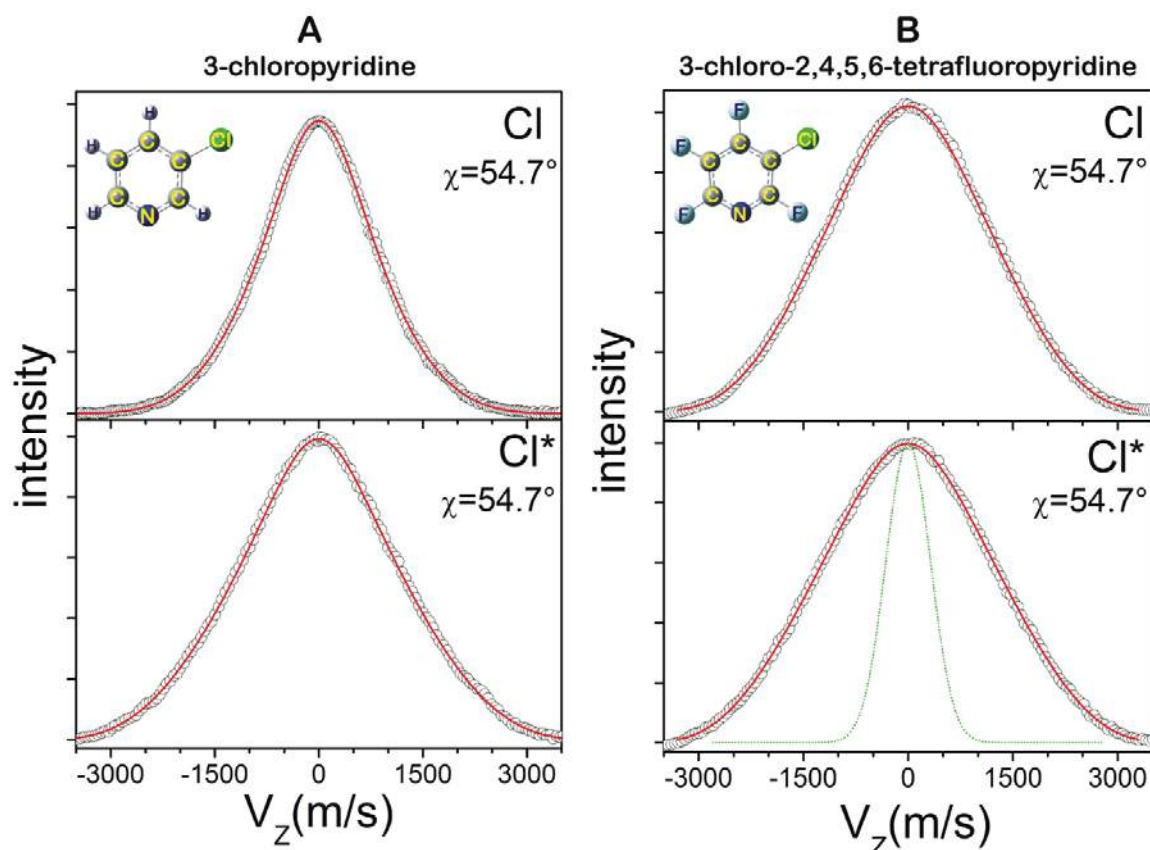
The  $\Phi(\text{Cl}^*)$  of 3-chloro-2,4,5,6-tetrafluoropyridine (ClFPy) is greater than 3-chloropyridine (ClPy) and it may be due to change in position of crossover point between repulsive states in which one correlates with Cl and other with Cl\* product. Further, the strength of coupling between these states is also responsible for the relative quantum yield of Cl\*. All these effects can be understood, in detail, by studying spin-orbit coupled

PESs theoretically. Also, the lowering of  $\pi\sigma^*$  state in the ClFPy may be the one of the factor that changes the crossover point and subsequently the Cl\* yield.

However, in the present case dissociation from ground state also possible and the fraction of ground and excited state dissociation channel is not known. Hence, it is difficult to make detail discussion on relative quantum yield of Cl\*

#### 4.4.3 Translational energy distribution and anisotropy parameter

The time domain TOF profiles of the Cl and Cl\* atoms were converted to the velocity domain as discussed in the chapter 2. The TOF profiles of the Cl and Cl\* have been found to be independent of laser polarization. Hence, in figure 4.2, we have shown two TOF profiles recorded for the Cl/Cl\*, fragments, for the laser polarization at the magic angle  $\sim 54.7^\circ$  to the detection axis for both the compounds studied. TOF data were analyzed as described in the Chapter 2.



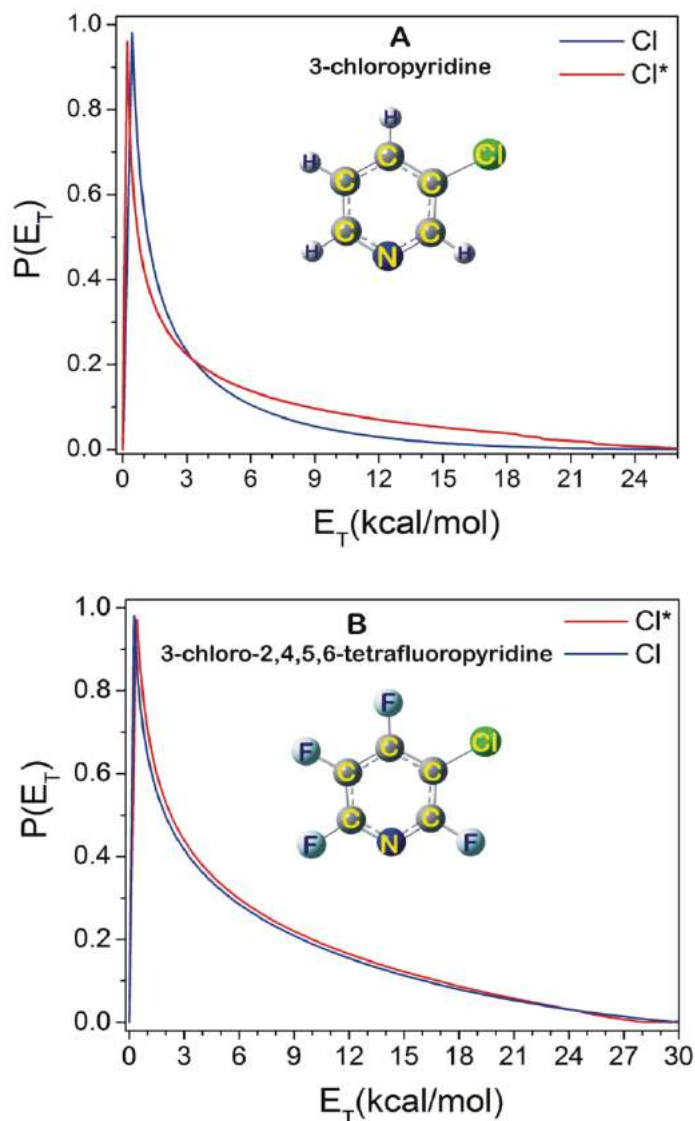
**Figure 4.2:** REMPI-TOF profiles of Cl ( $^2P_{3/2}$ ) and Cl\* ( $^2P_{1/2}$ ) produced from the photodissociation of A) 3-chloropyridine and B) 3-chloro-2,4,5,6-tetrafluoropyridine at 235 nm at magic angle ( $\chi = 54.7^\circ$ ). The circles are the experimental data and the solid red line is a

*forward convolution fit. The instrument function is depicted as the green dotted curve in lower panel of B.*

The predicted TOF spectra were calculated, convoluted with the instrumental response function, and the final calculated TOF profiles are displayed by the red solid line (figure 4.2). It should be noted that the TOF profile for both Cl and Cl\* are well fitted with one set of fitting parameter only. However, this does not imply that there is only one route for the Cl atom elimination channel. Generally, for most of the Cl substituted aromatic molecules, multiple channels have been observed for Cl atom elimination path [3]. However, if such multiple channels have broader energy distribution, then in such scenario, it will appear as one channel with very broad energy distribution. The photofragment translational energy distributions,  $P(E_T)$ , determined from the data in the figure 4.2, for the Cl and Cl\*, are depicted in figure 4.3. The average translational energies of the Cl and Cl\* channels are  $3.7 \pm 1.0$  and  $7.0 \pm 1.5$  kcal/mol, respectively for 3-chloropyridine. Similarly, for 3-chloro-2,4,5,6-tetrafluoropyridine, the average translational energies of the Cl and Cl\* channels are determined to be  $8.0 \pm 1.5$  and  $9.0 \pm 1.5$  kcal/mol, respectively. Since the TOF profiles for Cl and Cl\* are independent of laser polarizations, the  $\beta$  parameter is well characterized by a value of  $\sim 0$ , within the experimental uncertainties.

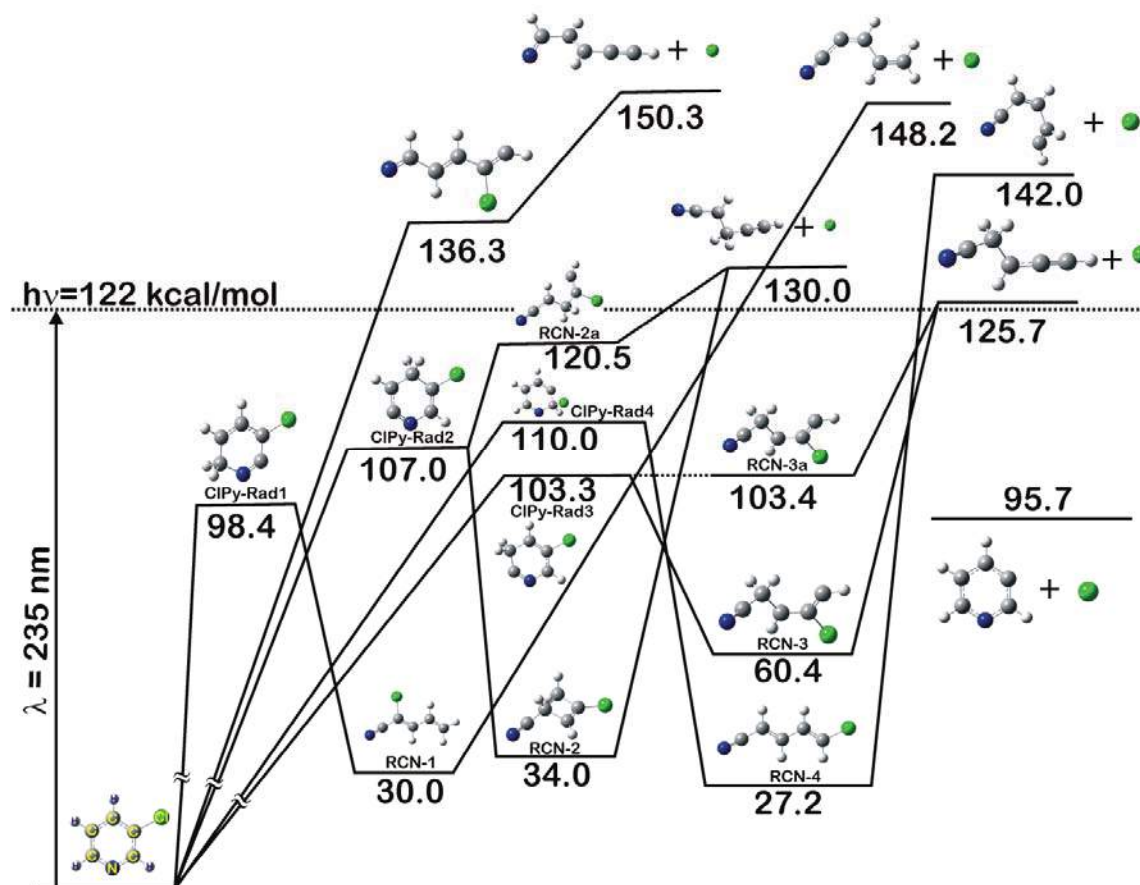
#### **4.4.4 Theoretical calculation on ground state dissociation of 3-chloropyridine**

Molecular orbital (MO) calculations were carried out to generate the relative potential energy diagram for the dissociation channels, of 3-chloropyridine on its ground state. These calculations were done mainly to establish various channels that generates Cl atom. Calculations were done at MP2/6-311++G(d,p) level of theory, using Gaussian suite of program [29]. All the ground state stationary points were calculated for the various dissociation channels. However, calculation pertaining to the various transition states



**Figure 4.3:** Centre-of-mass recoil translational energy distribution derived from figure 4.2 for Cl ( $^2P_{3/2}$ ) and Cl\* ( $^2P_{1/2}$ ), produced in the photodissociation of A) 3-chloropyridine and B) 3-chloro-2,4,5,6-tetrafluoropyridine at 235 nm.

involved in the above reactions were not attempted. Hence, we have reported various channels occurring on the ground state PES of 3-chloropyridine only. The relative energy levels are schematically represented in figure 4.4, with the energy of each channels marked in kcal/mol.



**Figure 4.4:** Relative energy diagram in kcal/mol, along with the structures, for the various products in the photodissociation of 3-chloropyridine at 235 nm in its ground state.

The initial step is shown as either the cleavage of the C–Cl bond, forming pyridine radical (Py-Rad1) and Cl atom, or the H/Cl atom migration forming various types of radicals (ClPy-Rad1, ClPy-Rad2, ClPy-Rad3, ClPy-Rad4). Another initial step may be the ring opening after the cleavage of the N–C bond. However, this channel is a higher energy channel well above the photon energy of ~122 kcal/mol. Various chloropyridine radicals formed after the H/Cl atom migration, namely, ClPy-Rad1, ClPy-Rad2, ClPy-Rad3, ClPy-Rad4, finally stabilizes itself after the ring opening. The ring opening process of these various chloropyridine radicals formed after the H/Cl atom migrations leads to the formation of various unsaturated stable nitrile compounds, mostly with conjugated C=C bond, namely, RCN-1, RCN-2, RCN-3, RCN-4 as shown in figure. The most stable nitrile is RCN-4 which is ClHC=CH–CH=CHCN. There are various structures possible

for these nitriles. However, in the figure the most stable structures are shown. These nitriles are very stable and can have their own dissociation mechanisms. In figure we have shown only the Cl atom dissociation channel for these nitriles. From our calculations, it is clear that the lowest energy channel for the Cl atom formation mechanism is the direct dissociation of C–Cl bond forming the pyridine radical and Cl atom as shown in Eq. (4.2). The  $\Delta H$  value for this particular channel was further improved with single point energy calculation done at QCISD(T)/6-311++G(2d,2p) level of theory. The calculated  $\Delta H$  value comes out to be 95.0 kcal/mol.



## 4.5 Discussion

### 4.5.1 Nature of excitation at 235 nm

In the following paragraphs, we will discuss the UV absorption spectra of the compounds of interest, i.e. 3-chloropyridine and its fluorinated version i.e. 3-chloro-2,4,5,6-tetrafluoropyridine along with their various excited states with their respective transitions. The onset of optical absorption in 3-chloropyridine is at about 4.3 eV (290 nm). This spectrum of 3-chloropyridine with  $\lambda_{\text{max}} \approx 265$  nm, has a long vibrational progression. The nature of this band has been attributed to the vibrational origin of the  $\pi^* \leftarrow \pi$  transition. On the other hand, UV absorption of 3-chloro-2,4,5,6-tetrafluoropyridine with  $\lambda_{\text{max}} \approx 257$  nm, extends up to 280 nm (figure 4.1). However, it does not show any vibronic structure similar to that of 3-chloropyridine. To understand the nature of the transitions involved in these halogenated pyridines at 235 nm, Time-Dependent Density Functional Theory (TD-DFT) calculations were performed, in detail, on chloropyridine, along with the fluorine substituted one. Ground state geometries were

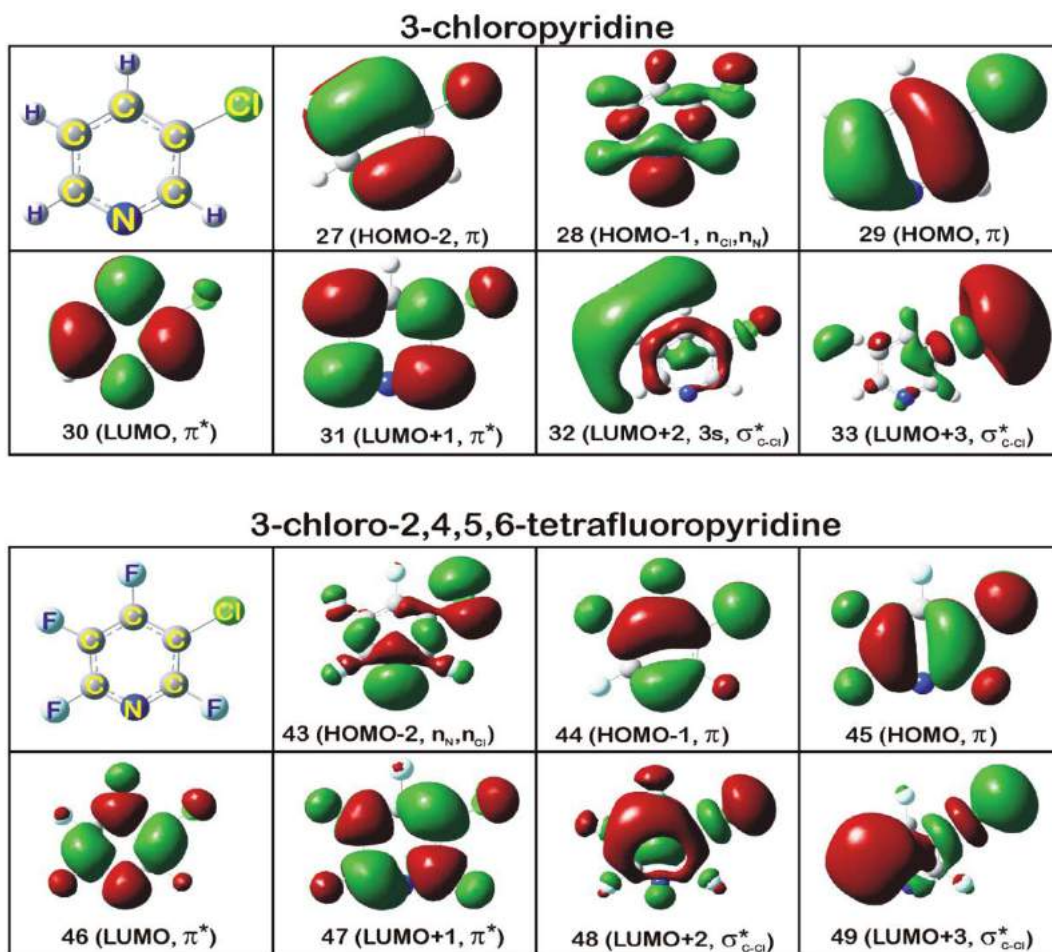


optimized for 3-chloropyridine ( $C_s$ ) and 3-chloro-2,4,5,6-tetrafluoropyridine ( $C_s$ ), employing Density Functional Theory (DFT) calculation, using aug-cc-pVDZ set of basis sets, maintaining their point group, as mentioned in the parenthesis. The vertical excitation energies for various transitions were then obtained using TD-DFT employing the augmented basis set, with diffuse and triple zeta functions, namely, aug-cc-pVTZ. Although the calculated vertical transition energies slightly differ as compared to the experimental results, the nature of transitions and that of the orbitals involved are accurately predicted, using this method [72,73]. The orbitals participating in the different electronic transitions were visualized using suitable visualization program, for better understanding of the process and are given in figure 4.5. The vertical excitation energies and the respective oscillator strengths of several low-lying singlet states of 3-chloropyridine and 3-chloro-2,4,5,6-tetrafluoropyridine are shown in table 4.1. Various singlet excited states are considered, out of which, almost all states are valence states. The various computed HOMO, LUMO and other MOs involved in the transition of all the above compounds are depicted in figure 4.5 and will be now discussed in brief. For both the molecules, the valence states are primarily due to excitations from the  $\pi$  orbitals, mostly, HOMO and HOMO-1, to  $\pi^*$  orbitals, mostly, LUMO. The other valence states are from the nonbonding electrons of N and Cl ( $n_N, n_{Cl}$ ) orbitals to  $\pi^*$  orbitals. Few other valence states also arise from  $\pi$  orbitals to  $\sigma^*_{C-Cl}$  for these chloropyridines. Besides these valence states, Rydberg states involving excitations to a diffuse 3s orbital are also included, for comparison.

## Photodissociation of Halogenated Pyridines at 235 nm

**Table 4.1:** Vertical excitation energies (eV) and oscillator strengths (given in parentheses) of low-lying singlet states of 3-chloropyridine and 3-chloro-2,4,5,6-tetrafluoropyridine with respective designation. The  $C_s$  symmetry designation for both the compounds, nature of transition and MOs involved in the transitions are also included in the table.

	3-chloropyridine		3-chloro-2,4,5,6-tetrafluoropyridine	
Excited state	State designation and nature of transition	Vertical excitation energy with oscillator strength (in parenthesis)	State designation and nature of transition	Vertical excitation energy with oscillator strength (in parenthesis)
S <sub>1</sub>	1A" 28→30 n <sub>N</sub> →π*	4.84 eV, 256nm (0.0041)	2A' 45→46 44→47 π→π*	5.25 eV, 236nm (0.0776)
S <sub>2</sub>	2A' 29→30 π→π*	5.22eV, 237nm (0.0501)	1A" 45→48 π→σ* <sub>C-Cl</sub>	5.78 eV, 214nm (0.0012)
S <sub>3</sub>	2A" 28→31 n <sub>N</sub> →π*	5.23eV, 237nm (0.0000)	3A' 45→47,46 π→π*	6.05 eV, 205nm (0.0830)
S <sub>4</sub>	3A' 29→31 27→30 π→π*	5.94eV, 209nm (0.1099)	2A" 43→46 n <sub>Cl, N</sub> →π*	6.27 eV, 198nm (0.0020)
S <sub>5</sub>	3A" 29→32 π→3s	6.31eV, 197nm (0.0016)	3A" 44→48 45→49 π→σ* <sub>C-Cl</sub>	6.60 eV, 188nm (0.0033)
S <sub>6</sub>	4A" 29→33 π→σ* <sub>C-Cl</sub>	6.67eV, 186nm (0.0065)	4A" 43→47 n <sub>Cl, N</sub> →π*	6.68 eV, 186nm (0.0000)
S <sub>7</sub>	4A' 28→32 n→3s	6.69eV, 185nm (0.0082)	4A' 44→46 45→47 π→π*	6.82eV, 182nm (0.2439)
S <sub>8</sub>	5A' 27→30 28→32 π→π* n <sub>N</sub> →3s	6.84eV, 181nm (0.2104)	5A" 45→49 π→σ* <sub>C-Cl</sub>	6.83eV, 182nm (0.0001)



**Figure 4.5:** Computed HOMO, LUMO, along with other MOs involved in the transition of 3-chloropyridine and 3-chloro-2,4,5,6-tetrafluoropyridine.

For 3-chloropyridine, the  $S_1(1A'')$  state arise from an  $\pi^* \leftarrow n$  transition, with an oscillator strength of  $\sim 0.004$  at 4.84 eV (256 nm). Similarly, the  $S_2(2A')$  arise from  $\pi^* \leftarrow \pi$  transition, with an oscillator strength of  $\sim 0.050$  at 5.22 eV (237 nm). For  $S_2$  state, the calculated value is slightly overestimated using this method as compared with the experimental value of  $\lambda_{\max} = 4.68$  eV (265 nm, see spectrum, figure 4.1). However, the calculated  $\lambda_{\max}$  value of 5.94 eV (209 nm) for the second  $\pi^* \leftarrow \pi$  transition which is designated as  $S_4(3A')$  state matched perfectly with the experimental value of  $\lambda_{\max} = 210$  nm (see spectrum, figure 4.1). The fifth ( $S_5, 3A''$ ) and sixth ( $S_6, 4A''$ ) excited states arise from  $\sigma^*_{C-Cl} \leftarrow \pi$  transitions with oscillator strengths of 0.0016 and 0.0065 at 6.31 eV (197 nm) and 6.67 eV (186 nm), respectively. The seventh excited state,  $S_7(4A')$ , is basically a

3s Rydberg state with an oscillator strength of 0.0082 at 6.69 eV (185 nm). The eighth excited state,  $S_8(5A')$  is another  $\pi\pi^*$  state, with a considerable oscillator strength of 0.2104 at 6.84 eV (181 nm).

However, for 3-chloro-2,4,5,6-tetrafluoropyridine, the  $S_1(2A')$  state is an  $\pi\pi^*$  state with an oscillator strength of 0.0776 at 5.25 eV (236 nm). The second excited state,  $S_2(1A'')$ , arises from the  $\sigma_{C-Cl}^*\leftarrow\pi$  transition with an oscillator strength of 0.0012 at 5.78 eV (214 nm). Here, it should be noted that the  $\sigma_{C-Cl}^*\leftarrow\pi$  transition appears at much lower in energy as compared to the 3-chloropyridine. The third excited state,  $S_3(3A')$ , arises from a  $\pi^*\leftarrow\pi$  transition with an oscillator strength of 0.0830 at 6.05 eV (205 nm). The first  $n_{N,n_{Cl}}\pi^*$  excited state designated as  $S_4(2A'')$  appears at 6.27 eV (198 nm) with an oscillator strength of 0.0020. Similarly, the fifth ( $S_5, 3A''$ ) and sixth ( $S_6, 4A''$ ) excited states arise from  $\sigma_{C-Cl}^*\leftarrow\pi$  and  $\pi^*\leftarrow n_{N,n_{Cl}}$  transitions with oscillator strengths of 0.0030 and  $\sim 0.0$  at 6.60 eV (188 nm) and 6.68 eV (186 nm), respectively. The seventh ( $S_7, 4A'$ ) and ninth ( $S_9, 5A'$ ) excited states arise from  $\pi^*\leftarrow\pi$  transitions with oscillator strengths of 0.2439 and 0.3613 at 6.82 eV (182 nm) and 7.00 eV (177 nm), respectively. At this point, it is worth mentioning that the ratio of absorption cross-section for both the compounds, namely, 3-chloropyridine and 3-chloro-2,4,5,6-tetrafluoropyridine determined experimentally agrees well with the ratio of oscillator strengths calculated theoretically within the experimental error.

Considering the corresponding wavelengths for vertical excitation energies and the respective oscillator strengths of the various transitions, it is evident that at 235 nm, both the molecules, namely, 3-chloropyridine and 3-chloro-2,4,5,6-tetrafluoropyridine have a  $\pi^*\leftarrow\pi$  transition. Since the excited state, with  $\pi^*\leftarrow\pi$  transition, adiabatically correlates only with highly excited photoproducts, which is not feasible in a single-photon excitation in the present case, it is assumed that the initially prepared  $\pi\pi^*$  states cross

over to the nearby states, mostly some  $\sigma^*_{\text{C-Cl}}$  state, from where the C–Cl bond can cleavages, forming Cl atoms. Also, the initially prepared  $\pi\pi^*$  state can undergo rapid internal conversion to the ground state, from where various other dissociation channels can occur, in addition to the above mentioned pathways as discussed in earlier section.

#### 4.5.2 Translational energy release and anisotropy parameter

In the context of Cl atom formation channel, the photoexcitation of 3-chloropyridine and 3-chloro-2,4,5,6-tetrafluoropyridine at 235 nm (122 kcal/mol) generates Cl atom with absorption of one photon in the simple C–Cl bond cleave process as given in equation 4.2. As discussed earlier,  $\Delta H$  value for the equation 4.2 is calculated to be 95.0 kcal/mol for 3-chloropyridine. For the above reaction, the available energy,  $E_{\text{avail}}$ , which is defined as  $E_{\text{photon}} - \Delta H$ , comes out to be 27.0 kcal/mol. The various other channels generating the Cl atom depicted in figure 4.4 and discussed in earlier section are well above the photon energy of 122 kcal/mol. Hence, it is clear that the lowest energy channel for the Cl atom formation mechanism is the direct cleavage of C–Cl bond forming the pyridine radical and Cl atom as shown in equation 4.2 and this is the only channel responsible for the generation of Cl atom. However, the C–Cl bond cleavage process may be either from the excited state or from the ground state which we will be discussing in the following paragraph.

In both the cases, 3-chloropyridine and 3-chloro-2,4,5,6-tetrafluoropyridine,  $P(E_T)$  for Cl/Cl\* formation channel was well described by one component only. In case of 3-chloropyridine the  $P(E_T)$  for Cl ( $^2P_{3/2}$ ) channel peaks near origin ( $\sim 1$  kcal/mol), and extends up to  $\sim 22$  kcal/mol (figure 4.3). Similarly, the  $P(E_T)$  for Cl\* ( $^2P_{1/2}$ ) channel also peaks near origin, and extends up to  $\sim 24$  kcal/mol (figure 4.3). In case of 3-chloro-2,4,5,6-tetrafluoropyridine also, the  $P(E_T)$  for Cl ( $^2P_{3/2}$ ) channel peaks near origin ( $\sim 1$  kcal/mol), and extends up to  $\sim 26$  kcal/mol (figure 4.3). Similarly, the  $P(E_T)$  for Cl\* ( $^2P_{1/2}$ )

channel also peaks near origin, and extends up to  $\sim 26$  kcal/mol (figure 4.3). Here, it should be noted that the average translational energy value,  $E_T$ , for Cl/Cl\* for 3-chloropyridine is lower than the  $E_T$  value for 3-chloro-2,4,5,6-tetrafluoropyridine for Cl atom elimination channel. Similar results were also reported in the case of chlorobenzene and perfluorochlorobenzene. In the same study they have also indicated the higher  $E_{avail}$  value for the Cl atom elimination channel in fluorinated benzene as compared to unfluorinated one. Similar indication was also found in our translational energy distribution curve for both the compounds studied. However, a  $\Delta H$  value of 95.0 kcal/mol was taken for both the compounds for all the calculation. The assumption of same  $\Delta H$  value for both chloropyridine and its fluorinated derivative is analogous to the chlorobenzene and its fluorinated chlorobenzene where bond dissociation energy for both these molecules is same and determined from literature.

Various simple models such as impulsive and statistical model are often used to understand the partitioning of the available energy into various degrees of freedom of the fragments [22,23,70,94]. It is well known that the partitioning of energy is mainly governed by the nature of the dissociative potential energy surface, and can be predicted using above models. Mostly, the energy partitioning during the dissociative event on a repulsive surface is well described by an impulsive model. In this model, the distribution of energy among the product states is governed by the repulsive force along the breaking bond of the parent molecule into the fragments. In this model, the fraction of the available energy ( $E_{avail}$ ) released as translational energy is given by

$$E_T = \left( \frac{\mu_{C-Cl}}{\mu_{(Py-Rad1)-Cl}} \right) E_{avail} \quad \text{and} \quad f_T = E_T/E_{avail} \quad (4.3)$$

where  $\mu_{C-Cl}$  is the reduced mass of the C and Cl atoms,  $\mu_{(Py-Rad1)-Cl}$  is the reduced mass of the pyridine radical and Cl,  $E_{avail}$  is the available energy ( $\sim 27$  kcal/mol) and  $f_T$  is the

fraction of the available energy going into the translational modes of the fragments. In the case of 3-chloropyridine and 3-chloro-2,4,5,6-tetrafluoropyridine, the ratio of the reduced masses is 0.37 and 0.31 respectively. The experimental average translational energies ( $E_T$ ) for the Cl and Cl\* in case of ClPy are found to be  $3.7 \pm 1.0$  and  $7.0 \pm 1.5$  kcal/mol, respectively, giving the  $f_T$  values of 0.14 and 0.26. Similarly, the  $E_T$  values for the Cl and Cl\* in the case of 3-chloro-2,4,5,6-tetrafluoropyridine are found to be  $8.0 \pm 1.5$  and  $9.0 \pm 1.5$  kcal/mol, respectively, giving the  $f_T$  values of 0.30 and 0.36 (table 4.2). The relative quantum yield ( $\Phi$ ) values which are determined by method mentioned in the section 4.4.2 are also listed in table 4.2. The experimentally determined  $f_T$  thus obtained slightly deviates from the impulsive model in case of 3-chloropyridine. However, in case of 3-chloro-2,4,5,6-tetrafluoropyridine, experimentally determined  $f_T$  values perfectly match with the value predicted using the impulsive model.

However, in a dissociation process where a rapid internal conversion to the ground electronic state, followed by the subsequent slow dissociation occurs, the excess energy is partitioned statistically amongst the available degrees of freedom of the products. In such case, a statistical model of energy partitioning can be well applied for understanding the energy partitioning and the dissociation process. Under these circumstances, a relatively small amount of the excess energy is partitioned into translational motion of the products especially in a large molecule with many low frequency modes. For this kind of dissociation process, a priori calculations are generally adopted, along with a simple analytical expression established by Klots, relating the mean translational energy release,  $E_T$ , and the  $E_{avail}$ , for a statistical barrierless dissociation process.

## Photodissociation of Halogenated Pyridines at 235 nm

**Table 4.2:** The average translational energy,  $\langle E_T \rangle$ , available energy ( $E_{\text{avail}}$ ),  $f_T$  value, and the relative quantum yield ( $\Phi$ ) for photodissociation of 3-chloropyridine and 3-chloro-2,4,5,6-tetrafluoropyridine at  $h\nu=235$  nm. The excitation energy is 122 kcal/mol. The  $D_0^0$  (C–Cl) is taken as 95.0 kcal/mol. All energies are in kcal/mol.

Molecule	Channel	$\langle E_T \rangle$	$E_{\text{avail}}$	$f_T = \langle E_T \rangle / E_{\text{avail}}$	$\Phi$
3-chloropyridine	Cl	3.7±1.0	27.0	0.14	0.91±0.08
	Cl*	7.0±1.5	24.6	0.28	0.09±0.02
3-chloro-2,4,5,6-tetrafluoropyridine	Cl	8.0±1.5	27.0	0.30	0.89±0.08
	Cl*	9.0±1.5	24.6	0.36	0.11±0.03

This simple expression give a  $f_T$  value of  $\sim 0.06$ . The experimental  $f_T$  values of 0.14/0.28 for Cl/Cl\* atom elimination channel in 3-chloropyridine lie in between the values predicted by the impulsive and statistical models. A careful examination reveals that the  $f_T$  value for Cl\* (0.26) is higher than that for Cl (0.14), despite its low  $E_{\text{avail}}$  and also it lies more towards the value predicted by impulsive model. If the dissociation occurs on the ground state potential energy surface, then the  $f_T$  value is expected to be the same for both Cl and Cl\*. Hence, the initially prepared 3-chloropyridine in the  $\pi\pi^*$  state may crosses over to the nearby  $\pi\sigma^*$  state, and subsequently the C–Cl cleavage occurs. In case of 3-chloropyridine, the  $\pi\sigma^*$  state ( $4A''$ ) is sixth singlet excited state which is mainly responsible for the C–Cl bond cleavage in the excited state. However, in case of 3-chloro-2,4,5,6-tetrafluoropyridine, the  $\pi\sigma^*$  state ( $1A''$ ) is second singlet excited state. The effect of fluorination of chloropyridine has lowered the energy of the  $\pi\sigma^*$  state. To further investigate this issue, we have mapped the potential energy (PE) curves for various excited states for the Cl atom elimination channel for both the compounds, namely, 3-chloropyridine and 3-chloro-2,4,5,6-tetrafluoropyridine using TD-DFT methods along the

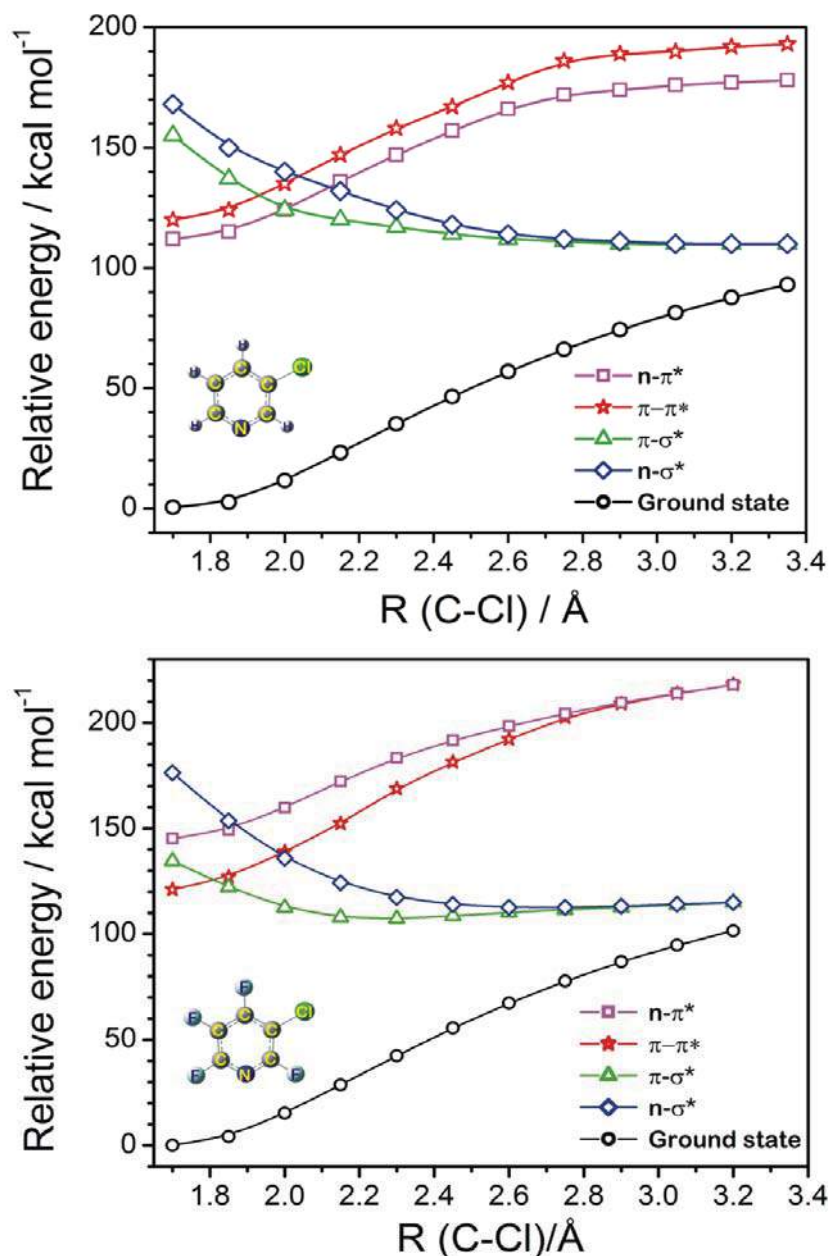


C–Cl bond length. For this purpose, single point TD-DFT calculations for various vertical excitation energies on different fixed C–Cl lengths were performed at uMPW1PW91/aug-cc-pVDZ level with all other internal coordinates of ground-state optimized at uMPW1PW91/ aug-cc-pVDZ level. For this purpose, the C–Cl bond lengths were varied from 1.7 Å to ~3.2 Å, which is asymptote to its dissociation limit. The sanity of the present theoretical method employed here is confirmed by comparing our results on vinylchloride with that of Nakatsuji and co-workers, for its electronic spectra and photodissociation, using symmetry-adapted cluster configuration interaction theory (SAC-CI) [50,71]. Figure 4.6 shows the result of above such calculation. From the figure it can be easily seen that the  $\pi\pi^*$  and  $n\pi^*$  states are bound in nature. As mentioned earlier, these states adiabatically correlate only with highly excited photoproducts, which is not feasible in a single-photon excitation in the present case. Whereas, the  $\pi\sigma^*$  state is repulsive in nature and intersect both  $\pi\pi^*$  and  $n\pi^*$  states at different C–Cl internuclear distances. For dissociation along the C–Cl, the crossover from initially prepared  $\pi\pi^*$  to  $\pi\sigma^*$  state is evident. However, the intersection and the energetics of  $\pi\sigma^*$  state with respect to  $\pi\pi^*$  state indicates that the C–Cl bond cleavage seems to be more favourable in case of 3-chloro-2,4,5,6-tetrafluoropyridine as compare to 3- chloropyridine.

The recoil anisotropy,  $\beta$ , for the Cl atom fragments measured in the present work is  $\sim 0$ , which indicates an isotropic dissociation process. However, the anisotropy even in an impulsive dissociation can be reduced or wiped out, due to several factors, such as mixed initial transition with parallel and perpendicular components, longer dissociation lifetime, dissociation not from a single geometry rather from a range of geometries etc. [95,96]. In this scenario, the experimental value of  $\beta$  does not give any indication of the direction of the velocity of the recoiling photofragment with respect to its molecular transition dipole moment. The absence of anisotropy is mostly attributed to the slow

dissociation process mainly due to the crossover from initially prepared bound  $\pi\pi^*$  to nearby dissociative  $\pi\sigma^*$  state, rather than the constraint in the geometry of the molecule.

Also, the dissociation process from the ground state with relatively longer dissociation lifetime leads to the absence of recoil anisotropy.

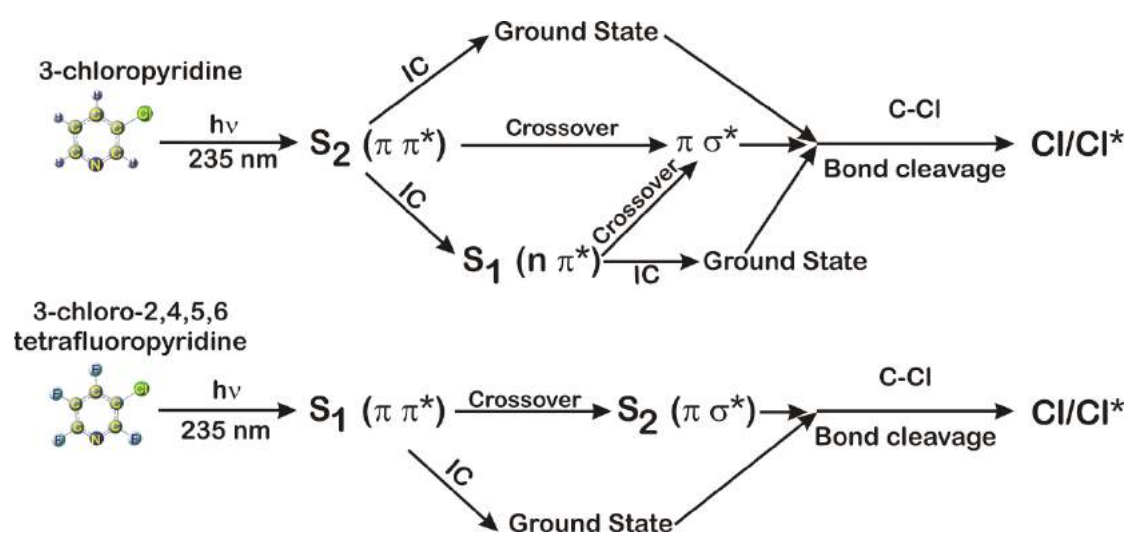


**Figure 4.6:** Various diabatic potential energy curves calculated for 3-chloropyridine and 3-chloro-2,4,5,6-tetrafluoropyridine along the C-Cl bond length with the other geometrical parameters optimized for the ground state using TD-DFT method

### 4.5.3 Mechanism of the dissociation process

We shall now discuss a complete picture of the dissociation process in conjunction with the various energy partitioning models and the PESs calculation with the help of Density Functional Theory. The TD-DFT calculation and the absorption spectra clearly show that the excitation of halogenated pyridines at 235 nm prepares the molecules in its  $\pi\pi^*$  state. The TD-DFT calculation clearly shows the bound nature of this state. The  $\pi\pi^*$  states adiabatically correlate only with highly excited photoproducts, which is not feasible in a single-photon excitation in the present case. Hence, a crossover from the initially prepared bound  $\pi\pi^*$  state to nearby dissociative  $\sigma^*$  state is necessary for the cleavage of C–Cl bond. However, in both the halogenated pyridines, the  $n\sigma^*$  state is quite high in energy as compare to  $\pi\sigma^*$  state and in such scenario, the crossover to the  $\pi\sigma^*$  state is the most probable route for the C–Cl bond cleavage (see figure 4.6). It is well known in the literature and also the current study reveals that the fluorine substitution lowers the energy of  $\pi\sigma^*$  state. The lowering of  $\pi\sigma^*$  state energy basically facilitate the crossover mechanism from  $\pi\pi^*$  state to nearby  $\pi\sigma^*$  state in case of 3-chloro-2,4,5,6-tetrafluoropyridine. In figure 4.6, it is clearly seen that the crossover in case of 3-chloropyridine occurs at longer C–Cl bond length ( $\sim 2.0$  Å) as compare to 3-chloro-2,4,5,6-tetrafluoropyridine ( $\sim 1.8$  Å) and this is due to the lowering of the  $\pi\sigma^*$  state energy. This situation is manifested itself in the average translational energy,  $E_T$ , of the Cl atom elimination channel. In case of 3-chloropyridine, the dissociation process can be seen as the dissociation from an exit barrier which is created from the avoided crossing of both the states, namely,  $\pi\pi^*$  and  $\pi\sigma^*$  state. In this scenario, the translational energy is mostly governed by barrier impulsive model where the amount of translational energy released into the photofragments is dependent on the height of the exit barrier. Also, the dissociation period will be longer as compare to the rotational period of the molecule

giving a zero value for the anisotropy parameter. The probability of internal conversion to ground state is high which is again manifested in the low average translation energy of the photofragment. Moreover, in 3-chloropyridine,  $\pi\pi^*$  state is lowest in energy and is designated as  $S_1$ . In this scenario, the  $S_2(\pi\pi^*) \rightarrow S_1(n\pi^*)$  relaxation process may also occur, which populates the  $S_1(n\pi^*)$  state. Then, the molecule can crossover to  $\pi\sigma^*$  state also. In this way, there are at least two mechanisms operating in photodissociation process of 3-chloropyridine in the excited state PES. However, in case of 3-chloro-2,4,5,6-tetrafluoropyridine the  $\pi\pi^*$  state is quite high in energy which is not accessible within the available photon energy of 122 kcal/mol. In this scenario, the only crossover which is possible is to the  $\pi\sigma^*$  near the Franck–Condon region. This situation makes the dissociation process similar to that from a pure repulsive state. Hence, in case of 3-chloro-2,4,5,6-tetrafluoropyridine the average translational energy is nicely described by an impulsive model. Also, the higher  $f_T$  values for  $\text{Cl}^*$  as compared to  $\text{Cl}$  and the low  $\Phi(\text{Cl}^*)$  values confirms the participation of excited states, namely,  $\sigma^*$  states in the dissociation process of above molecules. A schematic of mechanism for various  $\text{Cl}/\text{Cl}^*$  elimination channels can be seen in figure 4.7.



**Figure 4.7:** Schematic of mechanism for various  $\text{Cl}/\text{Cl}^*$  elimination channels for 3-chloropyridine and 3-chloro-2,4,5,6-tetrafluoropyridine.

#### 4.6 Conclusion

In summary, the photodissociation of two halogenated pyridines, namely, 3-chloropyridine and 3-chloro-2,4,5,6-tetrafluoropyridine, has been carried out at around 235 nm, and the dynamics of C–Cl bond dissociation is investigated, using resonance enhanced multiphoton ionization, coupled with a time-of-flight mass spectrometer. The excitation at 235 nm prepares both the molecules in the  $\pi\pi^*$  state. The dynamics of chlorine atom elimination channels in these two compounds were studied by determining the photofragment speed distribution, the anisotropy parameter,  $\beta$ , and the spin-orbit branching ratio. Polarization dependent and state-specific TOF profiles are obtained to get the translational energy distributions, using a forward convolution method and taking into account the fragment anisotropies. The anisotropy parameters for both Cl and Cl\* are the same, and characterized by values of  $\sim 0$ . The translational energy distributions for the chlorine atom elimination channel in both cases are best described by only one component. However, this does not imply that there is only one route for the Cl atom elimination channel. In general, if different multi-channel components have broader energy distributions, it may appear as one channel with very broad energy distribution. For 3-chloropyridine, the average translational energies for Cl and Cl\* channels are determined to be  $3.7 \pm 1.0$  and  $7.0 \pm 1.5$  kcal/mol, respectively. Similarly for 3-chloro-2,4,5,6-tetrafluoropyridine, the average translational energies for Cl and Cl\* are determined to be  $8.0 \pm 1.5$  and  $9.0 \pm 1.5$  kcal/mol, respectively. Relative quantum yield,  $\Phi(\text{Cl}^*)$ , is also determined for ClPy and ClFPy during the course of studies and found to be  $0.09 \pm 0.02$  and  $0.11 \pm 0.02$ , respectively. The energy partitioning into the translational modes is interpreted with the help of various models, such as impulsive and statistical models. The higher average translational energy released into the chlorine atom elimination channel in fluorine substituted chloropyridine is explained with the help of

theoretical calculation. The calculation suggests that the fluorine substitution increases the possibility of crossover to  $\pi\sigma^*$  state from initially prepared  $\pi\pi^*$  state. During the course of experiments, the absorption spectra for both the compounds studied were also obtained with their absolute absorption cross-sections.

## Chapter 5

### C–Br Bond Dissociation Dynamics of 4-bromo-2,3,5,6-tetrafluoropyridine

---

#### 5.1 Introduction

Various studies pertaining to the photodissociation of polyatomic molecules are important to understand a detailed dynamics of any chemical reaction at microscopic level. In particular, studies related to halogenated molecules have received great experimental and theoretical attention in recent years because of their environmental impact and fundamental interest in their dissociation dynamics. In this context, various experimental studies on the photodissociation of alkyl halides [46,49,50,97-102] and aryl halides especially halogenated benzenes[89-91,103-117] have been well studied. However, these kind of studies are very scarce in literature when it comes to studies on halogenated heterocyclic molecules[3,47,79,87]. The most studied heterocyclic compound is pyridine ( $C_5H_5N$ ), where one of the CH group in benzene is replaced by N. The importance of pyridine related research can be easily judged by its sheer volume of research article published in all areas of chemistry and biochemistry related journals. It is mostly used as a starting material in synthesis of intermediates for production of insecticides and herbicides. Also, many substituted pyridines are involved in bioactivity with application in pharmaceutical drugs and agricultural products. Apart from its applications in various industries, it has acute toxicity and apparently teratogenic in

nature. Halogenated pyridines are also reported to have mutagenic activity. Pyridine and its derivatives enter the environment due to its high water solubility which leads to contamination of surface and ground water. Apart from the reaction with atmospheric oxidants, photodissociation is one of the important mechanisms which determine the fate of these organic compounds in environment. In this context, we studied the photodissociation dynamics of 4-bromo-2,3,5,6-tetrafluoropyridine at 234 nm by detecting the Br/Br\* atoms using REMPI-TOF technique and experimental findings were supported with suitable computational calculations at various levels.

It is well known that pyridine and benzene show similar photophysical and photochemical properties. However, the presence of an additional  $n\pi^*$  state in pyridine just below the  $\pi\pi^*$  state makes a major difference between these compounds. Fluorescence from the  $n\pi^*$  state of the pyridine was first observed in the vapour phase and fluorescence quantum yield was also estimated [82,118]. In the same study, they observed a sharp decrease in quantum yield as excitation energy was raised to  $\pi\pi^*$  and this decrease was attributed to the fast non-radiative decay which was similar to the benzene [119]. Fluorescence lifetime was also measured in similar study which shows vibronic level dependency [83]. In an another study by Villa *et al.* mode independent decrease in quantum yield was observed at high excitation energy which was attributed to the intramolecular vibrational energy redistribution (IVR) process inducing internal conversion to ground electronic state [120]. Recently Wang *et al.* [81] investigated the dynamics of  $n\pi^*$  state by femtosecond time-resolved mass spectrometry and photoelectron imaging method combined with (1+2) REMPI via the Rydberg state. They also suggested that ultrafast channel is due to IVR induced internal conversion as observed by Villa *et al.* In the theoretical side, excitation energies of pyridine were



## C–Br Bond Dissociation Dynamics of 4-bromo-2,3,5,6-tetrafluoropyridine

calculated using complete active space self consistent field (CASSCF) method and compared with experimental results [84].

As mentioned earlier, studies related to substituted/halo pyridines are limited in literature. Photolytic destruction and mineralisation of 2-halogenated pyridine solution was studied at 254 nm [85] to understand its environmental effects and various intermediates were identified, the major being 2-hydroxypyridine. In another study, the substitution effect was studied in these halopyridines to understand the extent of inductive and resonance effect using He I photoelectron spectroscopy where these two effects operate simultaneously [121]. Monohalogenated pyridines have been subjected to various spectroscopic studies. Ultraviolet absorption spectra were measured in iso-octane and ethyl alcohol solution in the region of 208-294 nm [122]. Only singlet-singlet  $\pi^* \leftarrow \pi$  transition was observed. Infrared and Raman spectra were also recorded and various transitions were assigned with the help of density functional theory [123]. Similarly, the absorption spectra of 2-fluoro-5-bromopyridine were recorded in the vapour phase and found that the 0,0 band of  $\pi^* \leftarrow \pi$  transition shows red shift compared to that of pyridine vapour [124].

In the present context, it is worth comparing the various dynamics feature of halogenated benzene photodissociation process with that of halogenated pyridines. Photodissociation of bromobenzene has been studied at 266 nm in great detail by various groups using different techniques [116,125,126]. The outcome of these investigations reveals that Br atom formed via predissociative channel i.e. initially excited  $\pi\pi^*$  state crossover to repulsive  $n\sigma^*$  state. Whereas at 234 nm, direct dissociation from  $n\sigma^*$  state was observed [113]. In another study, dibromobenzene and tribromobenzene were studied at 266 nm using femtosecond pump-probe spectroscopy [109]. The result suggested that the predissociation process from  $\pi\pi^*$  state to the repulsive  $n\sigma^*$  state is common in these

molecules. Similarly, Lin and co-workers [127] observed two different channels for *o*-,*m*-,*p*-dibromobenzenes dissociation pathways and suggested the involvement of the bound triplet state. Unlike bromobenzenes, bromofluorobenzenes shows different kind of photodissociation pathways with increasing number of substituted fluorine atoms due to involvement of low lying  $\pi\sigma^*$  state [103].

In our earlier studies, we have reported the dynamics of halogen atoms (Cl and Br) formation in the photodissociation process of halogenated heterocyclic molecules such as halogenated furans [93], thiophenes [47], 1,2,5-thiadiazoles [3] and pyridines [5] using REMPI-TOF technique at  $\sim 234$  nm. These studies reveal the importance of curve crossing process in the excited states. In this context, we have studied the Br atom formation dynamics in the photodissociation process of 4-bromo-2,3,5,6-tetrafluoropyridine using REMPI-TOF-MS at  $\sim 234$  nm. It is also interesting to see whether there is any ground state contribution for the Br atom formation process as observed in case of chloropyridine or the dissociation is solely from the excited state. We have also studied the fluorine substitution effect on the photodissociation dynamics, relative quantum yield determination of Br and Br\* and translational energy distribution. This study will also provide an answer about the substitution effect of fluorine atom on the nature of various excited states in an aromatic molecule. Also, the results will be compared with our earlier results on photodissociation of chloropyridines at  $\sim 234$  nm.

## 5.2 Experimental

The experiment was performed using a molecular beam time-of-flight mass spectrometer system (MB-TOF-MS), as described before in chapter 2. The 4-bromo-2,3,5,6-tetrafluoropyridine (98% purity) supplied by Aldrich was used after repeated freeze-pump-thaw cycles. Helium was bubbled through the sample, maintained at room temperature, and the mixture was expanded through the nozzle at a stagnation pressure of

1500 Torr. It was ensured that any interference to the measurements due to cluster photofragmentation was absent, or negligible, by operating at a low stagnation pressure, and using only the rising part of the molecular beam pulse. The power dependence measurements revealed a three photon dependency, which is consistent with one-photon dissociation of test molecules, followed by (2+1) REMPI of the bromine atoms, assuming that the ionization step is saturated. Apart from the power dependence studies, we also systematically monitored the shape and the width of TOF profiles of Br atoms at various laser intensities to rule out any interference from high intensity of the laser.

### 5.3 Analysis

The TOF profiles of Br and Br\* are measured at different laser polarizations. The translational energy distribution and the anisotropy parameter for both Br and Br\* are determined from these TOF profiles, using a commonly used forward convolution (FC) technique, as described in chapter 2. Using this method, the parameters are adjusted until a satisfactory agreement with the experimental data is achieved. Once the photofragment speed distributions have been determined, these were used to obtain the corresponding translational energy distributions.

### 5.4 Computational methods

The molecular geometry for the ground electronic state was optimized at the Møller Plesset second order perturbation theory by employing a 6-311+G(d) basis set. The potential energy curves of the ground and excited states along the dissociation coordinate of the Br atom from the equilibrium ground state geometry were computed using multi-configurational quasidegenerate second order perturbation theory (QDMCPT2) [128,129]. Eight active orbitals were chosen for correlating ten electrons. The vertical excitation energies and the transition dipole moments for the equilibrium ground state geometry were computed using equation of motion coupled cluster theory

with singles and doubles (EOM-CCSD) levels of electron correlations[130]. The QDMCPT2 and the EOM-CCSD calculations were carried out using 6–31G\* basis. The EOM-CCSD calculation was also repeated for a higher 6–31+G\* basis set. All these calculations were carried out with GAMESS-US quantum chemistry package [30]. The potential energy curves corresponding to different electronic states are constructed at various C–Br bond lengths. The electronic energy curves were also constructed using Time-Dependent Density Functional Theory (TD-DFT) [131,132]. For this, excited states calculations were performed at uMPW1PW91/aug-cc-pVDZ level of theory for various C–Br bond length geometries which are optimized in the ground state at uMPW1PW91/aug-cc-pVDZ level of theory.

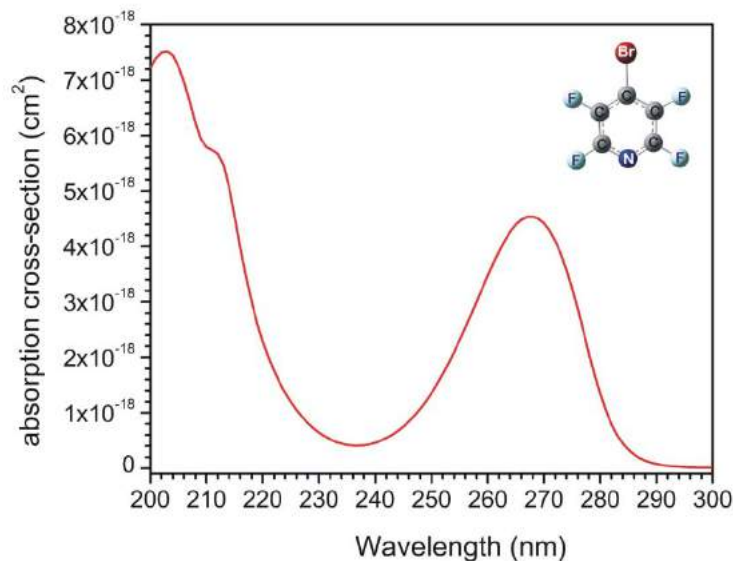
## 5.5 Results

### 5.5.1 Absorption spectra and absolute cross-section

The absorption spectra of 4-bromo-2,3,5,6-tetrafluoropyridine (BTFP) was recorded using a commercial UV spectrophotometer at various pressures. The absolute absorption cross-sections were then calculated using Beer-Lambert law. Figure 5.1 shows such absorption spectra of 4-bromo-2,3,5,6-tetrafluoropyridine with its absolute absorption cross-section. The absolute absorption cross-section values were further verified by measuring the same at 234 nm using a 50-cm long absorption cross-section cell as described in chapter 3. The absorption cross-section found to be  $(4.2 \pm 1.5) \times 10^{-19}$  cm<sup>2</sup> molecule<sup>-1</sup> at 234 nm.

### 5.5.2 Spin-orbit branching ratio

Doppler profiles of Br (<sup>2</sup>P<sub>3/2</sub>) and Br\* (<sup>2</sup>P<sub>1/2</sub>) atoms produced in the dissociation of 4-bromo-2,3,5,6-tetrafluoropyridine are scanned in the wavelength region of 42789.9 and 42727.7 cm<sup>-1</sup>. The relative quantum yield of the Br atom formed in different spin-orbit states (X, X\*), were calculated by normalizing the integrated intensity, i.e., the peak areas



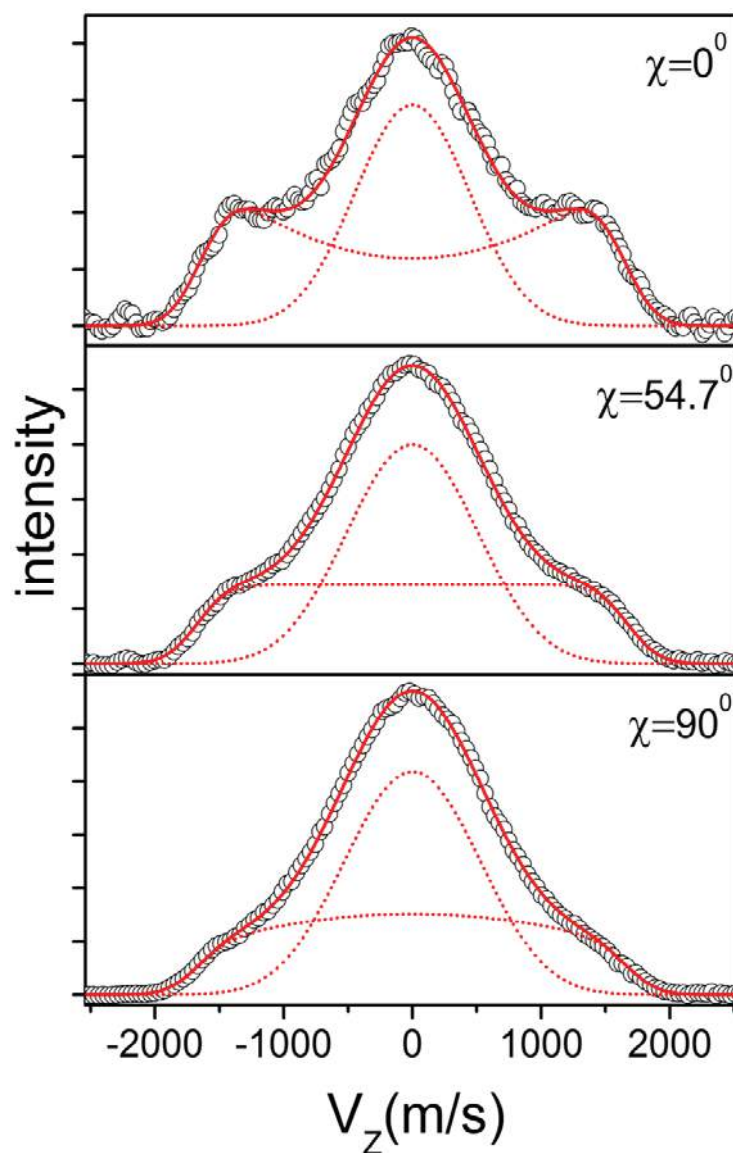
**Figure 5.1:** UV absorption spectrum of 4-bromo-2,3,5,6-tetrafluoropyridine at room temperature with the absolute absorption cross-section.

$S(X)$ , or  $S(X^*)$ , of the respective (2+1) REMPI transitions with respect to the laser intensity, and the ratio of the two-photon absorption coefficients. The ratio of the measured areas  $S(X)$  and  $S(X^*)$  of (2+1) REMPI lines is proportional to the product ratio,  $N(X)/N(X^*)$ , after due correction with respect to their relative ionization probability. The  $N(X)$  ( $X = \text{Br}$  or  $\text{Br}^*$ ) designate the number density of  $X$  produced during the photodissociation process. The intensities  $S(X)$  and  $S(X^*)$  were obtained by integrating the measured ion signal intensities over the proper range, covering the Doppler width and the probe laser bandwidth. From the experimentally measured integrated intensity ratios,  $S(\text{Br}^*)/S(\text{Br})$ , one can easily obtain the product ratios,  $N(X)/N(X^*)$ . The relative ionization probability,  $k$  was taken to be  $0.17 \pm 0.05$ [133].

The relative quantum yields,  $\Phi(X)$  and  $\Phi(X^*)$ , can be determined from the product ratio, and  $\Phi(X^*)$  can be expressed as  $\Phi(X^*) = N(X^*)/[N(X^*) + N(X)]$ . The  $\Phi(\text{Br}^*)$  obtained in the photodissociation of 4-bromo-2,3,5,6-tetrafluoropyridine is found to be  $0.13 \pm 0.10$

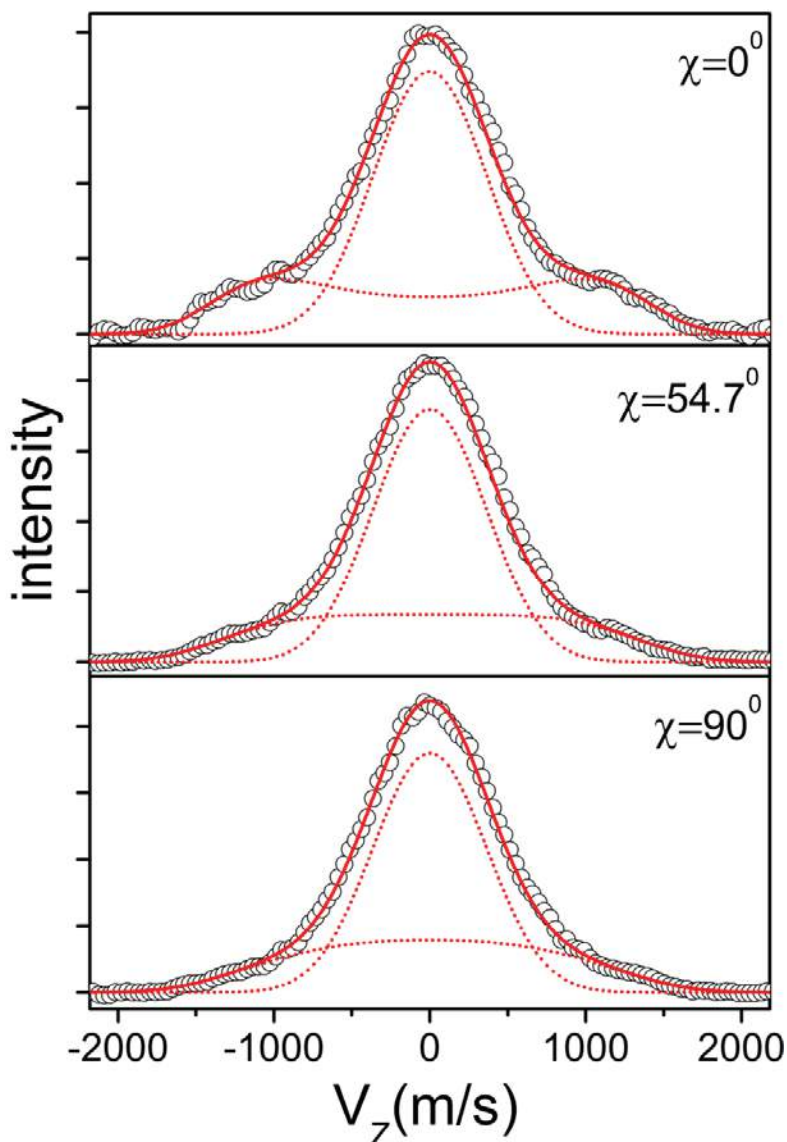
### 5.5.3 Translational energy distribution and anisotropy parameter

Figures 5.2 and 5.3 show TOF profiles for Br and Br\* formed in the photodissociation of BTFP at 234 nm respectively. These TOF profiles are at different laser polarizations, at the  $\chi$  values of  $0^\circ$ ,  $54.7^\circ$  (the magic angle), and  $90^\circ$  respectively.



**Figure 5.2:** REMPI-TOF profiles of Br ( $^2P_{3/2}$ ) produced from the photodissociation of 4-bromo-2,3,5,6-tetrafluoropyridine at 234 nm. The circles are the experimental data, the dashed lines are forward convolution fit for two different channels, namely, fast and slow and the solid line shows the sum. Three panels, namely, upper, middle and lower panels correspond to different experimental geometries with  $\chi=0^\circ$ ,  $\chi=54.7^\circ$ , and  $\chi=90^\circ$  respectively.

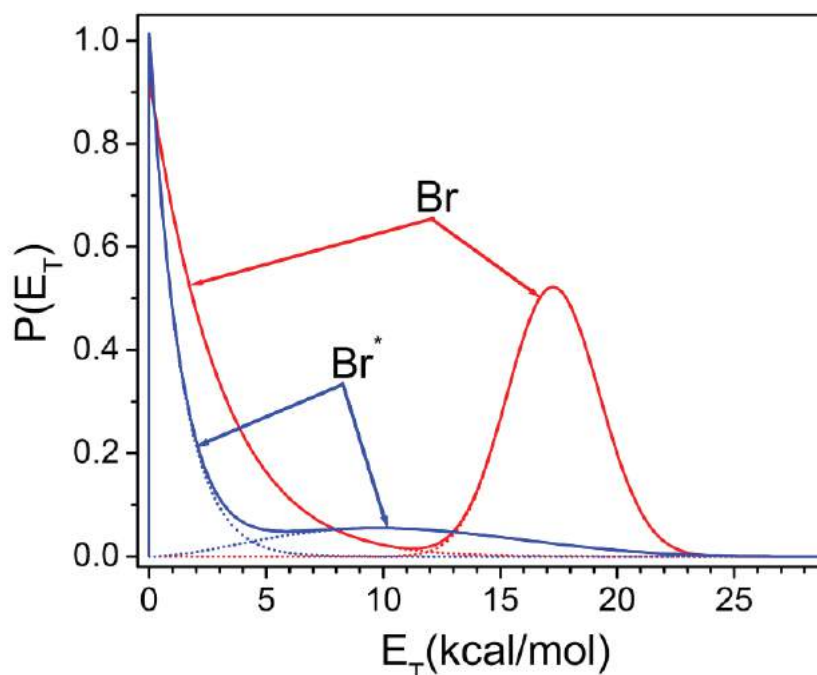
The circles are the experimental data and the solid line is a forward convolution fit calculated as discussed in chapter 2. Inspection of figures 5.2 and 5.3 clearly reveals that



**Figure 5.3:** REMPI-TOF profiles of  $\text{Br}^*$  ( $^2P_{1/2}$ ) produced from the photodissociation of 4-bromo-2,3,5,6-tetrafluoropyridine at 234 nm. The circles are the experimental data, the dashed lines are forward convolution fit for two different channels, namely, fast and slow and the solid line shows the sum. Three panels, namely, upper, middle and lower panels correspond to different experimental geometries with  $\chi=0^\circ$ ,  $\chi=54.7^\circ$ , and  $\chi=90^\circ$  respectively.

the TOF profile consists of two components corresponding to two types of translational energy distribution, namely faster and slower, for both Br and  $\text{Br}^*$  elimination channel shown as the dashed lines in the figure. For Br elimination channel, both, the faster and slower translational energy components are of equal weightage. However, for  $\text{Br}^*$  elimination channel, the faster component consists of  $\sim 35\%$  of the total fragments, while the slower component consists of the remaining  $\sim 65\%$ . Figure 5.4 shows the centre-of-

mass photofragment translational energy distribution,  $P(E_T)$ , for both Br and Br\* atom elimination channel calculated from their respective TOF profile as discussed in chapter 2.



**Figure 5.4:** Centre-of-mass recoil translational energy distribution derived from figure 5.2 and 5.3 for Br ( $^2P_{3/2}$ ) and Br\* ( $^2P_{1/2}$ ), produced in the photodissociation of 4-bromo-2,3,5,6-tetrafluoropyridine at 234 nm.

For Br elimination channel average translational energies of fast and slow component are determined to be  $17.3 \pm 1.5$  and  $2.6 \pm 1.0$  kcal/mol respectively. Similarly, for Br\* elimination channel, average translational energies of fast and slow component are determined to be  $11.1 \pm 1.5$  and  $1.5 \pm 1.0$  kcal/mol. It was not possible to determine anisotropy parameter for the two components independently. In our earlier publication, we have assumed identical anisotropy for each channel, and the anisotropy was determined. However, in the present case, the anisotropy for the slow component is assumed to be zero. This assumption of zero anisotropy for slow component is quite reasonable as the slow component arises mostly from the ground state photodissociation process which lacks anisotropy dependency. Hence, in the present study, the anisotropy parameter for the fast component was determined by assuming a zero anisotropy

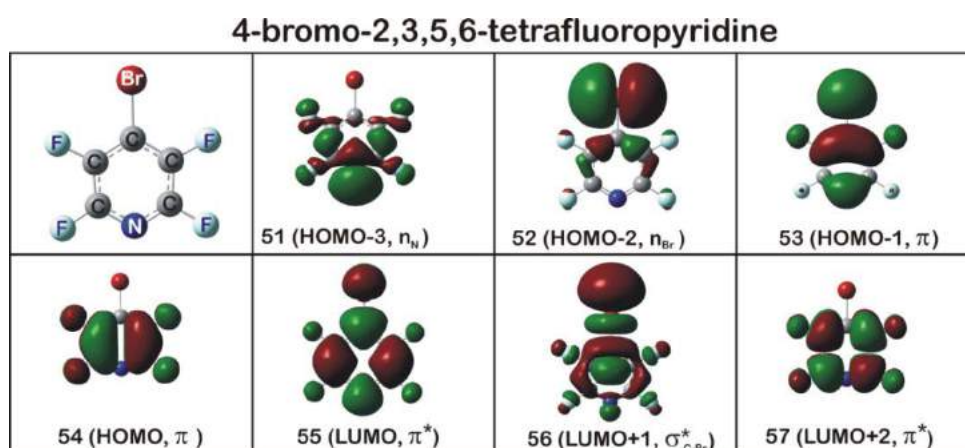


parameter for slow component. Thus, the anisotropy for Br and Br\* fragments was determined to be  $0.60 \pm 0.02$ .

## 5.6 Discussion

### 5.6.1 Nature of excitation at 234 nm

Figure 5.1 shows the optical absorption spectrum of 4-bromo-2,3,5,6-tetrafluoropyridine. The onset of the optical absorption is about 290 nm (4.27 eV) with  $\lambda_{\text{max}}$  at 268 nm (4.62 eV) for BTFP. Similar to the chloropyridine and fluorinated chloropyridine, the origin of this band has been attributed due to the  $\pi^* \leftarrow \pi$  transition. Also, it does not show any vibronic structure similar to that of fluorinated chloropyridine. To understand the nature of transitions responsible for various observed absorption bands, vertical excitation energy calculations were performed using Time-Dependent Density Functional Theory (TD-DFT) method, in detail. Equilibrium ground state geometry was optimized employing density functional theory calculation at uMPW1PW91/aug-cc-pVDZ level of theory maintaining the  $C_{2v}$  geometry. Vertical excitation energies were then calculated at uMPW1PW91/aug-cc-pVTZ level of theory. Although the calculated vertical transition energies slightly differ as compared to the experimental results, the nature of transitions and that of the orbitals involved are accurately predicted, using this method [72,73,134,135]. The orbitals participating in the different electronic transitions were visualized using suitable visualization program, for better understanding of the process and are given in figure 5.5. Various lowest singlet excited states arising from different electronic transitions are listed in table 5.1. Similar calculation was also done using EOM-CCSD method, as described earlier, for first three singlet excited states. The results were very much similar in nature. Hence, hereafter we will discuss these excited states obtained using TD-DFT method only.



**Figure 5.5:** Computed HOMO, LUMO, along with other MOs involved in the transition of 4-bromo-2,3,5,6-tetrafluoropyridine.

**Table 5.1:** Vertical excitation energies ( eV, nm) and oscillator strengths (given in parentheses) of low-lying singlet states of 4-bromo-2,3,5,6-tetrafluoropyridine with respective designation calculated using TD-DFT method. The  $C_{2v}$  symmetry designation, nature of transition and MOs involved in the transitions are also included in the table.

4-bromo-2,3,5,6-tetrafluoropyridine (BTFP)		
	State designation and nature of transition	Vertical excitation energy with oscillator strength(in parenthesis)
S <sub>1</sub>	1 <sup>1</sup> B <sub>2</sub> 54 → 55 π - π*	5.09 eV, 244 nm (0.0759)
S <sub>2</sub>	1 <sup>1</sup> A <sub>2</sub> 54 → 56 π - σ* <sub>C-Br</sub>	5.41 eV, 229 nm (0.0000)
S <sub>3</sub>	1 <sup>1</sup> B <sub>1</sub> 53 → 56 π - σ* <sub>C-Br</sub>	5.75 eV, 216 nm (0.0001)
S <sub>4</sub>	2 <sup>1</sup> A <sub>1</sub> 53 → 55 π - π*	5.83 eV, 212 nm (0.1149)
S <sub>5</sub>	2 <sup>1</sup> A <sub>2</sub> 52 → 55 n <sub>Br</sub> - π*	6.11 eV, 203 nm (0.0000)
S <sub>6</sub>	2 <sup>1</sup> B <sub>1</sub> 51 → 55 n <sub>N</sub> - π*	6.13 eV, 202 nm (0.0017)
S <sub>7</sub>	2 <sup>1</sup> B <sub>2</sub> 52 → 56 n <sub>Br</sub> - σ* <sub>C-Br</sub>	6.46 eV, 192 nm (0.0002)
S <sub>8</sub>	3 <sup>1</sup> A <sub>1</sub> 54 → 57 π - π*	6.65 eV, 186 nm (0.4227)
S <sub>9</sub>	3 <sup>1</sup> B <sub>2</sub> 53 → 57 π - π*	6.78 eV, 183 nm (0.1433)

Nine singlet excited states are considered, out of which, almost all states are valence states. These valence states are primarily due to excitations from the  $\pi$  orbitals, mostly, HOMO and HOMO–1, to  $\pi^*$  orbitals, mostly, LUMO. The other valence states arise from the non-bonding electrons of N and Br ( $n_N$ ,  $n_{Br}$ ) orbitals to  $\pi^*$  orbitals. Few other valence states also arise from  $\pi$  orbitals to  $\sigma^*_{C-Br}$  for this molecule. Besides these valence states, Rydberg states involving excitations to a diffuse 3s orbital are also included. Results from TD-DFT calculation shows that the first excited state is  $1^1B_2$  state arising from a  $\pi^* \leftarrow \pi$  transition at 5.09 eV (244 nm) with an oscillator strength of 0.0759. For  $S_1$  state, the calculated value is slightly overestimated using this method as compared with the experimental value of  $\lambda_{max} = 4.62$  eV (268 nm, see spectrum, figure 5.1). However, the calculated  $\lambda_{max}$  value of 5.83 eV (212 nm) for the second  $\pi^* \leftarrow \pi$  transition which is designated as  $S_4$  ( $2^1A_1$ ) state matched very well with the experimental value of  $\lambda_{max} = 203$  nm (see spectrum, figure 5.1). Similarly, the second ( $S_2$ ,  $1^1A_2$ ) and third ( $S_3$ ,  $1^1B_1$ ) excited states arise from mainly  $\sigma^*_{C-Br} \leftarrow \pi$  transitions with almost non-existent oscillator strengths at 5.41 eV (229 nm) and 5.75 eV (216 nm), respectively. The presence of non-bonding lone pair electrons of N ( $n_N$ ) and Br ( $n_{Br}$ ) give rises to various electronic transitions which originate from these lone pair orbitals. The next three excited states arise from either  $n_N$  or  $n_{Br}$ . The fifth state ( $S_5$ ,  $2^1A_2$ ) originates from  $\pi^* \leftarrow n_{Br}$  transition with zero oscillator strength. Similarly, the sixth state ( $S_6$ ,  $2^1B_1$ ) originates from  $\pi^* \leftarrow n_N$  transition at 6.13 eV (202 nm) with an oscillator strength value of 0.0017. The seventh excited state is basically a  $\sigma^*_{C-Br} \leftarrow n_{Br}$  ( $S_7$ ,  $2^1B_2$ ) transition at 6.46 eV (192 nm) with an oscillator strength of 0.0002. The eighth ( $S_8$ ,  $3^1A_1$ ) and ninth ( $S_9$ ,  $3^1B_2$ ) excited states arise from  $\pi^* \leftarrow \pi$  transition with really high oscillator strengths of 0.4277 and 0.1433 respectively.

The above discussion on the vertical excitation energies using TD-DFT method clearly shows a non-linear behaviour as compared to experimentally observed spectral peaks. This variation is quite common with TD-DFT calculation because of various reasons. The first one is related to the single excitation methodology adapted for the TD-DFT calculation. However, if the excited state is not fully described by single excitation or rather a multi excitation, then the vertical excitation energy calculated for that particular state can be completely different and non-linear behaviour can be seen in the vertical excitation energies. Moreover, the vertical excitation energy of the excited state near conical intersection also results into the non-linearity. These types of results are very common in literature. For example, in benzoic acid and its derivatives, the calculated excitation energies are sometimes blue-shifted relative to experiment, sometimes red-shifted, and sometimes a good match[136]. Considering the corresponding wavelengths for vertical excitation energies and the respective oscillator strengths of the various transitions, it is evident that at 234 nm the BTFP has a  $\pi^* \leftarrow \pi$  transition. Since the excited state, with  $\pi^* \leftarrow \pi$  transition, basically a bound state and adiabatically correlates only with highly excited photoproducts, which is not feasible in a single-photon excitation in the present case, it is assumed that the initially prepared  $\pi\pi^*$  states crossover to the nearby states, mostly to some  $\sigma^*_{\text{C-Br}}$  state, from where the C–Br bond can be cleaved, forming Br atoms. Although, assignment and nature of various excited states using computational methods suggest the cross-over of  $\pi\pi^*$  state to  $\pi\sigma^*_{\text{C-Br}}$  state, the actual scenario could be confirmed with wavelength dependent photodissociation dynamics studies, which is now underway in our laboratory.

### 5.6.2 Translational energy release and anisotropy parameter

The power dependence studies clearly indicate that the Br atoms are formed in the monophotonic process after the photoexcitation of BTFP at 234 nm (122 kcal/mol) in the

## C–Br Bond Dissociation Dynamics of 4-bromo-2,3,5,6-tetrafluoropyridine

simple C–Br bond cleavage process. In the present study, the C–Br bond dissociation energy for 4-bromo-2,3,5,6-tetrafluoropyridine was taken as, 82 kcal/mol, similar to that in bromobenzene [92]. For the C–Br bond cleavage reaction, the available energy,  $E_{\text{avail}}$ , which is defined as  $E_{\text{photon}} - \Delta H$ , comes out to be 40.0 kcal/mol for the Br ( $^2P_{3/2}$ ) atom formation channel. Similarly, for the Br\* ( $^2P_{1/2}$ ) atom formation channel, the  $E_{\text{avail}}$  comes out to be 29.5 kcal/mol taking a value of 10.5 kcal/mol for the spin-orbit excitation energy. The various other channels generating the Br atom apart from the simple C–Br bond cleavage are also considered. However, the lowest energy channel for the Br atom formation mechanism is the direct cleavage of C–Br bond forming the fluoropyridine radical and Br atom as shown below and this is the only channel responsible for the generation of Br atom. However, this direct C–Br bond cleavage process may be either from the excited state or from the ground state which we will be discussing in the following paragraph.



In the present study on BTFP,  $P(E_T)$  for Br/Br\* formation channel was well described by two components, namely, slow and fast, as shown in figure 5.4. The  $P(E_T)$  for slow Br channel peaks at origin, and extends up to  $\sim 11$  kcal/mol. Similarly, for the fast Br channel, the  $P(E_T)$  peaks at  $\sim 17$  kcal/mol and extends up to  $\sim 24$  kcal/mol. However, the  $P(E_T)$  for Br\* is strikingly different from the Br elimination as seen in figure 5.4. For Br\* channel, the slow peaks near origin and extends up to  $\sim 5$  kcal/mol and  $P(E_T)$  for fast Br\* channel also peaks at  $\sim 10$  kcal/mol, and extends up to  $\sim 24$  kcal/mol. The nature and the average energy for the slow component for both the Br and Br\* elimination channel is similar and statistical in nature which hints that the slow components mostly arises from the ground state dissociation process. However, it should

be noted that the average translational energy value,  $E_T$ , for fast Br is higher than the  $E_T$  value for Br\*. This may be due to the fact that the  $E_{\text{avail}}$  is different for these spin-orbit states. Also, the nature of  $P(E_T)$ , of the fast Br and Br\* are different. For Br elimination channel the translational energy distribution is sharp, whereas, for Br\* it is quite broad.

The partitioning of the available energy into various degrees of freedom of the fragments is mainly governed by the nature of the dissociative potential energy surface and can be predicted using simple models, such as impulsive [22] and statistical [21,70,94]. It is well known that the energy partitioning in a dissociative event on a repulsive surface is well described by an impulsive model. This model predicts the fraction ( $f_T$ ) of the available energy ( $E_{\text{avail}}$ ) released as translational energy ( $E_T$ ), which is given by  $E_T = \left( \frac{\mu_{\text{C-Br}}}{\mu_{(\text{C}_5\text{NF}_4)\text{-Br}}} \right) E_{\text{avail}}$  and  $f_T = E_T/E_{\text{avail}}$ , where  $\mu_{\text{C-Br}}$  is the reduced mass of the C and Br atoms,  $\mu_{\text{C}_5\text{NF}_4\text{-Br}}$  is the reduced mass of  $\text{C}_5\text{NF}_4$  and Br, and  $E_{\text{avail}}$  is the available energy and  $f_T$  is the fraction of the available energy going into the translational modes of the fragments. In the present case, the ratio of the reduced masses is 0.2, which gives a  $f_T$  value using impulsive model. The experimental  $f_T$  values for fast Br and Br\* are determined to be 0.43 and 0.38 which are considerably higher than the value of 0.20 predicted by impulsive model. Similar results were obtained in the photodissociation process of alkyl halides and aryl halides also. In the photolysis of bromobenzene at 193 nm, the  $f_T$  value determined to be 0.46 [92]. In the same study, the  $P(E_T)$  for bromine dissociation process clearly shows two peaks in the translational energy distribution curve similar to our results. The high  $f_T$  values were described as the “heavy-atom” effect without elaborating the mechanism. However, high  $f_T$  values (values higher than predicted by an impulsive model) were not obtained in the case of both chlorobenzene and iodobenzene in the same study. Similar high  $f_T$  values were also obtained at 266 nm and 234 nm photodissociation of bromobenzene [105,113,126,127]. Various theoretical

calculations were also performed to understand the dissociation dynamics of bromobenzene, in particular [104,111,112]. All these studies, both, experiment and theoretical, clearly indicate the role of fast intersystem crossing from the initially prepared bound  $\pi\pi^*$  state to repulsive  $\pi\sigma^*/n\sigma^*$  state. However, if the dissociation is considered on the repulsive potential energy surface (PES) then the translational energy distribution should be best described by an impulsive model. As discussed earlier, the experimental  $f_T$  values are much higher as compared to value predicted by an impulsive model in the case of bromine containing alkyl and aryl halides. The present situation of higher  $f_T$  values prompted us to apply the hybrid model, employed by North *et al.*[23] for the dissociation occurring on the excited PES with barrier. In this model, the  $E_{\text{avail}}$  is divided into two parts namely, the excess energy above the exit barrier ( $E_{\text{stat}}$ ) and the exit barrier energy ( $E_{\text{imp}}$ ). The partitioning of  $E_{\text{stat}}$  and  $E_{\text{imp}}$  is treated independently by the statistical and modified impulsive models, respectively and added to obtain the total translational energy released into the photofragments. Generally, in this type of dissociation, the  $E_T$  does not change much with  $E_{\text{avail}}$ . Similar results were obtained in our earlier studies on various saturated and unsaturated carboxylic acids, and also on the  $\alpha,\beta$ -enone system [137-139]. Photodissociation studies on acryloyl chloride by Butler and co-worker [140,141] at 193 and 234 nm show similar translational energy release for Cl atom which was supported with theoretical calculation by Cui *et al.* [142]. Hence, we strongly believe that the dissociation cannot be ruled out on excited PES with an exit barrier in the present study. To further investigate this issue, we have mapped PES for various excited states for the Br atom elimination channel using two different approaches, one at single and other at multi reference level. In the first approach, we applied TD-DFT method which is a single-reference method to calculate the PE curves of various excited states along the C–Br bond length. For this purpose, single point calculations on different

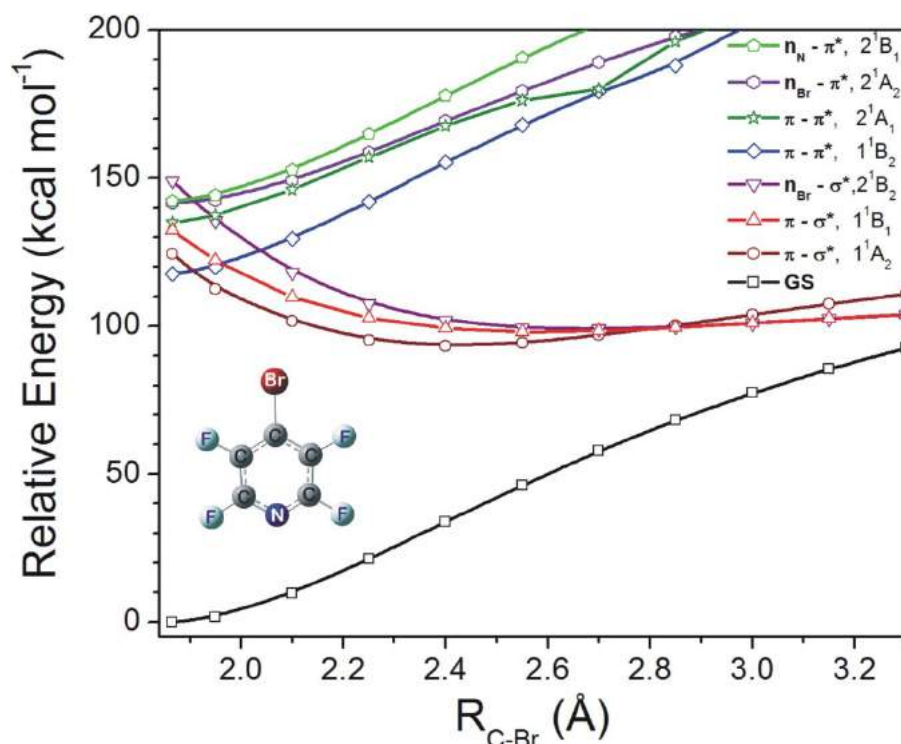
## C–Br Bond Dissociation Dynamics of 4-bromo-2,3,5,6-tetrafluoropyridine

C–Br bond lengths were performed at uMPW1PW91/aug-cc-pVTZ level with all other internal coordinates kept at the ground-state values, which were optimized at uMPW1PW91/aug-cc-pVDZ level. For this purpose, the C–Br bond lengths were varied from 1.8 Å to 3.3 Å, which is asymptote to dissociation limit. It has been observed in our many previous studies that the TD-DFT method adequately predicts the nature of various dissociative PES in case of halogenated pyridines and thidiazole. The second approach calculates various PESs using a Multi State Multi Reference Perturbation Theory (MS-MR-PT) incorporating Møller-Plesset Second order (MP2) correction which is generally known as Multi Configuration Quasi Degenerate second order Perturbation Theory (MCQDPT2). In this method, ground state geometry of BTFP was optimized employing MP2 method, using 6–311+g(d) basis set, maintaining the  $C_{2v}$  point group. Then, C–Br bond distance was varied from 1.7 Å to 3.1 Å. In each  $R(\text{C–Br})/\text{Å}$  distance the vertical excitation energies of the various lowest-lying singlets were calculated using MCQDPT2 employing the 6–31g(d) basis set. In this calculation, 10 electrons (6  $\pi$  ring electrons, 2 non bonding electrons of Br and Nitrogen each) are active in 5 occupied and 3 virtual orbitals. The output of such calculation can be seen in figures 5.6 and 5.7.

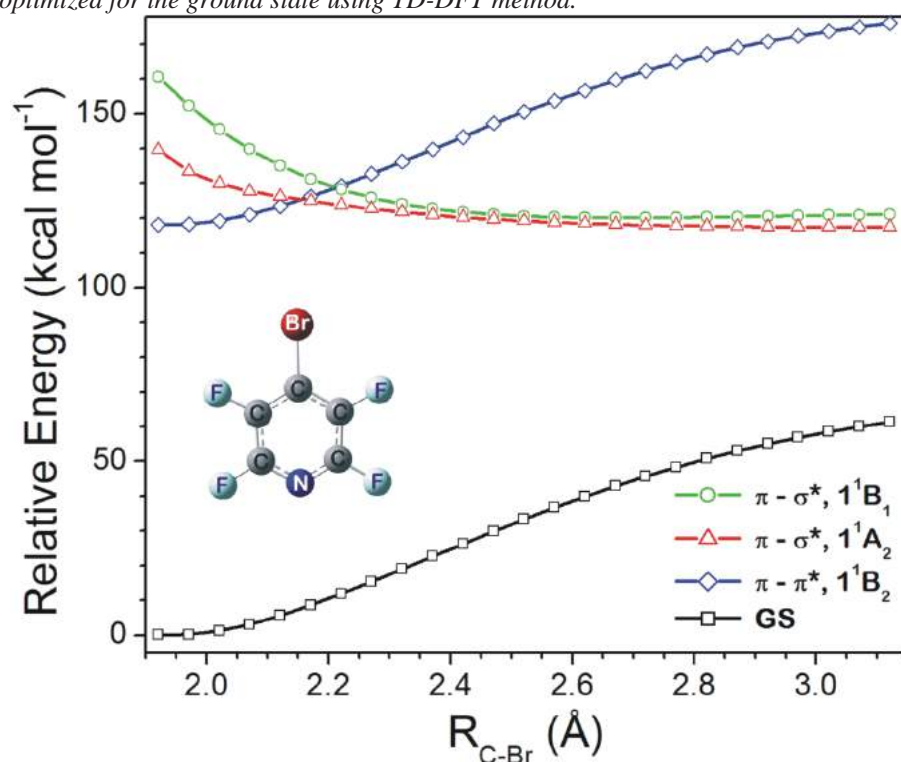
In the present case, the choice of any third co-ordinate apart from the C–Br bond distance in dissociation process does not arise because of its planar structure and also the dissociation process proceeds in the same plane. Hence, we have performed the theoretical calculation with C–Br bond distance. It is inferred from the calculation that the initially excited  $\pi\pi^*$  state crossovers to  $\pi\sigma^*$  which forms Br atom. From figure 5.6 it can be easily seen that the  $\pi\pi^*$  and  $n\pi^*$  states are bound in nature and it is well known in the literature that these states adiabatically correlate only with highly excited photoproducts, which is not feasible in a single-photon excitation in the present case.



C–Br Bond Dissociation Dynamics of 4-bromo-2,3,5,6-tetrafluoropyridine



**Figure 5.6:** Various diabatic potential energy curves calculated for 4-bromo-2,3,5,6-tetrafluoropyridine along the C–Br bond length with the other geometrical parameters optimized for the ground state using TD-DFT method.



**Figure 5.7:** Various diabatic potential energy curves calculated for 4-bromo-2,3,5,6-tetrafluoropyridine along the C–Br bond length using multi configuration quasi degenerate second order perturbation theory (MCQDPT2). The ground state geometrical parameters are optimized at MP2 level.

## C–Br Bond Dissociation Dynamics of 4-bromo-2,3,5,6-tetrafluoropyridine

For dissociation process to take place along the C–Br bond, the crossover from initially prepared  $\pi\pi^*$  to  $\pi\sigma^*$  states is required. It is well known in the literature that if two states of different symmetry cross, they will ignore each other and their wave functions remain unperturbed and they represent the adiabatic solutions of the Schrödinger equation. Then the crossing is strictly allowed. However, if they have the same symmetry, they will mix with each other to give two adiabatic solutions which no longer cross. Then the crossing becomes avoided crossing. The probability of the crossing between these two adiabatic surfaces is completely dependent on the slope of these states and the energy gap at avoided crossing which given by Landau-Zener expression [143]. In the present case, the role of  $n\sigma^*$  state is negligible owing to its very high energy. Whereas, the  $\pi\sigma^*$  state is repulsive in nature and intersect both  $\pi\pi^*$  and  $n\pi^*$  states at different C–Br internuclear distances. Generally, these  $\sigma^*\leftarrow\pi$  transitions are electric dipole forbidden; however, gains oscillator strength by vibronic mixing with allowed transitions, here the  $\pi^*\leftarrow\pi$  transition, in the higher excited states. This can be clearly seen in the table 5.1. The third singlet excited state,  $1^1B_1$  which arises from a  $\sigma^*\leftarrow\pi$  transition shows non-zero oscillator strength which can facilitate the crossover process very efficiently. Hence, in the present case the crossover from  $\pi\pi^*$  state ( $1^1B_2$ ) to a  $\pi\sigma^*$  state ( $1^1B_1$ ) is more favourable compared to crossover to second singlet excited state ( $1^1A_2$ ), which also arises from  $\sigma^*\leftarrow\pi$  transition. The avoided crossing between  $\pi\pi^*$  state ( $1^1B_2$ ) and  $\pi\sigma^*$  states ( $1^1B_1, 1^1A_2$ ) results into the barrier in the dissociative PES. Using hybrid model and taking bond dissociation energy value of 82 kcal/mol for Br atom elimination channel, the location of avoided crossing is estimated in the region of  $\sim 105$  kcal/mol. However, the theoretical location of barrier or the point of crossover between the  $\pi\pi^*$  ( $1^1B_2$ ) and  $\pi\sigma^*$  ( $1^1B_1$ ) state is  $\sim 120$  kcal/mol using TD-DFT and  $\sim 130$  kcal/mol using MS-MR-PT method (see figures 5.6 and 5.7). The agreement seems to be reasonable assuming the

size of molecular system and the level of theory used. The dynamics of dissociation for BTFP excited below the region of avoided crossing (105 kcal/mol, ~270 nm) may be completely different. For the slow component, a statistical dissociation process is assumed where excess energy is partitioned statistically amongst the available degrees of freedom of the products which occurs predominantly, if the photo-excited parent molecule is long-lived. This may be applicable in a process where a rapid internal conversion to the ground electronic state, followed by the subsequent slow dissociation occurs. For this kind of dissociation process, a priori calculations were adopted [135,136], along with a simple analytical expression [21] relating the mean translational energy release,  $E_T$ , and the  $E_{avail}$ , for a statistical barrierless dissociation process, which give a  $f_T$  value of ~0.04. The calculated statistical value of  $f_T$  matches well with the experimental value of 0.06/0.04 for Br/Br\* atom elimination channel.

The anisotropy measured in the present work is ~0.60, vindicates the impulsive nature of dissociation process in BTFP. Generally, an impulsive dissociation is accompanied with an anisotropic distribution of the photoproducts, since the dissociation lifetime is much shorter than the rotational time period of the molecule. In the present case a reduced value of anisotropy parameter can be due to mixed initial transition with both parallel and perpendicular components. A positive and non-zero anisotropy parameter also indicates that the dissociation is faster than the rotational time period of the molecule. This aspect is very important for BTFP molecule considering the fact that the dissociation is assigned from the PES having an exit barrier.

In this context, it is worth comparing the dissociation dynamics of pyridine with the present molecular system i.e. BTFP. The article by Prather *et al.* [80] on the dissociation dynamics of pyridine clearly demonstrated that at 193 nm the molecular channels which arise from the ground state dissociation are the major channels. Whereas

the H atom formation channel which can arise either from the ground state and the excited state is only 11%. Later, in a similar work by Lin *et al.* they reinvestigated the dissociation dynamics of pyridine extensively both experimentally and theoretically [79]. They concluded that the ring opening dissociation channels play a very important role in photodissociation of pyridine at 193 nm. This is due to the fact that the H atom elimination channel has large dissociation energy (106–112 kcal/mol) compared to the other entire ring opening dissociation channels which occurs after H atom migration before the molecule dissociates into two fragments. The H atom migration and subsequent ring opening can occur in the energy range of as low as 91 kcal/mol. Now coming to the scenario in BTFP, the Br atom elimination channel is major channels due to its low dissociation energy. The C–Br bond dissociation energy in BTFP is 82 kcal/mol. In this scenario the F atom migration and subsequent ring opening in case of BTFP is negligible. To further support the above point, we have done *ab initio* calculation for the F atom migration in the BTFP. The TS for the F atom migration lies at 112 kcal/mol at MP2/6–311+g(d) level of theory which shows that the F atom migration and subsequent ring opening can be neglected in BTFP photodissociation.

### 5.6.3 Comparison with chloropyridine and effect of fluorine substitution

The dissociation dynamics of BTFP at 234 nm for Br atom elimination channel is very much different from its chlorine analogue, namely chloropyridine and fluorinated chloropyridine studied earlier by us [5]. However, the nature of excitation at ~234 nm ( $\pi^* \leftarrow \pi$  transition) is similar in all the cases. In the case of 3-chloropyridine (ClPy) the translational energy released,  $E_T$ , into the photofragments for Cl atom elimination channel was more of statistical in nature. Similarly, in the photodissociation of 3-chloro-2,4,5,6-tetrafluoropyridine (ClFPy), the  $E_T$  was nicely described by an impulsive model. However, the  $P(E_T)$  in both the cases lacks of sharp distribution and peaks at the origin.

This kind of behaviour in  $P(E_T)$  is completely different when compared with the dissociation dynamics in BTFP. As discussed earlier, the  $P(E_T)$  shows a sharp distribution for the fast Br atom indicating an impulse dissociation process accompanied by a non-zero anisotropy parameter. As described in our previous study, the lowest excited state,  $S_1$ , in case of ClPy arises from  $\pi^* \leftarrow n$  transition and the energy difference between first  $\pi\pi^*$  state and the dissociative PES, which is a  $\pi\sigma^*$  state, is  $\sim 1.45$  eV. This energy gap plays a crucial role in the crossover process from the initially prepared  $\pi\pi^*$  state to dissociative  $\pi\sigma^*$  state. Also, the presence of low lying  $n\pi^*$  state is important as the initially prepared  $\pi\pi^*$  state can crossover to this state which can completely change the dynamics of the dissociation process. In case of ClFPy, the substitution of fluorine atom completely changes the relative order of various excited states. The first excited state,  $S_1$ , is a  $\pi\pi^*$  state and the  $n\pi^*$  state is pushed higher in energy. Similarly, the  $\pi\sigma^*$  state starts appearing at lower energy. Also, the relative energy gap between  $\pi\pi^*$  and  $\pi\sigma^*$  state in ClFPy is decreased to 0.53 eV. These changes in the nature of excited state completely alter the dissociation dynamics. Similarly, in case of BTFP, the relative energy gap between  $\pi\pi^*$  and  $\pi\sigma^*$  state is further reduced to 0.32 eV and the  $n\pi^*$  state is pushed to higher energy.

## 5.7 Conclusion

In summary, the photodissociation of brominated fluoropyridine, namely, 4-bromo-2,3,5,6-tetrafluoropyridine has been carried out at around 234 nm, and the dynamics of C–Br bond dissociation is investigated, using resonance enhanced multiphoton ionization, coupled with a time-of-flight mass spectrometer. The molecule is excited with 234 nm laser which prepares the molecules in the  $\pi\pi^*$  state. The dynamics of bromine atom elimination channels was studied by determining the total translational energy distribution, the anisotropy parameter,  $\beta$ , and the spin-orbit branching ratio. Translational energy distributions for the bromine atom elimination channel was

determined using polarization-dependent and state-specific TOF profiles employing a forward convolution method and taking into account the fragment anisotropies. The translational energy distributions for the bromine atom elimination channel is best described by two components, namely, fast and slow. The anisotropy parameters for both Br and Br\* are the same, and characterized by values of  $0.60 \pm 0.05$ . A positive and non-zero anisotropy parameter also indicates that the dissociation is impulsive in nature and faster than the rotation period of the molecule. The average translational energies released into the Br and Br\* channels for the fast component are  $17.3 \pm 2.0$  and  $11.1 \pm 2.0$  kcal/mol, respectively. Similarly, for the slow component, the average translational energies imparted into the Br and Br\* channels are  $2.6 \pm 1.0$  and  $1.5 \pm 1.0$  kcal/mol, respectively. The relative quantum yields of Br and Br\* are  $0.87 \pm 0.15$  and  $0.13 \pm 0.06$ . The energy partitioning into the translational modes is interpreted with the help of various models, such as impulsive and statistical models. Theoretical calculations were performed at various levels and we have mapped PES for various excited states for the Br atom elimination channel using two different approaches, one at single and other at multi reference level. The TD-DFT approach has been used at single reference level while multi-configurational quasidegenerate second order perturbation theory (QDMCPT2) was used for multi reference level. Both theoretical approaches suggest that the initially prepared  $\pi\pi^*$  state crosses over to a nearby  $\pi\sigma^*$  repulsive state along the C–Br bond, from where the dissociation takes place. During the course of experiments, the absorption spectra were also obtained with absolute absorption cross-section. Finally, the results were compared with chlorinated pyridines and effect of fluorine substitution has been discussed.

# Chapter 6

## **Photodissociation Dynamics of Halogenated Pyrimidines at 235 nm**

---

### **6.1 Introduction**

Photodissociation of halogen (Cl and Br) containing organic molecules has attracted a lot of experimental and theoretical studies since these compounds produce halogen atoms which play an important role in atmospheric chemistry, particularly in ozone depletion. In general, impulsive atomic eliminations are observed in the dissociation process of these compounds which arise mainly from either a dissociative surface adiabatically, or non-adiabatically after curve crossing. In this context, various photodissociation studies of alkyl halides [144-152] and aryl halides [3,5,6,45,47,93,153-164] have been well studied. However, these kinds of studies are very scarce in literature when it comes to studies on halogenated heterocyclic molecules [2,24,35,46]. The most studied heterocyclic compound is pyridine (*c*-C<sub>5</sub>H<sub>5</sub>N), where one of the CH group in benzene is replaced by N. The interesting outcome of our recent studies on the photodissociation of halogenated pyridines motivated us to probe the dissociation dynamics of these heterocyclic compounds further. In this context, we have undertaken the present study on the photodissociation of halogenated pyrimidines.

Pyrimidines are six membered heterocyclic molecules with two nitrogen atoms at meta position. The presence of lone pair of nitrogen alters the photochemistry of pyrimidines from its hydrocarbon analogue, benzene, by introducing  $n_N\pi^*$  state which is

its lowest electronic excited state. This leads to the variation in their absorption, fluorescence, phosphorescence, vibronic coupling, and excited state dynamics and so on, which opens up an interesting photochemistry to study about. The absorption spectrum of pyrimidine in the region of 270-330 nm was first observed by Fred M. Uber [144]. The first absorption band is ~13 nm blue shifted as compared to benzene [145,146]. A new absorption band in the region of 250-290 nm was observed and attributed to  $\pi^* \leftarrow n$  transition. Theoretically, the  $n\pi^*$  state arises from a forbidden transition, but due to vibronic coupling with  $\pi\pi^*$  state, the  $\pi^* \leftarrow n$  transition gains some oscillator strength and the absorption is observed [147,148]. A weak emission from pyrimidine in liquid and vapour phase was observed and assigned as fluorescence from  $n\pi^*$  state, which was further studied by various groups [149-155]. A detail review on the various electronic states of these heterocyclic compounds clearly shows the importance of these studies [156-158]. The structure and dynamic properties of first excited state was studied by measuring fluorescence excitation spectrum [159].

Apart from its excited state properties, the ground state structure elucidation is also an interesting field of research because pyrimidine is an important building block in biomolecules. The ground state molecular structure was elucidated from various combined techniques [160,161]. High-resolution rovibrational spectrum using Fourier transform spectrometer [162] and theoretical calculation [163] confirms the  $C_{2v}$  symmetry for the ground state of pyrimidine. Also, pyrimidine is one of the building blocks of the nucleic acids and hence lots of studies have been done on the elastic collision of low energy electrons with halopyrimidines. The dissociation of pyrimidine in the energy range from threshold to 375eV has studied by using cross electron gas-beam system coupled with the VUV spectrometer [164].



Recently, the photodissociation of pyrimidine was studied by Ni and co-workers at 193 and 248 nm using ultraviolet photoionization and multimag ion imaging technique. They observed six dissociation channels at 193 nm photolysis. The dissociation rates were reported as  $\sim 5 \times 10^7$  and  $1 \times 10^6 \text{ s}^{-1}$  at 193 and 248 nm, respectively. In comparative studies, they suggested that by increasing the number of nitrogen atoms in the ring, ring opening is more favourable. The formation of CN was reported in the energy range of 14.7 to 25 eV.

Previously, we have reported the mechanism and dynamics of Cl and Br atom formation in the photodissociation process of halogenated heterocyclic molecules such as halogenated furans [93], thiophenes [47], 1,2,5-thiadiazoles [3] and pyridines [5,6] using REMPI-TOF technique at  $\sim 235$  nm. At 235 nm photoexcitation, all these heterocyclic compounds have  $\pi^* \leftarrow \pi$  transition, similar to benzene. In this context, we have studied the Cl atom formation dynamics in the photodissociation process of halogen substituted pyrimidines, namely, 2,4,6-trichloropyrimidine and 5-chloro-2,4,6-trifluoropyrimidine using REMPI-TOF-MS at  $\sim 235$  nm. It is also interesting to see whether there is any excited state contribution showing a positive non-zero anisotropy for the photodissociation process as observed in case of bromo-fluoropyridine or the dissociation is solely from the ground state [6]. We have also studied the fluorine substitution effect on the photodissociation dynamics, relative quantum yield determination of Cl and Cl\* and the translational energy distribution. This study will also provide an answer about the substitution effect of fluorine atom on the nature of various excited states in an aromatic molecule. The results will be compared with our earlier results on photodissociation of chloropyridines at 235 nm.

## 6.2 Experimental

The experiment was performed using a molecular beam time-of-flight mass spectrometer system (MB-TOF-MS), as described before in chapter 2. The 2,4,6-trichloropyrimidine (97% purity, Sigma-Aldrich) and 5-chloro-2,4,6-trifluoropyrimidine (99% purity Sigma-Aldrich) were used, without further purification. Helium was bubbled through the sample, maintained at room temperature, and the mixture was expanded through the nozzle at a stagnation pressure of 1500 Torr. It was ensured that any interference to the measurements due to cluster photofragmentation was absent, or negligible, by operating at a low stagnation pressure, and using only the rising part of the molecular beam pulse. The power dependence measurements revealed a three photon dependency, which is consistent with one-photon dissociation of test molecules, followed by (2+1) REMPI of the chlorine atoms, assuming that the ionization step is saturated. Apart from the power dependence studies, we also systematically monitored the shape and the width of TOF profiles of Cl atoms at various laser intensities to rule out any high intensity contribution from laser light.

## 6.3 Analysis

The TOF profiles of Cl and Cl\* are measured at different laser polarizations. The translational energy distribution and the anisotropy parameter for both Cl and Cl\* are determined from these TOF profiles, using a commonly used forward convolution (FC) technique, as described in chapter 2. Using this method, the parameters are adjusted until a satisfactory agreement with the experimental data is achieved. Once the photofragment speed distributions have been determined, these were used to obtain the corresponding translational energy distributions.

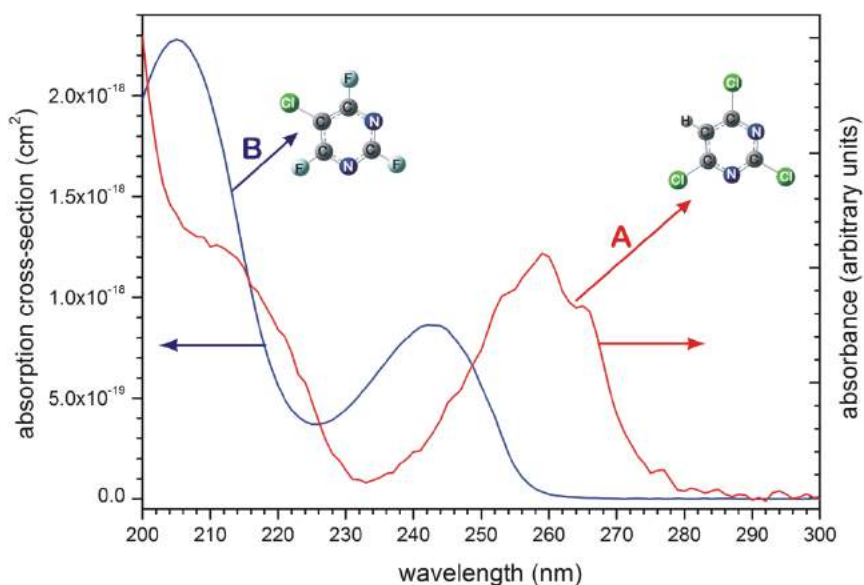
## 6.4 Computational methods

The molecular geometry for the ground electronic state is optimized at the Møller Plesset second order perturbation theory by employing 6-31+G(d) basis set. The potential energy curves of the ground and excited states along the dissociation coordinate of the Cl atom from the equilibrium ground state geometry are computed using single reference *ab initio* equation-of-motion coupled-cluster approaches with singles, doubles (EOM-CCSD) method [130,165-167]. EOM-CCSD calculations were carried out using 6-31+g(d) basis set at various C-Cl bond distances starting from  $\sim 1.7$  Å to  $\sim 2.6$  Å with 0.15 Å intervals, in general, and 0.02 Å intervals in crossing region for both the molecules. All these calculations were carried out with GAMESS-US quantum chemistry package [30].

## 6.5 Results

### 6.5.1 Absorption spectra and absolute cross-section

The absorption spectra of 5-chloro-2,4,6-trifluoropyrimidine were recorded using a commercial UV spectrophotometer at various substrate pressures. The absolute absorption cross-sections were then calculated using Beer-Lambert law. Figure 6.1 shows such absorption spectrum of 5-chloro-2,4,6-trifluoropyrimidine with absolute absorption cross-section. However, for 2,4,6-trichloropyrimidine, we were not able to perform the pressure dependent studies to determine absolute absorption cross-section due to its low vapour pressure. Hence, for 2,4,6-trichloropyrimidine, we have included the absorption spectrum with arbitrary absorbance in figure 6.1. For, 5-chloro-2,4,6-trifluoropyrimidine, the absolute absorption cross-section values were further verified by measuring the same at 235 nm using a 50-cm long absorption cross-section cell as described in chapter 3. The absorption cross-section at 235nm was found to be  $(6.3 \pm 1.2) \times 10^{-19}$  cm<sup>2</sup> molecule<sup>-1</sup> for 5-chloro-2,4,6-trifluoropyrimidine.



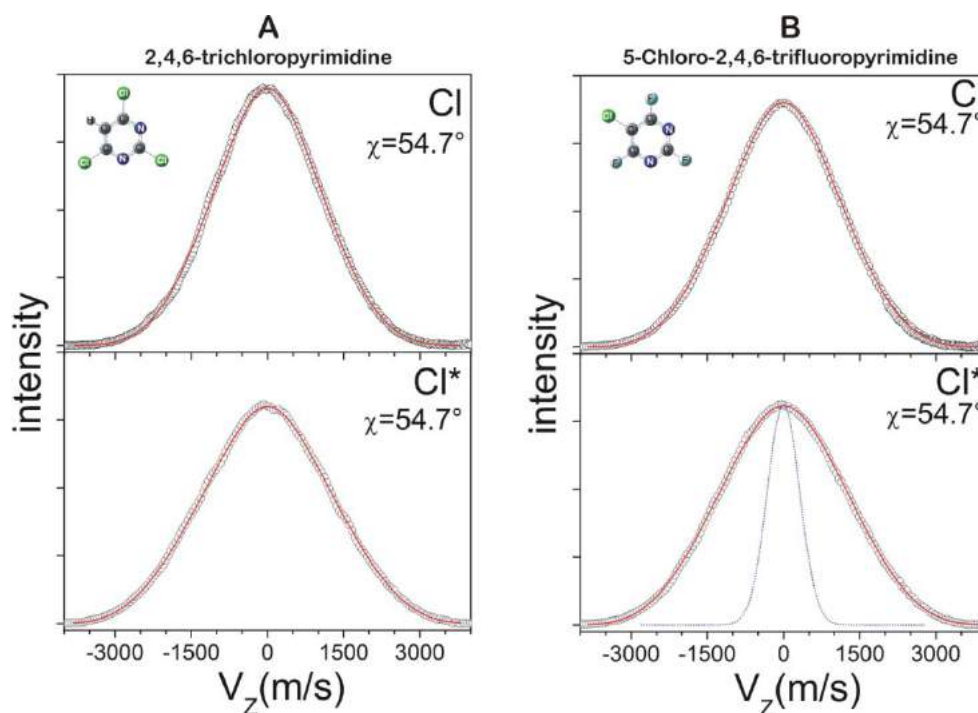
**Figure 6.1:** UV absorption spectra of (A) 2,4,6-trichloropyrimidine (B) 5-chloro-2,4,6-trifluoropyrimidine at room temperature.

### 6.5.2 Spin-orbit branching ratio

Doppler profiles of  $\text{Cl}(^2\text{P}_{3/2})$  and  $\text{Cl}^*(^2\text{P}_{1/2})$  atoms produced in the dissociation of 2,4,6-trichloropyrimidine and 5-chloro-2,4,6-trifluoropyrimidine were scanned in the wavelength region of  $42492.5\text{ cm}^{-1}$  and  $42516.1\text{ cm}^{-1}$ . The relative quantum yield of the Cl atom formed in different spin-orbit states (Cl, Cl\*), were calculated by normalizing the integrated intensity, i.e., the peak areas  $S(\text{Cl})$ , or  $S(\text{Cl}^*)$ , of the respective (2+1) REMPI transitions with respect to the laser intensity and the ratio of the two-photon absorption coefficients [24]. The intensities  $S(\text{Cl})$  and  $S(\text{Cl}^*)$  were obtained by integrating the measured ion signal intensities covering the Doppler width and the probe laser bandwidth. From the experimentally measured integrated intensity ratios,  $S(\text{Cl}^*)/S(\text{Cl})$ , one can easily obtain the product ratios  $N(\text{Cl}^*)/N(\text{Cl})$ . The relative quantum yield,  $\Phi(\text{Cl}^*)$ , as described in our earlier work [45] can be calculated as follows,  $\Phi(\text{Cl}^*) = N(\text{Cl}^*) / (N(\text{Cl}^*) + N(\text{Cl}))$ . The  $\Phi(\text{Cl}^*)$  obtained in the photodissociation of 2,4,6-trichloropyrimidine and 5-chloro-2,4,6-trifluoropyrimidine is found to be  $0.17 \pm 0.05$  and  $0.21 \pm 0.05$ , respectively.

### 6.5.3 Translational energy distribution and anisotropy parameter

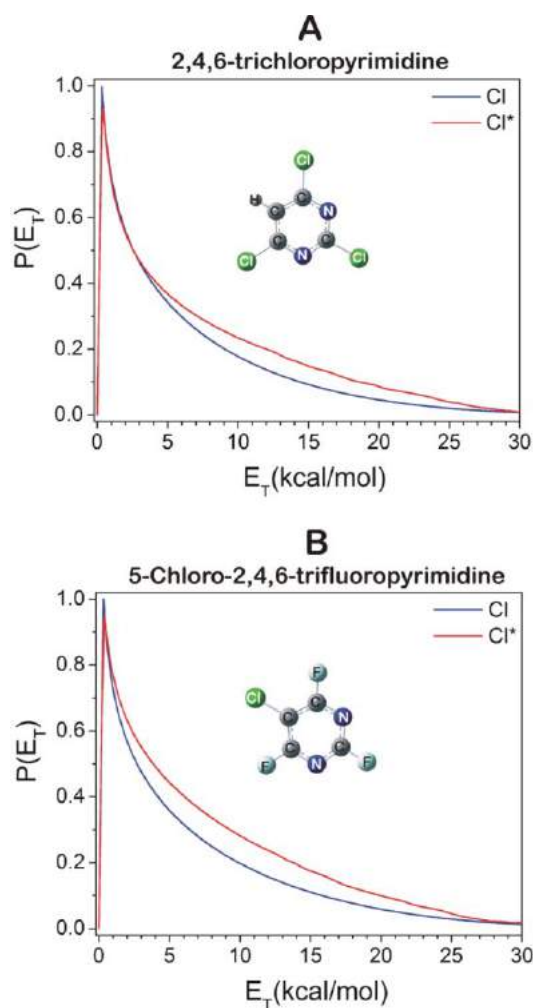
Figure 6.2 shows time-of-flight (TOF) profiles of Cl/Cl\* formed in the photodissociation of 2,4,6-trichloropyrimidine and 5-chloro-2,4,6-trifluoropyrimidine in the velocity domain. The TOF profiles were independent of laser polarization; hence, we



**Figure 6.2:** REMPI-TOF profiles of Cl ( $^2P_{3/2}$ ) and Cl\* ( $^2P_{1/2}$ ) produced from the photodissociation of (A) 2,4,6-trichloropyrimidine and (B) 5-chloro-2,4,6-trifluoropyrimidine at 235 nm at magic angle ( $\chi = 54.7^\circ$ ). The circles are the experimental data and the solid line is a forward convolution fit. The instrument function is depicted as the blue dotted curve in lower panel of B.

have shown only the TOF profile at the magic angle configuration i.e laser polarization at  $\sim 54.7^\circ$  with detector axis. The TOF profiles were analysed as described in our earlier section. The predicted TOF profiles are calculated, convoluted with the instrumental response function. The final calculated TOF profiles are displayed by the red solid line, whereas the circles are the experimental data. Figure 6.2 clearly shows that the obtained TOF profiles were fitted with only one set of fitting parameters. However, it does not necessarily mean that only one channel is occurring in the photodissociation process for the Cl/Cl\* formation process. Similar results were obtained in our previous studies on the photodissociation of heterocyclic compounds. The multi-channel formation route

combined with broader energy distribution can lead to the situation like above, where only one set of parameter is sufficient to fit the translational energy distribution. Details will be discussed in later section. For both the compounds studied, the photofragment translational energy distributions,  $P(E_T)$ , for Cl and Cl\* are determined from the data and shown in the figure 6.3. The average translational energies of the Cl and Cl\* channels are  $6.0 \pm 1.2$  and  $7.0 \pm 1.5$  kcal/mol, respectively for 2,4,6-trichloropyrimidine. Similarly, for 5-chloro-2,4,6-trifluoropyrimidine the average translational energies of the Cl and Cl\* channels are determined to be  $6.5 \pm 1.2$  and  $7.9 \pm 1.6$  kcal/mol, respectively. Since, the TOF profiles for Cl and Cl\* are independent of laser polarizations, the  $\beta$  parameter is well characterized by a value of  $\sim 0$ , within the experimental uncertainties.



**Figure 6.3.** Centre-of-mass recoil translational energy distribution derived from figure 6.2 for Cl ( $^2P_{3/2}$ ) and Cl\* ( $^2P_{1/2}$ ), produced in the photodissociation of (A) 2,4,6-trichloropyrimidine and (B) 5-chloro-2,4,6-trifluoropyrimidine at 235 nm.

## 6.6 Discussion

### 6.6.1 Absorption spectra and electronic transitions at 235 nm

The absorption spectra of 2,4,6-trichloropyrimidine and 5-chloro-2,4,6-trifluoropyrimidine are shown in figure 6.1. For 2,4,6-trichloropyrimidine, the onset of absorption is  $\sim 280$  nm which extends up to 232 nm with absorption maximum at  $\sim 260$  nm (4.77 eV). It shows a second hump at  $\sim 212$  nm (5.85 eV). The absorption spectrum measured matches very well with the spectrum in the literature. For 5-chloro-2,4,6-trifluoropyrimidine, the absorption starts at  $\sim 260$  nm with maximum at  $\sim 243$  nm (5.10 eV). The second peak is at  $\sim 205$  nm (6.05 eV). The first absorption band ( $\sim 260$ nm) of 2,4,6-trichloropyrimidine is  $\sim 17$  nm red shifted as compared to 5-chloro-2,4,6-trifluoropyrimidine. To understand various electronic transitions responsible for the absorption spectra, we have calculated vertical excitation energies for various transitions using EOM-CCSD method maintaining the  $C_{2v}$  geometry for both the molecules. Although the calculated vertical transition energies slightly differ as compared to the experimental results, the nature of transitions and that of the orbitals involved are accurately predicted, using this method [73]. The EOM-CCSD method is often regarded as the best compromise between accuracy and computational cost for medium-sized molecules. Various singlet excited states arising from different electronic transitions are listed in table 6.1. For both these molecules, the valence states are primarily due to excitations from the  $\pi$  orbitals, mostly, HOMO and HOMO-1 to  $\pi^*$  orbitals which are mostly, LUMO. The other valence states, such as  $n\pi^*$  states, arise from the participation of nonbonding electrons of N and Cl ( $n_{N,Cl}$ ). Few other valence states, such as,  $\pi\sigma^*$  states, also arise in these halogenated pyrimidines. The orbitals participating in the different electronic transitions were visualized using suitable visualization program for better understanding of the process and are given in figure 6.4.

## Photodissociation Dynamics of Halogenated Pyrimidines at 235 nm

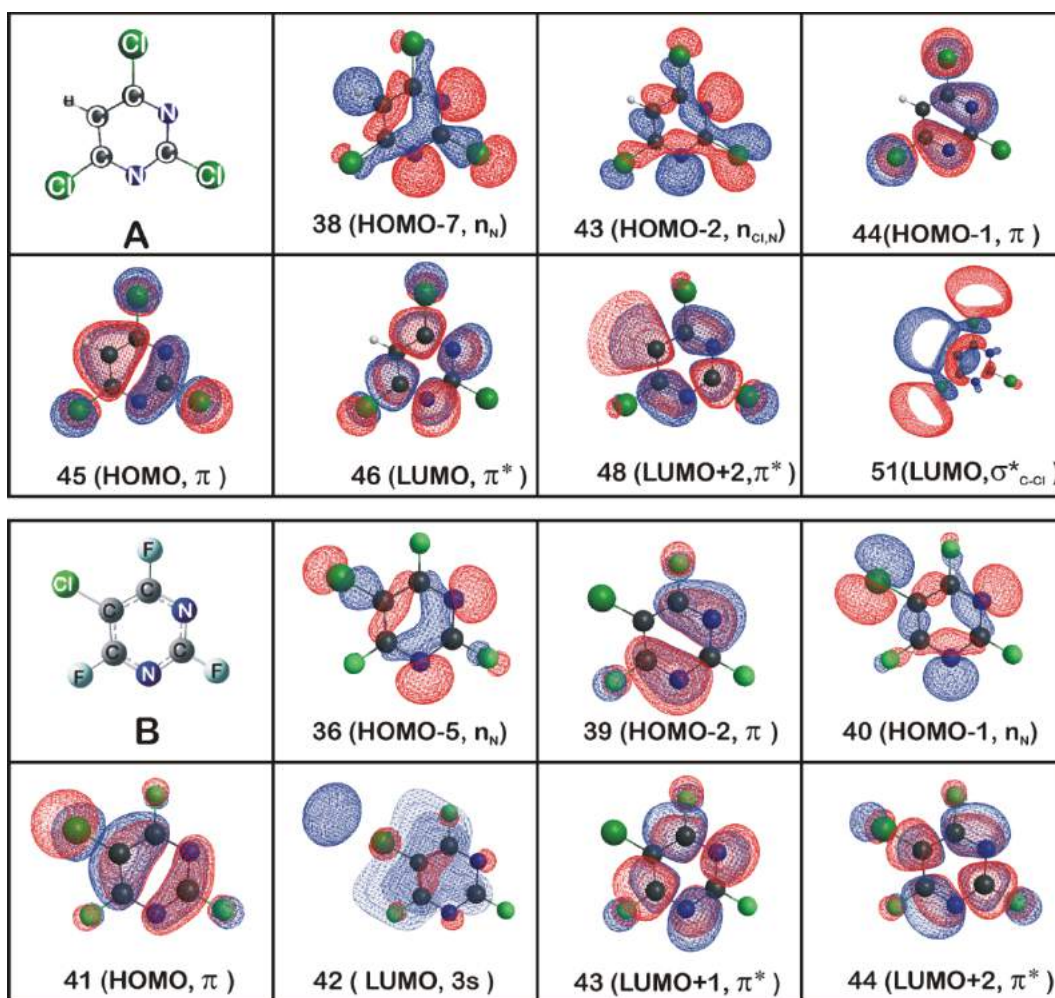
**Table 6.1** Vertical excitation energies and oscillator strengths (given in parentheses) of low-lying singlet states of 2,4,6-trichloropyrimidine and 5-chloro-2,4,6-trifluoropyrimidine with respective state designation calculated using EOM-CCSD. The  $C_{2v}$  symmetry designation, nature of transition and MOs involved in the transitions are also included in the table.

2,4,6-trichloropyrimidine			5-chloro-2,4,6-trifluoropyrimidine	
EOMCCSD/6-31+g(d)			EOMCCSD/6-31+g(d)	
Excited state	State designation and nature of transition	Vertical excitation energy (oscillator strength)	State designation and nature of transition	Vertical excitation energy (oscillator strength)
S <sub>1</sub>	1 <sup>1</sup> B <sub>1</sub> 43 → 46 n <sub>Cl,N</sub> → π*	5.16 eV (0.0067)	1 <sup>1</sup> B <sub>2</sub> 41 → 43 π → π*	5.47 eV (0.0447)
S <sub>2</sub>	1 <sup>1</sup> B <sub>2</sub> 44 → 48 π,n <sub>Cl</sub> → π*	5.16 eV (0.0534)	1 <sup>1</sup> B <sub>1</sub> 40 → 43 n <sub>N,Cl</sub> → π*	5.88 eV (0.0060)
S <sub>3</sub>	1 <sup>1</sup> A <sub>2</sub> 43 → 48 n <sub>Cl,N</sub> → π*	5.44 eV (0.0000)	1 <sup>1</sup> A <sub>2</sub> 40 → 44 n <sub>N,Cl</sub> → π*	6.19 eV (0.0000)
S <sub>4</sub>	2 <sup>1</sup> A <sub>1</sub> 45 → 48 π → π*	6.31 eV (0.0780)	2 <sup>1</sup> A <sub>1</sub> 41 → 44 π → π*	6.65 eV (0.2355)
S <sub>5</sub>	2 <sup>1</sup> A <sub>2</sub> 38 → 46 n <sub>N</sub> → π*	6.81 eV (0.000)	2 <sup>1</sup> B <sub>1</sub> 41 → 42 π → 3s	6.89 eV (0.0001)
S <sub>6</sub>	3 <sup>1</sup> A <sub>1</sub> 44 → 46 π,n <sub>Cl</sub> → π*	6.91 eV (0.5015)	3 <sup>1</sup> B <sub>1</sub> 41 → 42 π → 3s	7.39 eV (0.0005)
S <sub>7</sub>	2 <sup>1</sup> B <sub>2</sub> 44 → 48 π,n <sub>Cl</sub> → π*	7.02 eV (0.6122)	2 <sup>1</sup> A <sub>2</sub> 36 → 43 n <sub>N,Cl</sub> → π*	7.82 eV (0.0000)
S <sub>8</sub>	2 <sup>1</sup> B <sub>1</sub> 45 → 51 π → σ* <sub>C-Cl</sub>	7.36 eV (0.0005)	3 <sup>1</sup> A <sub>1</sub> 39 → 43 π → π*	7.87 eV (0.3671)

For 2,4,6-trichloropyrimidine, the first excited state, 1<sup>1</sup>B<sub>1</sub>, is a ππ\* state with oscillator strength of 0.0067 at 5.16 eV. Similarly, the vertical excitation energy for second excited state, 1<sup>1</sup>B<sub>2</sub> (S<sub>2</sub>) arising from a π\*←π transition, is 5.16 eV (~240 nm) with oscillator strength of 0.0534. For ππ\* state (S<sub>2</sub>), the calculated value is slightly overestimated using this method as compared with the experimental value of λ<sub>max</sub>=4.77 eV (260 nm, see spectrum, figure 6.1). Similarly, the second π\*←π transition leads to the formation of S<sub>4</sub> state (2<sup>1</sup>A<sub>1</sub>), whose vertical excitation energy calculated to be 6.31 eV(~196nm) with



oscillator strength of 0.0780. Here also, the calculated value is overestimated as compared to experimental value of  $\lambda_{\max}=5.85$  eV (212 nm).



**Figure 6.4:** Computed HOMO, LUMO, along with other MOs involved in the transition of (A) 2,4,6-trichloropyrimidine and (B) 5-chloro-2,4,6-trifluoropyrimidine

However, it should be noted that the difference between calculated value and experimental value is almost similar for both the  $\pi\pi^*$  states. Contrary to halogenated pyrimidines [5], the  $\pi\sigma^*$  ( $S_8$ ) state in the present case lie very high in energy. This situation suggests that these states do not play important role in the photodissociation process in the vicinity of Franck-Condon region.

In case of 5-chloro-2,4,6-trifluoropyrimidine, as mentioned earlier, the absorption starts at  $\sim 260$  nm with  $\lambda_{\max}=243$ nm (5.10 eV). Similarly, the second peak appears with  $\lambda_{\max}=205$  nm (6.05 eV). These observed peaks with high oscillator strength are generally

$\pi\pi^*$  states resulting from optically allowed transitions. Hence, we will compare the calculated vertical excitation energies of various  $\pi\pi^*$  states only. The first singlet excited state ( $S_1$ ) is  $1^1B_2$ , which arises from the  $\pi^*\leftarrow\pi$  transition at 5.47 eV ( $\sim 227$  nm) with oscillator strength of 0.0447. In this case also the calculated value is slightly higher than the experimental value of 5.10 eV (243 nm). Similarly, the vertical excitation energy of another state ( $2^1A_1$ ,  $S_4$ ) arising from  $\pi^*\leftarrow\pi$  transition is 6.65 eV ( $\sim 186$  nm) with oscillator strength of 0.2355. For this state also the calculated value is slightly higher than the experimental value of 6.05 eV (205 nm). The  $\pi\pi^*$  states for this molecule are namely,  $S_2$  and  $S_3$ , designated as  $1^1B_1$  and  $1^1A_2$  with oscillator strength of 0.0060 and 0.0000 respectively. Similar to 2,4,6-trichloropyrimidine, the  $\pi\sigma^*$  states lie very high in energy. The perfluoro effect for the lowering of  $\pi\sigma^*$  state observed in benzene and pyridine. However, the same for the heterocyclic molecule with two nitrogen atoms in the ring is not reported up to our knowledge. In the case of 2,4,6-trichloropyrimidine and 5-chloro-2,4,6-trifluoropyrimidine the presence of two nitrogen atoms gives rise to various  $\pi\pi^*$  states which increases the  $\pi\sigma^*$  state to higher energy.

Considering the excitation wavelength of 235 nm and the calculated vertical excitation energies, oscillator strengths of the respective transitions, it is evident that at 235 nm, both molecules are excited to a  $\pi\pi^*$  state. Since, these  $\pi\pi^*$  excited states are basically bound states and adiabatically correlates only with highly excited photoproducts, curve crossing phenomena play a major role in the photodissociation of these molecules which will be discussed in following section.

### 6.6.2 Translational energy release and the dissociation mechanism

The photoexcitation of 2,4,6-trichloropyrimidine and 5-chloro-2,4,6-trifluoropyrimidine at 235 nm ( $\sim 122$  kcal/mol) generates Cl atom with absorption of one photon. For both the molecules, C-Cl bond dissociation energy was calculated to be  $\sim 93$

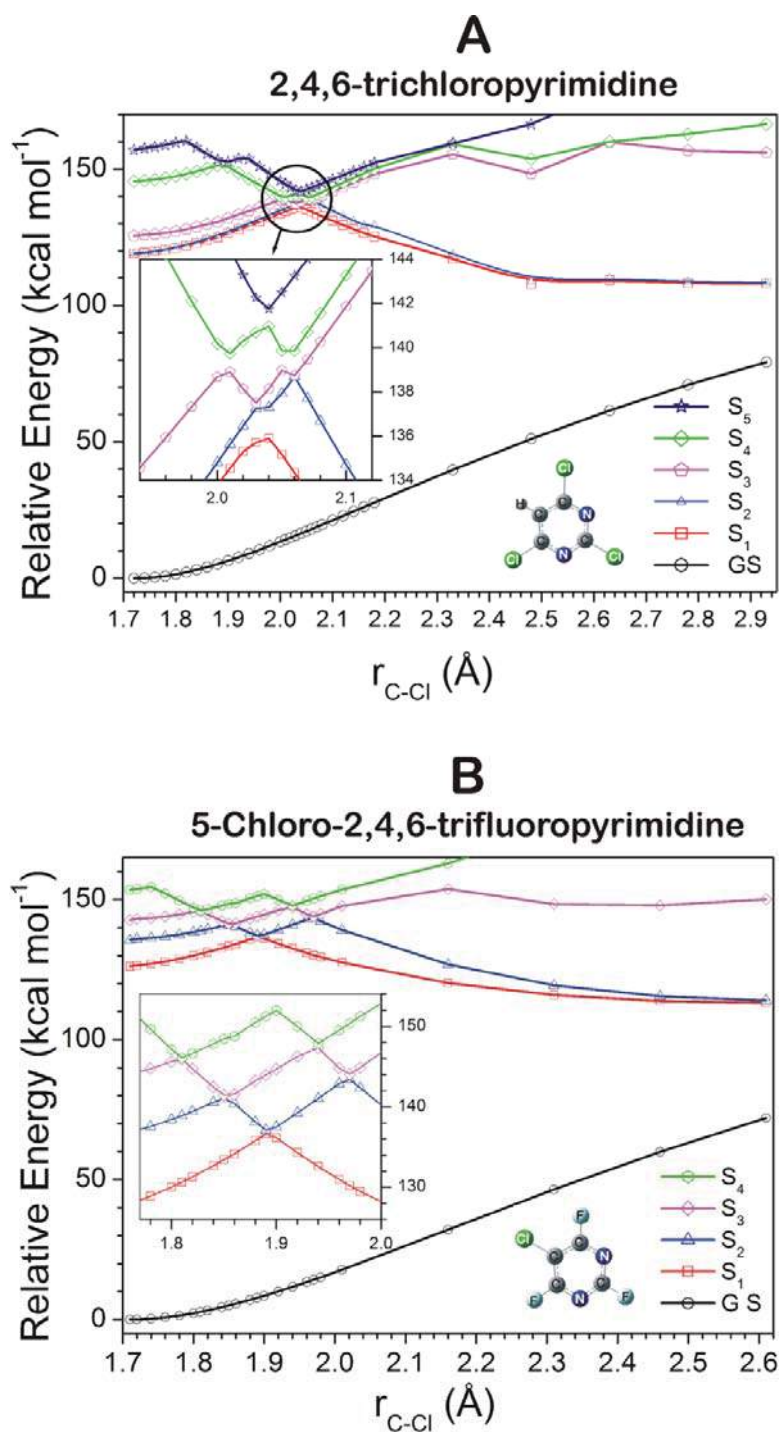
kcal/mol at G3 level of theory. The G3 level of theory is very accurate, and calculates  $\Delta H_{298}^0$  within an error of  $\sim 1$  kcal/mol, especially for halogenated heterocyclic compounds [68]. For the C-Cl bond cleavage reaction, the available energy,  $E_{\text{avail}}$ , which is defined as  $E_{\text{photon}} - \Delta H$ , comes out to be 29.0(26.6) kcal/mol for the Cl(Cl\*) atom formation channel. The various other channels generating the Cl atom apart from the simple C-Cl bond cleavage are also considered. Our studies shows that the lowest energy channel for the Cl atom formation mechanism on the ground state is the direct cleavage of C-Cl bond and this is the only channel responsible for the generation of Cl atom. However, the C-Cl bond cleavage process may occur from the excited state also which we will be discussing in the following paragraph.

In both the cases, 2,4,6-trichloropyrimidine and 5-chloro-2,4,6-trifluoropyrimidine, the  $P(E_T)$  for Cl/Cl\* formation channel was well described by one component only and the translational energy peaks near origin indicating a statistical type of distribution. Various simple models such as impulsive and statistical model are often used to understand the partitioning of the available energy into various degrees of freedom of the fragments. It is well known that the partitioning of energy is mainly governed by the nature of the dissociative potential energy surface (PES), and can be predicted using above models. Mostly, the energy partitioning during the dissociative event on a repulsive surface is well described by an impulsive model [22]. In this model, the distribution of energy among the product states is governed by the repulsive force along the breaking bond of the parent molecule into the fragments. In this model, the amount of the available energy ( $E_{\text{avail}}$ ) released as translational energy is given by  $E_T = \left( \frac{\mu_{\text{C-Cl}}}{\mu_{\text{Prd-Cl}}} \right) E_{\text{avail}}$ , where  $\mu_{\text{C-Cl}}$  is the reduced mass of the C and Cl atoms,  $\mu_{\text{(Prd)-Cl}}$  is the reduced mass of the pyrimidine radical and Cl. The  $E_{\text{avail}}$  in the present case is  $\sim 29$  kcal/mol. The fraction of the available energy going into the translational modes of the fragments is given by  $f_T = E_T/E_{\text{avail}}$ ,

which is ratio of reduced mass. In the case of 2,4,6-trichloropyrimidine and 5-chloro-2,4,6-trifluoropyrimidine, the ratio of the reduced masses is 0.32 and 0.32 respectively. The experimental average translational energies ( $E_T$ ) for the Cl and Cl\* in the case 2,4,6-trichloropyrimidine are found to be  $6.0 \pm 1.2$  and  $7.0 \pm 1.5$  kcal/mol, respectively, giving the  $f_T$  values of 0.20 and 0.26. Similarly, the  $E_T$  values for the Cl and Cl\* in the case of 5-chloro-2,4,6-trifluoropyrimidine are found to be  $6.5 \pm 1.2$  and  $7.9 \pm 1.6$  kcal/mol, respectively, giving the  $f_T$  values of 0.22 and 0.29. The experimentally determined  $f_T$  values for Cl atom elimination channel are lower, while that for Cl\* atom elimination channel are very close to impulsive model in both the cases.

However, for a dissociation process from the ground electronic state after rapid internal conversion from the initially prepared excited state, the excess energy is partitioned statistically amongst the available degrees of freedom of the products. Under these circumstances, a relatively small amount of the excess energy is partitioned into translational motion of the products especially in a large molecule with many low frequency modes. For this kind of dissociation process, a priori calculations are generally adopted [94,136], along with a simple analytical expression established by Klots [21], relating the mean translational energy release,  $E_T$ , and the  $E_{\text{avail}}$ , for a statistical barrierless dissociation process. These simple calculations give a  $f_T$  value of  $\sim 0.04$ . However, the experimental  $f_T$  values are higher than the statistical model. The above discussion clearly indicates that the dissociation is occurring from various PESs including excited states. To further investigate, we have mapped PESs for various excited states for the Cl atom elimination channel using EOM-CCSD method for both the molecules. For this purpose, EOM-CCSD calculations on different C–Cl bond lengths were performed using 6-31+g\* basis sets on the ground state geometries which were optimized at MP2/6-31+g\* level of theory. For this purpose, the C–Cl bond lengths were varied from 1.7Å to 2.8Å, which is

asymptote to dissociation limit. Figure 6.5 shows the results obtained from such studies for both the molecules. As discussed earlier (table 6.1), for 2,4,6-trichloropyrimidine, the first five excited states are bound states which mainly  $\pi\pi^*$  and  $n\pi^*$  states. The dissociation from these states is not possible considering the energy of the excitation.



**Figure 6.5:** Various adiabatic potential energy curves calculated for (A) 2,4,6-trichloropyrimidine and (B) 5-chloro-2,4,6-trifluoropyrimidine along the C-Cl bond length with the other geometrical parameters optimized for the ground state using MP2 method.

Hence, these bound states must cross to dissociative states, such as  $\sigma^*$  states, for the dissociation to occur. Similarly, for 5-chloro-2,4,6-trifluoropyrimidine, the first four states are bound states such as  $\pi\pi^*$  and  $n\pi^*$  states. From figure 6.5, it is evident that the crossing between  $\pi\pi^*/n\pi^*$  states to  $\sigma^*$  state is at 2.04 Å and 1.89 Å for 2,4,6-trichloropyrimidine and 5-chloro-2,4,6-trifluoropyrimidine, respectively. The location of crossing between the  $\pi\pi^*/n\pi^*$  states to  $\sigma^*$  state determine the depth of the respective bound state and indirectly the lifetime of the state. For 2,4,6-trichloropyrimidine and 5-chloro-2,4,6-trifluoropyrimidine, the depth of the  $\pi\pi^*$  state is ~16 and ~10 kcal/mol, respectively. This clearly indicates that the lifetime of  $\pi\pi^*$  state in 2,4,6-trichloropyrimidine is more and so is the probability of internal conversion to the ground state. Hence, the dissociation from the ground state is more significant in case of 2,4,6-trichloropyrimidine, which is clearly visible in the translational energy distribution. Besides, it is well known in the literature that the internal conversion process is important in nitrogen containing heterocyclic compound due to vibronic coupling between the  $\pi\pi^*$  and  $n\pi^*$  state [168]. However, the experimental  $E_T$  values for both the molecules are more than the value predicted by a statistical model. Even though the experimentally obtained TOF profiles are well described by single component, it does not necessarily mean that Cl atom formation is through one channel only. It may be due to the broad energy distribution of each channel. This clearly indicates that the dissociation from the excited state can't be ruled out. For dissociation to occur from the excited state, the initially prepared  $\pi\pi^*$  state must cross to the nearby  $\pi\sigma^*$  state. As mentioned earlier, the cross over point lies at ~136 kcal/mol at EOM-CCSD level of theory. Considering the difference between the calculated and experimental  $\lambda_{\max}$  value for the  $\pi\pi^*$  state which is ~10 kcal/mol, the crossover is not possible at ~122 kcal/mol (235 nm excitation) of energy. However, the initially prepared  $\pi\pi^*$  state may crossover to nearby excited triplet

states from where the dissociation may occur imparting a large amount of energy into the translational mode. It is well known in the literature that singlet-triplet radiationless transition is favourable in nitrogen containing heterocyclic compounds due to effective spin-orbit coupling interaction between singlet and triplet states [152,169]. In pyrimidine, the rate constant of intersystem crossing from  $S_1, S_2 \rightarrow T_1$  is reported as  $1.2 \times 10^8 \text{ s}^{-1}$  where as the intersystem crossing from  $T_1 \rightarrow S_0$  is almost zero [169]. It infers that if molecule is relaxed to  $T_1$  state, the probability of internal conversion to ground state is almost negligible. In this situation, the dissociation from the  $T_1$  state is the most favorable pathway. To further investigate the role of triplet state in the photodissociation process, we have mapped out the various potential energy surfaces of the triplet state also. The study clearly shows a barrier in the triplet state ( $T_1$ ) which is a  ${}^3\pi\pi^*$  state, much below the available energy of 122 kcal/mol, for the dissociation process. The dissociation from the excited triplet state leads to higher amount of translational energy released into the photoproduct which matches with experimental findings. The recoil anisotropy,  $\beta$ , for the Cl atom fragments measured in the present work is  $\sim 0$ , which indicates an isotropic dissociation process. Due to several intersystem crossing and multiple channels for the formation of Cl atom, the product angular distribution becomes isotropic.

## 6.7 Conclusion

In summary, the  $\text{Cl}({}^2\text{P}_j)$  atom formation in the photodissociation of two halogenated pyrimidines, namely, 2,4,6-trichloropyrimidine and 5-chloro-2,4,6-trifluoropyrimidine have been investigated at around 235 nm. The study was carried out using resonance enhanced multiphoton ionization, coupled with a time-of-flight mass spectrometer in conjunction with the computational studies such as EOM-CCSD method. Both the molecules are excited in their  $\pi\pi^*$  state at 235 nm. The dynamics of chlorine atom elimination channels were studied by determining the total translational energy

distribution, the anisotropy parameter,  $\beta$ , and the spin-orbit branching ratio. Polarization-dependent and state-specific TOF profiles were analyzed to determine the translational energy distributions for the chlorine atom elimination channel employing a forward convolution method and taking into account the fragment anisotropies. The translational energy distributions for the chlorine atom elimination channel was best described by only one component. The anisotropy parameters for both Cl and Cl\* was found to be  $\sim 0$  within experimental error. For 2,4,6-trichloropyrimidine, the average translational energy released into the Cl and Cl\* channels are determined to be  $6.0 \pm 1.2$  and  $7.0 \pm 1.5$  kcal/mol, respectively. Similarly, for 5-chloro-2,4,6-trifluoropyrimidine, the average translational energy imparted into the Cl and Cl\* channels are  $6.5 \pm 1.2$  and  $7.9 \pm 1.6$  kcal/mol, respectively. The relative quantum yields of Cl and Cl\* for both the molecules are similar and statistical in nature. The energy partitioning into the translational modes is interpreted with the help of various models, such as impulsive and statistical models. The nature of translational energy distribution, a zero value of anisotropy parameter and the average translational energy for the dissociation process suggest that major path for the Cl atom formation is through ground state dissociation. A minor channel arising from dissociation of the excited state, probably a triplet state, is also suggested. The PESs constructed using EOM-CCSD method for the ground and excited states along the dissociation coordinate of the Cl atom from the equilibrium ground state geometry suggest the role of triplet excited state in the photodissociation process. During the course of experiments, the absorption spectra for both the compounds studied were also obtained.



# Chapter 7

## Summary and Future Direction

---

The current thesis presents detailed studies on halogen atom (Cl and Br) formation dynamics in the UV photodissociation of five and six membered halogenated heterocyclic molecules with one to three hetero atoms, namely, N and S atoms in the ring. It is well known in the literature that the photodissociation of halogen containing molecules in the UV range generates halogen atoms which are detrimental for the ozone layer in the stratosphere[9]. Also, the presence of hetero atom introduces extra  $n\pi^*$  excited states, which are not present in similar homocyclic molecules like benzene. This situation opens up interesting excited state dynamics, e.g. radiationless transitions, vibronic and spin-orbit coupling, etc., to be studied in detail. I have undertaken this study to understand the dynamics of halogen atom formation in the photodissociation process of these compounds and also the effect of hetero atom on excited state dynamics of these heterocyclic molecules. In addition, the effect of fluorine atom substitution on the dynamics was also investigated. The MB-REMPI-TOF-MS technique was employed to detect the nascent halogen atom photofragments under collisionless conditions to obtain the dynamical information. The dynamics involved in the photodissociation process is deduced by translational energy distribution and anisotropy parameter obtained from polarization dependent time-of-flight (TOF) profiles. The mechanism of the photodissociation process has been proposed based on experimental results with the aid of computational calculations. This concluding chapter summarizes the results obtained from the

## Summary and Future Direction

experimental work and computational calculations carried out. It also includes the future directions which will give more insight into the dynamics of photodissociation processes.

The first chapter gives introduction about photodissociation dynamics, in general, and its importance. The photodissociation process is initiated with the absorption of a photon by a molecule. One of the significant processes after excitation is photodissociation of the molecule forming various photofragments. The photodissociation process can be from various electronic states depending on the overall dynamics of the process. Various theoretical models have been also used to understand the translational energy distributions which are useful to describe the dissociation process. Different vector correlations arising during the photodissociation process are also studied. The theoretical calculations were employed to interpret the experimental results. Therefore, a brief note on the computational chemistry and method employed was also explained in this thesis.

The second chapter describes experimental technique and the instrumentation employed to execute the work. The analysis procedure to obtain the dynamic parameters, namely translational energy distribution and anisotropy parameter from the experimental TOF profiles is discussed in detail.

The third chapter gives the details on photodissociation of 3,4-dichloro-1,2,5-thiadiazole. Cl atom formation dynamics was studied after exciting the molecule at 235 nm. The TOF profiles of Cl and Cl\* were independent of laser polarization and well described by single velocity component. The experimentally determined  $f_T$  value for Cl elimination channel was found to be considerably lower than the value predicted by using the impulsive model. The vertical excitation energy calculations were performed to get more insight into the photodissociation mechanism. The excitation at 235 nm prepares the molecule in  $\pi\pi^*$  state which is a bound state. The first repulsive state has repulsive nature along both C–Cl and N–S bond. Therefore, the PESs were generated along the C–Cl and

## Summary and Future Direction

N–S bond. These calculations suggested that, the N–S bond dissociation is more favourable compared to the C–Cl bond from both ground and excited state. From the experimental results and PESs it was concluded that C–Cl bond dissociation takes place from the excited state after crossing from the initially prepared  $\pi\pi^*$  to repulsive  $\pi\sigma^*_{\text{N-S, C-Cl}}$  and from ground state after internal conversion.

The ground state dissociation of 3,4-dichloro-1,2,5-thiadiazole was also studied at different UV excitations and the photoproducts were identified using absorption and emission spectroscopy. The photoproducts, namely, CN and Cl<sub>2</sub> were detected using emission and absorption method respectively. The absorption features of NC–C(Cl<sub>2</sub>)–N=S isomer were also observed in the absorption spectra, after photolysis at 235 nm. The possible mechanism for CN and Cl<sub>2</sub> formation is proposed.

In chapter 4, two halogenated pyridines, namely, 3-chloropyridine (ClPy) and 3-chloro-2,4,5,6-tetrafluoropyridine (ClFPy), were chosen to study their photodissociation dynamics forming Cl atom. The effect of fluorine atom on C–Cl bond dissociation dynamics was also studied. It was observed that the higher average translational energy released into the chlorine atom elimination channel in ClFPy compared to ClPy. The experimentally determined  $f_T$  value slightly deviates from the impulsive model in case of ClPy. However, in case of ClFPy, experimentally determined  $f_T$  value perfectly match with the value predicted using the impulsive model. The change in dynamics with fluorine substitution was explained with the help of computational studies. The fluorine substitution lowers the energy of  $\pi\sigma^*$  state which facilitates the crossover from  $\pi\pi^*$  state to nearby  $\pi\sigma^*$  state in case of ClFPy.

The chapter 5 gives the details on C–Br bond dissociation dynamics of 4-bromo-2,3,5,6-tetrafluoropyridine at around 234 nm. The translational energy distribution was well described by two components, namely, fast and slow. The TOF profiles were

## Summary and Future Direction

dependent on the laser polarization, which indicates the non-zero anisotropy parameter with a value of  $0.6 \pm 0.05$ . A positive and non-zero anisotropy parameter indicates that the dissociation is faster than the rotational time period of the molecule. The experimentally obtained  $f_T$  values for Br and Br\* elimination channels were considerably higher than the value calculated using the impulsive model. This indicates that dissociation occurs from the excited state PES with a barrier. To further elucidate this hypothesis, PESs of various excited state for the Br atom elimination channel were generated employing TD-DFT and MCQDPT2 method. From the experimental results and the calculated PESs, it was proposed that, excitation at 234 nm prepares the molecule in  $\pi\pi^*$  state. It is bound in nature and adiabatically correlates only with highly excited photoproducts, which is not feasible in a single-photon excitation in the present case. However, experimentally obtained higher  $f_T$  values for Br atom elimination channel with a non-zero anisotropy parameter indicates that there must be an avoided crossing of  $\pi\pi^*$  with the repulsive  $\pi\sigma^*$  state. Whereas, the lower  $f_T$  values for Br atom elimination channel indicates that the dissociation takes place from the ground state after internal conversion from the initially excited state.

In chapter 6, photodissociation dynamics of halogenated heterocyclic molecules containing two nitrogen atoms in the ring, namely 2,4,6-trichloropyrimidine and 5-chloro-2,4,6-trifluoropyrimidine, were presented. In both these molecules, TOF profiles were well described by single velocity component and independent of laser polarization, which indicated zero value of anisotropy parameter, within the experimental uncertainty. To get more insight into the dissociation mechanism, PESs were generated along the C–Cl bond employing EOM-CCSD method. For both of these molecules, excitation at 235 nm prepares the molecule in  $\pi\pi^*$  state. The crossover point from bound  $\pi\pi^*$  state to repulsive state is much higher in energy compare to the photon energy. Therefore, the dissociation

## Summary and Future Direction

from the singlet  $\pi\sigma^*/n\sigma^*$  was not possible channel in this case. However, experimentally obtained  $f_T$  values are higher than the statistical model which indicates that role of excited state PES. It has been suggested that the triplet state may play a crucial role in the dissociation process. Therefore, triplet state PESs were also generated employing same method. The crossover from  $^1\pi\pi^*$  to  $^3\pi\sigma^*$  was within the photon energy. Hence, in both these molecules initial excited state undergo intersystem crossing to triplet state from where the Cl atom formation take place. For these molecules, initial excited state is a bound state, thus the molecule can undergo internal conversion to ground state, and it can also leads to C–Cl bond dissociation from ground state.

As far the work presented in this thesis, a single laser beam was used for both photodissociation of parent molecule and detection of the photofragments. To get detailed information about the excited PESs and their interactions, different excited states of the molecules should be populated. This can be done by exciting the molecule at different frequencies of pump laser and detecting the photofragments with probe laser. Moreover, a velocity map imaging (VMI) can be used to improve the resolution in the translational energy distribution measurements which can indirectly gives internal energy distribution of the counterpart photofragments. The work presented in this thesis also discusses the fluorine atom substitution effect on the photodissociation processes. Other substitutions like methyl group and iodine atom may also change the dynamics dramatically by facilitating the intersystem crossing (ISC). The internal rotation of methyl group plays an important role in inducing the intersystem crossing. As iodine is a heavy atom, its substitution in the heterocyclic molecule can also increase the intersystem crossing process.



## References

- (1) L. J. Butler, D. M. Neumark, Photodissociation Dynamics *J. Phys. Chem.* 100 (1996) 12801
- (2) W. C. Wiley, I. H. McLaren, Time-of-Flight Mass Spectrometer with Improved Resolution *Rev. Sci. Instrum.* 26 (1955) 1150
- (3) D. Srinivas, H. P. Upadhyaya, Dynamics of Cl(<sup>2</sup>P<sub>j</sub>) Formation in the Photodissociation of Halogenated Thiadiazole at 235 nm: A Resonance Enhanced Multiphoton Ionization – Time of Flight (REMPI–TOF) study *J. Photochem. Photobiol., A* 322 (2016) 41
- (4) D. Srinivas, H. P. Upadhyaya, Ground State Dissociation Pathways for 3,4-dichloro-1,2,5-thiadiazole: Spectroscopic Observation and Fate of NC-C(Cl<sub>2</sub>)-N=S isomer *Chem. Phys. Lett.* 660 (2016) 182
- (5) D. Srinivas, H. P. Upadhyaya, Chlorine atom formation dynamics in the dissociation of halogenated pyridines after photoexcitation at 235 nm: A resonance enhanced multiphoton ionization-time of flight (REMPI-TOF) study *Chem. Phys.* 472 (2016) 208
- (6) D. Srinivas, Y. Sajeev, H. P. Upadhyaya, Resonance enhanced multiphoton ionization-time of flight (REMPI-TOF) detection of Br (<sup>2</sup>P<sub>j</sub>) atoms in the photodissociation of 4-bromo-2,3,5,6-tetrafluoropyridine at 234 nm: Effect of low-lying πσ\* states *J. Photochem. Photobiol., A* 345 (2017) 1
- (7) R. Schinke: *Photodissociation Dynamics*, Cambridge University press, 2006.
- (8) M. N. R. Ashfold, J. E. Baggott: *Molecular Photodissociation Dynamics*, Royal Society of Chemistry, 1987.
- (9) J. B. Burkholder, R. A. Cox, A. R. Ravishankara, Atmospheric Degradation of Ozone Depleting Substances, Their Substitutes, and Related Species *Chem. Rev.* 115 (2015) 3704
- (10) O. C. Zafiriou, Photochemistry of Halogens in the Marine Atmosphere *J. Geophys. Res.* 79 (1974) 2730
- (11) J. M. Hollas: *Modern Spectroscopy*, Wiley, 2013.
- (12) W. M. McClain, Two-Photon Molecular Spectroscopy *Acc. Chem. Res.* 7 (1974) 129
- (13) L. G. Christophorou: *Electron-molecule interactions and their applications*, Academic Press, 2010.
- (14) H. Sato, Photodissociation of Simple Molecules in the Gas Phase *Chem. Rev.* 101 (2001) 2687
- (15) P. Felder, Photofragment Translational Spectroscopy *Chimia* 48 (1994) 43
- (16) R. N. Zare, P. J. Dagdigian, Tunable Laser Fluorescence Method for Product State Analysis *Science* 185 (1974) 739
- (17) G. Radhakrishnan, D. NG, R. C. Estler, Multiphoton Ionization Detection of Photodissociation Fragments: NO From NO<sub>2</sub> *Chem. Phys. Lett.* 84 (1981) 260
- (18) D. W. Chandler, P. L. Houston, Two-dimensional Imaging of State-selected Photodissociation Products Detected by Multiphoton Ionization *J. Chem. Phys.* 87 (1987) 1445
- (19) A. M. Zheltikov, Coherent Anti-Stokes Raman Scattering: from Proof-of-the-principle Experiments to Femtosecond CARS and Higher Order Wave-mixing Generalizations *J. Raman Spectrosc.* 31 (2000) 653
- (20) M. D. Wheeler, S. M. Newman, A. J. Orr-Ewing, M. N. R. Ashfold, Cavity Ring-down Spectroscopy *J. Chem. Soc., Faraday Trans.,* 94 (1998) 337

## Reference

- (21) C. E. Klots, Thermochemical and kinetic information from metastable decompositions of ions *J. Chem. Phys.* 58 (1973) 5364
- (22) A. F. Tuck, Molecular Beam Studies of Ethyl Nitrite Photodissociation *J. Chem. Soc., Faraday Trans. 2* 73 (1977) 689
- (23) S. W. North, D. A. Blank, J. D. Gezelter, C. A. Longfellow, Y. T. Lee, Evidence for Stepwise Dissociation Dynamics in Acetone at 248 and 193 nm *J. Chem. Phys.* 102 (1995) 4447
- (24) R. Liyanage, Y. A. Yang, S. Hashimoto, R. Gordon, R. W. Field, Electronic control of the spin-orbit branching ratio in the photodissociation and predissociation of HCl *J. Chem. Phys.* 103 (1995) 6811
- (25) G. E. Hall, P. L. Houston, Vector Correlations in Photodissociation Dynamics *Annu. Rev. Phys. Chem.* 40 (1989) 375
- (26) P. L. Houston, Vector correlations in photodissociation dynamics *J. Phys. Chem.* 91 (1987) 5388
- (27) P. Atkins, R. Friedman: *Molecular Quantum Mechanics*, Oxford University press, 2005.
- (28) F. Jensen: *Introduction to Computational Chemistry*, John Wiley & Sons, Ltd, 2007.
- (29) M. J. Frisch, G. W. Trucks, H. B. Schlegel, G. E. Scuseria, M. A. Robb, J. R. Cheeseman, J. J. A. Montgomery, T. Vreven, K. N. Kudin, J. C. Burant, et.al, Gaussian 03, Revision B.04, Gaussian 03, Revision B.04, Gaussian, Inc., Pittsburgh PA, 2003.
- (30) M. W. Schmidt, K. K. Baldridge, J. A. Boatz, S. T. Elbert, M. S. Gordon, J. H. Jensen, S. Koseki, N. Matsunaga, K. A. Nguyen, S. Su, T. L. Windus, M. Dupuis, J. John A. Montgomery, General Atomic and Molecular Electronic Structure System *J. Comput. Chem.* 14 (1993) 1347
- (31) J. G. Anderson, D. W. Toohey, W. H. Brune, Free Radicals within the Antarctic Vortex: The Role of CFCs in Antarctic Ozone Loss *Science* 251 (1991) 39
- (32) J. C. Laube, M. J. Newland, C. Hogan, C. A. M. Brenninkmeijer, P. J. Fraser, P. Martinerie, D. E. Oram, C. E. Reeves, T. Röckmann, J. Schwander, E. Witrant, W. T. Sturges, Newly Detected Ozone-Depleting Substances in the Atmosphere *Nat. Geosci.* 7 (2014) 266
- (33) R. S. Stolarski, R. D. Rundel, Fluorine Photochemistry in the Stratosphere *Geophys. Res. Lett.* 2 (1975) 443
- (34) A. I. Chichinin, Chemical Properties of Electronically Excited Halogen Atoms X ( $^2P_{1/2}$ ) (X=F, Cl, Br, I) *J. Phys. Chem. Ref. Data* 35 (2006) 869
- (35) K. Bergmann, R. T. Carter, G. E. Hall, J. R. Huber, Resonance Enhanced Multiphoton Ionization Time-of-Flight Study of CF<sub>2</sub>I<sub>2</sub> Photodissociation *J. Chem. Phys.* 109 (1998) 474
- (36) W. S. McGivern, R. Li, P. Zou, S. W. North, Photodissociation dynamics of CH<sub>2</sub>BrCl studied using resonance enhanced multiphoton ionization (REMPI) with time-of-flight mass spectrometry *J. Chem. Phys.* 111 (1999) 5771
- (37) A. S. Bracker, E. R. Wouters, A. G. Suits, Y. T. Lee, O. S. Vasylutinskii, Observation of Coherent and Incoherent Dissociation Mechanisms in the Angular Distribution of Atomic Photofragment Alignment *Phys. Rev. Lett.* 80 (1998) 1626
- (38) R. J. Wilson, J. A. Mueller, P. L. Houston, Speed-Dependent Anisotropy Parameters in the UV Photodissociation of Ozone *J. Phys. Chem. A* 101 (1997) 7593
- (39) B. B. Laud: *Laser and Non-linear Optics*, Wiley Eastern Limited, 1993.
- (40) W. Koechner, M. Bass: *Solid-State Laser*, Springer, 1939.



## Reference

- (41) K. G. Bhushan: Introduction to Vacuum Technology, Indian Vacuum Society, 2013.
- (42) R. Schinke: Photodissociation dynamics, John Wiley & Sons Ltd., 1993.
- (43) A. J. R. Heck, D. W. Chandler, Imaging techniques for the study of chemical reaction dynamics *Annu. Rev. Phys. Chem.* 46 (1995) 335
- (44) K.-L. Han, G.-Z. He, Photochemistry of aryl halides: Photodissociation dynamics *J. Photochem. Photobiol. C* 8 (2007) 55
- (45) H. P. Upadhyaya, A. Saha, A. Kumar, T. Bandyopadhyay, P. D. Naik, P. N. Bajaj, Photodissociation Dynamics of Phosphorous Tri-Chloride ( $\text{PCl}_3$ ) at 235 nm Using Resonance Enhanced Multiphoton Ionization (REMPI) with Time-of-Flight (TOF) Mass Spectrometry *J. Phys. Chem. A* 114 (2010) 5271
- (46) M. Kawade, A. Saha, H. P. Upadhyaya, A. Kumar, P. D. Naik, P. N. Bajaj, Dynamics of Cl ( $^2P_j$ ) Atom Formation in the Photodissociation of Fumaryl Chloride ( $\text{ClCO} - \text{CH} = \text{CH} - \text{COCl}$ ) at 235 nm: A Resonance Enhanced Multiphoton Ionization (REMPI) Time-of-Flight (TOF) Study *J. Phys. Chem. A* 115 (2011) 1538
- (47) M. Kawade, A. Saha, H. P. Upadhyaya, A. Kumar, P. D. Naik, P. N. Bajaj, Photodissociation Dynamics of Halogenated Thiophenes at 235 nm: A Resonance Enhanced Multiphoton Ionization-Time-of-Flight (REMPI-TOF) Study *J. Phys. Chem. A* 116 (2012) 10656
- (48) A. Saha, M. Kawade, H. P. Upadhyaya, A. Kumar, P. D. Naik, P. N. Bajaj, Resonance Enhanced Multiphoton Ionization Time-of-Flight (REMPI-TOF) Study of Phosphorous Oxychloride ( $\text{POCl}_3$ ) Dissociation at 235 nm: Dynamics of Cl ( $^2P_j$ ) Formation *Chem. Phys.* 407 (2012) 83
- (49) A. Saha, M. N. Kawade, H. P. Upadhyaya, A. Kumar, P. D. Naik, Photoexcitation of 2-bromo-2-chloro-1,1,1-trifluoroethane (halothane) to repulsive surface  $\pi^*(\text{C}-\text{Br})$  at 234 nm: Dynamics of C-Br and C-Cl bond rupture *Chem. Phys.* 416 (2013) 1
- (50) A. Saha, H. P. Upadhyaya, A. Kumar, P. D. Naik, Resonance Enhanced Multiphoton Ionization Time-of-Flight (REMPI-TOF) Study of Tetrachloroethylene Photodissociation at 235 nm: Role of bound  $\pi - \sigma^*_{\text{C-Cl}}$  state *Chem. Phys.* 428 (2014) 127
- (51) Sr. V. Dobyns, L. Pierce, Microwave spectrum, structure, dipole moment, and quadrupole coupling constants of 1,2,5-thiadiazole *J. Am. Chem. Soc.* (1963) 3553
- (52) O. L. Stiefvater, The Complete Substitution Structure of 1,2,5-Thiadiazole *Z. Naturforsch* 33a (1978) 1511
- (53) J. T. Schirlin, D. A. Wann, S. F. Bone, H. E. Robertson, D. W. H. Rankin, Additivity of ring geometry distortion effects in unsaturated five-membered heterocyclic rings *J. Mol. Struct.* 922 (2009) 103
- (54) F. A. Momany, R. A. Bonham, The structure of 1,2,5-thiadiazole as determined by gas electron diffraction *J. Am. Chem. Soc.* 86 (1964) 162
- (55) M. H. Palmer, The electronic states of 1,2,5-thiadiazole studied by VUV absorption spectroscopy and ab initio configuration interaction methods *Chem. Phys.* 348 (2008) 130
- (56) T. Pasinszki, M. Krebsz, G. Vass, Ground and ionic states of 1,2,5-thiadiazoles: An UV-photoelectron spectroscopic and theoretical study *J. Mol. Struct.* 966 (2010) 85
- (57) E. Firkins, A. W. Richardson, A Non-planar Excited State of 1,2,5-Thiadiazole *Chem. Commun.* (1971) 1368

## Reference

- (58) M. H. Palmer, R. H. Findlay, J. N. A. Ridyard, A. Barrie, P. Swift, The Electronic Structure of Heteroaromatic Molecules; Non-empirical Calculations and Photoelectron Spectra for the Isomeric-Thiazole and -Thiadiazole *J. Mol. Struct.* 39 (1977) 189
- (59) X. Y. Cao, W. Wu, D. Wang, M. F. Ge, D. X. Wang, He I Photoelectron Spectroscopic Study on the Electronic Structure of the Derivatives of 1, 2, 5-thiadiazole *Acta Phys. Chim. Sin. (Wuli Huaxue Xuebao)* 16 (2000) 491
- (60) M. Krebsz, G. Tarczay, T. Pasinszki, Generation and Spectroscopic Identification of CICNS, CINCS and NCCNS *Chem. Eur. J.* 19 (2013) 17201
- (61) M. Krebsz, B. Hajgató, G. Bazsó, G. Tarczay, T. Pasinszki, Structure, Stability, and Generation of CH<sub>3</sub>CNS *Aust. J. Chem.* 63 (2010) 1686
- (62) R. Flammang, P. Gerbaux, E. H. Mørkved, M. W. Wong, C. Wentrup, Generation of New Nitrile N-Sulfides (NCCNS, R<sub>2</sub>NCNS, H<sub>3</sub>CSCNS, and CICNS) as Ions and Neutrals in the Gas Phase: Tandem Mass Spectrometry, Flash Vacuum Pyrolysis, and ab Initio MO Study *J. Phys. Chem.* 100 (1996) 17452
- (63) P. Gerbaux, Y. V. Haverbeke, R. Flammang, M. W. Wong, C. Wentrup, Generation of Nitrile N-Sulfide (RCNS) Radical Cations and Neutrals via Ion-Molecule Reactions: Tandem Mass Spectrometry and ab Initio MO Study *J. Phys. Chem. A* 101 (1997) 6970
- (64) P. A. Koutentis, C. Nicosia, 1,2,5-Thiadiazoles and Related Compounds *Sci. Synth.* 13 (2004) 297
- (65) Y. Cao, M. Zhang, C. Wu, S. Lee, M. E. Wroblewski, T. Whipple, P. I. Nagy, K. Takacs-Novak, A. Balazs, S. Toros, W. S. Messer, Synthesis and biological characterization of 1-methyl-1,2,5,6-tetrahydropyridyl-1,2,5-thiadiazole derivatives as muscarinic agonists for the treatment of neurological disorders *J. Med. Chem.* 46 (2003) 4273
- (66) Y. Hanasaki, K. Tsukuda, H. Watanabe, K. Tsuzuki, M. Murakami, N. Niimi, Thiadiazole derivatives and herbicide compositions containing the same *Eur. Pat. Appl. EP: 90-309183 19900822* (1991)
- (67) A. Merschaert, P. Boquel, H. Gorissen, J.-P. V. Hoeck, A. Borghese, L. Antoine, V. Mancuso, A. Mockel, M. Vanmarsenille, The ring opening of 3,4-dichloro-1,2,5-thiadiazole with metal amides. A new synthesis of 3,4-disubstituted-1,2,5-thiadiazoles *Tetrahedron Lett.* 47 (2006) 8285
- (68) Y. Garcia, F. Schoenebeck, C. Y. Legault, C. A. Merlic, K. N. Houk, Theoretical Bond Dissociation Energies of Halo-Heterocycles: Trends and Relationships to Regioselectivity in Palladium-Catalyzed Cross-Coupling Reactions *J. Am. Chem. Soc.* 131 (2009) 6632
- (69) H. P. Upadhyaya, U. B. Pavanaja, A. V. Sapre, K. V. S. R. Rao, J. P. Mittal, Chemiluminescent reaction of oxygen atoms with some nitrile compounds *Chem. Phys. Lett.* 227 (1994) 511
- (70) J. T. Muckermann, Information Theoretic Prior Functions for Large Molecular Systems *J. Phys. Chem.* 93 (1989) 179
- (71) S. Arulmozhiraja, R. Fukuda, M. Ehara, H. Nakatsuji, Electronic Spectra and Photodissociation of Vinyl Chloride: A Symmetry-Adapted Cluster Configuration Interaction Study *J. Chem. Phys.* 124 (2006) 034312
- (72) A. D. Laurent, D. Jacquemin, TD-DFT Benchmarks: A Review *Int. J. Quantum Chem.* 113 (2013) 2019
- (73) M. Caricato, G. W. Trucks, M. J. Frisch, K. B. Wiberg, Oscillator Strength: How Does TDDFT Compare to EOM-CCSD? *J. Chem. Theory Comput.* 7 (2011) 456

## Reference

- (74) D. Bousquet, R. Fukuda, P. Maitarad, D. Jacquemin, I. Ciofini, C. Adamo, M. Ehara, Excited-State Geometries of Heteroaromatic Compounds: A Comparative TD-DFT and SAC-CI Study *J. Chem. Theory Comput.* 9 (2013) 2368–2379
- (75) D. J. Seery, D. Britton, The continuous absorption spectra of chlorine, bromine, bromine chloride, iodine chloride, and iodine bromide *J. Phys. Chem.* 68 (1964) 2263
- (76) D. Mackay, W. Y. Shiu, K. C. Ma, S. C. Lee: Handbook of physical-chemical properties and environmental fate for organic chemicals, CRC press., 2006.
- (77) G. K. Sims, E. J. O'Loughlin, R. L. Crawford, Degradation of Pyridines in the Environment *Crit. Rev. Environ. Sci. Technol.* 19 (1989) 309
- (78) S. M. Liu, C. H. Wu, H. J. Huang, Toxicity and Anaerobic Biodegradability of Pyridine and Its Derivatives Under Sulfidogenic Conditions *Chemosphere* 36 (1998) 2345
- (79) M. F. Lin, Y. A. Dyakov, C. M. Tseng, A. M. Mebel, S. H. Lin, Y. T. Lee, C. K. Ni, Photodissociation Dynamics of Pyridine *J. Chem. Phys.* 123 (2005) 054309
- (80) K. A. Prather, Y. T. Lee, The Photodissociation of Pyridine at 193 nm *Isr. J. Chem.* 34 (1994) 43
- (81) B. Wang, B. Liu, Y. Wang, L. Wang, Ultrafast Dynamics of Pyridine in “Channel Three” Region *Int. J. Mass Spectrom.* 289 (2010) 92
- (82) I. Yamazaki, K. Sushida, H. Saba, Vapor-Phase Fluorescence Emissions of Pyridine and its Methyl Derivatives: Excitation-Energy Dependence of Nonradiative Electronic Relaxation *J. Chem. Phys.* 71 (1979) 381
- (83) I. Yamazaki, T. Murao, K. Yoshihara, M. Fujita, K. Sushida, H. Baba, Picosecond Fluorescence Decay From Vibrational Level in the S, ( $n,\pi^*$ ) State of Pyridine Vapour *Chem. Phys. Lett.* 92 (1982) 421
- (84) M. P. Flilscher, K. Andersson, B. O. Roos, Toward an Accurate Molecular Orbital Theory for Excited States: The Azabenrenes *J. Phys. Chem.* 96 (1992) 9204
- (85) D. R. Stapleton, I. K. Konstantinou, D. G. Hela, M. Papadaki, Photolytic Removal and Mineralisation of 2-Halogenated Pyridines *Water research* 43 (2009) 3964
- (86) M. C. Ortega-Liébaña, E. Sánchez-López, J. Hidalgo-Carrillo, A. Marinas, J. M. Marinas, F. J. Urbano, A Comparative Study of Photocatalytic Degradation of 3-Chloropyridine under UV and Solar Light by Homogeneous (Photo-Fenton) and Heterogeneous ( $\text{TiO}_2$ ) Photocatalysis *Appl. Catal., B* 127 (2012) 316
- (87) J. E. Freitas, M. A. El-Sayed, H. J. Hwang, The Wavelength Dependence of the Rates of Internal Energy Redistribution During the Photodissociation of 3-Iodopyridine *J. Phys. Chem.* 99 (1995) 7395
- (88) M. Kadi, J. Davidsson, A. N. Tarnovsky, M. Rasmusson, E. Åkesson, Photodissociation of Aryl Halides in the Gas Phase Studied With Femtosecond Pump-Probe Spectroscopy *Chem. Phys. Lett.* 350 (2001) 93
- (89) G.-J. Wang, R.-S. Zhu, H. Zhang, K.-L. Han, G.-Z. He, N.-Q. Lou, Photodissociation of Chlorobenzene at 266 nm *Chem. Phys. Lett.* 288 (1998) 429
- (90) T. Ichimura, Y. Mori, H. S. N. Nishi, Fast Photodecomposition of Chlorobenzene and m-chlorotoulene in Molecular Beams at 193nm *Chem. Phys. Lett.* 122 (1985) 51
- (91) T. Ichimura, Y. Mori, H. Shinohara, N. Nishi, Photofragmentation of Chlorobenzene: Translational Energy Distribution of the Recoiling Cl Fragment *Chem. Phys.* 189 (1994) 117
- (92) A. Freedman, S. C. Yang, M. Kawasaki, R. Bersohn, Photodissociation of Aryl and Aryl-alkyl Halides at 193 nm: Fragment Translational Energy Distributions *J. Chem. Phys.* 72 (1980) 1028

## Reference

- (93) A. Saha, H. P. Upadhyaya, A. Kumar, P. D. Naik, P. N. Bajaj, Dynamics of C-Cl Bond Fission in Photodissociation of 2-Furoyl Chloride at 235 nm Chem. Phys. 402 (2012) 74
- (94) D. B. Galloway, T. Glenewinkel-Meyer, J. A. Bartz, L. G. Huey, F. F. Crim, The Kinetic and Internal Energy of NO from the Photodissociation of Nitrobenzene J. Chem. Phys. 100 (1994) 1946
- (95) R. T. Carter, A. Hallou, J. R. Huber, Photodissociation of ClNO<sub>2</sub> at 235 nm Chem. Phys. Lett. 310 (1999) 166
- (96) E. J. Hints, X. Zhao, Y. T. Lee, Photodissociation of 2-bromoethanol and 2-chloroethanol at 193 nm J. Chem. Phys. 92 (1990) 2280
- (97) R. K. Sparks, K. Shobatake, L. R. Carlson, Y. T. Lee, Photofragmentation of CH<sub>3</sub>I: Vibrational Distribution of the CH<sub>3</sub> Fragment J. Chem. Phys. 75 (1981) 3838
- (98) M. Kawasaki, K. Kasatani, H. Sato, H. Shinohara, N. Nishi, Photodissociation of Molecular Beams of Halogenated Hydrocarbons at 193nm Chem. Phys. 88 (1984) 135
- (99) D. Krajnovich, L. J. Butler, Y. T. Lee, UV Photodissociation of C<sub>2</sub>F<sub>5</sub>Br, C<sub>2</sub>F<sub>5</sub>I, and 1,2-C<sub>2</sub>F<sub>4</sub>Br J. Chem. Phys. 81 (1984) 3031
- (100) G. N. A. V. Veen, T. Baller, A. E. D. Vries, Photofragmentation of CH<sub>3</sub>Br in the A-Band Chem. Phys. 92 (1985) 59
- (101) L. J. Butler, E. J. Hints, S. F. Shane, Y. T. Lee, The Electronic State-Selective Photodissociation of CH<sub>2</sub>BrI at 248, 210, and 193 nm J. Chem. Phys. 86 (1987) 2051
- (102) H. P. Upadhyaya, A. Saha, A. Kumar, P. D. Naik, Ultraviolet Photodissociation Dynamics of Trichloroethylene at 235 nm Indian J Phys 86 (2012) 165
- (103) O. A. Borg, Y.-J. Liu, P. Persson, S. Lunell, D. Karlsson, M. Kadi, J. Davidsson, Photochemistry of Bromofluorobenzenes J. Phys. Chem. A 110 (2006) 7045
- (104) S.-F. Chen, F.-Y. Liu, Y.-J. Liu, An ab initio Investigation of the Mechanisms of Photodissociation in Bromobenzene and Iodobenzene J. Chem. Phys. 131 (2009) 124304
- (105) X.-B. Gu, G.-J. Wang, J.-H. Huang, K.-L. Han, G.-Z. He, N.-Q. Lou, Photofragment Translational Spectroscopy of 1-Bromo-3-fluorobenzene and 1-Bromo-4-fluorobenzene at 266 nm J. Phys. Chem. A 105 (2001) 354
- (106) X.-B. Gu, G.-J. Wang, J.-H. Huang, K.-L. Han, G.-Z. He, N.-Q. Lou, Substitution Effects of Methyl: Photodissociation of m-, o- and p-chlorotoluene at 266 nm Phys. Chem. Chem. Phys 4 (2002) 6027
- (107) X.-B. Gu, G.-J. Wang, J.-H. Huang, K.-L. Han, G.-Z. He, N.-Q. Lou, Photodissociation of m-Bromotoluene at 266 nm Chem. Phys. 287 (2003) 285
- (108) T. Ichimura, Y. Mori, H. Shinohara, N. Nishi, Photofragmentation of Chlorotoluenes and Dichlorobenzenes: Substituent Effects on the Dissociation Mechanism and Angular Distribution of the Cl Fragment J. Chem. Phys. 107 (1997) 835
- (109) M. Kadi, J. Davidsson, The Photodissociation Dynamics of Dibromobenzenes and Tribromobenzene in the Gas Phase Studied with Femtosecond Pump-Probe Spectroscopy Chem. Phys. Lett. 378 (2003) 172
- (110) M. Kadi, E. Ivarsson, J. Davidsson, The Photodissociation Dynamics of o-, m- and p-Bromotoluene in the Gas Phase Studied With Femtosecond Pump-Probe Spectroscopy Chem. Phys. Lett. 384 (2004) 35
- (111) Y.-J. Liu, P. Persson, H. O. Karlsson, S. Lunell, M. Kadi, D. Karlsson, J. Davidsson, Photodissociation of Bromobenzene, Dibromobenzene and 1,3,5-Tribromobenzene J. Chem. Phys. 120 (2004) 6502

## Reference

- (112) Y.-J. Liu, P. Persson, S. Lunell, Theoretical Study of the Fast Photodissociation Channels of the Monohalobenzenes *J. Phys. Chem. A* 108 (2004) 2339
- (113) D. Paul, H. K. Kim, K. Hong, T. K. Kim, Dynamics of Br(<sup>2</sup>P<sub>1/2</sub>) Formation in the Photodissociation of Bromobenzene *Bull. Korean Chem. Soc* 32 (2011) 659
- (114) C. Qin, J. Wang, R.-S. Zhu, B. Zhang, The REMPI Spectra of o-, m- and p-Bromofluorobenzene and the Photodissociation of p-Bromofluorobenzene *J. Mol. Struct.* 273 (2012) 37
- (115) M. Rasmusson, R. Lindh, N. Lascoux, A. N. Tarnovsky, M. Kadi, O. Kühn, V. Sundström, E. Åkesson, Photodissociation of Bromobenzene in Solution *Chem. Phys. Lett.* 367 (2003) 759
- (116) B. Tang, R. Zhu, Y. Tang, L. Ji, B. Zhang, Photodissociation of Bromobenzene at 267 and 234 nm: Experimental and Theoretical Investigation of the Photodissociation Mechanism *Chem. Phys. Lett.* 381 (2003) 617
- (117) T.-H. Wang, C.-S. Hsu, W.-L. Huang, Y.-H. Lo, Structures, Molecular Orbitals and UV-vis Spectra Investigations on Br<sub>2</sub>C<sub>6</sub>H<sub>4</sub>: A computational Study *Spectrochim. Acta Part A* 115 (2013) 866
- (118) I. Yamazaki, H. Saba, Observation of Fluorescence of Pyridine in the Vapor Phase *J. Chem. Phys.* 66 (1977) 5826
- (119) I. Yamazaki, T. Murao, T. Yamanaka, K. Yoshihara, Intramolecular Electronic Relaxation and Photoisomerization Processes in the Isolated Azabenzene Molecules Pyridine, Pyrazine and Pyrimidine *Faraday Discuss. Chem. Soc.* 75 (1983) 395
- (120) E. Villa, A. Amirav, E. C. Lim, Single-Vibronic-Level and Excitation-Energy Dependence of Radiative and Nonradiative Transitions In Jet-Cooled S, Pyridine *J. Phys. Chem.* 92 (1988) 5393
- (121) C.-P. Ma, L. Yao, M.-F. Ge, Substituent Effects of Halopyridines *J. Mol. Struct.* 881 (2008) 123
- (122) H. P. Stephenson, Solution Spectra and Oscillator Strengths of Electronic Transitions of Pyridine and Some Monosubstituted Derivatives *J. Chem. Phys.* 22 (1954) 1077
- (123) C. S. Hiremath, J. Yenagi, J. Tonannavar, T. Sundius, Ab initio/DFT electronic structure calculations, spectroscopic studies and normal coordinate analysis of 2-chloro-5-bromopyridine *Spectrochim. Acta Part A* 77 (2010) 918
- (124) R. N. Medhi, R. Barman, K. C. Medhi, S. S. Jois, Ultraviolet Absorption and Vibrational Spectra of 2-fluoro-5-bromopyridine *Spectrochim. Acta Part A* 56 (2000) 1523
- (125) X.-P. Zhang, Z.-R. Wei, Y. Tang, T.-J. Chao, B. Zhang, K. C. Lin, Halogen Effect on the Photodissociation Mechanism for Gas-Phase Bromobenzene and Iodobenzene *ChemPhysChem* 9 (2008) 1130
- (126) H. Zhang, R.-S. Zhu, G.-J. Wang, K.-L. Han, G.-Z. He, N.-Q. Lou, Photodissociation of Bromobenzene at 266 nm *J. Chem. Phys.* 110 (1999) 2922
- (127) X.-P. Zhang, Z.-R. Wei, W.-B. Lee, T.-J. Chao, K.-C. Lin, Photodissociation of Dibromobenzenes at 266 nm by the Velocity Imaging Technique *ChemPhysChem* 9 (2008) 1721
- (128) H. Nakano, MCSCF reference quasidegenerate perturbation theory with Epstein-Nesbet partitioning *Chem. Phys. Lett.* 207 (1993) 372
- (129) H. Nakano, R. Uchiyama, K. Hirao, Quasi-degenerate perturbation theory with general multiconfiguration self-consistent field reference functions *J. Comput. Chem.* 23 (2002) 1166

## Reference

- (130) J. R. Gour, P. Piecuch, Efficient Formulation and Computer Implementation of the Active-Space Electron-Attached and Ionized Equation-of-Motion Coupled-Cluster Methods *J. Chem. Phys.* 125 (2006) 234107
- (131) R. Bauernschmitt, R. Ahlrichs, Treatment of Electronic Excitations within the Adiabatic Approximation of time Dependent Density Functional Theory *Chem. Phys. Lett.* 256 (1996) 454
- (132) R. E. Stratmann, G. E. Scuseria, M. J. Frisch, An Efficient Implementation of Time-Dependent Density-Functional Theory for the Calculation of Excitation Energies of Large Molecules *J. Chem. Phys.* 109 (1998) 8218
- (133) K. C. Lau, Y. Liu, L. J. Butler, Photodissociation of 1-bromo-2-butene, 4-bromo-1-butene, and cyclopropylmethyl bromide at 234nm studied using velocity map imaging *J. Chem. Phys.* 125 (2006) 144312
- (134) J. M. Herbert, X. Zhang, A. F. Morrison, J. Liu, Beyond Time-Dependent Density Functional Theory Using Only Single Excitations: Methods for Computational Studies of Excited States in Complex Systems *Acc. Chem. Res.* 49 (2016) 931
- (135) M. R. Silva-Junior, M. Schreiber, S. P. A. Sauer, W. Thiel, Benchmarks for electronically excited states: Time-dependent density functional theory and density functional theory based multireference configuration interaction *J. Chem. Phys.* 129 (2008) 104103
- (136) H.-B. Guo, F. He, B. Gu, L. Liang, J. C. Smith, Time-Dependent Density Functional Theory Assessment of UV Absorption of Benzoic Acid Derivatives *J. Phys. Chem. A* 116 (2012) 11870
- (137) H. P. Upadhyaya, A. Kumar, P. D. Naik, A. V. Sapre, J. P. Mittal, Dynamics of OH Formation in the Dissociation of Acrylic Acid in its ( $n,\pi^*$ ) and ( $\pi,\pi^*$ ) Transitions Excited at 248 and 193 nm *J. Chem. Phys.* 117 (2002) 10097
- (138) H. P. Upadhyaya, A. Kumar, P. D. Naik, Photodissociation Dynamics of Enolic-Acetylacetone at 266, 248, and 193 nm: Mechanism and Nascent State Product Distribution of OH *J. Chem. Phys.* 118 (2003) 2590
- (139) S. Xu, S. T. Park, J. S. Feenstra, R. Srinivasan, A. H. Zewail, Ultrafast Electron Diffraction: Structural Dynamics of the Elimination Reaction of Acetylacetone *J. Phys. Chem. A* 108 (2004) 6650
- (140) D. E. Szpunar, J. L. Miller, L. J. Butler, F. Qi, 193-nm photodissociation of acryloyl chloride to probe the unimolecular dissociation of  $\text{CH}_2\text{CHCO}$  radicals and  $\text{CH}_2\text{CCO}$  *J. Chem. Phys.* 120 (2004) 4223
- (141) K.-C. Lau, Y. Liu, L. J. Butler, Probing the barrier for  $\text{CH}_2\text{CHCO} \rightarrow \text{CH}_2\text{CH} + \text{CO}$  by the velocity map imaging method *J. Chem. Phys.* 123 (2005) 054322
- (142) G.-L. Cui, Q.-S. Li, F. Zhang, W.-H. Fang, J.-G. Yu, Combined CASSCF and MR-CI Study on Photoinduced Dissociation and Isomerization of Acryloyl Chloride *J. Phys. Chem. A* 110 (2006) 11839
- (143) W. S. McGivern, R. Li, P. Zou, S. W. North, Photodissociation Dynamics of  $\text{CH}_2\text{BrCl}$  Studied Using Resonance Enhanced Multiphoton Ionization (REMPI) with time-of-flight Mass Spectrometry *J. Chem. Phys.* 111 (1999) 5771
- (144) F. M. Uber, An Experimental Study of the Ultraviolet Absorption Spectrum of Pyrimidine *J. Chem. Phys.* 9 (1941) 777
- (145) M. A. El-Sayed, Effect of Reducing the Symmetry on the Spectra of Benzene in the 1500-2000 Å Region: Spectra of Pyridine, Pyrimidine, and Pyrazine *J. Chem. Phys.* 36 (1962) 552
- (146) J. E. Parkin, K. K. Innes, The Vacuum Ultraviolet Spectra of Pyrazine, Pyrimidine, and Pyridazine Vapors Part I. Spectra between 1550Å and 2000Å *J. Mol. Spectrosc.* 15 (1965) 407

## Reference

- (147) A. Bolovinos, P. Tsekeris, J. Philis, E. Pantos, G. Andritsopoulos, Absolute Vacuum Ultraviolet Absorption Spectra of Some Gaseous Azabenzenes *J. Mol. Spectrosc.* 103 (1984) 240
- (148) M. H. Palmer, I. C. Walker, M. F. Guest, A. Hopkirk, The electronic states of the azines. III. Pyrimidine, studied by VUV absorption, near-threshold electron energy-loss spectroscopy and ab initio multi-reference configuration calculations *Chem. Phys.* 147 (1990) 19
- (149) B. J. Cohen, H. Baba, L. Goodman, Fluorescence from Pyridazine and Pyrimidine ( $n, \pi^*$ ) States *J. Chem. Phys.* 43 (1965) 2902
- (150) I. Yamazaki, K. Uchida, H. Baba, Fluorescence Spectrum of Pyrimidine Vapor From The Zero-point Vibrational Level of  $^1B_1$  ( $n, \pi^*$ ) state *Chem Lett* 3 (1974) 1505
- (151) K. Uchida, I. Yamazaki, H. Baba, Fast and Slow Fluorescence Emissions From Pyrimidine Vapour *Chem. Phys. Lett.* 38 (1976) 133
- (152) A. E. W. Knight, C. M. Lawburgh, C. S. Parmenter,  $n, \pi^*$  Fluorescence From Selected Vibronic Levels of Pyrimidine Vapor: Frank-Condon Factors and Excited State Anharmonic Coupling *J. Chem. Phys.* 63 (1975) 4336
- (153) G. M. Nathanson, G. M. McClelland, Fluorescence Polarization from  $^1B_1$  pyrimidine: Evidence for Intramolecular Vibration-rotation Energy Transfer in a Highly Excited Molecule *J. Chem. Phys.* 84 (1986) 3170
- (154) Y. Sugahara, N. Mikami, M. Ito, Rotationally Resolved Fluorescence Excitation Spectra of Jet-Cooled Pyrimidine and Pyrimidine-Argon van der Waals Complex *J. Phys. Chem.* 90 (1986) 5619
- (155) J. J. Obrien, G. Fischer, B. K. Selinger,  $n, \pi^*$  Fluorescence From Selected Vibronic Levels of Pyrimidine- $d_4$  Vapour: Franck-Condon Factors, Ground and Excited State Anharmonic Coupling *Chem. Phys.* 117 (1987) 275
- (156) K. K. Innes, J. A. Merritt, W. C. Tincher, S. G. Tilford, Ultra-violet Absorption Spectra of the Diazines *Nature* 187 (1960) 500
- (157) K. K. Innes, H. D. McSwiney, Jr, J. D. Simmons, S. G. Tilford, Analysis of the  $A^1B_1-X^1A_1$  Electronic Transitions of Pyrimidine- $d_0$  and  $d_4$  Vapors *J. Mol. Spectrosc.* 31 (1969) 76
- (158) K. K. Innes, I. G. Ross, W. R. Moomaw, Electronic States of Azabenzenes and Azanaphthalenes: A Revised and Extended Critical Review *J. Mol. Spectrosc.* 132 (1988) 492
- (159) J. A. Konings, W. A. Majewski, Y. Matsumoto, D. W. Pratt, W. L. Meerts, Ultra High-resolution Fluorescence Excitation Spectrum of  $^1B_1$  pyrimidine in a molecular beam Structural Assignments, analysis of Singlet-triplet Perturbations, and Implications for Intersystem Crossing in The Isolated Molecule *J. Chem. Phys.* 89 (1988) 1813
- (160) S. Craddock, P. B. Liescheski, D. W. H. Rankin, H. E. Robertson, The  $r_\alpha$  Structures of Pyrazine and Pyrimidine by the Combined Analysis of Electron Diffraction, Liquid-Crystal NMR, and Rotational Data *J. Am. Chem. Soc.* 110 (1988) 2758
- (161) Z. Kisiel, L. Pszczołkowski, J. C. Lopez, J. L. Alonso, A. Maris, W. Caminati, Investigation of the Rotational Spectrum of Pyrimidine from 3 to 337 GHz: Molecular Structure, Nuclear Quadrupole Coupling, and Vibrational Satellites *J. Mol. Spectrosc.* 195 (1999) 332
- (162) S. Albert, M. Quack, High Resolution Rovibrational Spectroscopy of Pyrimidine: Analysis of the  $B_1$  modes  $\nu_{10b}$  and  $\nu_4$  and  $B_2$  mode  $\nu_{6b}$  *J. Mol. Spectrosc.* 243 (2007) 280

## Reference

- (163) F. Billes, H. Mikosch, S. n. Holly, A comparative study on the vibrational spectroscopy of pyridazine, pyrimidine and pyrazine J. Mol. Struct. (THEOCHEM) 423 (1998) 225
- (164) J. D. Hein, H. Al-Khazraji, C. J. Tiessen, D. Lukic, J. A. Trocchi, J. WMcConkey, Excited Atomic Fragments Following Electron Dissociation of Pyrimidine J. Phys. B: At. Mol. Opt. Phys. 46 (2013) 045202
- (165) J. F. Stanton, R. J. Bartlett, The equation of motion coupled-cluster method. A systematic biorthogonal approach to molecular excitation energies, transition probabilities, and excited state properties J. Chem. Phys. 98 (1993) 7029
- (166) H. Sekino, R. J. Bartlett, A linear response, coupled-cluster theory for excitation energy Int. J. Quantum Chem.: Quantum Chem. Symp. 26 (1984) 255
- (167) R. J. Bartlett, M. Musiał, Coupled-cluster theory in quantum chemistry Rev. Mod. Phys. 79 (2007) 291
- (168) Y. Mochizuki, K. Kaya, M. Ito, Vibronic Coupling of Pyridine in the  $n\pi^*$  Excited State J. Chem. Phys. 65 (1976) 4163
- (169) B. J. Cohen, L. Goodman, Radiationless Paths in the Diazines J. Chem. Phys. 46 (1967) 713